UNIVERSITÀ DEGLI STUDI DI MILANO

Facoltà di Scienze e Tecnologie

Dipartimento di Chimica

COMPOSITE PHOTOCATALYTIC MATERIALS FOR SOLAR ENERGY CONVERSION AND ENVIRONMENTAL APPLICATIONS

PhD Student in Industrial Chemistry (XXXI cycle):

Massimo BERNAREGGI

(R11413)

Supervisor: Prof. **Antonella Gervasini**

Co-supervisor: Prof. **Elena Selli**

Anno accademico 2017 – 2018

Table of Contents

List of Figures

List of Tables

Summary

My PhD project aimed at synthesising, characterising and testing different photocatalytic materials suitable for solar energy conversion and other environmental applications. Among the possible materials, the efforts have been focused on titanium dioxide, in the first part of my thesis, and tungsten trioxide, in the second part, as semiconductor photocatalysts.

Titanium dioxide is the most used photocatalytic material since it fulfils all the necessary requirements to be used as photocatalyst. The main advantage is related to the position of its band edges, which makes it suitable for a multiplicity of environmental/industrial applications. In fact, the electrons excited in its conduction band (CB) are energetic enough to reduce H^+ to H_2, its CB being the positioned at -0.2 eV *vs.* NHE. At the same time, photogenerated holes are strongly oxidising being at highly positive potentials. To overcome the fast electron-hole recombination, surface modification by noble metal nanoparticles (NPs) deposition is widely employed. In this context, the effect of different modification methods, *i.e.* Flame Spray Pyrolysis (FSP) and Magnetron Sputtering (MS), over H_2 production in the methanol photo-steam reforming reaction was tested. The efforts were focused onto TiO_2 modification with copper and platinum NPs.

Firstly, two series of titanium dioxide photocatalysts were prepared by FSP, containing either (i) Cu or (ii) both Cu and Pt nanoparticles. This technique proved to be very effective for the synthesis of single metal-containing TiO_2-based photocatalysts, attaining good

hydrogen production rates with Cu-only and Pt-only modified photocatalysts. The photocatalysts containing both Cu and Pt nanoparticles exhibit a bell-shaped photoactivity trend with increasing copper content, the highest hydrogen production rate being attained with the photocatalyst containing 0.05 wt.% Cu and 0.5 wt.% Pt (TPC0.05).

A second series of copper and/or platinum co-modified materials was obtained by surface modification of pre-existing TiO_2 powders employing pulsed-DC MS technique. Different deposition times and plasma composition during the Cu/Pt sputtering were investigated. HRTEM analyses revealed the presence of well dispersed metal clusters that appeared to be smaller (less than 1 nm) than those attained by other more conventional techniques. XRPD analysis revealed no modification of the TiO_2 crystal structure upon metal deposition. The presence of Pt clusters increased the photoactivity with respect to that of bare TiO_2, up to 7 times in the case of the sample obtained with the longest deposition time, *i.e.* 10 minutes. The plasma composition during Cu sputtering was found to strongly affect the photoactivity of the obtained materials, Cu alone deposited as co-catalyst in an Ar-only atmosphere imparting better photoactivity than Cu sputtered in Ar/O_2. When the deposition of Cu clusters was coupled with the deposition of Pt clusters, an additive effect of the two metals in increasing TiO_2 photoactivity was observed if Cu clusters were sputtered in the absence of oxygen.

The above-described results highlight the possibility to employ those techniques, *i.e.* FSP and MS, in industrial application for the large-scale synthesis of metal-modified powders. The former appears more suitable for single-metal modification, large and fast production. The latter, after proper optimisation of the parameters, is suitable for obtaining

tailored materials with metal clusters in short time and without structural changes.

The interesting results obtained with these Cu/Pt co-modified materials led us to perform a deeper investigation on the behaviour of the two metals under reaction conditions. We aimed at verifying the oxidation state stability of both Cu and Pt nanoparticles under two reaction conditions: methanol photo-steam reforming and methanol aerobic photo-oxidation. Such investigation consisted in X-ray Absorption Near Edge Spectroscopy (XANES) analyses coupled with Modulated Excitation Spectroscopy (MES). Two single metal-modified materials, FP-2Cu/TiO_2 and FP-2Pt/TiO_2, 2 wt.% metal loading, were prepared by flame spray pyrolysis under the same conditions of the previously reported FSP-made photocatalysts. The single metal-modified materials and a bare flame-made TiO_2 were tested in methanol oxidation reactions, under both anaerobic (steam reforming) and aerobic conditions. As expected, the Pt-modified photocatalyst showed the largest H_2 production whereas the copper-modified material exhibited a hydrogen production rate, r_{H_2}, close to that of bare TiO_2. In aerobic oxidation, instead, the presence of metal on the surface of the oxide caused a decrease in photo-activity with respect to bare TiO_2. Thus, a different behaviour of the metal-modified photocatalyst was observed under the two reaction conditions.

In order to explain these differences, Modulated Excitation X-ray Absorption Spectroscopy (MEXAS) experiments were performed. *In-situ* MEXAS is a valuable tool to elucidate the redox dynamics of the metal co-catalysts under photo-catalytic conditions. Under anaerobic conditions both Pt and Cu underwent irreversible reduction in all samples. On the other hand, under aerobic modulation conditions, both Cu and Pt NPs

alone underwent periodical oxidation in O_2 and reduction in CH_3OH. These results help to explain the different role of Cu and Pt co-catalysts under aerobic and anaerobic conditions and their reaction mechanism. In particular, only under aerobic conditions the oxidant reacts over the NPs surface, whereas under anaerobic conditions water adsorbs directly over the TiO_2 surface.

Furthermore, we studied the effect of a pre-reductive treatment over the photocatalytic activity of some selected samples. Indeed, the most active sample, *i.e.* TPC0.05, and the two corresponding single-metal modified materials, TPC0.0 (0.5 wt.% Pt on TiO_2) and TC0.05 (0.05 wt.% Cu on TiO_2), were tested in the methanol photo-steam reforming reaction after being pre-reduced in H_2 at high temperature. After being treated, the TPC0.0 exhibits an almost doubled activity with respect to the as-synthesised sample. On the contrary, a detrimental effect was observed with both Cu-modified photocatalysts.

We also verified the effect of temperature over the photocatalytic activity. The same three samples were thus pre-reduced and then tested in the methanol steam reforming reaction in the 40 – 350 °C temperature range. The TPC0.0 sample showed an increase in H_2 production rate from *ca.* 30 to 450 $mmol \cdot h^{-1} \cdot g_{cat}^{-1}$, associated with both an increased photocatalytic and thermal activity. The selectivity completely changed, switching from complete methanol oxidation at low temperature to the formation of syngas (CO + H_2) at T > 200 °C. Similar effects, but mitigated by the Cu presence, were observed with the Pt/Cu co-modified material. Indeed, syngas production at high temperature was slightly lower. Sample TC0.05, instead, behaved like bare TiO_2. Nevertheless,

temperature still influenced the photoactivity of these last two samples; at high temperature, were r_{H_2} is *ca.* 7 times larger than at 40 °C, the thermal contribution is negligible with respect to the photocatalytic one. Thus, we demonstrated that by carefully selecting the photocatalyst working temperature it is possible to tune the selectivity and the outlet gas composition of a photocatalytic reaction.

A possible alternative to TiO_2 in photocatalytic solar light exploitation consists in the second semiconductor oxide studied in parallel in this thesis, *i.e.* WO_3, having a narrow bandgap (2.6 – 2.8 eV). However, a voltage bias needs to be applied to attain photocatalytic water splitting with such a semiconductor, since its CB is lower in energy than the H^+/H_2 redox potential.

A series of WO_3 films were deposited upon tungsten foil substrates by reactive Radio-Frequency Diode Sputtering (RF-DS). The coatings were prepared starting from a W metal target, in O_2/Ar mixtures with different O_2 content (from 10 up to 40%), and total pressure (1.7 – 3 Pa). The analyses focused on four samples: two monolayer samples, *i.e.* 1L(1.7 Pa) and 1L(3 Pa), deposited at 1.7 and 3 Pa respectively, and two double layer ones, *i.e.* 2L(3+1.7 Pa) and 2L(1.7+3 Pa), obtained by growing WO_3 at the two pressures (first at 3 Pa, then at 1.7 Pa and vice versa). All samples were obtained by deposition in a 40% O_2/Ar atmosphere. The different characterisation techniques, *i.e.* UV-Vis, Mott-Schottky, XPS, revealed that the film deposited at 3 Pa possesses a 0.1 eV narrower bandgap with respect to the 1.7 Pa monolayer (2.8 *vs.* 2.9 eV), due to the up-shifting of the CB energy in the latter. Thus, the deposition of WO_3 at two different pressure leads to the formation of a n-n

heterojunction, suitable for electron-hole separation. This was further confirmed by linear voltammetry analyses: the 2L(3+1.7 Pa) sample exhibited the highest photocurrent among all samples.

Finally, several WO_3 thin films were prepared by magnetron sputtering (MS) aiming at exploring the effect of different operation parameters, such as total pressure, substrate temperature, pulse frequency, off time frequency, total power and deposition source, over the characteristics of the films. The final aim was to optimise the magnetron sputtering set-up for future applications. All samples were deposited over a metal Ti foil, starting from a pure metal W target in a reactive plasma. The films were characterised by UV-Vis-IR diffuse reflectance spectroscopy and by linear sweep voltammetry. Two different sources were compared: pulsed Direct Current (pDC) and Radio Frequency (RF) MS. It was found that the best WO_3 films, in terms of film porosity and photoactivity, can be attained with the pDC MS, at 100 W applied power, 2 Pa total pressure (20% O_2), 3 μs-off time and 100 kHz pulse frequency. The parameter optimisation could be useful for future synthesis of photoactive films for water splitting and other energy and environmental applications or for gas sensing applications.

Riassunto

Lo scopo del mio progetto di dottorato è stato quello di sintetizzare, caratterizzare e testare diversi materiali fotocatalitici adatti alla conversione dell'energia solare e ad altre applicazioni in campo ambientale. Tra i possibili materiali, mi sono focalizzato sul biossido di titanio, nella prima parte della tesi, e sul triossido di tungsteno, nella seconda parte, come materiali fotocatalitici.

Il biossido di titanio è il materiale più studiato in questo ambito poiché soddisfa tutti i requisiti necessari per essere impiegato in fotocatalisi. La caratteristica principale è la posizione dei limiti delle sue bande elettroniche, che lo rendono adatto per una molteplicità di applicazioni ambientali/industriali. Infatti, gli elettroni eccitati nella sua banda di conduzione (CB) sono abbastanza energetici da ridurre H^+ a H_2, dato che la sua CB è posizionata a -0.2 eV *vs.* NHE. Allo stesso tempo, le buche di potenziale sono fortemente ossidanti, essendo posizionate a potenziali estremamente positivi. Per evitare la rapida ricombinazione buca-elettrone, la tecnica più ampiamente utilizzata consiste nella modifica superficiale dell'ossido tramite deposizione di nanoparticelle (NP) di metalli nobili. In questo contesto, è stato testato l'effetto di diversi metodi di sintesi, come la tecnica della pirolisi in fiamma a spruzzo (FSP) e il Magnetron Sputtering (MS), per ottenere campioni attivi nella produzione di H_2 dalla reazione in fase gas di reforming fotocatalitico del metanolo. Gli sforzi si sono concentrati sulla modifica di TiO_2 con NP di rame e/o platino.

Sono state preparate con tecnica FSP due serie di fotocatalizzatori a base di biossido di titanio modificato con (i) solo nanoparticelle di Cu o (ii) con nanoparticelle sia di Cu sia di Pt. Questa tecnica si è rivelata molto efficace per la sintesi di fotocatalizzatori a base TiO_2 modificati con metallo singolo: in presenza di solo Cu o solo Pt, infatti, si sono ottenute buone velocità di produzione di idrogeno (r_{H_2}). La co-presenza di Cu e Pt, invece, causa un incremento di attività per bassi tenori di rame e una successiva diminuzione all'aumentare del carico di questo metallo. Infatti, il campione TPC0.05, contenente lo 0.5% di Pt e lo 0.05% di Cu ha mostrato la migliore fotoattività tra quelli sintetizzati.

Una seconda serie di materiali co-modificati con rame e/o platino è stata ottenuta modificando la superficie di polveri di TiO_2 impiegando la tecnica del magnetron sputtering a corrente continua pulsata (pDC-MS). È stata studiata l'influenza dei tempi di deposizione e della composizione del plasma durante la deposizione di Cu e Pt. Le analisi HRTEM hanno rivelato la presenza di cluster metallici ben dispersi più piccoli (di dimensioni inferiori a 1 nm) rispetto a quelli ottenuti con altre tecniche più convenzionali. Inoltre, le analisi XRPD non hanno rivelato alcuna modifica della struttura cristallina del TiO_2 a seguito della modifica superficiale. La presenza del Pt ha causato un incremento della r_{H_2} rispetto a quella della sola TiO_2 fino a 7 volte nel caso del campione ottenuto con il tempo di deposizione più lungo, 10 minuti. La composizione del plasma durante la deposizione del Cu è risultata in grado di influenzare fortemente la fotoattività dei materiali ottenuti: se il Cu è depositato in un'atmosfera di solo Ar, garantisce una migliore fotoattività rispetto ai campioni modificati con Cu depositato in presenza

di O_2. Quando entrambi i metalli, Pt e Cu, sono stati depositati sulla stessa polvere, è stato osservato un effetto sinergico tra i due, con conseguente aumento di attività fotocatalitica, solo se i cluster di Cu vengono depositati in assenza di O_2.

I risultati sopra riportati evidenziano la possibilità di impiegare entrambe le tecniche, FSP e MS, in applicazioni industriali per la sintesi su larga scala di polveri modificate con metalli. La prima tecnica sembra essere più adatta per sintesi rapide di materiali modificati con un solo metallo. La seconda, a seguito di una corretta ottimizzazione dei parametri, risulta utile per ottenere materiali modificati con cluster metallici in breve tempo e senza modifiche microstrutturali.

Gli interessanti risultati ottenuti con questi materiali co-modificati con Cu e/o Pt ci hanno spinto ad effettuare un'indagine più approfondita sul comportamento dei due metalli in condizioni di reazione. Abbiamo mirato a verificare la stabilità dello stato di ossidazione delle nanoparticelle di rame e di platino in due diverse reazioni: foto-ossidazione di metanolo in ambiente anaerobico e in ambiente aerobico. Tre campioni aggiuntivi sono stati preparati con la tecnica FSP a carichi di metallo maggiori rispetto ai precedenti: due materiali modificati con un solo metallo, FP-2Cu/TiO_2 e FP-2Pt/TiO_2 (carico di Cu e Pt al 2 wt.%). I due campioni e un campione di TiO_2 non modificato sono stati testati in entrambe le reazioni di ossidazione del metanolo. Come previsto, il fotocatalizzatore modificato con Pt ha mostrato la maggiore r_{H_2} mentre il materiale modificato con rame ha mostrato una produzione di H_2 simile a quella del biossido di titanio. In condizioni aerobiche, invece, la presenza di metallo sulla superficie dell'ossido ha causato una diminuzione della fotoattività rispetto al solo TiO_2. Pertanto, è stato osservato un

comportamento diverso dei fotocatalizzatori modificati con metallo nelle due condizioni di reazione.

Al fine di spiegare queste differenze sono state condotte analisi con tecnica *Modulated Excitation X-ray Absorption Spectroscopy* (MEXAS), che accoppia analisi XANES (*X-ray Absorption Near Spectroscopy*) con la *Modulated Excitation Spectroscopy* (MES). Questa tecnica, condotta *in situ*, è uno strumento prezioso per chiarire le dinamiche redox dei co-catalizzatori metallici in condizioni fotocatalitiche. In assenza di ossigeno, sia Pt che Cu subiscono una riduzione irreversibile in tutti i campioni. Al contrario, in condizioni di aerobiche, le NP di Cu e Pt, da sole, hanno subito periodiche ossidazioni in O_2 e riduzioni in presenza di CH_3OH. Questi risultati aiutano a spiegare il diverso ruolo dei co-catalizzatori a base Cu e Pt in condizioni aerobiche e anaerobiche e il loro meccanismo di reazione. In particolare, solo in condizioni aerobiche l'ossidante reagisce sulla superficie delle NP, mentre in condizioni anaerobiche l'acqua si adsorbe direttamente sulla superficie di TiO_2.

È stato successivamente studiato l'effetto della pre-riduzione di alcuni campioni selezionati sull'attività fotocatalitica. I campioni TPC0.05, co-modificato con Pt e Cu, TPC0.0 (0.5 wt.% Pt su TiO_2) e TC0.05 (0.05 wt.% Cu su TiO_2) sono stati testati nella reazione di foto-steam reforming da metanolo dopo essere stati pre-ridotti in H_2 ad alta temperatura. A seguito del trattamento, il campione TPC0.0 ha mostrato un'attività circa doppia rispetto al campione non ridotto. Al contrario, si è osservato un effetto negativo su entrambi i fotocatalizzatori modificati con Cu. Infine, è stato anche studiato l'effetto della temperatura sull'attività fotocatalitica. Gli stessi tre campioni sono stati quindi pre-

ridotti e testati nella stessa reazione nell'intervallo di temperatura 40 – 350 °C. Il campione TPC0.0 ha mostrato un aumento di r_{H_2} da circa 30 a 450 $mmol \cdot h^{-1} \cdot g_{cat}^{-1}$, associato ad una maggiore attività sia fotocatalitica che termica. La selettività della reazione è cambiata completamente, passando dall'ossidazione completa del metanolo a bassa temperatura alla formazione di syngas ($CO + H_2$) a T > 200 °C. Effetti simili, ma attenuati dalla presenza di Cu, sono stati osservati con il materiale di co-modificato Pt/Cu con una produzione di syngas ad alta temperatura leggermente inferiore. Il campione modificato con solo Cu, TC0.05, non ha invece mostrato grandi differenze rispetto al campione di TiO_2 puro. Tuttavia, ad alta temperatura la r_{H_2} è risultata per entrambi i campioni circa 7 volte maggiore rispetto che quella misurata a 40 °C, con un contributo puramente termico trascurabile. È stato così dimostrato che selezionando attentamente la temperatura di lavoro del fotocatalizzatore è possibile variare la selettività e la composizione finale dei prodotti di una reazione fotocatalitica, oltre che l'attività totale del campione.

Una possibile alternativa al TiO_2 in fotocatalisi consiste nel secondo ossido semiconduttore studiato in questa tesi, il WO_3, che possiede un band gap più ristretto (2.6 – 2.8 eV) rispetto al primo. È però necessaria l'applicazione di un *bias* elettrico per ottenere la riduzione dell'acqua a idrogeno a causa del posizionamento della CB a potenziali più positivi della coppia redox H^+/H_2.

Una serie di film WO_3 sono stati depositati su lamine di tungsteno metallico mediante sputtering reattivo a radiofrequenza (RF-DS). I film sono stati preparati usando un target di W metallico, depositando i campioni in una miscela O_2/Ar, a diversi contenuti di O_2 (da 10 a 40%) e

diverse pressioni totali (1.7 – 3 Pa). Le analisi si sono concentrate su quattro campioni: due campioni a singolo strato, 1L(1.7Pa) e 1L(3Pa), depositati rispettivamente a 1.7 e 3 Pa e due a doppio strato, ovvero 2L(3+1.7Pa) e 2L(1.7+3Pa), ottenuti facendo crescere WO_3 alle due diverse pressioni (prima a 3 Pa, poi a 1.7 Pa e viceversa). Tutti i campioni sono stati ottenuti mediante deposizione in atmosfera al 40% di O_2/Ar. Le diverse tecniche di caratterizzazione, UV-Vis, Mott-Schottky, XPS, hanno rivelato che il film depositato a 3 Pa ha un band gap di 0.1 eV più stretto rispetto al monostrato depositato a 1.7 Pa (2.8 *vs.* 2.9 eV), a causa dell'innalzamento della CB in quest'ultimo. Pertanto, la deposizione di WO_3 a due diverse pressioni ha portato alla formazione di una eterogiunzione di tipo n-n, adatta per la separazione elettrone-buca. Ciò è stato ulteriormente confermato dalle analisi di voltammetria lineare: il campione da 2L(3+1.7Pa) ha mostrato la fotocorrente più alta tra tutti i campioni.

Infine, diversi film sottili di ossido di tungsteno sono stati preparati mediante magnetron sputtering per verificare l'effetto che diversi parametri di deposizione, quali pressione totale, temperatura del substrato, frequenza di lavoro, *off time*, potenza totale e sorgente di deposizione, hanno sulle caratteristiche dei film. L'obiettivo finale è stato quello di ottimizzare le impostazioni dello strumento per future applicazioni. Tutti i campioni sono stati depositati su una lamina di Ti metallico, a partire da un target di W puro in un plasma reattivo (contenente ossigeno). I film sono stati caratterizzati attraverso tecniche di spettroscopia di riflettanza diffusa UV-Vis-IR e di voltammetria lineare. Sono state confrontate due diverse sorgenti di deposizione: corrente continua pulsata (pDC) e radio frequenza (RF). Si è constatato

che i migliori film WO_3, in termini di porosità e fotoattività, possono essere ottenuti con pDC MS impostato a 100 W di potenza, con pressione totale a 2 Pa (20% O_2), *off time* di 3 μs e frequenza di lavoro a 100 kHz. L'ottimizzazione dei parametri potrebbe essere utile per le future sintesi di film fotoattivi nella scissione dell'acqua e per altre applicazioni in campo energetico e ambientale, o per applicazioni di gas sensoristica.

Introduction

I.1. Energy and hydrogen production

With the beginning of the industrial revolution in the middle of 19th century, World's population has risen continuously, starting from *ca.* 1 billion and exceeding 7 billion people nowadays.[1] Such a growth is still continuing, with an expected population of 10 billion people within the next 30 years. This, together with an increasing wealth, especially in the Western World and, to a minor extent, also in the developing countries (the so-called BRICS), has required an even larger energy production. Indeed, only in the last 40 years the World's total energy consumption doubled, from 7 billion ton of oil equivalents (btoe) to almost 14.[2] Until the beginning of the 21st century, the main primary energy sources were fossil fuels, *i.e.* coal, oil and natural gas, with minor contributions of nuclear and hydroelectricity power (accounting for less than 15% overall).[3] Then, the increasing attention towards pollution problems connected to the large use of coal and oil led to the development and the exploitation of more environmentally-friendly renewable sources, such as photovoltaics, biomass or wind. These technologies are becoming more and more affordable, stable and cheaper, making their application easier and widespread. Actually,[4] almost 20% of the total energy production is obtained with these sources and their share keeps increasing. Considering the European Union (EU), such results are consistent with the 2020 package target (20% cut in greenhouse gas emissions from 1990 levels, 20% of EU energy from renewables and 20% improvement in energy efficiency).[5] Solar light exploitation, through photovoltaic panels, plays a

major role in this scenario. Indeed, solar energy is the largest and most widespread energy source on Earth, able to afford the World's energy demand of 1 year in 1 h of irradiation.[6,7]

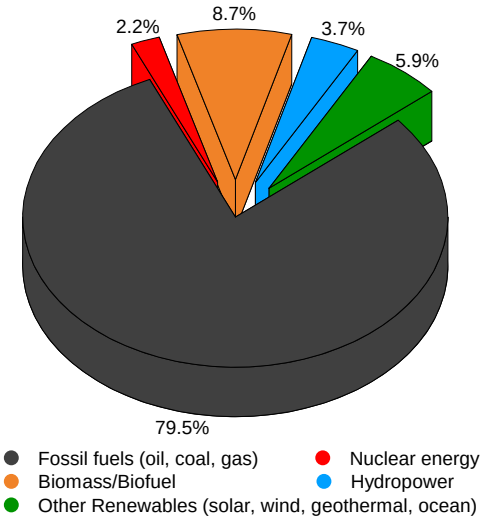

Figure I.1 *Estimated share of total final energy consumption, 2016*

However, the electricity produced by all these forms of energy, both fossil and renewable, can not be easily stored. Thus, the exploitation of renewable energy in transport systems is more difficult. Electric vehicles require stable and durable batteries with limited weight and dimensions and consequently limited capacity. The conversion of renewable sources into storable energy vectors is a parallel route to pursue in order to complete the transition from a fossil fuel-based society into a greener one. Biodiesel and biomasses, together with methane, are among the cleanest energy vectors, due to the limited carbon dioxide emission originated by their combustion.[8,9] Actually, biofuels account for 2.8% of the world energy consumption for transportation, and their growth is slow

due to the uncertainty about feedstock sustainability.[4] A third possible way to decrease our dependence on oil and carbon is the use of hydrogen as a fuel. Already in 1874, Jules Verne in his *The Mysterious Island*, alluded to H_2 as fuel:

"*Yes, my friends, I believe that water will someday be employed as fuel, that hydrogen and oxygen, which constitute it, used singly or together, will furnish an inexhaustible source of heat and light… I believe, then, that when the deposits of coal are exhausted, we shall heat and warm ourselves with water. Water will be the coal of the future.*"

Hydrogen, discovered by Cavendish in 1766, has several advantages over all traditional fuels, so that its implementation in everyday life should be strongly pursued.

First of all, H_2 is the most abundant element in the universe and, on Earth, it is ubiquitous, being present, bound to oxygen, in water molecules. In addition, it is the lightest fuel though characterised by the highest heat combustion, *i.e.* 34 kcal/g, which clearly surpasses those of oil (8.4 – 10.3 kcal/g), coal (7.8 kcal/g) and wood (4.2 kcal/g) in terms of energy per unit mass.[10,11] The main problem related to a large application of H_2-based systems is connected to its storage. Gaseous and liquid H_2 require heavy vessels and a lot of energy to pressurise or liquefy it. Furthermore, under such conditions H_2 becomes dangerous since an accidental mixing with an oxidant (air) could lead to explosions. For this reason, many researchers are looking for novel metal hydride-based materials, able to adsorb and release H_2 in gas form and to store it safely.[10]

Actually, hydrogen production is still bonded to fossil sources. The main processes to produce it are steam methane reforming, partial

oxidation of heavy hydrocarbon fractions, coal and biomass gasification and, to a minor extent, electrolysis in large electrolysers. These processes, apart from the last one, require high temperature and pressure, and this reduces the beneficial impact of using such a gas. Electrolysis, if coupled with photovoltaic panels or wind turbines, can be a green viable route for H_2 production from water.[11–13]

I.2. The third route: photocatalysis

Another possible way for clean hydrogen production finds its origin in the pioneering work of Fujishima and Honda[14] in the early 1970s. The photocatalytic water splitting approach demonstrated that by exploiting the right photocatalytic materials it is possible to obtain hydrogen from water, as in the case of electrolysis. For instance, these two Japanese researchers proved that by irradiating a semiconductor, *i.e.* TiO_2, with a suitable irradiation source, *i.e.* a UV lamp, photocatalytic water splitting can be achieved, according to the reaction:

$$2H_2O \xrightarrow{h\nu} 2H_2 + O_2 \qquad EQ\ I.1$$

where $h\nu$ represents the energy provided by photons.

In the best hypothesis, the same or other analogous reactions (connected to energy production or environmental remediation) might be achieved, employing semiconductor photocatalysts, under solar light irradiation. At mid latitudes the power density of solar radiation is averaged at *ca.* 1000 $W \cdot cm^{-2}$. Before reaching the Earth's surface, the Sun's spectrum resembles that of a black body at 5900 K. After crossing the different atmosphere layers, *i.e.* the stratosphere, the ionosphere and the ozone layer, part of the solar energy is absorbed by gas molecules such as O_3, CO_2 and H_2O. Thus, at sea level the solar spectrum, assumed as

AM1.5 standard, is accounted by *ca.* 4.5% UV photons in the 280 – 400 nm region (mainly UV-A and UV-B), *ca.* 50% of visible light (400 – 900 nm), the remaining being IR and longer wavelength radiations (Figure I.2).

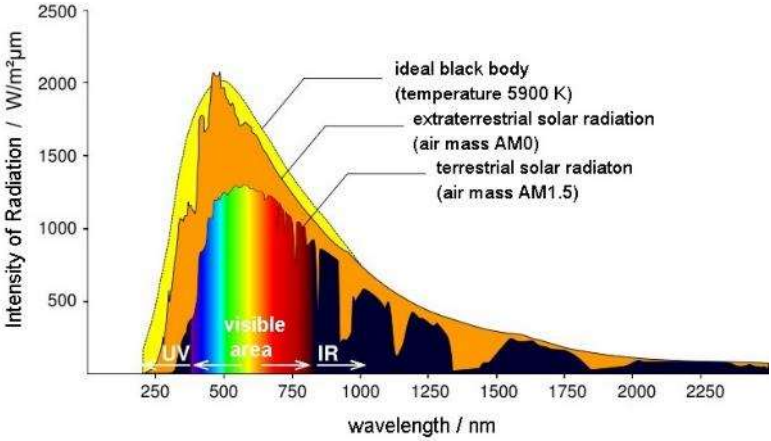

Figure I.2 *Solar spectrum at sea level (AM1.5) compared to the same spectrum in the outer atmosphere, consistent with an ideal black body spectrum at 5900 K.*

In photocatalysis the main aim is to develop materials able to exploit the larger part of solar costless radiation to drive reactions. Photocatalysis usually implies a change in the rate of a chemical reaction or its initial part due to the action of ultraviolet, visible or infrared radiation in the presence of a substance – the photocatalyst – that absorbs light and is involved in the chemical transformation of the reacting species. In heterogeneous photocatalysis, when the catalyst is a solid species, semiconductors are commonly used as photocatalysts. In fact, the electronic structure of these materials has a well-defined band-energy structure, called Band Gap (E_g), with a middle empty energy region where no electronic levels are available. This region extends from the top of the

electron-filled Valence Band (VB) to the bottom of the vacant Conduction Band (CB) (Figure I.3).

Semiconductor photocatalysts can be activated through the absorption of a photon possessing an energy equal or greater than that of the band gap, resulting in the promotion of an electron from the VB to the CB, e^-_{CB}, with the simultaneous generation of an electronic vacancy in the VB, called hole - h^+_{VB}. Both these species are highly reactive and thus either a reduction process driven by e^-_{CB} and/or an oxidation reaction due to h^+_{VB} filling, can occur with substrate molecules adsorbed on the semiconductor surface.

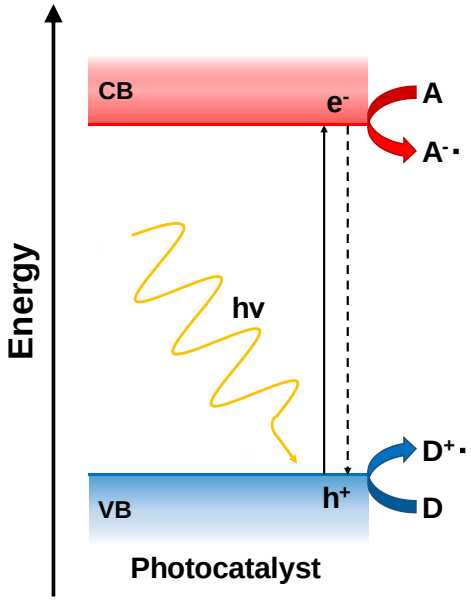

Figure I.3 *Scheme describing semiconductor photocatalyst activation by photons (hv); the photogenerated species, i.e. e^- and h^+, can react with electron acceptor (A) or donor (D) species at the surface of the material.*

In order to have the photogenerated electrons and holes reacting with adsorbed species, the redox potentials of the latter should match those of the photoproduced charge carriers. Thus, for example, photopromoted electrons must have a more negative potential, *i.e.* a higher energy, with respect to that of the $A/A^{-\cdot}$ redox couple (see Figure I.3). If this condition is satisfied, the CB electron is able to reduce the adsorbed species. In the same way, photogenerated holes can accept electrons from donor species if the VB potential is more positive, *i.e.* lower in energy, with respect to the $D/D^{+\cdot}$ redox couple. Considering the above-mentioned water splitting reaction, the conditions to be fulfilled to perform such reaction on the surface of a semiconductor photocatalyst are:

i. The CB must be at $E_{CB} < 0$ V *vs.* NHE (pH = 0) or
   $E_{CB} < -0.41$ V *vs.* NHE (pH = 7)
ii. The VB must be at $E_{VB} > 1.23$ V *vs.* NHE (pH = 0) or
   $E_{VB} < +0.82$ V *vs.* NHE (pH = 7)

In fact, the water splitting reaction process can be divided into two separate semi-reactions, as follows:

i. Reduction reaction $4H^+ + 4e^-_{CB} \rightarrow 2\boldsymbol{H_2}$ $E^0 = 0$ V (pH = 0)
ii. Oxidation reaction $2H_2O + 4h^+_{VB} \rightarrow \boldsymbol{O_2} + 4H^+$ $E^0 = 1.23$ V (pH = 0)

This means that, depending on the desired process, only some photocatalysts are suitable for driving the reaction. Looking at Figure I.4, one can observe that not all the semiconductor photocatalysts reported there are suitable for water splitting.

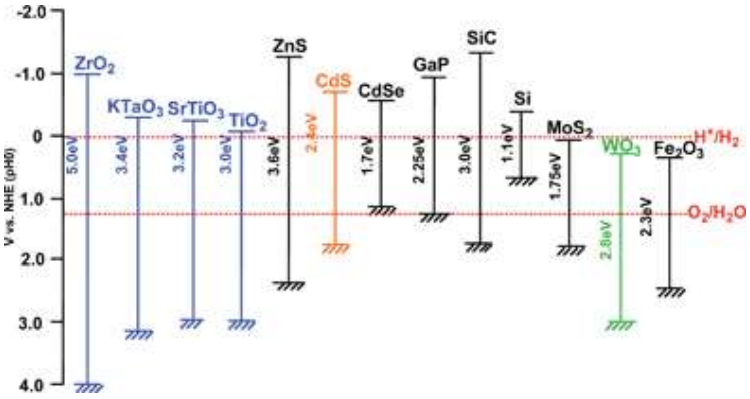

Figure I.4 *Band energy levels of semiconductor photocatalysts and redox potentials of water splitting.*[15]

According to their band positions, ZrO_2, TiO_2, ZnS, CdS, SiC, for example, can drive the photocatalytic water splitting reaction under irradiation of proper wavelength since both VB and CB are correctly positioned with respect to the H^+/H_2 and O_2/H_2O redox couples. Instead, CdSe and Si could only be used for water reduction, *i.e.* hydrogen production, since the VB has a higher energy with respect to the O_2/H_2O couple. On the opposite, materials such as WO_3 or Fe_2O_3 can drive water oxidation but not hydrogen generation, possessing a conduction band too low in energy. The only way to exploit the latter materials in the water splitting reaction, to attain both half-reactions, is the photoelectrochemical approach. The semiconductor acts as an oxygen evolution photoelectrode, while the photopromoted electrons are transferred, through an external circuit, to a counter electrode (usually made of Pt) and boosted by an applied electrical bias so that they possess enough energy to reduce protons.[16]

In addition to charge transfer toward the adsorbed species, also detrimental competitive paths can occur, leading to a photocatalytic

efficiency decrease. Electron-hole pairs recombination, the dotted line in Figure I.3, represents the main deactivation path; being a non-radiative process, the excess of energy is released as heat. It is also possible that, after charge transfer to the adsorbed species, a detrimental back-donation process occurs.

The charge recombination process is facilitated by impurities, lattice defects and crystal imperfections.[17–19] An impurity-free semiconductor is defined intrinsic, whereas a semiconductor doped with impurities is called extrinsic. Doping is a common strategy for engineering the properties of semiconductors since the introduction of aliovalent atoms within the crystal structure of the material causes variations in the electronic structure. For example, considering Si (Group IV), doping with a Group V element, such as P or N, causes the introduction of occupied energy levels within the band gap close to the conduction band, facilitating the promotion of electrons into the CB. On the contrary, doping Si with a Group III element, such as Al or B, introduces vacant energy levels close to the VB, allowing an easier formation of holes in the valence band. The former doping leads to the formation of so-called *n-type* semiconductors, where electrons are the majority charge carriers. When the latter kind of doping is performed, holes are the main charge carriers and they are referred to *p-type* semiconductors. These changes in the electronic structure affect also the so-called Fermi level. This is defined as the energy level where the probability of occupation by an electron is $1/2$ at 0 K. Thus, for pure Si and any other intrinsic semiconductor, the Fermi level (E_F) is located at the mid-point of the band gap. For extrinsic *n-type* semiconductors, E_F is

positioned closer to the CB, while for *p-type* semiconductors it lies closer to the VB.[20]

Since the milestone discovery of Fujishima and Honda,[14] most of the research attention in photocatalysis has been kept on titanium dioxide, due to the exceptional properties of this semiconductor over the already studied ZnO,[21] NiO[22] or CdS.[23] However, in the last few years an increasing number of new photocatalysts have been synthesised and tested as possible alternatives to TiO_2. These materials are not derived from titanium dioxide by any of the usual modifications, such as coupling with an additional phase (heterojunction), doping, or morphological changes. Instead they are completely different compounds with distinct composition and structure. In this context, the feasibility of using some well-known photocatalysts such as ZnO, WO_3 or CdS has been reconsidered in the light of recent advances in nanotechnology. Among these, mixed oxides of transition metals such as V, Nb, or Ta, with main group elements such as Bi, Ga, In, or Sb have been extensively investigated as alternative photocatalytic materials.[15,24,25] Besides, sulphides and nitrides of different metals have been frequently selected to obtain semiconductors with photoactivity in the visible range.[26]

Usually, oxides are more stable against photocorrosion with respect to sulphides and nitrides, but their disadvantage is related to the wide band gap. Indeed, the VB of oxide semiconductors is often positioned almost at the same energy since it is formed by the overlapping of the oxygen *2p* orbitals and the metal cation influences more the position of the CB, constituted by d orbitals. Thus, changing the anion from O^{2-} to N^{3-} or S^{2-} allows to shift the conduction band position to higher energy, reducing the E_g.[26,27]

Aim of the Thesis

As already mentioned, changing semiconductor material is not the only path to follow in order to improve light exploitation. Doping,[28–31] surface metal modification[32–34] or heterojunction systems[35–38] have already demonstrated to be effective for enhancing the photoactivity of deeply investigated semiconductors such as TiO_2 and WO_3. In this thesis project we concentrated our focus over the two most widespread photocatalysts, titanium dioxide and tungsten trioxide.

Titanium dioxide has been studied in terms of its surface modification by deposition of metal nanoparticles, for instance platinum and copper. We observed how the synthetic route affects the final photocatalytic performance, in terms of photocatalytic hydrogen production by methanol photo-steam reforming. The intriguing results led us to perform a deeper investigation of the *in-situ* behaviour of the materials by X-Ray Absorption Spectroscopy (XAS). Furthermore, the effect of temperature over the photocatalytic activity has also been object of preliminary studies.

In the second part of this thesis, results obtained with WO_3 thin films, synthesised by sputtering techniques, are also presented. Those films were tested in the photo-electrochemical water splitting reaction. In this case, we studied the optimisation of a WO_3-WO_3 heterojunction. Such a system was obtained through the engineering of the electronic structure of the oxide by changes in the synthetic conditions, affecting the stoichiometry of the material. Furthermore, an investigation on the influence that several magnetron sputtering deposition parameters have over the photoactivity of WO_3 thin films is presented.

References

1 United Nations, *World Popul. Prospect. 2017*, 2017, 1–46.
2 Agency for Natural Resources and Energy, *Key World Energy Statistics 2017*, OECD, Cambridge, 2017.
3 BritishPetroleum, *BP Statistical Review of World Energy*, London, 2018.
4 REN21, *Renewables 2018 · Global Status Report*, 2018th edn., 2018.
5 E. Commission, 2020 climate & energy package, https://ec.europa.eu/clima/policies/strategies/2020_en, (accessed 10 August 2018).
6 N. S. Lewis and D. G. Nocera, *Proc. Natl. Acad. Sci.*, 2006, **103**, 15729–15735.
7 K. Rajeshwar, R. McConnel and S. Licht, *Solar Hydrogen Generation*, Springer New York, New York, NY, 2008.
8 C. O. Tuck, E. Perez, I. T. Horvath, R. A. Sheldon and M. Poliakoff, *Science*, 2012, **337**, 695–699.
9 A. Demirbas, *Prog. Energy Combust. Sci.*, 2007, **33**, 1–18.
10 I. P. Jain, *Int. J. Hydrogen Energy*, 2009, **34**, 7368–7378.
11 C. J. Winter, *Int. J. Hydrogen Energy*, 2009, **34**, 1–52.
12 S. Shaw and E. Peteves, *Int. J. Hydrogen Energy*, 2008, **33**, 3249–3263.
13 A. Ursua, L. M. Gandia and P. Sanchis, *Proc. IEEE*, 2012, **100**, 410–426.
14 A. Fujishima and K. Honda, *Nature*, 1972, **238**, 37–38.
15 A. Kudo and Y. Miseki, *Chem. Soc. Rev.*, 2009, **38**, 253–278.
16 K. Rajeshwar, *J. Appl. Electrochem.*, 2007, **37**, 765–787.
17 S. W. Verbruggen, *J. Photochem. Photobiol. C Photochem. Rev.*, 2015, **24**, 64–82.
18 N. Serpone, *J. Photochem. Photobiol. A Chem.*, 1997, **104**, 1–12.
19 A. M. Peiró, C. Colombo, G. Doyle, J. Nelson, A. Mills and J. R. Durrant, *J. Phys. Chem. B*, 2006, **110**, 23255–23263.
20 A. W. Bott, *Sol. Energy*, 1964, **8**, 87–91.
21 H. D. Muller and F. Steinbach, *Nature*, 1970, **225**, 728–729.
22 F. Steinbach, *Nature*, 1969, **221**, 657–658.
23 A. V. Pamfilov and Y. S. Mazurkevich, *Ukr. Khimicheskii Zhurnal (Russian Ed.)*, 1962, **28**, 1014–1018.
24 K. Maeda and K. Domen, *J. Phys. Chem. C*, 2007, **111**, 7851–7861.
25 F. E. Osterloh, *Chem. Mater.*, 2008, **20**, 35–54.
26 M. D. Hernández-Alonso, F. Fresno, S. Suárez and J. M. Coronado, *Energy Environ. Sci.*, 2009, **2**, 1231–1257.
27 S. N. Habisreutinger, L. Schmidt-Mende and J. K. Stolarczyk, *Angew. Chemie - Int. Ed.*, 2013, **52**, 7372–7408.
28 M. Asiltürk, F. Sayilkan and E. Arpaç, *J. Photochem. Photobiol. A Chem.*, 2009, **203**, 64–71.
29 M. Ratova, G. T. West, P. J. Kelly, X. Xia and Y. Gao, *Vacuum*, 2015, **114**, 205–212.
30 D. Paluselli, B. Marsen, E. L. Miller and R. E. Rocheleau, *Electrochem.*

Solid-State Lett., 2005, **8**, G301–G303.
31 M. V. Dozzi, A. Zuliani, I. Grigioni, G. L. Chiarello, L. Meda and E. Selli, *Appl. Catal. A Gen.*, 2016, **521**, 220–226.
32 M. V. Dozzi, G. L. Chiarello, M. Pedroni, S. Livraghi, E. Giamello and E. Selli, *Appl. Catal. B Environ.*, 2017, **209**, 417–428.
33 G. L. Chiarello, M. H. Aguirre and E. Selli, *J. Catal.*, 2010, **273**, 182–190.
34 G. L. Chiarello, E. Selli and L. Forni, *Appl. Catal. B Environ.*, 2008, **84**, 332–339.
35 H. Li, W. Zhang, L. X. Guan, F. Li and M. M. Yao, *Mater. Sci. Semicond. Process.*, 2015, **40**, 310–318.
36 J. Low, J. Yu, M. Jaroniec, S. Wageh and A. A. Al-Ghamdi, *Adv. Mater.*, 2017, **29**, 1601694.
37 M. M. Momeni and Y. Ghayeb, *J. Appl. Electrochem.*, 2015, **45**, 557–566.
38 Y. Pihosh, I. Turkevych, K. Mawatari, T. Asai, T. Hisatomi, J. Uemura, M. Tosa, K. Shimamura, J. Kubota, K. Domen and T. Kitamori, *Small*, 2014, **10**, 3692–3699.

First Part:

TITANIUM DIOXIDE MATERIALS

Chapter 1:

TITANIUM DIOXIDE

1.1. TiO_2 and its properties

As one of the earliest studied *n-type* photocatalysts, titanium dioxide has been widely used in environmental purification,[1–4] self-cleaning,[5–7] H_2 production,[8–14] photosynthesis,[15] CO_2 reduction,[16,17] organic synthesis,[18,19] in solar cells,[20–22] etc. Over the past years, TiO_2 attracted a great attention from the scientific community as a photocatalyst, being a non-toxic, environmentally-friendly, relatively cheap, chemically stable (*i.e.* not subject to photoanodic corrosion) solid. Another advantage is that TiO_2 is active in both liquid media (water) and gas atmosphere (air). But the greatest advantage of this semiconductor is connected to its band positions, that make it suitable for a great variety of reactions. Indeed, as for many other oxide semiconductors, the VB of TiO_2 lies at high potential (E^0 = 3.0 V *vs.* NHE at pH = 0), *i.e.* at relatively low energy, giving it high oxidation ability. This explains the wide application of TiO_2 in oxidation reactions relevant for environmental applications. At the same time, the bottom of the CB is located at negative potentials (the exact position depends on the crystal structure of the oxide), making it appropriate for water reduction.

On the other hand, the use of TiO_2 presents some drawbacks such as:[23]

1. small number of photons absorbed in the visible region with the consequent need to irradiate with UV light, due to its relatively large band gap;

2. high recombination rate of the photoproduced electron–hole pairs, a characteristic which is common to all semiconductor photocatalysts;
3. sometimes it is difficult to significantly improve the performances by loading or doping with foreign species, because they may often work as recombination centres;
4. deactivation in the absence of water vapour in gas–solid systems when aromatic molecules must be abated;
5. difficulty to support powdered TiO_2 on some materials.

All these advantages and disadvantages are common to the three crystalline structures of TiO_2: anatase, rutile and brookite. The first two forms are the most used in photocatalysis since they are easier to synthesise, while brookite is a natural phase more difficult to obtain in the laboratory.

Figure 1.1 shows the crystal structure and building blocks of anatase (a), rutile (b) and brookite (c). Anatase and rutile have tetragonal structures while the brookite form is orthorhombic. Anatase and rutile show equal TiO_6 octahedron building blocks in a distorted configuration. In anatase, the octahedron structure is more distorted than in rutile (see Figure 1.1 a and b for comparison). The tetragonal unit cell of anatase has four TiO_2 units and the Ti and O coordination numbers are six and three, respectively. On the other hand, the rutile unit cell contains two TiO_2 units, instead of four, with the same coordination numbers of Ti and O as in anatase.

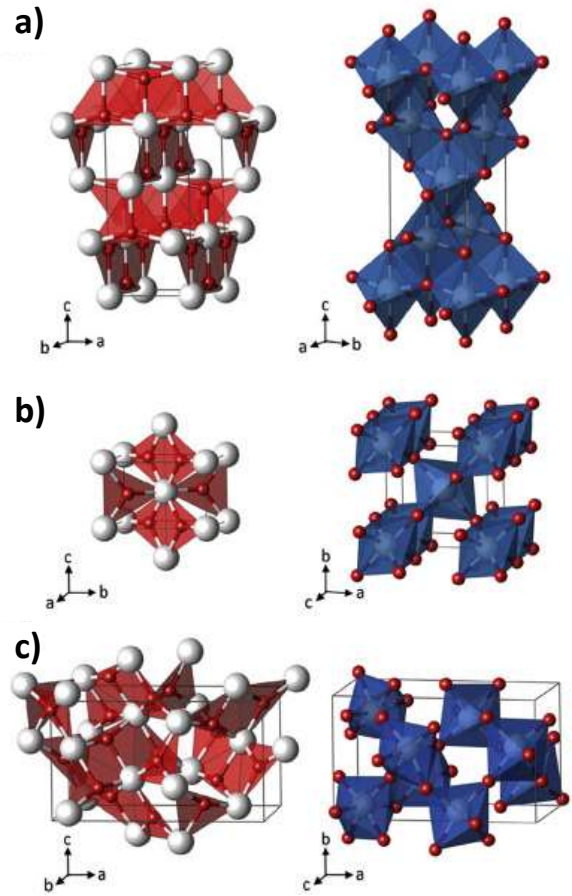

Figure 1.1 *Planar Ti_3O building-block representation (left) and TiO_6 polyhedra (right) for the TiO_2 phases a) anatase, b) rutile and c) brookite (Ti (white); O (red)).*[24] *The experimental lattice parameters are reported in Table 1.1.*

The lattice parameters of the titania phases are shown in Table 1.1. In both anatase and rutile there are two different lengths of titanium-oxygen bonds in each octahedron.[24,25] Anatase has four Ti–O distances of 1.937 ± 0.003 Å and two Ti–O distances of 1.964 ± 0.009 Å. Rutile has

four Ti–O bond lengths of 1.946 ± 0.003 Å, and two of 1.984 ± 0.004 Å. The unit cell volumes of the polymorphs are 34.02 $Å^3$ for anatase, 31.12 $Å^3$ for rutile and 32.20 $Å^3$ for brookite.[24]

Table 1.1 *Lattice parameters, density and band-gap energy of TiO_2 polymorphs.*[24,25]

Phase	Crystal Structure	Space Group	*a* (Å)	*b* (Å)	*c* (Å)	Density (g/cm^3)	Band Gap (eV)
Anatase	Tetragonal	$I4_1/amd$	3.784	3.784	9.515	3.83	3.20
Rutile	Tetragonal	$P4_2/mnm$	4.594	4.594	2.958	4.24	3.00
Brookite	Orthorhombic	*Pbca*	9.16	5.43	6.51	3.17	3.26

Thermodynamically, anatase and brookite are metastable phases, while rutile is the most stable one. Thus, typically rutile can be obtained by calcination of the metastable phases at high temperature. The transition from the anatase to the rutile phase occurs at *ca*. 600 °C at atmospheric pressure.

These differences in crystal structure cause different mass densities and electronic band structures for the two main TiO_2 polymorphs. Indeed, titanium dioxide is characterised by an allowed and indirect band gap, which is equal to 3.2 and 3.0 eV for the anatase and rutile phase, respectively. The band gap bottom-occupied states, *i.e.* the valence band (VB), are mostly O *2p* atomic orbitals-derived, while the conduction band (CB) is mainly Ti *3d*-derived.

The narrower rutile band gap with respect to that of anatase allows the former to absorb more visible light photons. Indeed, while anatase is able to absorb light up to 387 nm (only 3.65% of solar light exploitation) due to its larger E_g, rutile can absorb up to 413 nm (6.1%). Anatase also

has higher surface area than rutile, leading to enhanced adsorption ability and even generation of more active sites (such as oxygen vacancies).

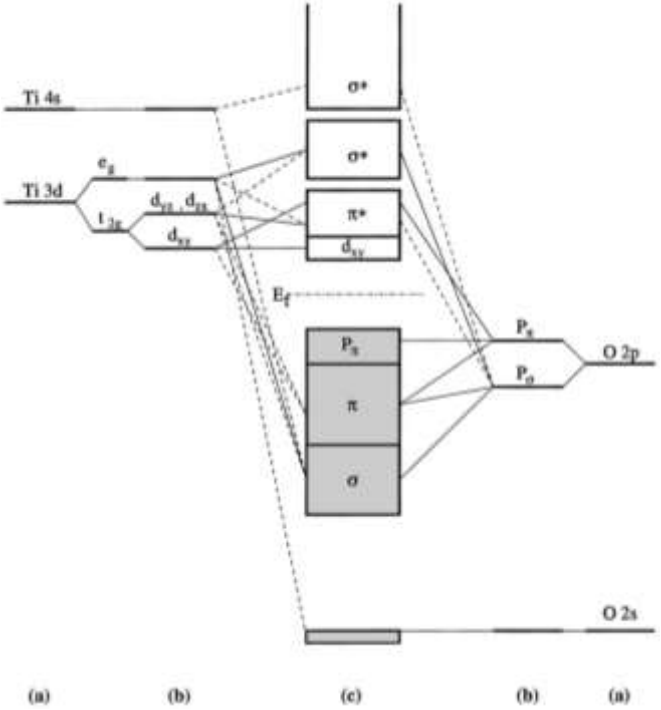

Figure 1.2 *Molecular orbital structure for anatase TiO_2 polymorph. a) atomic levels, b) crystal – field split levels, c) final interaction states.*[26]

Additionally, although rutile has better charge carrier mobility due to its higher crystallinity than anatase, the latter can generate more efficient charge separation due to the existence of a larger number of oxygen vacancies. Because of these advantages, anatase usually shows much higher photocatalytic activity than rutile and thus it is more used in photocatalytic applications, despite the more limited solar light absorption.[25]

1.2. Improving TiO_2 activity

In order to overcome the drawbacks of titanium dioxide, several routes have been followed. These focused mainly to enhance the light harvesting capability of the oxide, by engineering the band gap properties, to improve the charge carrier separation, maximising the efficiency of the reactions. The former target can be achieved by doping TiO_2 either with anions and/or cations, causing vacancies and defects production that alter the colour and the reactivity of the material. The latter, instead, usually consists in modifying the titania surface by metal/metal oxides/metal sulphides nanoparticles or by the formation of heterojunction systems that increase the charge couples lifetime.

1.2.1. Doping with cations

Impurity levels could be introduced within the band gap by replacing Ti atoms with other metal cations in the TiO_2 lattice. These levels can act as electron acceptors or donors, depending on their position in the energy gap, and allow titanium dioxide to absorb visible light. Fe^{3+} and Cr^{3+} doping, for example, extends TiO_2 activity up to 550 nm since, upon light absorption, the 3*d* electrons of the impurity are promoted from the intra-band gap states to the CB of titanium dioxide.[27,28] The beneficial effect of cation doping is not only limited to the light absorption extension, but also to the capability of the dopant ions to trap electrons and/or holes, thus increasing their life. In this perspective, Fe proved to be a better dopant than Cr since the former is able to trap both electrons and holes, while the latter can trap only one type of charge carrier.[29] Similarly to iron, Cu and Mn are better dopants than Cr, Ni and Co for the same reason.[30]

In general, doping TiO_2 with cations with higher valence, such as W^{6+}, Ta^{5+}, Nb^{5+}, results in increasing photoactivity, while the opposite occurs with cations with lower valence.[31] This phenomenon is connected not only to the introduction of intra-band gap states that allow to increase light absorption, but also to the upward shift of the Fermi level towards the conduction band, thus increasing the concentration of e_{CB}^- in the CB.

Considering all possible effects that a cation doping can have, Hoffmann *et al.* concluded that Fe^{3+}, Mo^{5+}, Ru^{3+}, Os^{3+}, Re^{5+}, V^{4+}, and Rh^{3+} at 0.1–0.5 at.% significantly increase the photo-reactivity for both oxidation and reduction, while Co^{3+} and Al^{3+} doping decreases the photoactivity.[32,33]

1.2.2. Doping with anions

Anion doping affects mainly the valence band structure, since dopant atoms substitute oxygen, whose *2p* orbitals constitute the VB. This kind of modification has the same final target of cation doping, *i.e.* extending the light absorption into the visible range. This is possible since anion doping generally causes an upward shift of the valence band, thus decreasing the band gap. Among all possible dopants, *i.e.* C, N, F, P, S, nitrogen is considered the most suitable one for doping the anatase phase since its *p* orbitals mix with those of O, narrowing the band gap by introducing localized state above the VB.[31,34–36] Other elements such as C and P could also introduce some mid-states within the band gap. Carbon-doped TiO_2 is usually obtained by high temperature synthetic processes, such as metal Ti combustion[37] or by flame spray pyrolysis technique;[37] also reactive magnetron sputtering[38,39] or Ti anodization[40] have proved to be viable alternatives. Light absorption extension has been achieved up to 535 nm.[38-40]

In the recent years much attention has been dedicated to fluorine doping. Its beneficial effect is not related to changes into the electronic structure of TiO_2, but to an increased temperature range stability of the anatase phase, allowing for a higher temperature of anatase to rutile phase transition resulting in better material crystallinity.[41–45] Moreover, it can be also exploited for controlling the nanoparticles shape, since its presence as capping agent during the synthesis favours the growth of larger {001} facets possessing high oxidation reactivity.[46,47]

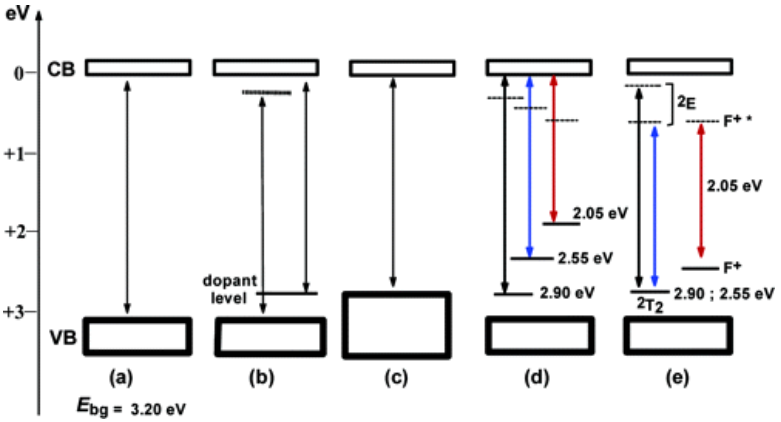

Figure 1.3 *Various schemes illustrating the possible changes that might occur to the band gap electronic structure of anatase TiO_2 on doping with various non-metals: (a) band gap of pristine TiO_2; (b) doped TiO_2 with localized dopant levels near the VB and the CB; (c) band gap narrowing resulting from broadening of the VB; (d) localized dopant levels and electronic transitions to the CB; (e) electronic transitions from localized levels near the VB to their corresponding excited states for Ti^{3+} and F^+ centres.*[48]

1.2.3. Surface metal modification

The aim of metal loading over the surface of titanium dioxide is to enhance charge separation. Indeed, metal nanoparticles deposited on TiO_2

act as sinkholes for photopromoted electrons. Then, the properties of the employed metal influence the final reduction capability of the photocatalyst. Considering H_2 production, this technique demonstrated to be the most efficient in increasing photoactivity. Usually, noble metals, like Pt or Au, are deposited because they possess large a work function (5.12 – 5.93 eV for Pt, 5.31 – 5.47 for Au[49]), meaning that they can easily capture e_{CB}^-.[8,12,14,42,50] In addition, platinum has the lowest activation energy for proton reduction. Consequently, Pt is widely used as co-catalyst for hydrogen production. Gold is also an efficient H_2 evolution co-catalyst, but its effectiveness results to be lower than that of Pt (about 30% less under analogous experimental conditions).[51] Beside these two metals, also Pd, Ag, Rh, Ir have been explored, but without reaching the same efficiency increase.[14,52–55] However, the use of highly expensive and rare noble metals, such as Pt or Au, makes the diffusion of these photocatalysts more difficult due to their large costs. Thus, in recent years the exploitation of less expensive metals, such as Ru, Ni, Co, and Cu, has been investigated. The latter, in particular, has attracted much attention due to its ability to accept not only photopromoted electrons from the CB but also photoexcited electrons directly from the TiO_2 VB through the interfacial charge transfer (IFCT) mechanism. This capability enhances the light exploitation to the visible range, up to 500 nm. However, since copper can be easily oxidised and reduced under mild conditions, its efficiency can vary with the reaction environment, boosting or deteriorating the photoactivity.[4,56–58]

A further and promising development of this research lead to the modification of titania with mixed noble and non-noble metal nanoparticles. The aim was both to increase the photoactivity with respect

to the single metal modified materials and to limit the amount of noble metal loading. It has been found that coupling Au with non-noble metals like Ni, Pd or Co causes an important increase in H_2 production rate. Kowalska *et al.* reported that a NiAu/TiO_2 (1 at.% total loading) exhibited a hydrogen production rate greater than the sum of those obtained with the corresponding single metal modified (0.5 at.% each) due to synergistic effects among the two different metals.[13] Similar results were attained by coupling Ag or Pt with Cu. The last combination proved to be very effective in hydrogen production. However, copper oxidation state becomes essential to guarantee high photocatalytic efficiency. Dozzi *et al.* reported large H_2 production by methanol photo-steam reforming with TiO_2 modified into two subsequent steps by copper and platinum deposition.[59] They demonstrated that, in order to get important improvement in photocatalytic hydrogen production, Cu should be in intimate contact with the substrate surface so that it gets stabilised in a prevailing metal form. If this condition is satisfied, Cu can easily transfer electrons from the CB of titanium dioxide to the outer deposited Pt, which is more efficient in proton reduction.

1.2.4. Surface modification by metal oxides

In addition to metal co-catalysts, also metal oxides and, to a minor extent, metal sulphides can help improving the photoactivity of TiO_2. Regarding H_2 production, nickel is probably the most studied metal in this context. However, it is still uncertain which is the most efficient form. Indeed, NiO is a *p-type* semiconductor, thus its deposition over TiO_2 should generate a *p-n type* heterojunction that promotes charges separation.[60] However, it has been also proposed that Ni/NiO, or NiO_x, is an even better co-catalyst than the pure oxide,[61] but also $Ni(OH)_2$ clusters

lead to high H_2 production rates.[62] However, many oxides used as co-catalysts improve the H_2 production rate indirectly. In fact, oxides like RuO_2, IrO_2, CoO_x, MnO_x are known to be efficient water oxidation catalysts.[63,64] Thus, their deposition over TiO_2 improves charge separation as they accept photogenerated holes from TiO_2 VB and exploit them for O_2 production. In this way, the longer living e_{CB}^- have a higher probability to reduce protons.

Metal sulphides or oxysulphides can be used as efficient co-catalysts for hydrogen production as well, even with great improvement in photoactivity.[65–68] For example, Zhang *et al.* reported a NiS/TiO_2 photocatalyst exhibiting a 30-times higher H_2 production with respect to the bare oxide.[69] Also, MoS_2 has been reported as possible alternative in this field.[70] However, the greatest problem of this type of compounds is their poor stability: they can be easily oxidised and can readily decompose, especially in aqueous solution.[25] These important drawbacks greatly limit their large-scale application.

1.2.5. Heterojunction systems

The use of TiO_2-based multi-oxide materials is very promising to extend the usefulness of titanium dioxide into the visible region. By coupling TiO_2 with a different oxide possessing a structure with a narrower band gap, visible light can be utilized to produce an electron−hole pair. Assuming a favourable band-offset, the electron photoproduced in the CB of the coupled oxide can migrate to the CB of TiO_2, while the hole is trapped in the second material. Thus, redox reactions can occur at the separate surfaces since the likelihood of charge recombination has been diminished. In principle, a heterojunction composite structure can then be rationally designed in order to produce a

favourable band-offset and band positions to develop a photocatalyst suitable for the needs of specific reactions, such as water splitting.[71]

For instance, the combination of TiO_2 and WO_3 seems to be very promising, not only because tungsten trioxide absorbs in the visible region of the spectrum (its band gap is *ca.* 2.8 eV), but mainly because its CB position, lower in energy with respect to that of titanium dioxide, allows for an efficient electron-hole separation by electron transfer from the conduction band of TiO_2 to the CB of WO_3, while photogenerated holes remain trapped within the TiO_2 particles.[72,73] However, the CB of tungsten trioxide is positioned at positive potentials (E_{CB} = +0.2 eV); this implies that such heterojunction is not able to reduce protons and so it can not be use in H_2 production systems, unless an external source of energy, *i.e.* electricity, is applied.

Another example of possible heterojunction is that with ZnO. The aim of this system should be to increase charges lifetime rather than extending the activity in the visible range, since zinc oxide, as TiO_2, possesses a wide band gap (3.2 eV) with a slightly different band position.[74] Similar considerations could be stated for the TiO_2/SnO_2 coupling. The band gap of tin oxide allows it to absorb only UV light.[75] However, recently it has been reported that doping SnO_2 with Co leads to visible light activation of the oxide, opening different possibilities and opportunities for this heterojunction.[76]

A completely different system is that between titanium dioxide and ZrO_2. In this case, the heterojunction is exploited for changing the acidity characteristic of TiO_2 surface. Being more acidic, ZrO_2 has been employed to improve surface adsorption of CO_2 when using TiO_2 for carbon dioxide reduction reaction.[77,78]

References

1 S. N. Frank and A. J. Bard, *J. Am. Chem. Soc.*, 1977, **99**, 303–304.
2 J. J. Murcia, M. C. Hidalgo, J. A. Navío, V. Vaiano, D. Sannino and P. Ciambelli, *Catal. Today*, 2013, **209**, 164–169.
3 T. Sano, N. Negishi, K. Takeuchi and S. Matsuzawa, *Sol. Energy*, 2004, **77**, 543–552.
4 M. Miyauchi, H. Irie, M. Liu, X. Qiu, H. Yu, K. Sunada and K. Hashimoto, *J. Phys. Chem. Lett.*, 2016, **7**, 75–84.
5 T. Watanabe, A. Nakajima, R. Wang, M. Minabe, S. Koizumi, A. Fujishima and K. Hashimoto, *Thin Solid Films*, 1999, **351**, 260–263.
6 A. Nakajima, K. Hashimoto, T. Watanabe, K. Takai, G. Yamauchi and A. Fujishima, *Langmuir*, 2000, **16**, 7044–7047.
7 I. P. Parkin and R. G. Palgrave, *J. Mater. Chem.*, 2005, **15**, 1689–1695.
8 G. L. Chiarello, L. Forni and E. Selli, *Catal. Today*, 2009, **144**, 69–74.
9 G. L. Chiarello, M. V. Dozzi and E. Selli, *J. Energy Chem.*, 2017, **26**, 250–258.
10 A. V. Puga, *Coord. Chem. Rev.*, 2016, **315**, 1–66.
11 M. Jung, J. N. Hart, D. Boensch, J. Scott, Y. H. Ng and R. Amal, *Appl. Catal. A Gen.*, 2016, **518**, 221–230.
12 G. L. Chiarello, E. Selli and L. Forni, *Appl. Catal. B Environ.*, 2008, **84**, 332–339.
13 C. E. Barrios, E. Albiter, J. M. Gracia y Jimenez, H. Tiznado, J. Romo-Herrera and R. Zanella, *Int. J. Hydrogen Energy*, 2016, **41**, 1–14.
14 G. L. Chiarello, M. H. Aguirre and E. Selli, *J. Catal.*, 2010, **273**, 182–190.
15 A. R. Koirala, S. Docao, S. B. Lee and K. B. Yoon, *Catal. Today*, 2015, **243**, 235–250.
16 K. Kočí, L. Obalová and Z. Lacný, *Chem. Pap.*, 2008, **62**, 1–9.
17 I. Grigioni, M. V. Dozzi, M. Bernareggi, G. L. Chiarello and E. Selli, *Catal. Today*, 2017, **281**, 214–220.
18 B. Kraeutler and A. J. Bard, *J. Am. Chem. Soc.*, 1978, **100**, 4317–4318.
19 G. Palmisano, V. Augugliaro, M. Pagliaro and L. Palmisano, *Chem. Commun.*, 2007, **0**, 3425–3437.
20 B. O'Regan and M. Grätzel, *Nature*, 1991, **353**, 737–740.
21 K. L. Chopra, S. R. Das and M. Grätzel, *Nature*, 2001, **414**, 338–344.
22 M. Grätzel, *J. Photochem. Photobiol. C Photochem. Rev.*, 2003, **4**, 145–153.
23 A. Di Paola, E. García-López, G. Marcì and L. Palmisano, *J. Hazard. Mater.*, 2012, **211**–**212**, 3–29.
24 N. Rahimi, R. A. Pax and E. M. A. Gray, *Prog. Solid State Chem.*, 2016, **44**, 86–105.
25 Y. Ma, X. Wang, Y. Jia, X. Chen, H. Han and C. Li, *Chem. Rev.*, 2014, **114**, 9987–10043.
26 R. Asahi, Y. Taga, W. Mannstadt and A. J. Freeman, *Phys. Rev. B*, 2000, **61**, 7459–7465.

27 M. Khan, S. Woo and O. Yang, *Int. J. Hydrogen Energy*, 2008, **33**, 5345–5351.

28 E. Borgarello, J. Kiwi, M. Graetzel, E. Pelizzetti and M. Visca, *J. Am. Chem. Soc.*, 1982, **104**, 2996–3002.

29 R. Dholam, N. Patel, M. Adami and A. Miotello, *Int. J. Hydrogen Energy*, 2009, **34**, 5337–5346.

30 M. I. Litter and J. A. Navío, *J. Photochem. Photobiol. A Chem.*, 1996, **98**, 171–181.

31 K. E. Karakitsou and X. E. Verykios, *J. Phys. Chem.*, 1993, **97**, 1184–1189.

32 W. Choi, A. Termin and M. R. Hoffmann, *J. Phys. Chem.*, 1994, **98**, 13669–13679.

33 J. Choi, H. Park and M. R. Hoffmann, *J. Phys. Chem. C*, 2010, **114**, 783–792.

34 C. Di Valentin, E. Finazzi, G. Pacchioni, A. Selloni, S. Livraghi, M. C. Paganini and E. Giamello, *Chem. Phys.*, 2007, **339**, 44–56.

35 C. Di Valentin, G. Pacchioni and A. Selloni, *Phys. Rev. B*, 2004, **70**, 085116.

36 J. Wang, D. N. Tafen, J. P. Lewis, Z. Hong, A. Manivannan, M. Zhi, M. Li and N. Wu, *J. Am. Chem. Soc.*, 2009, **131**, 12290–12297.

37 S. U. M. Khan, *Science (80-.).*, 2002, **297**, 2243–2245.

38 R. Klaysri, M. Ratova, P. Praserthdam and P. J. Kelly, *Nanomaterials*, 2017, **7**, 113.

39 M. Ratova, R. Klaysri, P. Praserthdam and P. J. Kelly, *Vacuum*, 2018, **149**, 214–224.

40 C. Xu, Y. A. Shaban, W. B. Ingler and S. U. M. Khan, *Sol. Energy Mater. Sol. Cells*, 2007, **91**, 938–943.

41 M. V. Dozzi, A. Zuliani, I. Grigioni, G. L. Chiarello, L. Meda and E. Selli, *Appl. Catal. A Gen.*, 2016, **521**, 220–226.

42 G. L. Chiarello, M. V. Dozzi, M. Scavini, J.-D. Grunwaldt and E. Selli, *Appl. Catal. B Environ.*, 2014, **160**–**161**, 144–151.

43 M. V. Dozzi, C. D'Andrea, B. Ohtani, G. Valentini and E. Selli, *J. Phys. Chem. C*, 2013, **117**, 25586–25595.

44 M. V. Dozzi, L. Artiglia, G. Granozzi, B. Ohtani and E. Selli, *J. Phys. Chem. C*, 2014, **118**, 25579–25589.

45 M. V. Dozzi and E. Selli, *Mater. Sci. Semicond. Process.*, 2016, **42**, 36–39.

46 M. Maisano, M. V. Dozzi, M. Coduri, L. Artiglia, G. Granozzi and E. Selli, *ACS Appl. Mater. Interfaces*, 2016, **8**, 9745–9754.

47 M. Maisano, M. V. Dozzi and E. Selli, *J. Photochem. Photobiol. C Photochem. Rev.*, 2016, **28**, 29–43.

48 N. Serpone, *J. Phys. Chem. B*, 2006, **110**, 24287–24293.

49 D. R. R. Lide, W. M. M. Haynes, G. Baysinger, L. I. Berger, D. L. Roth, D. Zwillinger, M. Frenkel and R. N. Goldberg, *CRC Handbook of Chemistry and Physics*, CRC Press, Boca Raton, FL, Internet V., 2005.

50 M. Bernareggi, M. V. Dozzi, L. G. Bettini, A. M. Ferretti, G. L. Chiarello and E. Selli, *Catalysts*, 2017, **7**, 301.

51 G. R. Bamwenda, S. Tsubota, T. Nakamura and M. Haruta, *J. Photochem. Photobiol. A Chem.*, 1995, **89**, 177–189.

52 T. Sreethawong and S. Yoshikawa, *Catal. Commun.*, 2005, **6**, 661–668.

53 A. V. Korzhak, N. I. Ermokhina, A. L. Stroyuk, V. K. Bukhtiyarov, A. E. Raevskaya, V. I. Litvin, S. Y. Kuchmiy, V. G. Ilyin and P. A. Manorik, *J. Photochem. Photobiol. A Chem.*, 2008, **198**, 126–134.

54 G. Wu, T. Chen, G. Zhou, X. Zong and C. Li, *Sci. China Ser. B Chem.*, 2008, **51**, 97–100.

55 J. Kim, D. Monllor-Satoca and W. Choi, *Energy Environ. Sci.*, 2012, **5**, 7647–7656.

56 H. Irie, S. Miura, K. Kamiya and K. Hashimoto, *Chem. Phys. Lett.*, 2008, **457**, 202–205.

57 K. Kamiya, S. Miura, K. Hashimoto and H. Irie, *Electrochemistry*, 2011, **79**, 793–796.

58 H. Irie, K. Kamiya, T. Shibanuma, S. Miura, D. A. Tryk, T. Yokoyama and K. Hashimoto, *J. Phys. Chem. C*, 2009, **113**, 10761–10766.

59 M. V. Dozzi, G. L. Chiarello, M. Pedroni, S. Livraghi, E. Giamello and E. Selli, *Appl. Catal. B Environ.*, 2017, **209**, 417–428.

60 C.-J. Chen, C.-H. Liao, K.-C. Hsu, Y.-T. Wu and J. C. S. Wu, *Catal. Commun.*, 2011, **12**, 1307–1310.

61 W. Shangguan, *Sci. Technol. Adv. Mater.*, 2007, **8**, 76–81.

62 J. Yu, Y. Hai and B. Cheng, *J. Phys. Chem. C*, 2011, **115**, 4953–4958.

63 B. H. Meekins and P. V. Kamat, *J. Phys. Chem. Lett.*, 2011, **2**, 2304–2310.

64 L. Liu, Z. Ji, W. Zou, X. Gu, Y. Deng, F. Gao, C. Tang and L. Dong, *ACS Catal.*, 2013, **3**, 2052–2061.

65 X. Zong, H. Yan, G. Wu, G. Ma, F. Wen, L. Wang and C. Li, *J. Am. Chem. Soc.*, 2008, **130**, 7176–7177.

66 H. Yan, J. Yang, G. Ma, G. Wu, X. Zong, Z. Lei, J. Shi and C. Li, *J. Catal.*, 2009, **266**, 165–168.

67 F. Zhang, K. Maeda, T. Takata and K. Domen, *Chem. Commun.*, 2010, **46**, 7313–7315.

68 X. Zong, G. Wu, H. Yan, G. Ma, J. Shi, F. Wen, L. Wang and C. Li, *J. Phys. Chem. C*, 2010, **114**, 1963–1968.

69 L. Zhang, B. Tian, F. Chen and J. Zhang, *Int. J. Hydrogen Energy*, 2012, **37**, 17060–17067.

70 Q. Xiang, J. Yu and M. Jaroniec, *J. Am. Chem. Soc.*, 2012, **134**, 6575–6578.

71 M. Dahl, Y. Liu and Y. Yin, *Chem. Rev.*, 2014, **114**, 9853–9889.

72 F. Riboni, L. G. Bettini, D. W. Bahnemann and E. Selli, *Catal. Today*, 2013, **209**, 28–34.

73 Y. Tae Kwon, K. Yong Song, W. In Lee, G. Jin Choi and Y. Rag Do, *J. Catal.*, 2000, **191**, 192–199.

74 R. Zha, R. Nadimicherla and X. Guo, *J. Mater. Chem. A*, 2015, **3**, 6565–

6574.
75 K. Vinodgopal, I. Bedja and P. V Kamat, *Analyzer*, 1996, **4756**, 2180–2187.
76 D. Chandran, L. S. Nair, S. Balachandran, K. Rajendra Babu and M. Deepa, *J. Sol-Gel Sci. Technol.*, 2015, **76**, 582–591.
77 K. Kočí, L. Matějová, M. Reli, L. Čapek, V. Matějka, Z. Lacný, P. Kustrowski and L. Obalová, *Catal. Today*, 2014, **230**, 20–26.
78 B. M. Reddy and A. Khan, *Catal. Rev.*, 2005, **47**, 257–296.

Chapter 2:

EXPERIMENTAL PROCEDURES AND SET-UP

In this chapter the main experimental details about synthesis, particular analytic techniques and testing set-up, related to TiO_2-based materials, are described. The synthesis or the modification of the different photocatalysts was performed both in Prof. Selli's laboratory at the Università degli Studi di Milano and in Prof. Kelly's group at the Manchester Metropolitan University. A specific spectroscopic technique, *i.e.* the Modulated Excitation X-ray Absorption Spectroscopy (MEXAS), exploited at the European Synchrotron Radiation Facility (ESRF) in Grenoble, France, are discussed in detail together with its theoretical principles. Finally, the photocatalytic test set-up used to determine the photocatalytic behaviour of the different materials is also described.

2.1. Synthesis techniques

2.1.1. Flame Spray Pyrolysis

Flame Spray Pyrolysis (FSP) is a scalable, continuous and well-established method for the production of nanoparticles in large quantities. It is a liquid-fed aerosol flame synthesis technique. This means that the metal precursor is a combustible liquid that is sprayed and ignited. Developed in 1977 by Sokolowski *et al.*[1] for the synthesis of Al_2O_3, its widespread adoption started *ca.* 20 years later.[2]

Typically, the burner is composed of a central nozzle, surrounded by a flamelet ring. Through the former, the precursor solution is injected, carried by an O_2 stream, to the supporting flamelet, where it burns. The flame is usually fed by methane or hydrogen and oxygen in stoichiometric ratio to allow the full combustion of the precursor solution. The main difference with respect to the flame-assisted spray pyrolysis (FASP) concerns the precursor solution. In FASP it is an aqueous solution, while in FSP it is an organic solvent solution which can burn, thus contributing to the combustion enthalpy of the system. Of course, the precursors must be soluble in the organic solvent. This difference leads to the main advantage of FSP over FASP: oxide particles are usually nano-sized and homogeneous.[2–4] The collection of nanoparticles depends on the geometry of the system; a glass conveyor, an electrostatic collector or a filter with a backing pump are the most commonly-adopted solutions.

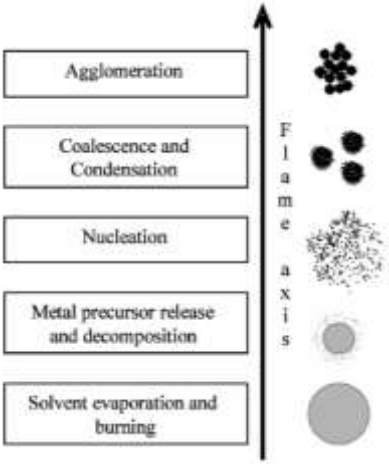

Figure 2.1 *Scheme of the principle of particle formation and growth into the flame.*[5]

We exploited this technique to synthesise several titanium dioxide-based samples in single step. Some of these materials also contained Cu and/or Pt nanoparticles and this implies that not only the TiO_2 precursor, *i.e.* titanium tetraisopropoxide (TTIP), was present in the burning solution, but also those of the two metals. For instance, copper acetate hydrate and hexachloroplatinic acid were the precursors used for Cu and Pt nanoparticles, respectively. The solvent was a mixture of xylenes and propanoic acid. The standard synthesis consisted in burning 50 mL of a 0.6 M TTIP solution, eventually containing the desired amounts of Cu or Pt precursors, in a xylenes and propionic acid mixture. The ratio between the components could vary between 3:2 to 2:1, depending on the amount of additional metal precursors, that are less soluble in non-polar solvents. CH_4 and O_2 gas flows of 2 and 1 $L \cdot min^{-1}$, respectively, were used for the supporting flames, while an O_2 flow of 5 $L \cdot min^{-1}$ was set for the dispersion gas. The pressure drop was set at 2 bar.

High surface area, crystalline materials can be easily obtained through FSP. In case of metal modification of the support oxide, small metal nanoparticles are distributed all over the surface of TiO_2, thus increasing their beneficial effectiveness.[5,6]

2.1.2. Magnetron Sputtering

With respect to the above described technique, *i.e.* FSP, magnetron sputtering and the other techniques described in the following paragraphs were used to modify a pre-existent powder by metal nanoparticles deposition. A more detailed description of this technique will be given in Chapter 8. Briefly, a small magnetron sputtering system equipped with an electrically floating substrate holder underneath the magnetron was employed for TiO_2 powder modification. The shaker mechanism allowed

to continuously mix the powders while Pt or Cu atoms were evaporated by the target. In addition to the single-metal modified materials, in the case of Pt and Cu co-modified powders the two metals were sputtered in subsequent steps. With respect to flame spray pyrolysis, the technique should allow a better control of the nanoparticles dimension.

2.1.3. Grafting

This impregnation technique was exploited for copper deposition over titanium dioxide. Following the work of Irie *et al.*[7,8] and the further development made in our laboratory,[9] 2 g of TiO_2 were first dispersed in ultrapure water (20 mL) and sonicated for 15 min. Then the proper amount of $Cu(NO_3)_2 \cdot 3H_2O$ was dissolved in 1.0 mL of MilliQ water and added to the TiO_2 dispersion. The so-obtained suspension was heated at 90 °C under stirring until all solvent evaporated. The material was then dried at 110 °C for 24 h. Usually, after this modification, also platinum was deposited, but with a different technique (Deposition/Precipitation). According to Irie *et al.*,[7,8] this procedure leads to visible-light sensitivity of titanium dioxide occurring through an interfacial charge transfer mechanism (IFCT), implying that grafted Cu(II) ions can accept photoexcited electrons directly from the valence band of TiO_2. This electron transfer reduces Cu(II) to Cu(I), that is a good oxygen reduction catalyst. Dozzi *et al.*[9] reported that the same system, additionally modified with Pt nanoparticles, strongly enhances charge separation, since Cu(I) re-oxidises back to Cu(II) by transferring the electron to Pt.

2.1.4. Deposition/Precipitation

This technique was employed to deposit platinum nanoparticles on TiO_2. The procedure followed the original Haruta's method[10] modified

with the use of urea as precipitating agent instead of NaOH.[11] For instance, 0.500 g of Cu-grafted TiO_2 were sonicated in ultrapure water for 15 min and then added to a $H_2PtCl_6 \cdot xH_2O$ and urea aqueous solution (0.1 $g \cdot L^{-1}$ and 0.42 M for Pt and urea, respectively). The suspension was stirred for 6 hours and kept at 100 °C. At the end of this treatment, the pH of the solution was *ca*. 8.5. After being precipitated and re-suspended, the powder was treated with an excess of $NaBH_4$ to reduce Pt. Finally, the solid was washed several times in order to remove chlorine ions. This method is suitable for small NPs deposition (smaller than 5 nm).

2.2. Modulated Excitation X-ray Absorption Spectroscopy

2.2.1. X-ray Absorption Spectroscopy

X-ray Absorption Spectroscopy (XAS) is caused by photons with energy larger than 5 keV, the so-called hard X-rays. It is a bulk, element specific technique, able to reveal the short-range order and the local structure of the responsive atoms. A XAS spectrum shows the variation of μ, the absorption coefficient, as a function of the incident X-ray photon energy in the region of the selected binding energy (E_0). A spectrum typically ranges from 150 eV below up to 1000 eV above E_0. The element specificity characteristic of this technique relies on E_0, that depends on the atomic number. Such a wide energy range can be divided into different parts: the X-ray Absorption Near Edge Structure (XANES), from -50 up to +100 eV above E_0, and the Extended X-ray Absorption Fine Structure (EXAFS), from +50 to +1000 eV above E_0 (Figure 2.2).[12]

The former is strongly affected by the oxidation state, the coordination environment and the type of ligands of the absorber atom.

The XANES spectrum appears linear and smooth below the absorption edge, but it increases abruptly at the edge, and then it oscillates above it. The intense peak at the edge is called white line.

EXAFS, instead, is useful to study the local structure of the system, up to *ca.* 10 Å from the absorbing atom. The typical oscillations of an EXAFS spectrum are due to the positive or negative interferences between the outgoing (from the absorbing atom) and the backscattered (from neighbouring atom) photoelectrons. Since these interferences are related to the interatomic distances, the study of the oscillations allows one to determine the local structure around the absorbing atom.[12]

Due to the high energy required, the XAS analyses can be performed only at synchrotron radiation facilities; furthermore, the polychromatic light of these sources allows to easily switch between different energies without important intensity losses. In a synchrotron, an electron, accelerated close to the speed of light, interacts with arrays of magnets along the storage ring. The magnets allow to bend the electron trajectory within the ring, but such a perturbation in the electromagnetic field of the electrons causes the emission of photons in a wide range of wavelengths. The result is the so-called synchrotron light, which is highly brilliant and collimated. Si double monochromators, placed tangentially to the storage ring, are used to select and scan the wavelengths suitable for the analysis.

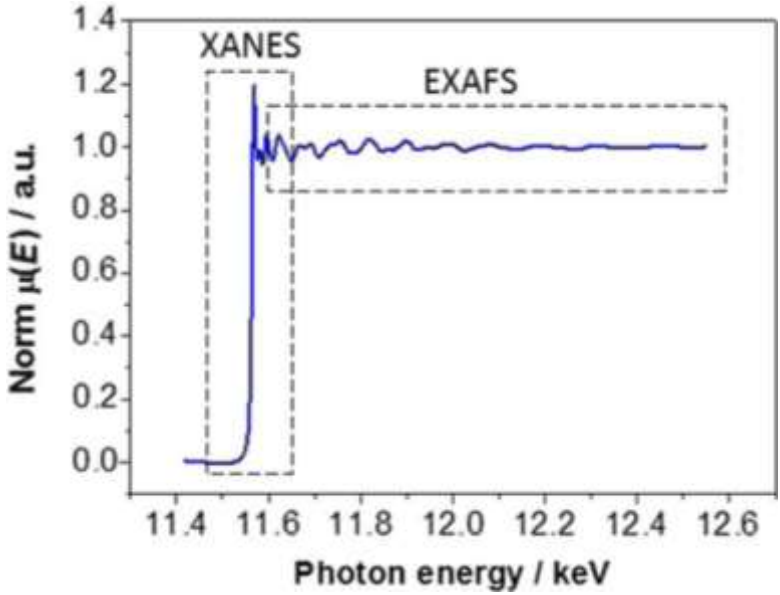

Figure 2.2 *Normalised XAS spectrum with XANES and EXAFS region highlighted.*[12]

2.2.2. Modulated Excitation Spectroscopy

Modulated Excitation Spectroscopy (MES) is a powerful tool to face problems related to the identification of active species and sites of catalysts under *operando* conditions. MES is achieved by the periodic variation of the external conditions in order to obtain a response by the investigated material. Thus, the catalyst is perturbed by continuous changes of an external parameter, *i.e.* concentration, pressure, temperature, potential, pH, etc, while the spectroscopic acquisition is done.[13–15] The species involved in the modulation cycle are expected to change reversibly and periodically with time. To further improve the signal to noise ratio and the response of the active species, thus hiding the signals related to the atoms unaffected by stimulation, the MES exploits

the Phase Sensitive Detection function (PSD), or demodulation function:[14]

$$A(\varphi^{PSD}) = \frac{2}{T}\int_0^T A(t)\sin(k\omega t + \varphi^{PSD})\,dt \qquad EQ\ 2.1$$

Thus, PSD is the function that transforms a set of time-resolved data $A(t)$, with $0 < t < T$ (T being the modulation period), into a new set of phase-resolved data $A(\varphi^{PSD})$, with $0° < \varphi^{PSD} < 360°$ (φ^{PSD} is the demodulation phase angle). $\omega(2\pi/T)$ is the stimulation frequency and K is the demodulation index ($K = 1$ is the fundamental harmonic).[15] In catalysis this technique has been widely used coupled to infrared spectroscopy (IR), such as attenuated total reflection infrared (ATR-IR) spectroscopy,[16–18] infrared reflection-absorption spectroscopy (IRRAS)[14,19,20] or diffuse reflectance infrared Fourier transform spectroscopy (DRIFTS).[21–23] More recently MES-PSD coupled technique has been applied also to X-ray absorption spectroscopy.[13–15] Despite being a bulk analysis, the improvement given by MES to XAS allowed some form of surface sensitivity, making possible to check variation in the oxidation state, the local coordination and the short-range order as a consequence of external stimulation.

Typically, two kinds of stimulation are used in MES: sinusoidal and square-wave stimulations. The former stimulation is simpler to treat theoretically for the quantitative analysis of the responses. On the other hand, square-wave stimulation is usually easier to generate experimentally, in particular in the case of concentration stimulation, which is generated by switching between two flows of different concentrations. The PSD function can be directly applied to analyse responses also to square-wave stimulation and the benefits of MES are

kept, due to the large fundamental frequency component of a square-wave. The time-domain response to a square-wave stimulation can be calculated as the response to the sinusoidal-wave stimulation (See Figure 2.3). Indeed, according to the well-known Fourier decomposition, a square-wave (SW) of amplitude A is written as the sum of sinusoidal waves of odd frequencies:[21]

$$SW = \frac{4}{\pi}A\left(\sin\omega t + \frac{1}{3}\sin 3\omega t + \frac{1}{5}\sin 5\omega t + \cdots\right) =$$

$$= \frac{4}{\pi}A\sum_{n=1}^{\infty}\frac{1}{2n-1}\sin[(2n-1)\omega t] \qquad EQ\ 2.2$$

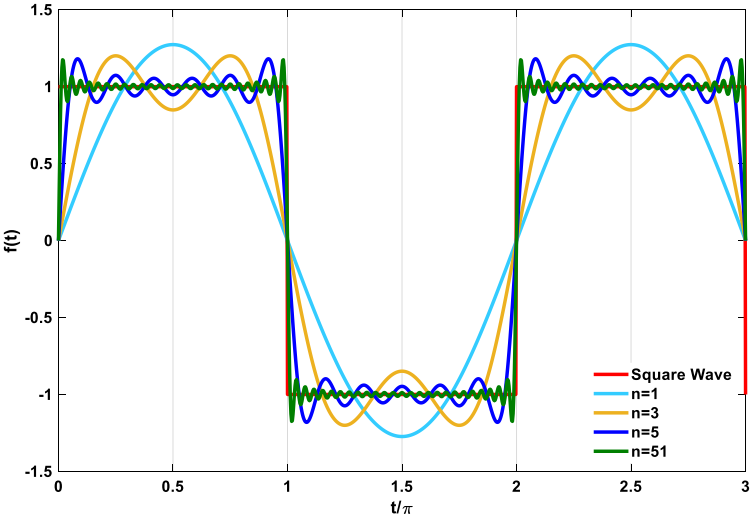

Figure 2.3 *Example of Fourier series for n = 1, 3, 5, 51 compared to the square-wave function. By increasing the order of the sum, the approximation to SW becomes closer.*

Obviously, the real experimental response only resembles a square-wave function. The system can be subjected to phase-lags and delays depending on the set-up geometry and on the experimental

parameters. Usually, short modulation periods cause larger delays and a response more similar to a triangle-wave function (see the black line in the third panel of Figure 2.4), whereas longer modulation periods and more intense stimulation (*i.e.* higher flows or concentrations) allow the system to change and reach the equilibrium within the modulation semi-period (see blue line in the first panel of Figure 2.4).[21] In addition, large cell volumes or long connections (*e.g.* from the flow source) introduce phase lags in the experiment.

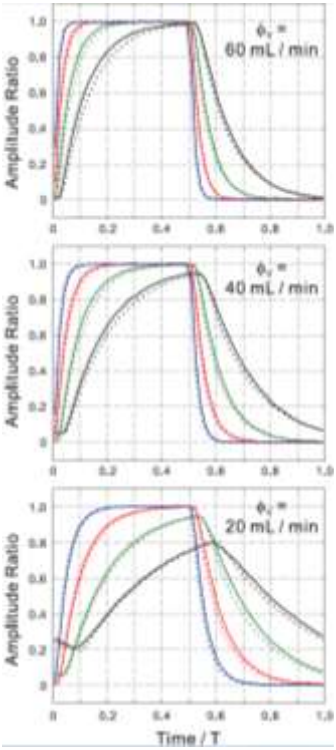

Figure 2.4 *Different system responses obtained by changing gas flow (60, 40, 20 mL·min^{-1} from top to bottom panel) and modulation periods (blue: 516.1 s; red: 257.9 s; green: 128.8 s; black 64.2 s). Solid lines correspond to experiments, dotted lines to simulations.*[21]

In a typical modulation experiment, several modulation periods compose the analysis. Before applying the PSD function, the acquired spectra are averaged over the modulation period. Usually, the first modulation periods are discarded from the averaging step since at the beginning the material has not reached an equilibrium under the experimental conditions. The PSD function is then applied to the averaged single modulation period.

After the application of the demodulation function, the dataset switches from the time domain to the phase domain. The phase resolved spectrum enhances the small differences, hardly observable by comparing two spectra or their difference spectrum, which makes easier the interpretation of the *operando* data. This characteristic becomes particularly relevant when PSD is applied to bulk spectroscopic techniques, such as XAS or XRD; in these scenarios, the external modulation can affect only the surface of the materials or only small nanoparticles distributed over a support, like metal supported catalysts. Thus, the signals related to the bulk or to the support must be suppressed. The Modulated Excitation X-ray Absorption Spectroscopy technique (MEXAS) has already demonstrated that it can massively enhance the spectra variations, related to the external stimulation. It is a valid alternative to the differential Δμ-XANES technique, having a better signal to noise ratio and being intrinsically an *in-situ* analysis. More recent applications of this technique also demonstrated that it can be successfully applied to the EXAFS region of the XAS spectrum with the detection of changes in coordination number and bond distances as low as 1% and 0.001 Å, respectively.[15]

Figure 2.5 shows the difference between the simpler differential spectrum approach and the phase-resolved spectrum.

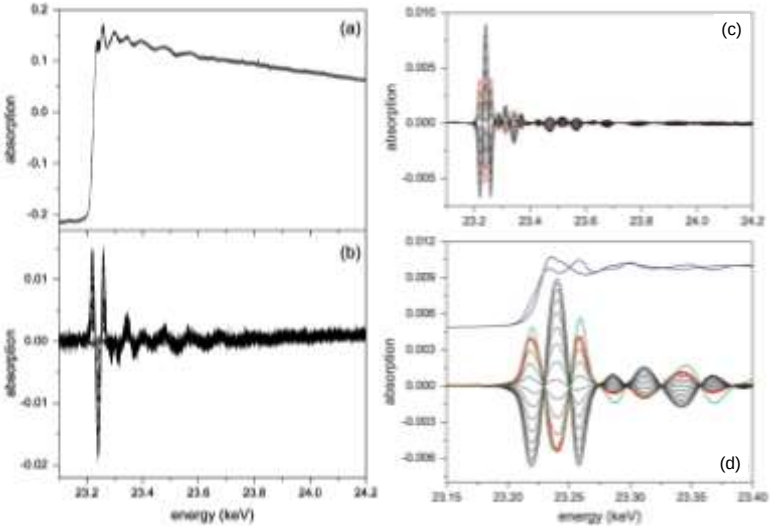

Figure 2.5 *(a) Time resolved XAS spectra at Rh K-edge; (b) Selected difference spectra within a single period of the modulation experiment; (c) Phase-resolved spectra (φ^{PSD} = 0–120°) obtained by phase sensitive detection from spectra in (a); (d) Enlargement of (c) together with the scaled spectra of the Rh foil and bulk Rh_2O_3, for comparison.*[14]

The time resolved spectra at Rh K-edge recorded by Ferri *et al.*[14] at ESRF are shown in panel (a). The difference spectrum in panel (b) were obtained by subtracting the last spectra of each modulation semi-period. This spectrum highlights that changes occur both in the XANES and the EXAFS region, but the background noise covers most of the EXAFS signal. On the opposite, the phase-resolved spectrum, reported in panel (c), clearly shows the variation of the spectrum with respect to the phase domain. Thanks to this technique, the signal to noise ratio allows one to observe also the small changes in the EXAFS part of the spectrum.

Chiarello *et al.* recently demonstrated that the MEXAS technique can be applied to quantitative EXAFS, being able to extrapolate even minute structural changes of the inspected materials under operando conditions.[15]

2.3. Methanol photo-steam reforming set-up

The activity of the TiO_2-based photocatalysts, obtained with the above-reported techniques, was evaluated by means of the gas phase methanol steam reforming reaction. According to the reaction equation

$$CH_3OH + H_2O \xrightarrow{h\nu, TiO_2} 3H_2 + CO_2$$

a molecule of alcohol, *i.e.* methanol, is oxidised up to carbon dioxide with the simultaneous production of 3 molecules of hydrogen. The reaction occurs thanks to the presence of the photocatalyst that, by absorbing photons, oxidises the organic substrate, filling its photogenerated holes, and reduces protons by electron transfer from the CB of the semiconductor to the adsorbed substrate. With respect to a more traditional water splitting reaction, where only water is present as reactant, the presence of the alcohol makes hydrogen production easier since it is a more efficient hole scavenger than water. This leads to longer-living electrons and, thus, to larger H_2 productions.[24]

The photocatalytic tests were performed in a home-made stainless-steel circuit, already described in the literature[25] but modified as shown in Figure 2.6.

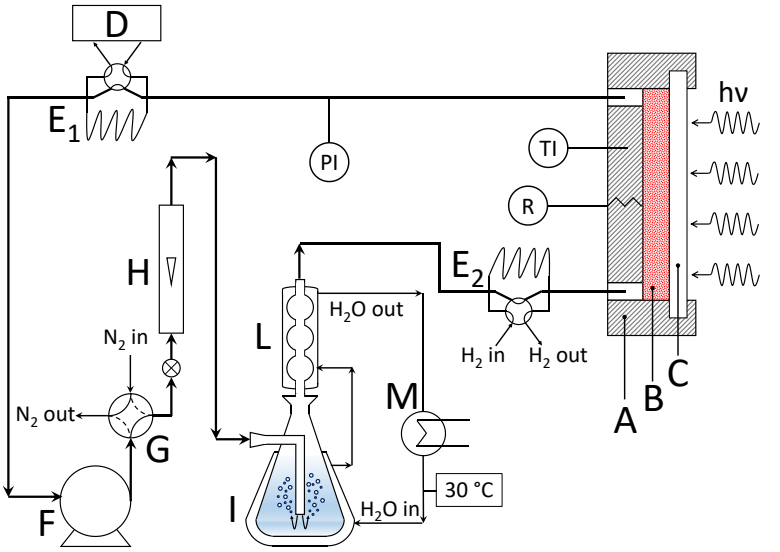

Figure 2.6 *Sketch of the experimental setup for gas phase photocatalytic activity measurements: (A) Stainless-steel photoreactor; (B) Photocatalytic bed; (C) Pyrex-glass window; (D) Detector (gas chromatograph with TC and FID detectors); (E1,E2) Six ways sampling valves; (F) Metal bellows pump; (G) Four ways ball valve (solid line: position for gas-phase recirculation; dotted line: position for purging phase or continuous stream measurements); (H) Manual gas flowmeter; (I) Thermostated flask; (L) Condenser; (M) Thermostat; (TI) and (PI) Temperature and pressure indicators; (R) Heating cartridges.*

Usually, photocatalytic tests were performed in recirculating mode. Thus, the reaction products accumulate in the gas phase or, if soluble, in the liquid phase. Alternatively, when the tests were performed in continuous mode, the (G) valve is switched to the second position, corresponding to the dotted lines, and the gas stream from the cell is discharged while a continuous flow is supplied by a flowmeter connected to a gas bottle.

The gas, after being controlled by the flowmeter (H), bubbles into the liquid solution within the thermostated flask (I) and then passes through the condenser (L). Once it reaches the photocatalytic reactor (A), it comes in contact with the photocatalyst bed (B). From the cell exhaust, the gas flows to the sampling valve connected to the gas chromatograph (D), then to the pump (F) and finally the circuit closes, or the gas can be discharged, depending on the position of (G). Prior to any photocatalytic run, the whole system is purged with pure nitrogen at 100 $mL \cdot min^{-1}$ so that oxygen is removed from both the gas phase and the liquid phase. The purging step lasts *ca.* 30-40 min; during this phase, the (G) valve is positioned as described by the dotted lines. Then, the (G) valve is switched to the other position and the pump is switched on in order to move the gas phase at 60 $mL \cdot min^{-1}$ within the circuit. Before starting the reaction, the gas phase is recirculated for 15 min to ensure an equilibrium with the photocatalyst surface. Then, a shutter is removed and the lamp can irradiate the photocatalytic bed, starting the reaction. In the case of methanol steam reforming reaction, the flask (I) is filled with a 20 vol.% solution of methanol in water, corresponding to a 0.1 molar fraction of the alcohol. Such solution is kept at 30 °C by a thermostat.

The main difference of the actual set-up with respect to that reported in the literature[25] is related to the photoreactor. Previously, it consisted in a Plexiglas cell with a Pyrex glass window on the front, to allow irradiation. Actually, the reactor is made of stainless-steel, and this allows us to heat the cell up to 350 °C when high temperature pre-treatments or reactions are desired. Figure 2.7 shows the technical scheme of the reactor. The material of the reactor also helps in controlling the temperature of the photocatalytic bed, since the dispersion of heat

generated by the lamp (as IR photons) is faster than with Plexiglas. Eventually, an external cooling circuit (compressed air- or water-based) can be connected to the cell (number (6) in Figure 2.7).

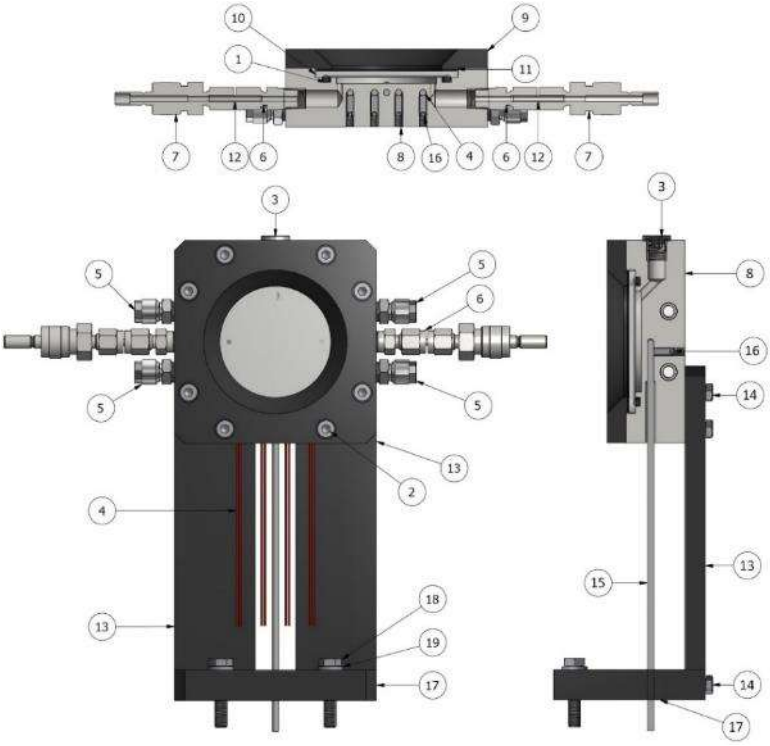

Figure 2.7 *Scheme of the photocatalytic reactor used in the methanol photo-steam reforming: (1) O-ring; (2,14,16) Screws; (3) Cap with O-ring; (4) Heating cartridges; (5) Cooling system connectors; (6,7,12) Quick-fit connectors block; (8) Photoreactor main body; (9) Photoreactor flange; (10) Pyrex window; (11) Gasket; (13) Photoreactor clamp; (15) Thermocouple; (17) Clamp base; (19) Washer.*

The photocatalytic bed can be easily loaded through the hole capped by (3). It consists in quartz beads (20-40 mesh) covered by the

semiconductor powder. For instance, 7.1 g of beads are mixed with the photocatalyst, *ca.* 15 mg, by adding 1 mL of water; then, the mixture is placed in an oven at 70 °C for 2 h. With this treatment, the photocatalyst adheres on the surface of the beads, obtaining high dispersion of the powder.

The photocatalytic bed is irradiated by a 300 W xenon arc lamp (LSH302, LOT-Oriel) through the window. Its emission spectrum (reported in Figure 2.8) ranges from 350 to the IR region.

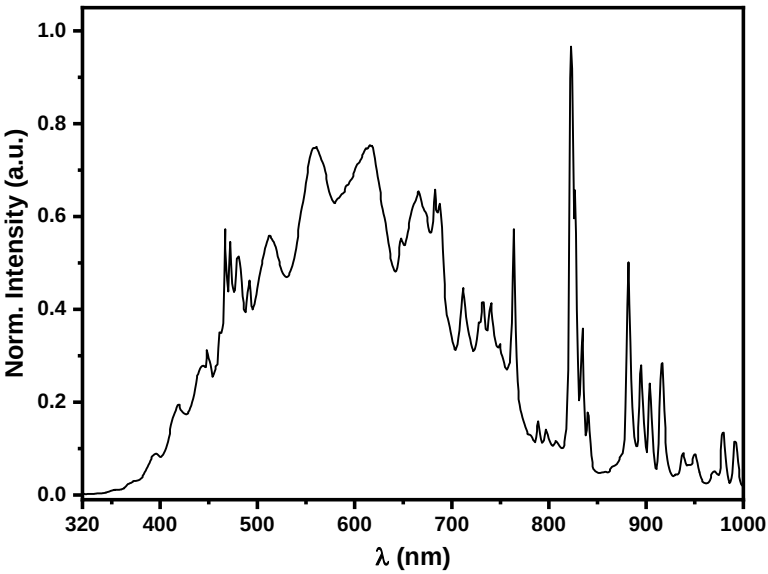

Figure 2.8 *Normalised emission spectrum of the 300 W Xe arc lamp used with the methanol steam reforming set-up.*

The gas chromatograph (GC, Agilent 6890N) is equipped with two columns, a HP-PLOT U to resolve hydrocarbons and a Molesieve 5A for permanent gases separation, and two detectors, a Thermo-Conductivity Detector (TCD) and a Flame Ionisation Detector (FID). The latter is

coupled with a methanation system, based on a Ni catalyst, to transform CO_2 and CO into CH_4 before the FID. The carrier gas is N_2. A typical chromatogram is reported in Figure 2.9: the top signal is related to the FID, the bottom to the TCD.

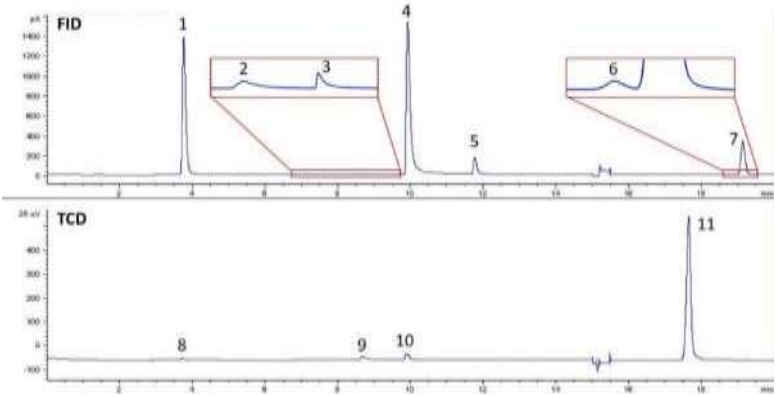

Figure 2.9 *Typical chromatogram recorded under recirculating conditions with a flame-made Pt-modified sample. FID detector on top, TCD detector at bottom. Peaks: 1 and 8) CO_2; 2) H_2CO; 3 and 9) H_2O; 4 and 10) MeOH; 5) CH_3OCH_3; 6) CH_4; 7) CO; 11) H_2.*

During the methanol steam reforming reaction, we usually observed CO_2 (1), H_2CO (2), H_2O (3), CH_3OH (4), CH_3OCH_3 (5), CH_4 (6) and CO (7) with the flame detector and CO_2 (8), H_2O (9), CH_3OH (10), H_2 (11) with the thermal conductivity detector. Thanks to a previous calibration, peaks (1), (2), (6), (7) and (8) allow the quantification of the corresponding products. In addition to these products, also formic acid is quantified by ionic chromatography (IC). The analysis is performed with a Metrohm 761 Compact IC instrument on the solution of the flask at the end of the kinetic run.

In the case of continuous tests, with the 4-way valve (G) switched to the dotted line position (Figure 2.6), the gas flow during the run was set at 60 mL·min^{-1} by means of an electronic flowmeter (EL-FLOW Base, Bronkhorst). Additionally, a second bubbling flask, filled with a $NaHCO_3/Na_2CO_3$ solution, was positioned at the exhaust of the system, in order to trap the photoproduced formaldehyde and formic acid. These two products were quantified by the colorimetric Nash's method and by IC analyses, respectively, at the end of the photocatalytic test. Some continuous tests were performed by following a controlled temperature slope with a 2 °C·min^{-1} gradient, starting from 40 °C up to 350 °C. In such scenario, the photocatalyst was pre-treated in order to reduce the co-catalyst to its metal state. Indeed, the reductive treatment was achieved by heating the reactor up to 350 °C (10 °C·min^{-1}) and keeping at that temperature for 30 min under a 10 vol.% H_2/N_2 flow.

The results of photocatalytic tests are usually reported as H_2 production rate (r_{H_2}), obtained as the slope of the straight lines of the produced hydrogen amount (normalized per unit catalyst weight) *vs.* the irradiation time plots. The selectivity in hydrogen production is calculated from the rates of CO_2, CO, H_2CO and HCOOH formation (r_{CO_2}, r_{CO}, r_{H_2CO} and r_{HCOOH}), as the ratio between these latter and the rate of H_2 production from methanol, by taking into account the stoichiometry of the corresponding formation reactions:

$$CH_3OH + H_2O \xrightarrow{hv,TiO_2} 3H_2 + CO_2 \qquad S_{CO_2} = \frac{3r_{CO_2}}{r_{H_2}}$$

$$CH_3OH \xrightarrow{hv,TiO_2} 2H_2 + CO \qquad S_{CO} = \frac{2r_{CO}}{r_{H_2}}$$

$$CH_3OH \xrightarrow{hv,TiO_2} H_2 + H_2CO \qquad S_{H_2CO} = \frac{r_{H_2CO}}{r_{H_2}}$$

$$CH_3OH + H_2O \xrightarrow{hv,TiO_2} 2H_2 + HCOOH \qquad S_{HCOOH} = \frac{2r_{HCOOH}}{r_{H_2}}$$

Furthermore, the same system was also exploited for methanol oxidation reaction in the presence of O_2. Instead of outgassing in pure N_2, the reactor was purged in air (O_2:N_2, 20:80) and the flask was filled with methanol only. In order to reach similar methanol activity coefficient, with respect to those under steam reforming conditions, the flask was cooled down to -15 °C. The reaction was performed in continuous mode.

References

1 M. Sokolowski, A. Sokolowska, A. Michalski and B. Gokieli, *J. Aerosol Sci.*, 1977, **8**, 219–230.

2 R. Strobel, A. Baiker and S. E. Pratsinis, *Adv. Powder Technol.*, 2006, **17**, 457–480.

3 S. E. Pratsinis and S. Vemury, *POWDER Technol.*, 1996, **88**, 267–273.

4 L. Mädler, H. K. Kammler, R. Mueller and S. E. Pratsinis, *J. Aerosol Sci.*, 2002, **33**, 369–389.

5 G. L. Chiarello, I. Rossetti and L. Forni, *J. Catal.*, 2005, **236**, 251–261.

6 G. L. Chiarello, D. Ferri and E. Selli, *Appl. Surf. Sci.*, 2018, **450**, 146–154.

7 H. Irie, S. Miura, K. Kamiya and K. Hashimoto, *Chem. Phys. Lett.*, 2008, **457**, 202–205.

8 H. Irie, K. Kamiya, T. Shibanuma, S. Miura, D. A. Tryk, T. Yokoyama and K. Hashimoto, *J. Phys. Chem. C*, 2009, **113**, 10761–10766.

9 M. V. Dozzi, G. L. Chiarello, M. Pedroni, S. Livraghi, E. Giamello and E. Selli, *Appl. Catal. B Environ.*, 2017, **209**, 417–428.

10 M. Haruta, *Catal. Today*, 1997, **36**, 153–166.

11 M. V. Dozzi, L. Prati, P. Canton and E. Selli, *Phys. Chem. Chem. Phys.*, 2009, **11**, 7171–7180.

12 G. S. Patience, *Experimental methods and instrumentation for chemical engineers*, Elsevier B.V., Second edi., 2017, vol. 6.

13 D. Ferri, M. A. Newton and M. Nachtegaal, *Top. Catal.*, 2011, **54**, 1070–1078.

14 D. Ferri, M. S. Kumar, R. Wirz, A. Eyssler, O. Korsak, P. Hug, A. Weidenkaff and M. A. Newton, *Phys. Chem. Chem. Phys.*, 2010, **12**, 5634–5646.

15 G. L. Chiarello and D. Ferri, *Phys. Chem. Chem. Phys.*, 2015, **17**, 10579–10591.

16 R. Wirz, T. Bürgi and A. Baiker, *Langmuir*, 2003, **19**, 785–792.

17 A. Urakawa, R. Wirz, T. Bürgi and A. Baiker, *J. Phys. Chem. B*, 2003, **107**, 13061–13068.

18 T. Bürgi and A. Baiker, *J. Phys. Chem. B*, 2002, **106**, 10649–10658.

19 N. Maeda, A. Urakawa and A. Baiker, *J. Phys. Chem. C*, 2009, **113**, 16724–16735.

20 A. Urakawa, N. Maeda and A. Baiker, *Angew. Chemie - Int. Ed.*, 2008, **47**, 9256–9259.

21 A. Urakawa, T. Bürgi and A. Baiker, *Chem. Phys.*, 2006, **324**, 653–658.

22 A. Urakawa, T. Bürgi and A. Baiker, *Chimia (Aarau).*, 2006, **60**, 231–233.

23 A. Urakawa, T. Bürgi, H.-P. P. Schläpfer and A. Baiker, *J. Chem. Phys.*, 2006, **124**, 054717.

24 G. L. Chiarello, D. Ferri and E. Selli, *J. Catal.*, 2011, **280**, 168–177.

25 G. L. Chiarello, L. Forni and E. Selli, *Catal. Today*, 2009, **144**, 69–74.

Chapter 3:

FLAME-MADE Cu/TiO_2 AND $Cu-Pt/TiO_2$ PHOTOCATALYSTS FOR HYDROGEN PRODUCTION

3.1. Introduction

The continued use of fossil fuels led to an increased greenhouse effect; thus, renewable and cleaner energy sources are immediately required. As already discussed in the Introduction, hydrogen is considered the main alternative to fossil fuels and technologies based on H_2 exploitation as an energy vector are already mature, such as fuel cells or internal hydrogen combustion engines.[1,2] Photocatalysis can provide a straightforward route to hydrogen production from water solutions, possibly converting solar light into chemical energy in the form of H-H bond.

Titanium dioxide still remains the most widely investigated photocatalyst oxide due to its advantageous physical and chemical properties.[3,4] As mentioned in Chapter 1, the fast recombination of photoproduced electron-hole couples can be overcome by modifying TiO_2 with noble metal (Au, Ag, Pd, Pt) nanoparticles (NPs).[5] Additionally, the rate of photocatalytic hydrogen production from water can be largely increased by performing the reaction in the presence of organic compounds that scavenge the holes photoproduced in the

semiconductor valence band (VB) more efficiently than water, making the reaction irreversible.[6–11]

Aiming at enhancing the photoactivity of titanium dioxide by modification with non-noble metals (*e.g.*, Ni, Cu, Co), thus reducing the photocatalyst costs, Irie *et al.*[12] deposited copper on titanium dioxide powders by grafting.[13] In fact, Cu^{2+} ions are able (i) to accept electrons from the conduction band (CB) of TiO_2, since the redox potential of the Cu^{2+}/Cu^{+} couple is more positive than the CB edge of TiO_2; and (ii) to accept photoexcited electrons directly from the VB of TiO_2, also under visible light irradiation. Both these electron transfer paths contribute to improve the separation of photoproduced charge carriers, with a consequent photoactivity enhancement.[10]

In this context, synergistic effects in photoactivity have been observed in the case of copper-platinum co-modified TiO_2 when small amounts of Cu were deposited together with Pt NPs, under both aerobic[14] and anaerobic conditions.[15,16] A strong synergistic effect between copper and platinum NPs deposited over TiO_2 has been recently demonstrated in hydrogen production by methanol photo-steam reforming by our research group.[17]

In this chapter, we investigate another, potentially less time consuming, synthetic path to produce Cu and Cu-Pt co-modified TiO_2 photocatalysts in single step, *i.e.*, flame spray pyrolysis (FSP), and report on the structural characterisation of the so obtained materials in relation to their photoactivity in methanol photo-steam reforming. The FSP technique demonstrated to be an effective method to synthesise TiO_2 photocatalyst powders containing noble metal NPs with high anatase content and crystallinity, high surface area and excellent metal

dispersion,[18–21] which are particularly suitable for photocatalytic hydrogen production from aqueous solutions. In addition, three photocatalysts obtained either by grafting copper and/or by depositing platinum by wet methods on flame-made TiO_2 were also investigated for comparison.

3.2. Materials and Methods

3.2.1. Synthesis of the Photocatalysts

Except for commercial P25 TiO_2 from Degussa (Evonik), all investigated photocatalysts were home-prepared by FSP in a single step,[22] employing a commercial FSP system (NPS10 Tethis S.p.A.). The precursor solutions to be burned were prepared by mixing 25 mL of a 1.2 M titanium(IV)-tetraisopropoxide (TTIP) solution in xylene with a fixed volume (*i.e.*, 5 mL) of a Pt-containing mother solution and/or variable volumes of a Cu-containing solution. This latter was prepared by dissolving 0.381 g of copper acetate monohydrate into 100 mL of propanoic acid. The Pt-containing mother solution was prepared by dissolving 0.135 g of hexachloroplatinic acid (30 wt.% real Pt content) into 50 mL of propanoic acid.

To maintain the combustion enthalpy constant in all synthesis, the xylene to propanoic acid volume ratio was, thus, kept fixed (7:4) by diluting all solutions with 10 mL of xylene and with the required volume of propanoic acid, up to a 50 mL constant final volume.

The so-obtained solutions were injected into the burner at 4 $mL \cdot min^{-1}$ by means of a syringe pump through a capillary tube and dispersed by a pure oxygen flow (5.0 $L \cdot min^{-1}$). The spray was ignited by a methane/oxygen flamelet ring surrounding the nozzle. The methane and

oxygen flow rates were 1.0 $L \cdot min^{-1}$ and 2.0 $L \cdot min^{-1}$, respectively, and the pressure drop across the nozzle was kept constant at 2 bar. The obtained powders were collected on glass fiber filters (Whatman, model GF6, 257 mm in diameter) positioned 64 cm over the burner, on top of a steel vessel connected to a vacuum pump (Seco SV 1040C by Busch).

Two series of photocatalysts were synthesized: the first series, labelled FP-(X)Cu-T, consisted of copper modified titanium dioxide powders; the second series, labelled FP-(X)Cu/Pt-T, consisted of platinum and copper containing powders. X corresponds to the Cu/Ti nominal weight percent ratio, ranging from 0 to 0.5, while the Pt/Ti nominal weight percent ratio in the second series was fixed at 0.5. Bare titanium dioxide containing no Cu and Pt NPs was also produced by FSP and named FP-T.

Three additional samples were prepared by combining different metal NPs deposition techniques. Sample (0.1)Cu/Pt-FP-T was obtained from FP-T, by grafting 0.1 wt.% of copper[23] and 0.5 wt.% of platinum by the deposition-precipitation (DP) method,[24] in two consecutive steps. Sample (0.1)Cu/FP-Pt-T was obtained by grafting Cu on the surface of FP-(0.0)Cu/Pt-T, followed by the addition of an aqueous $NaBH_4$ solution in slight excess. Sample Pt-FP-(0.1)Cu-T was obtained by DP of Pt NPs on FP-(0.1)Cu-T. Briefly, the grafting method[23] consists in drying by heating at 90 °C under vigorous stirring an aqueous suspension containing ($Cu(NO_3)_2 \cdot 3H_2O$) and the dispersed TiO_2 powder. The DP technique[24] consists of stirring a heated aqueous suspension containing the starting photocatalyst and H_2PtCl_6 in the presence of urea to induce the precipitation of Pt NPs, followed by reduction of the so obtained powder with $NaBH_4$ in an aqueous dispersion.

All chemicals were purchased from Sigma-Aldrich and used as received.

3.2.2. Characterization of the Photocatalysts

XRPD analyses were performed using a Philips PW3020 powder diffractometer (PANalytical,), operating at 40 kV and 40 mA and exploiting copper Kα radiation (λ = 1.54056 Å) as X-ray source. The diffractograms were recorded by scanning between 5° and 80° 2θ angles, with a 0.05° step. Phase quantitative analysis was made by the Rietveld refinement method,[25] using Quanto software (Ver. 1.0);[26] the mean anatase crystallite size was calculated by applying the Scherrer equation,[27] from the width of the most intense reflection at 2θ = 25.4°.

The BET specific surface area (SSA) was measured by N_2 adsorption/desorption at liquid nitrogen temperature in a Micromeritics ASAP 2010 (Micromeritics) apparatus after out-gassing in vacuo at 150 °C for 2 h. UV-VIS diffuse reflectance (R) analysis was performed with a Jasco V-670 spectrophotometer (Jasco) equipped with a PIN-757 integrating sphere, using barium sulphate as a reference. The results are presented as absorption (A) spectra (A = 1 − R).

XPS data were collected by a PHI-5500 Physical Electronics spectrometer equipped with an aluminium anode (Kα = 1486.6 eV) as the monochromatized source, operating at 200 W applied power, with a 58.7 eV pass energy, 0.5 eV energy step, and a 0.15 s step time. The vacuum level during the analyses was *ca.* 10^{-9} Torr and a neutralizer was used in order to avoid surface electrostatic charge accumulation on the nonconductive samples.

HRTEM analysis was carried out with a Zeiss LIBRA 200FE transmission electron microscope, equipped with STEM-HAADF and

EDX (Oxford X-Stream 2 and INCA software). The microscope has a 200 kV field emission gun-like source with an in-column second-generation omega filter for energy-selective spectroscopy. The sample was dispersed in isopropanol and then a drop of the suspension was deposited on a 300 mesh holey carbon copper or molybdenum grid.

3.2.3. Photocatalytic Tests

The photocatalytic activity in hydrogen production from methanol photo-steam reforming was evaluated in the already described stainless steel closed system[5] (Chapter 2.3). The photocatalytic bed, placed in the front hollow of the photoreactor, was prepared by mixing 15 ± 2 mg of photocatalyst and 7.10 ± 0.05 g of 20–40 mesh (0.42–0.85 mm) quartz beads with 1 mL of distilled water, followed by drying in an oven at 70 °C for at least 2 hours. Prior to any run, the whole system was purged to remove any trace of oxygen and other atmospheric gases. In this series of tests, the temperature of the photoreactor was fixed at 40 °C. The gas phase, saturated with methanol and water vapours by bubbling nitrogen into a 20 vol.% methanol/water solution kept at 30 °C, was continuously recirculated at a fixed rate (60 $mL \cdot min^{-1}$) by means of a bellow pump for 15 min before starting the test. During the photocatalytic run, the gas flow was also set at 60 $mL \cdot min^{-1}$. The absolute pressure inside the system, initially 1.2 bar, gradually increased during the run due to the accumulation of gas products. The light source was the 300 W xenon arc lamp whose emission spectrum is reported in Figure 2.8. The light intensity on the photocatalyst was 0.31 $W \cdot cm^{-2}$, as measured with an optical power meter (model PM200 by Thorlabs) equipped with a thermal power sensor (Thorlabs S302C).

The gas-phase composition was analysed on-line during the irradiation period by means of a gas chromatograph (GC, Agilent 6890N) equipped with two capillary columns (Molesieve 5A and HP-PlotU), two detectors (flame ionization and thermo conductivity) and a Ni-catalyst system for carbon dioxide and carbon monoxide methanation. As a standard analysis, H_2, CO_2, CO, CH_4, and H_2CO were monitored. The amount of formic acid produced during the photoreaction and accumulated in the aqueous solution was instead determined by ion chromatography at the end of the run, employing a Metrohm 761 Compact IC instrument, equipped with an anionic Metrosep A column.

The results of photocatalytic tests are reported as H_2 production rate (r_{H_2}) and of selectivity[28] towards CO_2 and CO, as discussed in Chapter 2.3.

To ensure the reproducibility of the data, the photocatalytic tests were repeated at least twice with each sample, using the same photocatalytic bed; at the end of each run, the methanol aqueous solution in the flask was changed and the whole system was thoroughly purged with N_2 in the dark for 30 min before starting a new run.

3.3. Results and Discussion

3.3.1. Photocatalyst Characterization

3.3.1.1. XRPD and BET Analyses

As shown in Figure 3.1, the X-ray powder diffraction (XRPD) pattern of pure titanium dioxide FP-T showed a biphasic crystalline composition (89% anatase, 11% rutile) with no evidence of brookite reflections; the mean crystallite size of the anatase phase was 14 nm (Table 3.1). The XRPD analyses of both FP-(X)Cu-T and FP-(X)Cu/Pt-T

series indicate that the anatase crystallite mean size appear to increase with increasing copper content, as well as the rutile/anatase ratio, a phenomenon which has already been observed in previous studies.[29]

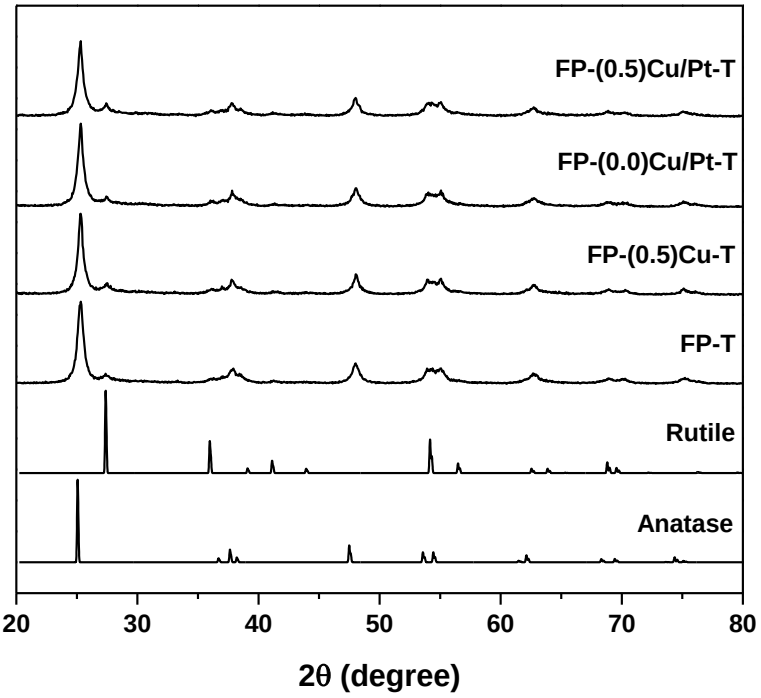

Figure 3.1 *XRPD pattern of selected photocatalyst samples, with standard reference patterns of the anatase and rutile phases.*

Nevertheless, no reflections due to the metals or to copper oxides were detected, suggesting that they are finely dispersed in small NPs.

As reported in Table 3.1, the specific surface area (SSA) of the FP-(X)Cu-T series was only slightly higher than that of the FSP-made pure TiO_2 (110 $m^2 \cdot g^{-1}$), while the whole FP-(X)Cu/Pt-T series showed a

somewhat higher SSA with respect to the other samples, with the FP-(0.05)Cu/Pt-T photocatalyst possessing the highest SSA, *i.e.*, 153 $m^2 \cdot g^{-1}$.

Table 3.1 *Crystal phase composition, average anatase particles diameter d_A, and specific surface area SSA of the FSP-made photocatalysts.*

Photocatalyst	Anatase (%)	Rutile (%)	d_A (nm)	SSA ($m^2 \cdot g^{-1}$)
FP-T	89	11	14	110
FP-(0.05)Cu-T	83	17	14	116
FP-(0.1)Cu-T	92	8	14	119
FP-(0.5)Cu-T	79	21	17	115
FP-(0.0)Cu/Pt-T	87	13	14	131
FP-(0.05)Cu/Pt-T	92	8	13	153
FP-(0.1)Cu/Pt-T	88	12	13	130
FP-(0.2)Cu/Pt-T	82	18	15	127
FP-(0.3)Cu/Pt-T	84	16	15	129
FP-(0.5)Cu/Pt-T	82	18	15	121

3.3.1.2. UV-Vis Absorption Properties

The ultraviolet-visible (UV-Vis) absorption spectra of the FP-(X)Cu-T series together with that of bare FP-T are collected in Figure 3.2a. First of all, reference FP-T sample shows an important absorption tail in the whole visible light range originated from the carbonaceous impurities characteristic of FSP-made samples.[21,30,31] In the presence of copper the absorption of the materials increases, all FP-(X)Cu-T samples showing an extra absorption contribution in the 400–500 nm region, to be ascribed to the direct interfacial charge transfer (IFCT) of electrons from the VB of TiO_2 to Cu(II) surface species.[12] In addition, specific Cu(II) *d-d* transitions, evidenced by the absorption in the 700–800 nm region in the spectrum of FP-(0.5)Cu-T (see Figure 3.2b), confirm that the here

employed single-step FSP synthesis of Cu-containing TiO_2 stabilizes surface Cu_xO species, with copper in an oxidized state.

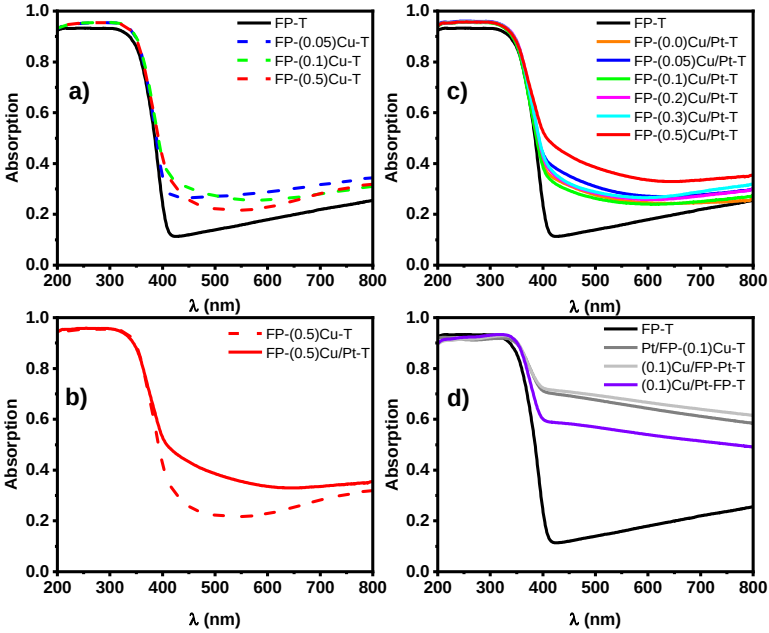

Figure 3.2 *UV-Vis absorption spectra of (a) the FP-(X)Cu-T series; (b) FP-(0.5)Cu-T in comparison with FP-(0.5)Cu/Pt-T; (c) the FP-(X)Cu/Pt-T series and (d) the hybrid Pt and Cu co-modified TiO_2 samples prepared by combining FSP with Cu grafting and/or Pt NP deposition through the DP route.*

All Pt-containing TiO_2 samples showed enhanced absorption with respect to the corresponding FP-(X)Cu-T photocatalysts (Figure 2c *vs.* Figure 2a), as clearly evidenced in Figure 2b, where the absorption spectrum of FP-(0.5)Cu/Pt-T is compared with that of FP-(0.5)Cu-T. However, the materials of the FP-(X)Cu/Pt-T series (characterised by a light grey color) showed a much lower absorption with respect to the Pt-Cu/TiO_2 "hybrid" samples prepared by combining the FSP technique with

alternative TiO_2 surface modification routes implying post-deposition metal reduction (Figure 3.2c *vs.* Figure 3.2d). This indirectly confirms that, in FSP-made Pt/TiO_2 samples, platinum is also mostly present in oxidized, rather than in metallic, form[32] and that post-deposition chemical reduction may promote the reduction of both metal co-catalysts into metallic NPs (Figure 3.2d). Importantly, hybrid materials with identical co-catalyst content showed the same optical absorption profiles, independently of their preparation sequence (see Pt/FP-(0.1)Cu-T and (0.1)Cu/FP-Pt-T in Figure 3.2d). Compared to such materials, (0.1)Cu/Pt-FP-T, prepared by directly contacting the two metal precursors with the FP-T powder in subsequent steps, absorbs less light in the visible range and shows a UV-Vis absorption spectrum comparable to that of the photocatalyst obtained by applying exactly the same two-step deposition procedure to commercial P25.[17]

3.3.1.3. XPS Analysis

X-Ray photoelectron spectroscopy (XPS) analysis (see for example Figure 3 and Table 2) confirms the presence of ca. 20 at.% of carbon in FSP-made materials. The C *1s* signal exhibits a band peaking at *ca.* 284.8 eV, which can be attributed to organic carbon, and a second peak at *ca.* 288 eV, ascribable to carbonaceous traces. The O *1s* signal consists of a main peak at *ca.* 530.3 eV, originating from oxygen linked to titanium (Ti–O bonds) and a minor peak at *ca.* 532.5 eV compatible with oxygen in carbonate species, CO, CO_2, and in physisorbed water. The Ti *2p* doublet signal is almost identical for all samples (Figure 3.3), with the main peak at *ca.* 458.8 eV and the second one at 464.5 eV, both typical of Ti^{4+} in TiO_2.[33] The absence of shoulders at lower energy points to a negligible contribution of sub-stoichiometric titanium dioxide

(TiO_{2-x}) or of Ti–OH surface groups.[34–36] This is also confirmed by the O/Ti ratio greater than 2 (Table 3.2). No signals originated from platinum and copper photoemission could be detected, their intensity possibly being below the detection limit.

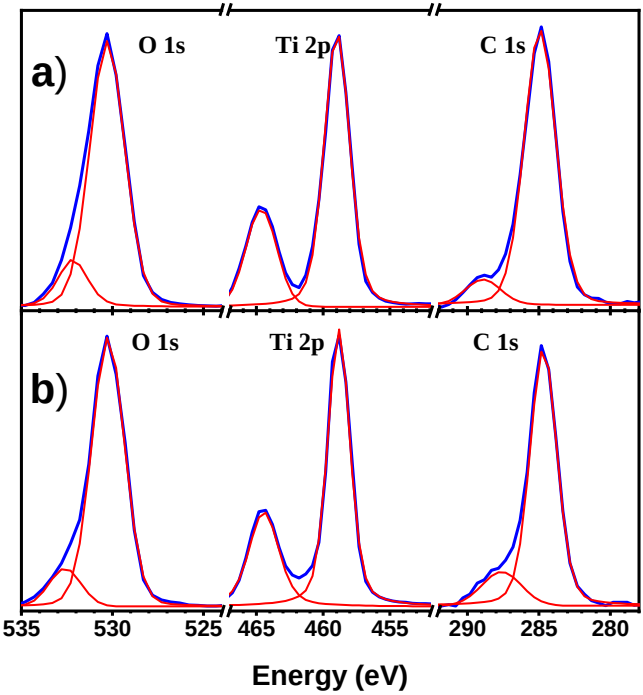

Figure 3.3 *XPS spectra of the O 1s, Ti 2p, and C 1s regions for (a) FP-(0.0)Cu/Pt-T and (b) FP-(0.5)Cu/Pt-T.*

Table 3.2 *Results of the XPS analysis for 3 selected FP-(X)Cu/Pt-T photocatalysts.*

Photocatalyst	Concentration (at%)			O/Ti Ratio
	O *1s*	Ti *2p*	C *1s*	
FP-(0.0)Cu/Pt-T	55.4	23.5	19.7	2.36
FP-(0.05)Cu/Pt-T	54.6	23.1	21.0	2.36
FP-(0.5)Cu/Pt-T	53.5	22.2	23.4	2.41

3.3.1.4. HRTEM Analysis

Transmission electron microscopy (TEM) investigation of FP-(0.0)Cu/Pt-T (Figure 4a) and of FP-(0.5)Cu/Pt-T confirms the typical morphology of the flame made powder consisting of micro-aggregates of spherical nanocrystals. The TiO_2 particle size distribution obtained by counting 170 NPs (Figure 3.4b) is in the 4–28 nm range, with an average value of 11 nm and a standard deviation of 5 nm.

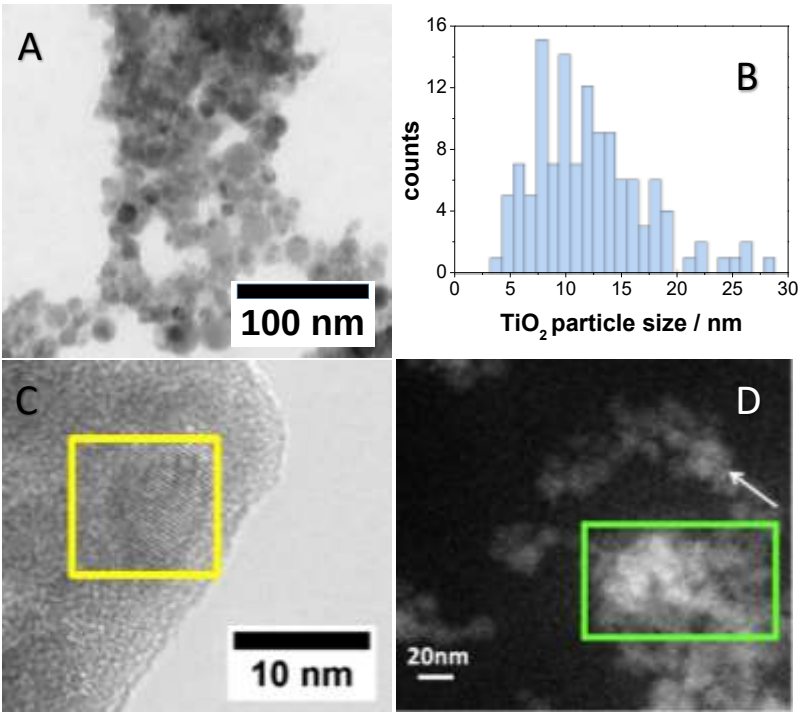

Figure 3.4 *(a) TEM; (b) TiO_2 particle size distribution; (c) HRTEM; and (d) STEM-HAADF investigation of FP-(0.0)Cu/Pt-T. The green rectangle in (d) shows the acquisition area of the EDX spectrum. The white arrow points a surface Pt NP appearing as a bright dot due to the Z-contrast.*

The high resolution TEM (HRTEM) image shown in Figure 3.4c confirms that the TiO_2 NPs are monocrystalline and that their crystal structure corresponds to the anatase phase. Indeed, the plane distance calculated by FFT analysis of the nanocrystals appearing within the yellow frame in Figure 3.4c is 3.5 Å, corresponding to the d-spacing of the [101] plane of anatase.

Pt NPs can be revealed by scanning transmission electron spectroscopy-high angular annular dark field (STEM-HAADF) analysis as bright dots on the TiO_2 surface because of its higher Z-contrast compared to the lighter Ti and O elements. However, Pt NPs can hardly be distinguished in Figure 3.4d (see for example the point indicated by the white arrow), in line with the fact that Pt is finely and homogeneously dispersed on the TiO_2 surface in the form of approximately 1 nm sized NPs. The presence of Pt was confirmed by energy dispersive X-ray spectroscopy (EDX) analysis, giving a 0.4 wt.% of Pt for FP-(0.0)Cu/Pt-T, in good agreement with its nominal 0.5 wt.% content. Similarly, EDX analysis of the FP-(0.5)Cu/Pt-T (dispersed on a molybdenum grid to avoid artefact on the Cu signal) confirmed the 0.5 wt.% Cu content and its homogeneous dispersion on TiO_2.

3.3.2. Photocatalytic Activity

In the photocatalytic steam reforming of methanol, the alcohol acts as an efficient hole scavenger, thus decreasing the electron-hole recombination rate and making conduction band electrons more readily available for H^+ reduction. Hydrogen production is, thus, coupled with methanol oxidation up to CO_2. Several intermediates, such as carbon monoxide, formic acid, or formaldehyde, are produced together with other side products, such as methane or ethane. H_2, CO_2, and CO

accumulate at a constant rate in the closed recirculation system during the photocatalytic tests, according to pseudo-zero order kinetics.

The results obtained in methanol photo-steam reforming photocatalytic tests are reported in Figure 3.5 and 3.6, in terms of hydrogen production rate, r_{H_2}, and selectivity to CO_2 and CO, S_{CO_2} and S_{CO}, as in previous studies.[28] We note, first of all, that the higher rate of hydrogen production r_{H_2} obtained with FP-T with respect to P25 TiO_2 (3.6 *vs.* 2.7 $mmol \cdot h^{-1} \cdot g_{cat}^{-1}$) can be ascribed to the higher surface area and to the larger anatase content. On the other hand, these two reference samples behave in the same way regarding side-product formation, with similar selectivities towards carbon dioxide and monoxide (Figure 3.5). The r_{H_2} values obtained with the photocatalysts of the FP-(X)Cu-T series were all around 7 $mmol \cdot h^{-1} \cdot g_{cat}^{-1}$, more than twice of those obtained with the bare materials, with a slightly decreasing rate with increasing copper loading. In addition to the beneficial effect on H_2 production rate, the presence of Cu species on the TiO_2 surface also influences the selectivity to CO in methanol photo-steam reforming, the higher the amount of this metal, the lower being the selectivity to carbon monoxide. Thus, in the presence of copper as co-catalyst, preferential complete oxidation of methanol to carbon dioxide occurs, rather than to carbon monoxide, with a consequent higher rate of hydrogen production. In fact, full oxidation of one methanol molecule produces three H_2 molecules, while incomplete methanol oxidation to carbon monoxide produces two molecules of hydrogen per methanol molecule.[28]

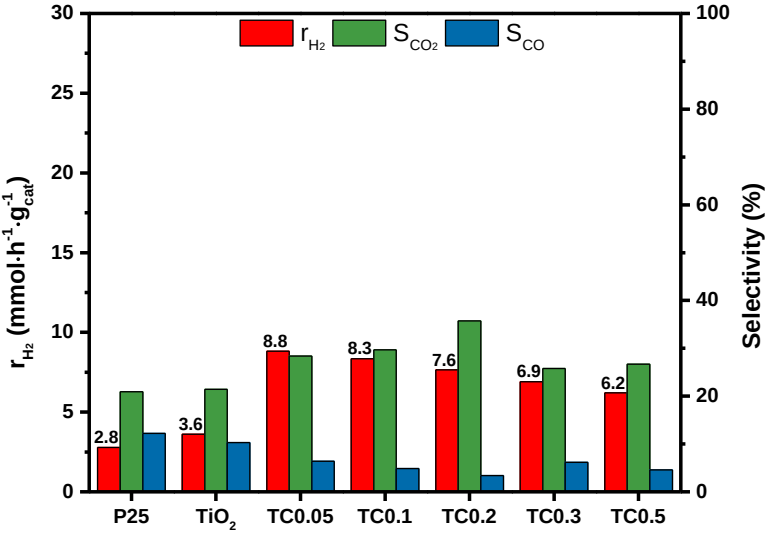

Figure 3.5 *H_2 production rate (left ordinate) and selectivity to CO_2 and CO (right ordinate) obtained with Cu-containing TiO_2 photocatalysts prepared by FSP in single- step.*

With respect to the Cu/TiO_2 photocatalysts obtained by grafting Cu on P25 TiO_2[17] the photocatalysts of the FP-(X)Cu-T series showed a lower selectivity towards CO and a higher rate of hydrogen production. Considering two photocatalysts with the same 0.1 wt.% Cu nominal content, the hydrogen production rate obtained with the FSP-made one is almost double (6.9 *vs.* 3.8 $mmol \cdot h^{-1} \cdot g_{cat}^{-1}$), with a halved selectivity to CO (6.1% *vs.* 10.8%). This might be a consequence of the formation of small NPs of crystalline copper oxides during the FSP synthesis, acting as semiconductors and thus forming a heterojunction with TiO_2, which improves the separation of the photoproduced charge couples.[37] In Cu/TiO_2 photocatalysts produced by the grafting technique the oxidized copper species on the TiO_2 surface are expected to be in amorphous form,

as grafting is carried out at room temperature and, thus, their action mechanism, consisting of switching between the Cu^{2+} and Cu^{+} oxidation states, may be different.[12]

The presence of Pt on the FP-(X)Cu/Pt-T photocatalysts led to much higher photoactivity in terms of hydrogen production rate with respect to pure TiO_2 and to a *ca.* doubled photoactivity with respect to the FP-(X)Cu-T series. Platinum, due to its high work function (5.93 eV for the 111 crystal plane),[38] is a well-known, very efficient co-catalyst of TiO_2, particularly contributing to increased H^{+} photocatalytic reduction leading to molecular hydrogen evolution.[16,28,33,39,40]

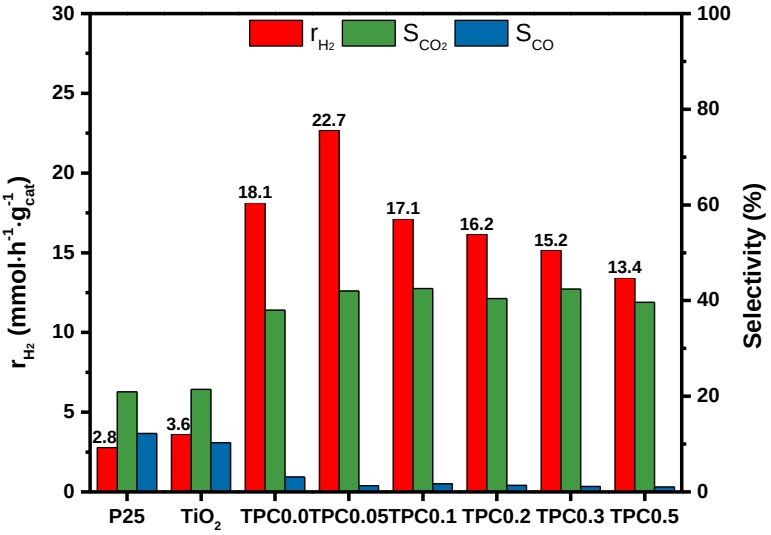

Figure 3.6 *H_2 production rate (left ordinate) and selectivity to CO_2 and CO (right ordinate) obtained with Cu/Pt-containing TiO_2 photocatalysts prepared by FSP in one step.*

As shown in Figure 3.6, the rate of photocatalytic hydrogen production obtained with the FSP-made Cu-Pt co-modified

photocatalysts showed a bell-shaped trend, with the best performance in terms of r_{H_2} (22.7 $mmol \cdot h^{-1} \cdot g_{cat}^{-1}$) being achieved with FP-(0.05)Cu/Pt-T, followed by the Pt-only containing sample FP-(0.0)Cu/Pt-T. Further increase of the copper content of the FSP-made photocatalysts had instead detrimental effects on the hydrogen production rate, with r_{H_2} values lower than that obtained with copper-free FP-(0.0)Cu/Pt-T. The formation of an alloy between Cu and Pt during the FSP synthesis with the resulting decrease in the total work function of metal NPs and consequent decreased efficiency in H^+ reduction in comparison to pure platinum NPs, may be at the origin of such a behaviour.[28] At the same time, the increase of nominal Cu content employed during the FSP synthesis may promote the formation of larger copper oxide domains, implying reduced Cu-TiO_2 interactions, which possibly determine a decrease of photocatalytic H_2 evolution.[41]

Anyway, with increasing copper content in the FSP-made Cu-Pt/TiO_2 photocatalysts the selectivity towards carbon dioxide reached values up to 42% in the case of Cu- and Pt-containing photocatalysts, while the selectivity towards CO was significantly reduced. In fact, S_{CO} dropped from 3.1% and 3.4% for FP-(0.0)Cu/Pt-T and FP-(0.5)Cu-T, respectively, to 1.0% for FP-(0.5)Cu/Pt-T.

Concerning the photoactivity achieved by the "hybrid" samples, as shown in Figure 3.7, a limited increase in r_{H_2} up to 10.6 $mmol \cdot h^{-1} \cdot g_{cat}^{-1}$ was attained upon platinum deposition by the DP method (see Pt/FP-(0.1)Cu-T *vs.* FP-(0.1)Cu-T), as a consequence of the above mentioned positive role played by platinum NPs in favouring electron-hole separation. On the other hand, Pt/FP-(0.1)Cu-T exhibits a photoactivity very similar to that obtained with (0.1)Cu/FP-Pt-T, in terms of both

hydrogen production rate and selectivity to by-products. The obtained r_{H_2} value is lower than that attained with the corresponding unmodified photocatalyst, *i.e.*, FP-(0.0)Cu/Pt-T, and points to a negative effect of copper grafting on the photoactivity of Pt-containing FSP-made TiO_2. Surprisingly, (0.1)Cu/Pt-FP-T, obtained by Cu grafting followed by Pt deposition using the DP method on flame-made bare TiO_2, exhibits a hydrogen production rate much higher than that of the other two "hybrid" samples, containing the same nominal amount of metals.

Differently from the results obtained in our previous work on Cu-Pt modified TiO_2 photocatalysts prepared starting from commercial TiO_2,[17] with the presently investigated FSP-made Cu and Pt-containing TiO_2 photocatalysts no synergistic effect between the two metal co-catalysts was observed. In fact, with none of them a r_{H_2} value was attained greater than the sum of those observed with the corresponding single metal (Pt or Cu)-modified TiO_2 photocatalyst. Nevertheless, a limited improvement in photoactivity was observed for very low copper content, *i.e.*, in the case of FP-(0.05)Cu/Pt-T.

Thus, FSP proves to be an effective way to synthesize single metal-containing TiO_2-based photocatalysts, since both Cu-only and Pt-only containing FSP-made TiO_2 samples showed very high photoactivity in hydrogen production, performing better than TiO_2-based photocatalysts with analogous composition produced through wet-phase techniques, such as grafting of Cu or Pt deposition through the DP method.

Importantly, the beneficial effects induced in H_2 production by combining Cu(II) grafting with Pt NPs deposition on the TiO_2 surface by means of the DP procedure has been confirmed also in the case of bare

FSP-made TiO_2, *i.e.* not only for commercial P25.[17] In fact, though implying a more time-consuming procedure, the mild modification conditions ensured by these wet-phase techniques may avoid the undesired formation of a Cu-Pt alloy, with the consequent stabilization of Cu nanoclusters, able to promote the transfer of photoexcited electrons from TiO_2 towards Pt NPs, where H_2 evolution occurs.[17]

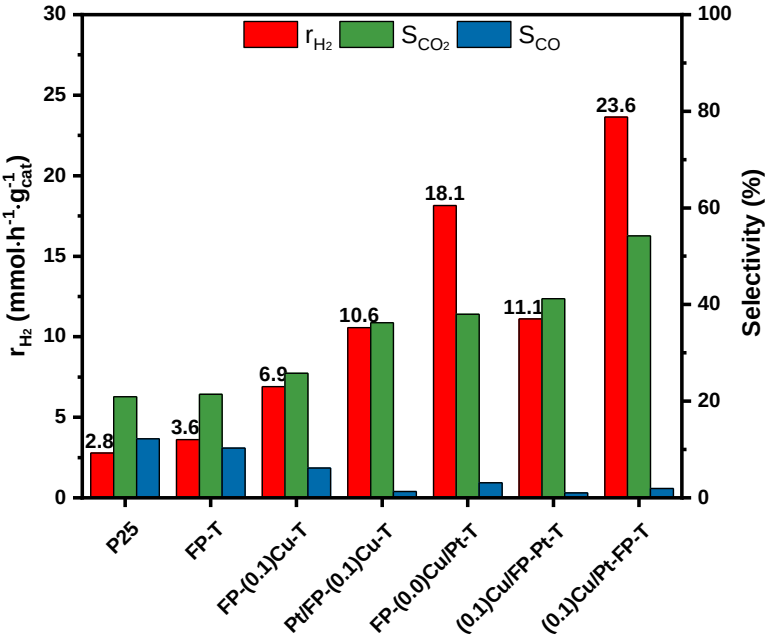

Figure 3.7 *H_2 production rate (left ordinate) and selectivity to CO_2 and CO (right ordinate) obtained with photocatalysts prepared by combining different preparation techniques (see text).*

3.4. Conclusions

In conclusion, FSP proves to be an effective way to synthesize highly-performing single metal-containing TiO_2-based photocatalysts for

photocatalytic hydrogen production. However, the highest synergistic effect between the Cu and Pt co-catalysts was attained with photocatalysts prepared by wet-phase methods on bare FSP-made TiO_2, *i.e.* Cu(II) grafting followed by Pt NP deposition.

Copper overloading (up to 0.5 wt.%) of FSP-made photocatalysts is detrimental for H_2 production rate, probably due to Cu-Pt alloying under the here employed harsh synthesis conditions. Nevertheless, the addition of very low amounts of copper (0.05 wt.%) during the FSP synthesis of Pt/TiO_2 guarantees a *ca.* 20% improvement of the overall photocatalytic hydrogen production, together with a lower selectivity towards the less desired carbon monoxide side-product.

References

1 R. S. Cherry, *Int. J. Hydrogen Energy*, 2004, **29**, 125–129.
2 R. Chaubey, S. Sahu, O. O. James and S. Maity, *Renew. Sustain. Energy Rev.*, 2013, **23**, 443–462.
3 N. Rahimi, R. A. Pax and E. M. A. Gray, *Prog. Solid State Chem.*, 2016, **44**, 86–105.
4 Y. Ma, X. Wang, Y. Jia, X. Chen, H. Han and C. Li, *Chem. Rev.*, 2014, **114**, 9987–10043.
5 G. L. Chiarello, L. Forni and E. Selli, *Catal. Today*, 2009, **144**, 69–74.
6 P. Gomathisankar, T. Noda, H. Katsumata, T. Suzuki and S. Kaneco, *Front. Chem. Sci. Eng.*, 2014, **8**, 197–202.
7 A. Perez-Larios, A. Hernández-Gordillo, G. Morales-Mendoza, L. Lartundo-Rojas, A. Mantilla, R. Gomez, A. Pérez-Larios, A. Hernández-Gordillo, G. Morales-Mendoza, L. Lartundo-Rojas, Á. Mantilla and R. Gómez, *Catal. Today*, 2016, **266**, 9–16.
8 Q. Wang, N. An, Y. Bai, H. Hang, J. Li, X. Lu, Y. Liu, F. Wang, Z. Li and Z. Lei, *Int. J. Hydrogen Energy*, 2013, **38**, 10739–10745.
9 T. Kawai and T. Sakata, *Nature*, 1980, 286, 474–476.
10 H. J. Choi and M. Kang, *Int. J. Hydrogen Energy*, 2007, **32**, 3841–3848.
11 G. L. Chiarello, M. V. Dozzi and E. Selli, *J. Energy Chem.*, 2017, **26**, 250–258.
12 H. Irie, K. Kamiya, T. Shibanuma, S. Miura, D. A. Tryk, T. Yokoyama and K. Hashimoto, *J. Phys. Chem. C*, 2009, **113**, 10761–10766.
13 Y. Liu, Z. Wang and W. Huang, *Appl. Surf. Sci.*, 2016, **389**, 760–767.
14 Y. Shiraishi, H. Sakamoto, Y. Sugano, S. Ichikawa and T. Hirai, *ACS Nano*, 2013, **7**, 9287–9297.
15 F. Teng, M. Chen, N. Li, X. Hua, K. Wang and T. Xu, *ChemCatChem*, 2014, **6**, 842–847.
16 M. Jung, J. N. Hart, D. Boensch, J. Scott, Y. H. Ng and R. Amal, *Appl. Catal. A Gen.*, 2016, **518**, 221–230.
17 M. V. Dozzi, G. L. Chiarello, M. Pedroni, S. Livraghi, E. Giamello and E. Selli, *Appl. Catal. B Environ.*, 2017, **209**, 417–428.
18 W. Y. Teoh, L. Mädler, D. Beydoun, S. E. Pratsinis and R. Amal, *Chem. Eng. Sci.*, 2005, **60**, 5852–5861.
19 R. Strobel, A. Baiker and S. E. Pratsinis, *Adv. Powder Technol.*, 2006, **17**, 457–480.
20 S. E. Pratsinis and S. Vemury, *POWDER Technol.*, 1996, **88**, 267–273.
21 G. L. Chiarello, E. Selli and L. Forni, *Appl. Catal. B Environ.*, 2008, **84**, 332–339.
22 G. L. Chiarello, I. Rossetti and L. Forni, *J. Catal.*, 2005, **236**, 251–261.
23 T. Morikawa, Y. Irokawa and T. Ohwaki, *Appl. Catal. A Gen.*, 2006, **314**, 123–127.
24 M. V. Dozzi, L. Prati, P. Canton and E. Selli, *Phys. Chem. Chem. Phys.*, 2009, **11**, 7171–7180.

25 H. M. Rietveld, *J. Appl. Crystallogr.*, 1969, **2**, 65–71.
26 A. Altomare, M. C. Burla, C. Giacovazzo, A. Guagliardi, A. G. G. Moliterni, G. Polidori and R. Rizzi, *J. Appl. Crystallogr.*, 2001, **34**, 392–397.
27 P. Scherrer, *Göttinger Nachrichten Math. Phys.*, 1918, **2**, 98–100.
28 G. L. Chiarello, M. H. Aguirre and E. Selli, *J. Catal.*, 2010, **273**, 182–190.
29 A. Teleki, N. Bjelobrk and S. E. Pratsinis, *Sensors Actuators, B Chem.*, 2008, **130**, 449–457.
30 G. L. Chiarello, I. Rossetti, P. Lopinto, G. Migliavacca and L. Forni, *Catal. Today*, 2006, **117**, 549–553.
31 G. L. Chiarello, I. Rossetti, L. Forni, P. Lopinto and G. Migliavacca, *Appl. Catal. B Environ.*, 2007, **72**, 227–232.
32 G. L. Chiarello, M. V. Dozzi, M. Scavini, J.-D. Grunwaldt and E. Selli, *Appl. Catal. B Environ.*, 2014, **160**–**161**, 144–151.
33 M. V. Dozzi, A. Zuliani, I. Grigioni, G. L. Chiarello, L. Meda and E. Selli, *Appl. Catal. A Gen.*, 2016, **521**, 220–226.
34 E. A. Reyes-Garcia, Y. Sun, K. R. Reyes-Gil and D. Raftery, *Solid State Nucl. Magn. Reson.*, 2009, **35**, 74–81.
35 J. Yang, H. Bai, X. Tan and J. Lian, *Appl. Surf. Sci.*, 2006, **253**, 1988–1994.
36 T. Caruso, C. Lenardi, R. G. Agostino, M. Amati, G. Bongiorno, T. Mazza, A. Policicchio, V. Formoso, E. MacCallini, E. Colavita, G. Chiarello, P. Finetti, F. Šutara, T. Skála, P. Piseri, K. C. Prince and P. Milani, *J. Chem. Phys.*, 2008, **128**, 094704.
37 D. DeMeo, S. MacNaughton, S. Sonkusale and T. Vandervelde, in *Nanowires - Implementations and Applications*, ed. A. Hashim, InTech, Rijeka, Croatia, 2011, pp. 141–156.
38 D. R. R. Lide, W. M. M. Haynes, G. Baysinger, L. I. Berger, D. L. Roth, D. Zwillinger, M. Frenkel and R. N. Goldberg, *CRC Handbook of Chemistry and Physics*, CRC Press, Boca Raton, FL, Internet V., 2005.
39 A. V. Vorontsov and V. P. Dubovitskaya, *J. Catal.*, 2004, **221**, 102–109.
40 G. L. Chiarello, D. Paola and E. Selli, *Photochem. Photobiol. Sci.*, 2011, **10**, 355–360.
41 M. Jung, J. Scott, Y. H. Ng, Y. Jiang and R. Amal, *Int. J. Hydrogen Energy*, 2014, **39**, 12499–12506.

Chapter adapted from "M. Bernareggi, M. V. Dozzi, L. G. Bettini, A. M. Ferretti, G. L. Chiarello and E. Selli, *Catalysts*, 2017, **7 (10)**, 301" and reproduced with Editor's permission. doi.org/10.3390/catal7100301

Chapter 4:

Cu AND Pt CLUSTERS DEPOSITION ON TiO_2 POWDERS BY DC MAGNETRON SPUTTERING FOR PHOTOCATALYTIC HYDROGEN PRODUCTION

4.1. Introduction

Photocatalytic steam reforming, conceivably exploiting biomass as organic hole scavenger, is addressed to a viable alternative to traditional H_2 production processes.[1] Titanium dioxide, despite its relatively large bandgap,[2] is still one of the most effective photocatalysts.[3] As already reported in Chapter 1, its photocatalytic performance can be increased in the presence of an organic compound, such as methanol, ethanol or glycerol, acting as hole scavenger,[4–6] and of noble metal (Au, Pt, Pd, Ag) nanoparticles on the semiconductor surface acting as efficient electron traps.[4,7] Further addition of non-noble metal (*i.e.* Cu or Ni) nanoparticles may increase the photocatalytic activity and also lead to visible light activation of the photocatalysts.[8–10] As demonstrated in Chapter 3, among all compositions, titanium dioxide-based materials modified with both a noble metal and a non-noble metal, *e.g.* with Pt and Cu, respectively, proved to be more efficient than the corresponding monometallic materials.[11,12]

Pulsed-Direct Current (pDC) magnetron sputtering (MS) is a well-known technique used for the production of thin films. This technology is widely employed on the industrial scale due to its scalability and versatility, and to the repeatability and high quality of the obtained coatings. In fact, MS is exploited for many applications, ranging from solar glazing products to micro-electronic coatings, from tool protecting layers to packaging coatings,[13] allowing the deposition of both metallic and non-metallic coatings over various substrates. Recently, pDC MS has been employed on the laboratory scale also for metal nanoparticles production and deposition on the surface of solid[14–17] or liquid supports,[18–20] thus avoiding the contaminations of solvents and/or precursors typically occurring with more conventional techniques.

So far, only by the group of Teixeira *et al.* investigated the possibility of exploiting this technique to modify materials in powder form[15,16] and found that high metal loadings (larger than 0.5 wt.%) can be obtained even with short sputtering times. The great enhancement of the catalytic activity of the so obtained materials was attributed to the unimodal distribution and small average diameters (*ca.* 1.5 nm) of the deposited metal nanoparticles.

In this work, we present some preliminary results on Cu and/or Pt clusters deposition on TiO_2 powders by pDC MS, employing a home-made apparatus.[21] This set-up is based on an oscillating bowl (powder holder) placed under the magnetrons. The oscillations force the powder particles to roll and mix around the bowl while the metal atoms are sputtered from the magnetron target. The obtained materials were tested as photocatalysts in methanol photo-steam reforming for hydrogen production.

4.2. Experimental

4.2.1. Photocatalytic materials

Copper and platinum were deposited over commercial P25 TiO_2 powders (Sigma-Aldrich) by pulsed direct current magnetron sputtering in the already described rig.[22] A sketch of the employed set-up is shown in Figure 4.1. Briefly, the deposition system consisted in a sputter-down configuration, with a single 7.5 cm diameter type II unbalanced planar magnetron installed on the roof of the sputtering chamber. Thus, the target was facing an electrically floating substrate holder placed 5 cm underneath the magnetron, allowing a continuous powder mixing during the sputtering process via a shaker mechanism. The magnetron was powered by an Advanced Energy Pinnacle Plus power supply. The metal targets were sputtered at 250 W, 350 kHz, 50% duty cycle (corresponding to a pulse-off period of 1.4 μs, when the cathode voltage is reversed). The deposition process was performed in an Ar-only atmosphere for both Pt and Cu deposition and also in a 1:1 O_2/Ar plasma for copper deposition. The working pressure was fixed, for all depositions, at *ca.* 2.6 Pa, after having evacuated the chamber below $5 \cdot 10^{-3}$ Pa by means of a rotary (Leybold Trivac 16B) and a turbomolecular (Leybold TurboVac i90) pump. The desired pressure was achieved by adjusting the gate valve between the chamber and the turbomolecular pump. The total gas flow during deposition was fixed at 20 sccm for all runs.

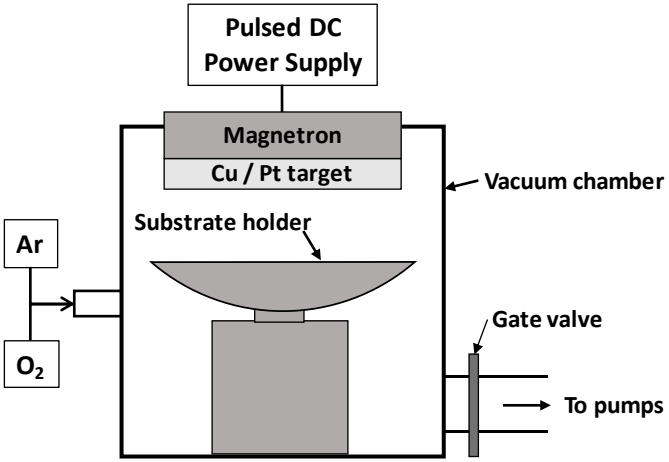

Figure 4.1 *Sketch of the employed pDC magnetron sputtering set-up.*

3 g of P25 TiO_2 were treated for different times (1-10 min) in different atmospheres. The so obtained modified photocatalyst samples are named as "P25" followed by deposition time (in min) and by the symbol of the sputtered metal(s), in the order in which they were deposited. In the case of copper, the Cu symbol is also followed by the main gas used during deposition. For instance, P25+1Cu-O_2+5Pt indicates the P25-based sample first modified by a 1 min-long Cu deposition in O_2/Ar atmosphere followed by a 5 min-long platinum deposition in argon. Copper deposition always preceded platinum deposition, as in Chapter 3[12] in which the two metals were deposited by different techniques.

4.2.2. Photocatalyst characterisation

UV-Vis diffuse reflectance spectra of all powders were recorded on a Jasco V-670 spectrophotometer equipped with a PIN-757 integrating

sphere using barium sulphate as a reference. The reflectance R was then converted in absorption according to: $A = 1 - R$.

X-Ray powder diffraction (XRPD) was carried out with a Panalytical Xpert diffractometer operating at 40 kV voltage and 30 mA current using the Cu Kα radiation (λ = 1.54056 Å), with the patterns recorded in the $20° < 2\theta < 100°$ range (scan step = 0.013°). The crystal phase composition was evaluated by Rietveld refinement[23] using the Quanto software.[24] The Scherrer equation, from the most intense reflection at $2\theta = 25.4°$, was exploited to calculate the mean anatase crystallite size.[25]

Inductively Coupled Plasma Optical Emission Spectroscopy (ICP-OES) analyses were performed with a Perkin Elmer Optima 8000 ICP-OES. Pt and Cu were dissolved by dispersing the sample in aqua regia (3:1 HCl:HNO_3 solution) at 90 °C for 3 h.

HRTEM analysis was carried out with a Zeiss LIBRA 200FE transmission electron microscope, equipped with STEM-HAADF and EDX (Oxford X-Stream 2 and INCA software). The microscope has a 200 kV field emission gun-like source with an in-column second-generation Omega filter for energy-selective spectroscopy. The samples were dispersed in isopropanol and then a drop of the suspension was deposited on a 300 mesh holey carbon copper (for Pt containing samples) or molybdenum (for Cu containing samples) grid.

4.2.3. Photocatalytic tests

The photocatalysts were tested in hydrogen production from methanol photo-steam reforming reaction by exploiting the standard set-up[12] described in Chapter 2.3. 15 ± 2 mg of sample were dispersed in *ca.* 1 mL of MilliQ water and mixed with (7.10 ± 0.05) g of quartz grains and

then dried in oven at 70 °C for at least 2 h. The so-obtained photocatalytic bed was loaded into the home-made steel photo-reactor, sealed with a Pyrex glass window. Before starting any run, the system was thoroughly purged with pure nitrogen in order to remove any trace of oxygen from both the gas phase and the 20 vol% methanol/water solution, kept at 30 °C. The gas phase, saturated with the solution vapours, was recirculated by means of a metal Bellows pump at 60 mL min^{-1}. The photocatalytic bed was irradiated by the 300 W xenon arc lamp (LOT-Oriel), switched on 30 min before the run and positioned at 20 cm from the photo-reactor.

The recirculating phase was sampled and analysed automatically at regular intervals by the gas-chromatograph (Agilent 6890N) connected to the circuit. Formic acid production was evaluated by analysing the liquid solution with an ion chromatograph.

The photocatalytic tests were repeated at least twice in order to verify their reproducibility. At the end of each run, the liquid solution was replaced with a new one and the system was thoroughly purged in pure nitrogen in the dark for 40 min before starting a new run.

4.3. Results and discussion

4.3.1. Photocatalysts characterisation

The results of elemental ICP analysis on the produced photocatalysts are collected in Table 4.1. The platinum loading is *ca.* twice the copper loading attained under similar sputtering conditions, with *ca.* 0.7 wt.% Pt *vs. ca.* 0.34 wt.% Cu deposited after 10 min-long deposition. This is actually due to the much higher atomic weight of Pt with respect to Cu (195 *vs.* 63.5, respectively). Indeed, the average deposition rate of Cu under Ar atmosphere is significantly higher than that

of Pt (*e.g.*, 8.9 *vs.* 6.1 μmol s^{-1} after 10 min-long deposition, respectively). This is consistent with the higher relative sputtering yield of Cu with respect to that of Pt. The average deposition rate of Pt increased with increasing overall deposition time, while that of Cu decreased. As expected, the presence of O_2 during the sputtering process caused an important decrease in the Cu sputtering yield, likely due to target poisoning, since after 10 min deposition only 0.1 wt.% Cu was deposited on the TiO_2 powder under such conditions.

The absorption spectra of the prepared materials, shown in Figure 4.2, confirm that Cu and/or Pt clusters were deposited on the TiO_2 surface, because a characteristic absorption appeared in the visible region. No shift in the band gap absorption onset could be observed in the spectra of the modified samples compared to that of pristine TiO_2. Thus, the room temperature sputtering process in vacuum does not affect at all the main structural characteristics of the supporting powder, in contrast with other metal deposition methods, *e.g.* grafting or deposition-precipitation,[11] which require a post-thermal treatment of the material.

Table 4.1 *ICP results reporting Pt and/or Cu loading on different samples and average metal deposition rate during sputtering.*

Sample	Deposition time (s)	Amount (wt.%)		Average deposition rate (μmol s^{-1})	
		Pt	Cu	Pt	Cu
P25+1Pt	60	0.04	/	3.4	
P25+10Pt	600	0.71	/	6.1	
P25+1Cu-Ar+5Pt	60 + 300	0.19	0.07	3.2	18.4
P25+1Cu-Ar	60	/	0.05		13.1
P25+10Cu-Ar	600	/	0.34		8.9
P25+10Cu-O_2	600	/	0.09		2.4

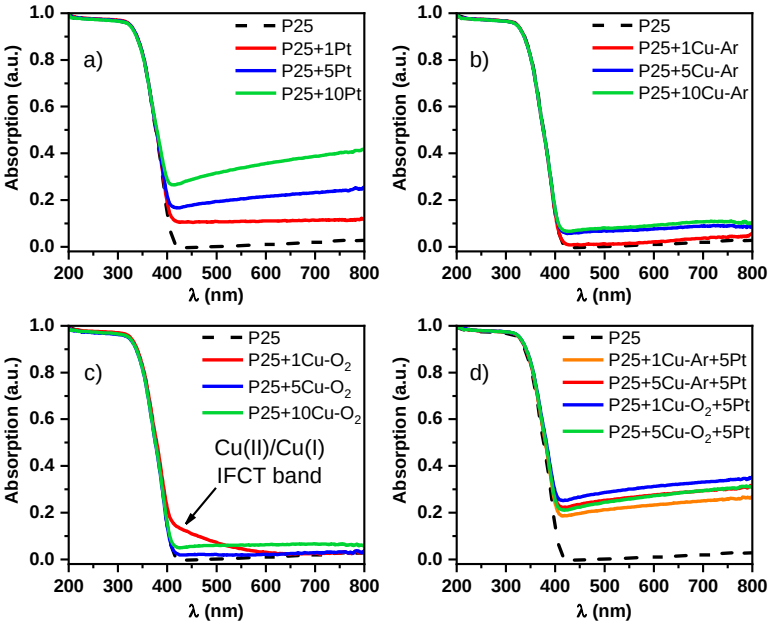

Figure 4.2 *Absorption spectra of the (a) P25+xPt, (b) P25+xCu-Ar, (c) P25+xCu-O_2 (x = 1, 5 and 10 min), (d) Cu and Pt co-modified photocatalyst series, all compared with the absorption spectrum of bare P25 TiO_2 (dashed black line).*

Pt-modified TiO_2 photocatalysts show an extended optical absorption in the visible range due to the presence of the noble metal that makes these samples greyish (Figure 4.2a). As expected, the absorption in the 400–800 nm range increases for longer deposition times, in agreement with the Pt loading increase.

The absorption spectra of Cu modified TiO_2 materials are characterized by the presence of a typical absorption band in the 600–800 nm region, due to the Cu *d-d* transition, and/or an absorption tail in the 400–500 nm region attributed to the interfacial charge transfer (IFCT) phenomenon between TiO_2 valence band electrons and Cu(II) species.[11]

The absorption spectra of the photocatalysts modified with Cu sputtering in an Ar-only atmosphere (see Figure 4.2b) exhibit an absorption in the visible range, due to the presence of copper nanoparticles, increasing with increasing deposition time, but no absorption tail between 400 and 500 nm related to an IFCT. Such absorption feature appears only in the absorption spectrum of P25+1Cu-O_2 (Figure 4.2c), suggesting the presence of atomically dispersed Cu(II) species (consistent with its unique yellowish colour) in the low copper loading deposited in an oxidising atmosphere. Moreover, the absorption spectra of the photocatalysts obtained by Cu sputtering in an Ar/O_2 plasma (Figure 4.2c) show a weaker absorption in the visible range with respect to the absorption spectra of the analogous photocatalysts obtained by Cu sputtering in an Ar-only atmosphere. This is compatible with the lower deposition rate attained under reactive conditions. Finally, the absorption spectra of the Cu and Pt co-modified samples are basically dominated by the absorption profile of Pt nanoparticles in the visible region.

Figure 4.3 shows that the XRPD patterns of the metal modified materials are identical to that of pristine TiO_2. In fact, the Rietveld refinement of XRPD data confirmed that the amount of anatase and rutile phases did not change after metal deposition, as well as the anatase crystallite mean size, calculated through the Scherrer equation (see Table 4.2). All samples are composed of a mixture of *ca.* 85% anatase and 15% rutile, with an average anatase crystalline size of 23 nm. No additional reflections related to metal Pt and Cu or copper oxides can be observed, due to their low loading and fine dispersion on the TiO_2 surface.

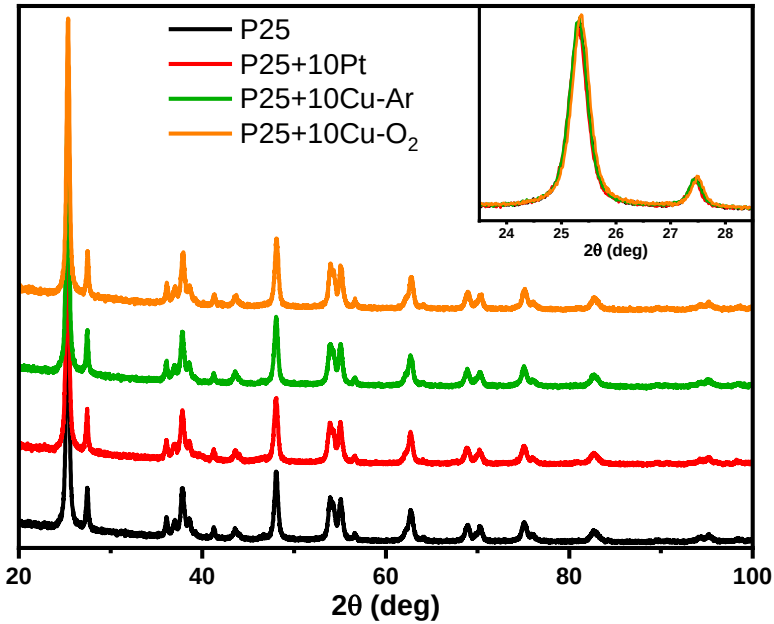

Figure 4.3 *XRPD patterns of selected samples. The inset shows superimposed patterns in the 24–28° 2θ range, demonstrating that the sputtering treatment did not alter the crystal structure.*

Table 4.2 *Average diameter of anatase nanoparticles $d_{anatase}$ and crystal phase composition.*

Sample	$d_{anatase}$ (nm)	Anatase (%)	Rutile (%)
P25	24	86	14
P25+10Pt	23	85	15
P25+10Cu-Ar	23	86	14
P25+10Cu-O_2	24	87	13

The STEM-HAADF and EDX analyses of P25+10Pt shown in Fig. 4.4 reveal that the Pt particles are irregularly dispersed on the TiO_2 surface. In particular, areas with finely dispersed Pt clusters (area 1 in Figure 4.4 and its magnification shown in Figure 4.5b) can be

distinguished from areas with dense aggregates of Pt nanoparticles (area 2 in Figure 4.4 and its magnification shown in Figure 4.5a). This is very likely due to a non-perfect mixing of the powder during the sputtering process and generates a bimodal distribution of the Pt particles size, as shown in Figure 4.5d. In particular, the mean particle size obtained by fitting the distribution with two Gaussian functions are 0.8 nm (0.5 nm standard deviation) and 2.2 nm (1.1 nm standard deviation). This particle size is similar or even smaller than that recently attained with other techniques, such as deposition-precipitation or flame spray pyrolysis,[26] or even pDC MS.[15] The EDX quantitative elemental analysis of Pt in Area 1 of Figure 4.4 gives a 0.7 wt.% Pt loading, while that of area 2 yields a 18 wt.% Pt loading. The Pt loading of area 1 measured by EDX is in agreement with the overall Pt loading determined by ICP analysis (0.71 wt.%, see Table 4.1). Thus, we can conclude that the major fraction of Pt is present in the form of well dispersed clusters (*i.e.* with particles size below 2 nm) together with some islands of Pt nanoparticle aggregates (it must be considered that HRTEM is a local probe). Similar Pt particles shape and distribution was detected by HRTEM analysis independently of the deposition time (*i.e.* in samples with different metal loadings). This suggests that different deposition settings, for instance a lower sputtering power (*i.e.* a lower Pt sputter rate), as well as longer deposition times could lead to a more uniform Pt clusters distribution.

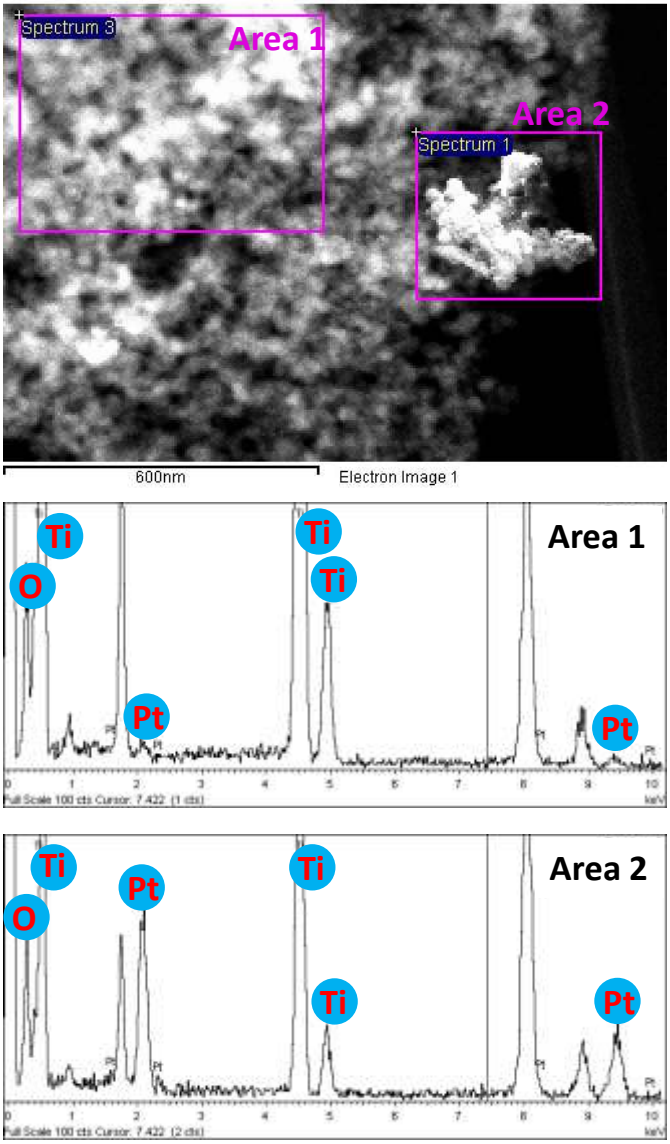

Figure 4.4 *STEM-HAADF and EDX analyses of the P25+10Pt sample.*

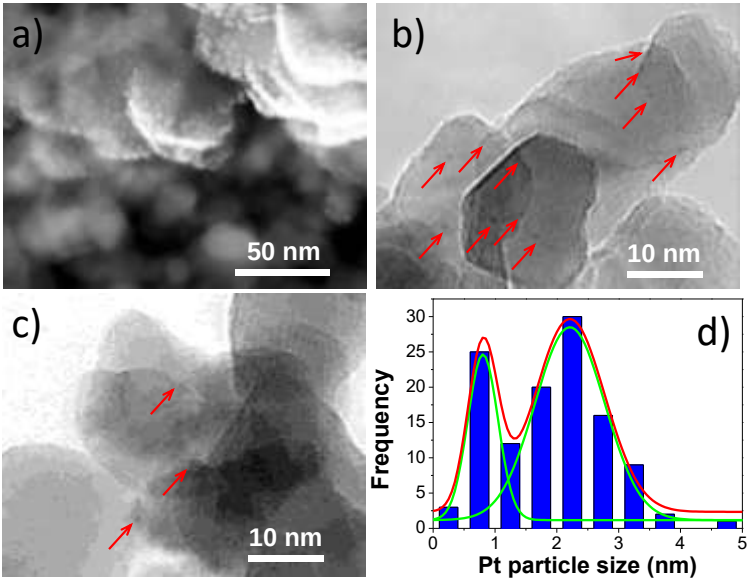

Figure 4.5 *(a) STEM-HAADF image of P25+10Pt and HRTEM micrographs of (b) P25+10Pt and (c) P25+10Cu-Ar. (d) Pt particle size distribution of P25+10Pt. The red curve is the distribution fitting obtained using two Gaussian curves (green curves). The red arrows in (b) and (c) point to Pt and Cu clusters, respectively.*

Figure 4.5c shows the HRTEM image of P25+10Cu-Ar. Cu clusters are more difficult to detect by STEM than Pt clusters, because Cu has a Z-contrast similar to that of Ti. Nevertheless, some Cu clusters can be recognized on the TiO_2 surface, with a shape and dispersion similar to those of Pt clusters.

4.3.2. Methanol photo-steam reforming tests

As already introduced in Chapter 2, during the photocatalytic steam reforming process, methanol undergoes oxidation up CO_2 through the formation of formaldehyde and formic acid as intermediates, while

methane, CO, and dimethylether are usually found as minor side products, as reported in previous work.[26] The gaseous products (H_2, CO_2 and CO) accumulate at constant rate in the recirculating gas phase within the same run (pseudo zero-order kinetics).

As expected, the presence of Pt clusters on the TiO_2 surface is beneficial to the photoactivity of the material, regardless of their amount. Indeed, the larger work function of Pt (5.12 − 5.93 eV), with respect to that of TiO_2 (4.6 – 4.7 eV), implies a Fermi level located at lower energy. Thus, the electrons photo-promoted into the TiO_2 CB are easily transferred to Pt clusters, while photo-produced holes remain in the TiO_2 VB, with the consequent decrease of electron-hole pair recombination probability.

The work function of Cu is 4.53 − 5.10 eV, *i.e.* lower than that of Pt but in a range that can exceed that of TiO_2. This implies that also metallic Cu can in principle act as sink of photo-promoted electrons, though being less efficient than Pt. In fact, the highest photocatalytic performance was attained with P25+10Pt, the photocatalyst obtained by 10 min-long Pt sputtering, leading to a 6-fold increase in H_2 production rate (r_{H_2}) with respect to that of bare titania (Figure 4.6a). The selectivity towards CO_2 and HCOOH increases with increasing Pt amount in the photocatalyst, while the opposite occurs for CO and H_2CO (Table 4.3 and 4.4). These effects are well established for Pt-modified TiO_2 because the noble metal is very effective in pushing methanol oxidation up to CO_2.

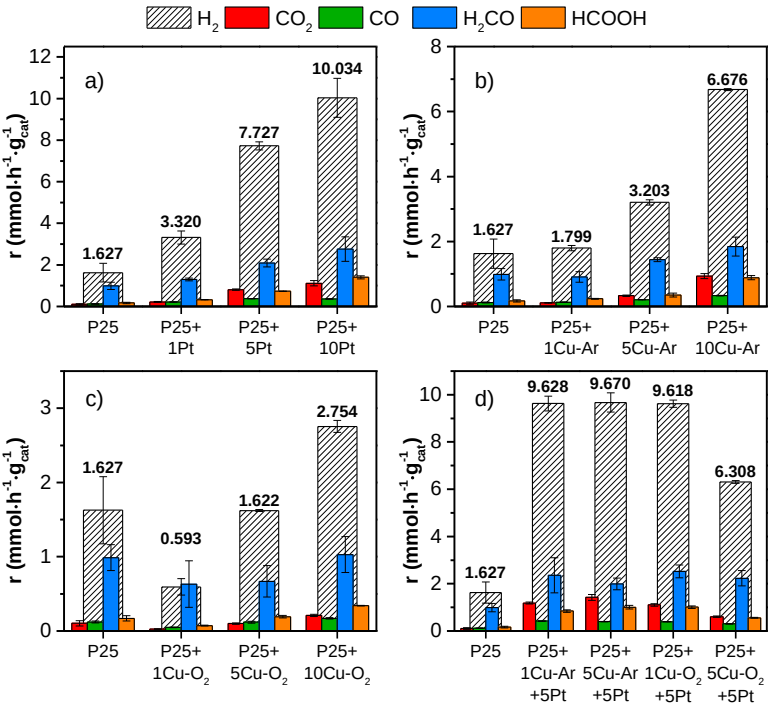

Figure 4.6 *Hydrogen and by-products production rates obtained with (a) Pt-modified TiO_2, (b) Ar-sputtered Cu-modified TiO_2, (c) Ar/O_2-sputtered Cu-modified TiO_2, (d) Pt and Cu co-modified TiO_2, compared to bare, unmodified P25 TiO_2.*

A similar behaviour, but to a lesser extent, can be observed for photocatalysts modified with Cu clusters sputtered in Ar-only plasma (Figure 4.6b). In the case of P25+10Cu-Ar, a 4-fold increase of r_{H_2} was achieved with respect to that of bare titania. As for Pt sputtered TiO_2, also for Cu sputtered TiO_2 the selectivity to CO_2 increases and that to CO decreases with an increase in metal loading up to 42% and 9%, respectively (Table 4.3 and 4.4). The selectivity to formic acid remains almost constant to *ca.* 25%. Conversely, Cu deposition in a reactive

environment (*i.e.* O_2/Ar plasma) was detrimental in the case of P25+1Cu-O_2, or gave very low photoactivity enhancement (Figure 4.6c), P25+10Cu-O_2 being the only photocatalyst of this series showing an increased H_2 production rate with respect to bare TiO_2. Thus, for this type of reaction copper in reduced state appears to be a better performing co-catalyst of TiO_2 than copper oxides.[27]

Table 4.3 *Photocatalytic performance of the investigated materials in methanol photo-steam reforming, in terms of rates of products formation, r. Reaction conditions: 0.015 g of photocatalyst fed in recirculation mode with 60 mL·min^{-1} of a 2% CH_3OH / 3% H_2O / N_2 (balance) gas mixture.*

Sample	Production rate / mmol·h^{-1}·g$_{cat}^{-1}$					
	H_2	CO_2	CO	H_2CO	HCO_2H	CH_4
P25	1.63	0.10	0.12	1.76	0.17	$8\cdot10^{-4}$
P25+1Pt	3.32	0.22	0.22	2.33	0.33	$2\cdot10^{-3}$
P25+5Pt	7.73	0.81	0.38	3.74	0.73	$3\cdot10^{-3}$
P25+10Pt	10.03	1.12	0.36	4.93	1.40	$6\cdot10^{-3}$
P25+1Cu-Ar	1.80	0.11	0.13	1.63	0.24	$7\cdot10^{-4}$
P25+5Cu-Ar	3.20	0.33	0.21	2.58	0.35	$7\cdot10^{-4}$
P25+10Cu-Ar	3.68	0.93	0.34	3.29	0.88	$2\cdot10^{-3}$
P25+1Cu-O_2	0.59	0.03	0.05	1.13	0.07	$8\cdot10^{-4}$
P25+5Cu- O_2	1.62	0.10	0.12	1.20	0.19	$5\cdot10^{-4}$
P25+10Cu- O_2	2.75	0.21	0.17	1.84	0.34	$2\cdot10^{-3}$
P25+1Cu-Ar+5Pt	9.63	1.18	0.42	4.21	0.85	$3\cdot10^{-3}$
P25+5Cu-Ar+5Pt	9.67	1.42	0.40	3.55	1.01	$4\cdot10^{-3}$
P25+1Cu-O_2+5Pt	9.62	1.10	0.39	4.51	1.01	$2\cdot10^{-3}$
P25+5Cu- O_2+5Pt	6.31	0.61	0.30	3.99	0.56	$1\cdot10^{-3}$

Table 4.4 *Photocatalytic performance of the investigated materials in methanol photo-steam reforming, in terms of percent selectivity in relation to hydrogen production, S.*

Sample	Selectivity in relation to H_2 production /%			
	CO_2	CO	H_2CO	HCO_2H
P25	18.8	15.7	67.2	21.3
P25+1Pt	19.8	13.0	39.2	19.7
P25+5Pt	31.4	9.8	27.1	18.9
P25+10Pt	33.4	7.2	25.9	28.0
P25+1Cu-Ar	18.5	14.6	51.0	26.4
P25+5Cu-Ar	25.8	15.2	63.4	22.1
P25+10Cu-Ar	42.0	10.0	27.6	26.5
P25+1Cu-O_2	14.8	17.3	42.3	25.6
P25+5Cu- O_2	18.6	14.6	41.3	23.8
P25+10Cu- O_2	22.9	12.4	37.7	24.8
P25+1Cu-Ar+5Pt	36.8	8.7	24.5	17.5
P25+5Cu-Ar+5Pt	44.1	8.3	20.6	20.8
P25+1Cu-O_2+5Pt	34.4	8.2	26.3	21.0
P25+5Cu- O_2+5Pt	28.8	9.6	35.4	17.7

By comparing the two Cu-only modified photocatalyst series, sputtering copper in Ar-only gives better results than sputtering copper in Ar+O_2 atmosphere. This is possibly related to the lower Cu loading achieved after the same deposition time, due to the lower copper sputtering rate in O_2 containing plasma, and also to the different Cu oxidation state. In particular, the photocatalytic performance attained with P25+1Cu-O_2 is lower than that of pristine TiO_2 (Figure 4.6c). P25+1Cu-O_2 is the only sample showing the characteristic IFCT absorption feature in Figure 4.2c, involving the direct transition of an electron from the TiO_2 valence band to surface Cu(II) species with the consequent copper reduction to Cu(I). However, the redox potential of Cu(II)/Cu(I) couple is

expected to be more positive than that of the H^+/H_2 couple. Thus, electrons photo-promoted into the copper oxide clusters are not useful for hydrogen production and Cu(I) can be oxidized back to Cu(II) by valence band holes with the consequent loss of photon energy and decrease of the overall photocatalytic performance.

We also modified TiO_2 by deposition of both metals, Cu sputtering always preceding Pt sputtering, in line with the deposition sequence optimised in previous studies.[11] Cu was sputtered for either 1 or 5 min, whereas the Pt deposition time was fixed at 5 min. Figure 4.6d shows that with the photocatalysts obtained by sputtering copper in an Ar-only plasma for 1 or 5 min, the rate of hydrogen production (9.6 $mmol \cdot h^{-1} \cdot g_{cat}^{-1}$) was close to the sum of the rates attained with the corresponding single-metal modified materials. Thus, in such materials copper and platinum clusters on the TiO_2 surface appear to produce additive, rather than synergistic effects on photoactivity. A similar r_{H_2} value was also attained with P25+1Cu-O_2+5Pt, while the corresponding Cu-only modified P25+1Cu-O_2 sample showed very low photoactivity. Thus, in this case the hydrogen production rate value was larger than the sum of the H_2 production rates obtained with the singly modified materials. This behaviour is similar to that reported in a recent work by Dozzi *et al.*[11], which evidenced that only a small amount of Cu (*ca.* 0.1 wt.%) has a promoting effect on the performance of Pt/TiO_2 photocatalysts. In contrast, larger amounts of copper sputtered in the presence of O_2, followed by Pt sputtering, proved to have negative effects on the photocatalytic activity, with a decrease of r_{H_2} down to 6.3 $mmol \cdot h^{-1} \cdot g_{cat}^{-1}$ in the case of P25+5Cu-O_2+5Pt. All Pt-Cu co-modified materials, apart from P25+5Cu-O_2+5Pt, showed very similar r_{H_2} values (Figure 4.6d),

suggesting that the presence of Pt clusters on the TiO_2 surface is determining their photoactivity in terms of hydrogen production. However, it must be noticed that the co-presence of Cu and Pt clusters on TiO_2 has a positive effect in increasing the selectivity to CO_2 (up to 44% *vs.* 31%) and decreases that to CO (down to 8% *vs.* 10%).

4.4. Conclusions

This work demonstrates that pulsed-DC magnetron sputtering is a potentially excellent technique to produce large amounts of photocatalyst powders modified with tailored metal nanoparticles in a short time, also avoiding any structural change of the starting material. The operation conditions need to be optimised to increase the homogeneity of the metal clusters dispersion, for instance by lowering the sputtering power and by adopting longer deposition times, or a higher powder shaking frequency during metal sputtering. The properties of the deposited metal clusters also depend on the composition of the plasma during sputtering. In fact, when sputtered under Ar-only plasma, Cu sputtered clusters on TiO_2 behave as typical metal co-catalysts, enhancing TiO_2 photoactivity with increasing loading, though without any synergistic effect when co-deposited with Pt.

References

1 A. V. Puga, *Coord. Chem. Rev.*, 2016, **315**, 1–66.

2 J. Schneider, M. Matsuoka, M. Takeuchi, J. Zhang, Y. Horiuchi, M. Anpo and D. W. Bahnemann, *Chem. Rev.*, 2014, **114**, 9919–9986.

3 Y. Ma, X. Wang, Y. Jia, X. Chen, H. Han and C. Li, *Chem. Rev.*, 2014, **114**, 9987–10043.

4 G. L. Chiarello, M. V. Dozzi and E. Selli, *J. Energy Chem.*, 2017, **26**, 250–258.

5 H. J. Choi and M. Kang, *Int. J. Hydrogen Energy*, 2007, **32**, 3841–3848.

6 T. Kawai and T. Sakata, *Nature*, 1980, 286, 474–476.

7 G. L. Chiarello and E. Selli, *Recent Patents Eng.*, 2010, **4**, 155–169.

8 M. G. Méndez-Medrano, E. Kowalska, A. Lehoux, A. Herissan, B. Ohtani, D. Bahena, V. Briois, C. Colbeau-Justin, J. L. Rodríguez-López and H. Remita, *J. Phys. Chem. C*, 2016, **120**, 5143–5154.

9 A. L. Luna, E. Novoseltceva, E. Louarn, P. Beaunier, E. Kowalska, B. Ohtani, M. A. Valenzuela, H. Remita and C. Colbeau-Justin, *Appl. Catal. B Environ.*, 2016, **191**, 18–28.

10 M. Nischk, P. Mazierski, Z. Wei, K. Siuzdak, N. A. Kouame, E. Kowalska, H. Remita and A. Zaleska-Medynska, *Appl. Surf. Sci.*, 2016, **387**, 89–102.

11 M. V. Dozzi, G. L. Chiarello, M. Pedroni, S. Livraghi, E. Giamello and E. Selli, *Appl. Catal. B Environ.*, 2017, **209**, 417–428.

12 M. Bernareggi, M. V. Dozzi, L. G. Bettini, A. M. Ferretti, G. L. Chiarello and E. Selli, *Catalysts*, 2017, **7**, 301.

13 P. J. Kelly and R. D. Arnell, *Vacuum*, 2000, **56**, 159–172.

14 Y. Zhang, H. Ma, M. Yi, Z. Shen, X. Yu and X. Zhang, *Mater. Des.*, 2017, **125**, 94–99.

15 M. P. Languer, F. R. Scheffer, A. F. Feil, D. L. Baptista, P. Migowski, G. J. Machado, D. P. De Moraes, J. Dupont, S. R. Teixeira and D. E. Weibel, *Int. J. Hydrogen Energy*, 2013, **38**, 14440–14450.

16 R. V. Gonçalves, R. Wojcieszak, H. Wender, C. Sato B. Dias, L. L. R. Vono, D. Eberhardt, S. R. S. R. Teixeira and L. M. Rossi, *ACS Appl. Mater. Interfaces*, 2015, **7**, 7987–7994.

17 R. V. Gonçalves, R. Wojcieszak, P. M. Uberman, D. Eberhardt, E. Teixeira-Neto, S. R. S. R. Teixeira and L. M. Rossi, *Catal. Commun.*, 2014, **48**, 50–54.

18 H. Wender, P. Migowski, A. F. Feil, L. F. de Oliveira, M. H. G. Prechtl, R. Leal, G. Machado, S. R. Teixeira and J. Dupont, *Phys. Chem. Chem. Phys.*, 2011, **13**, 13552–13557.

19 H. Wender, R. V. Gonçalves, A. F. Feil, P. Migowski, F. S. Poletto, A. R. Pohlmann, J. Dupont and S. R. Teixeira, *J. Phys. Chem. C*, 2011, **115**, 16362–16367.

20 H. Wender, P. Migowski, A. F. Feil, S. R. Teixeira and J. Dupont, *Coord. Chem. Rev.*, 2013, **257**, 2468–2483.

21 M. Ratova, P. J. Kelly, G. T. West, L. Tosheva and M. Edge, *Appl. Surf. Sci.*, 2017, **392**, 590–597.
22 M. Ratova, R. Klaysri, P. Praserthdam and P. J. Kelly, *Mater. Sci. Semicond. Process.*, 2017, **71**, 188–196.
23 H. M. Rietveld, *J. Appl. Crystallogr.*, 1969, **2**, 65–71.
24 A. Altomare, M. C. Burla, C. Giacovazzo, A. Guagliardi, A. G. G. Moliterni, G. Polidori and R. Rizzi, *J. Appl. Crystallogr.*, 2001, **34**, 392–397.
25 P. Scherrer, *Göttinger Nachrichten Math. Phys.*, 1918, **2**, 98–100.
26 G. L. Chiarello, M. H. Aguirre and E. Selli, *J. Catal.*, 2010, **273**, 182–190.
27 M. Janczarek and E. Kowalska, *Catalysts*, 2017, **7**, 317.

Chapter adapted from "M. Bernareggi, G. L. Chiarello, G. West, M. Ratova, A. M. Ferretti, P. Kelly and E. Selli, *Catal.Today*, 2018, *in press*" and reproduced with Editor's permission. doi.org/ 10.1016/j.cattod.2018.07.011

Chapter 5:

REDOX DYNAMICS OF Pt AND Cu DEPOSITED ON TiO_2 DURING PHOTOCATALYTIC METHANOL OXIDATION STUDIED BY *in situ* ME-XAS

5.1. Introduction

The activity of heterogeneous catalysts, including the photocatalytic materials, is strongly affected by the structure, the oxidation state and the redox dynamics of the surface active sites. This is even more important when the catalyst efficiency is influenced by active nanoparticles (NPs) dispersed over the surface of the support.[1] For instance, the modification of titanium dioxide with metals, acting as photopromoted electrons trap, usually leads to an increased photoactivity with respect to the corresponding bare material.[2] However, the beneficial effect of the same metal could vary to a great extent when the modified photocatalyst is exploited in hydrogen production (*i.e.*, under anaerobic conditions) or in organic pollutants mineralisation (*i.e.*, under aerobic conditions). For example, platinum deposited over the TiO_2 surface is well-known to bring great improvements in hydrogen production from alcohols photo-reforming with respect to pristine titanium dioxide, with

optimal metal loading.[2,3] On the contrary, in organics oxidation reactions Pt NPs can be both beneficial, but to a more limited extent,[4] or even detrimental for the photocatalytic activity.[5] Other important variables are connected to the synthetic route. This can imply a reduction step of the metal precursor[2,6,7] or it can be in single-step together with the synthesis of the oxide substrate,[3,8] and this highly influences the final oxidation state of the nanoparticle. Also the metal particle size and distribution can affect the photocatalyst stability and activity.[9]

In this context, the knowledge of the real active phase of metal-modified materials becomes important to better direct the synthetic paths or to adapt the reaction conditions in order to stabilise the most active, or the most suitable, species. However, the main challenge in the spectroscopic analyses of such composite materials is discerning the signal variation originated by the few atoms involved in the adsorption/desorption mechanisms, at the surface of the nanoparticles, from the static signal of the bulk. The exploitation of high energy X-rays, like in the X-ray absorption spectroscopy (XAS), delivers the intrinsic advantages of element specificity and large penetration depth of such radiation, along with information of the local coordination and the oxidation states. Nevertheless, low analyte concentration in the matrix or highly absorbing elements present into the support can decrease the effectiveness of the analysis. To improve the sensitivity of the technique to the small variations occurring to the catalyst under *operando* conditions, the combination of the time-resolved XAS analyses with Modulated Excitation Spectroscopy (MES) has proved to be a valuable tool. MES is achieved through the cyclic variation of the experimental conditions, such as the gas composition on the sample, in terms of a

square-wave stimulation.[10–12] A phase Sensitive Detection (PSD) function is then exploited by MES to gain better signal to noise ratio and to hide all those parts of the spectra unaffected by the periodic stimulation, *e.g.* the bulk of nanoparticles or of the catalyst.

The Modulated Excitation X-ray Absorption Spectroscopy (MEXAS) has proved to largely enhance and to highlight even the small variations occurring to metal nanoparticles, *i.e.* Pd, Pt, Rh, Ru, under several modulation experiment, exploiting different gas combinations, like CO *vs.* NO,[13,14] H_2 *vs.* O_2,[15,16] CH_4 *vs.* O_2.[17] The essential condition to have a response from this kind of experiment is that the investigated process is reversible.[13–17]

Recently, it has been demonstrated that through the MEXAS technique it is possible to extrapolate a broad range of information, from minute structural changes to kinetic behaviour, from an alumina-supported Pd nanoparticles influenced by reduction/oxidation cycles.[16]

In this chapter, the results are reported on the behaviour of a Pt-modified and a Cu-modified titanium dioxide material prepared in a single-step synthesis, during methanol oxidation reaction under anaerobic and aerobic conditions. These two metals are among the most widespread ones in photocatalysis due to their photocatalytic enhancing capabilities, but their behaviour under different reaction conditions, as mentioned above, is still unclear. MEXAS characterisation allowed us to better understand how Pt and Cu change in the presence or in the absence of O_2 and how this is connected to their photoactivity. In order to reduce the XAS acquisition time, thus getting a better time-resolution, these sample were prepared with a high metal loading (nominal 2 wt.%).

5.2. Experimental section

5.2.1. Photocatalysts Synthesis

The samples were prepared in single step by flame spray pyrolysis (FSP),[18] employing a commercial FSP system (NPS 10 by Tethis S.p.A). All chemicals were purchased by Sigma Aldrich and used as received. The burned solutions contained the precursors of titanium dioxide (titanium tetraisopropoxide TTIP), and, when necessary, of Cu or Pt. 50 mL of a 0.6 M TTIP in xylene solution were mixed with 25 mL of propanoic acid solution containing the proper amount of Cu or Pt precursors (copper acetate monohydrate and hexachloroplatinic acid, respectively), in order to have a final 2 wt% metal loading on TiO_2. Such a relatively high metal loading was chosen for spectroscopic reasons, *i.e.* in order to have sufficient statistics during the time resolved XAS spectra measurements. The so-obtained solutions were injected to the nozzle (4 $mL \cdot min^{-1}$) by means of a syringe pump, sprayed with 5.0 $L \cdot min^{-1}$ of O_2 and burned through a methane/oxygen flamelet ring (1.0 $L \cdot min^{-1}$ and 2.0 $L \cdot min^{-1}$ flow rates for CH_4 and O_2 respectively). The so-produced powders were collected on glass fibre filters (Whatman) placed above the burner.

5.2.2. Photocatalysts Characterisation

The effective Cu or Pt loading on the samples was measured by ICP analyses with a Perkin Elmer Optima 8000 IPC-OES. Both samples were completely dissolved by using a hot (378 K) aqua regia (3:1 HCl:HNO_3 molar ratio, 10 mL) and HF (2.5 mL) solution for 4 h and then diluted to appropriate concentration. Additionally, FP-2Cu/TiO_2 was also

treated in hot aqua regia without hydrofluoric acid in order to dissolve surface Cu only. The obtained solution was filtered to remove the undissolved solid support and analysed after proper dilution.

The BET specific surface area (SSA) was measured by N_2 adsorption at liquid nitrogen temperature on an ASAP 2020 apparatus, after out-gassing in vacuo at 150 °C for at least 2 h.

XRD patterns were recorded by using copper Kα radiation (λ = 1.54056 Å) in a Philips PW3020 powder diffractometer, operating at 40 kV and 40 mA. Phase quantification was performed using the "*Quanto*" software,[19] applying the Rietveld refinement method;[20] the mean anatase and rutile crystallite sizes were obtained through the Scherrer equation,[21] from the width of the most intense reflections (2θ = 25.4° and 2θ = 27.4° for anatase and rutile, respectively).

UV-Vis diffuse reflectance spectra were measured with a Jasco V-670 spectrophotometer equipped with an integrating sphere (PIN-757), using barium sulphate as a reference. Spectra are reported both as absorption (A) spectra (where A = 1 – R, R being the reflectance) and as the Tauc plot of Kubelka – Munk transformation, which allows to estimate the band gap.

5.2.3. Photocatalytic tests

The samples were tested in the gas phase photocatalytic methanol oxidation reaction under both aerobic or anaerobic conditions. In the former case the photoreactor was fed with a 3.6% CH_3OH / 3.8% H_2O / N_2 gas stream (photo-steam reforming reaction), in the latter case with 18% CH_3OH / 20% O_2 / N_2. The gas stream was obtained by bubbling pure N_2 into a 20 vol% CH_3OH in H_2O solution kept 30 °C, or air in pure methanol kept at 0 °C. The amount of methanol and water vapours in the

obtained gas stream were calculated according to the Raoult's law for a non-ideal solution (T = 303 K, P_{TOT} = 1 bar, x_{CH_3OH} = 0.1; $p^0_{CH_3OH}$ = 0.219 bar, γ_{CH_3OH} = 1.635, $p^0_{H_2O}$ = 0.042 bar and γ_{H_2O} = 1.635).

The kinetic tests were performed using a stainless steel setup similar to the one described elsewhere[22] but operating in continuous feeding mode (*i.e.,* no recirculation). Briefly, 15 mg of photocatalyst powder were dispersed onto *ca.* 7 g of 20 – 40 mesh (0.42 – 0.85 mm) quartz grains by adding few droplets of water, mixing with a spatula and drying in oven at 70 °C for at least 1 h. The so-obtained photocatalytic bed was then loaded into a home-made stainless-steel photoreactor (50 mm diameter and 2 mm depth), equipped with a Pyrex glass optical window with a cut-off edge located at *ca.* 320 nm. The gas flow rate was set at 60 $mL \cdot min^{-1}$ by means of a mass flow meter (EL-FLOW Base, Bronkhorst). The outlet of the photoreactor was connected to a 6-way injection valve of a gas chromatograph (GC, Agilent 6890N) and then to a bubbler filled with a $NaHCO_3/Na_2CO_3$ aqueous solution acting as a trap for the photo-produced formic acid and formaldehyde.

The GC was equipped with two capillary columns (MoleSieve 5A and HP-Plot U), two detectors (TCD and FID) and a Ni-based catalyst for CO and CO_2 methanation. Prior to any analysis, the system was thoroughly purged in dark for 20 min with pure N_2 (in the case of the steam reforming reaction, to remove any trace of O_2) or with air. A 300 W xenon arc lamp (LSH302, LOT-Oriel) placed at 20 cm from the reactor was employed as light source. During a photocatalytic test, the photoreactor was irradiated for 190 min while the formation of the gaseous products was continuously monitored by GC analysis starting 2 min after the beginning of the irradiation and then every 19 min.

The overall formic acid formation was determined at the end of any run by ion chromatographic analysis of the aqueous solution contained in the trap, using a Metrohm 761Compact IC instrument. Formaldehyde was determined by spectrophotometric analysis exploiting the Nash method.[23,24] Briefly, after proper dilution, the solution contained in the trap flask was added to an equivalent volume of Nash's reagent (25 g ammonium acetate, 2.1 mL acetic acid and 0.2 mL acetylacetone, dissolved in ultrapure water, up to a total volume of 100 mL) and stirred for 1 h. Formaldehyde concentration was determined by the absorption at 413 nm, after proper calibration, with a Jasco V-670 spectrophotometer.

Selectivity to the by-products was calculated for the methanol steam reforming reaction as the ratio between the production rate of the selected sub-product and the hydrogen production rate corrected for the stoichiometry of the formation reaction.[2]

5.2.4. MEXAS measurements

We performed two different modulation experiments for each sample, mimicking the corresponding photocatalytic experiments: switching *i*) from 5%O_2/He + UV-Vis to 3.6% CH_3OH/He in the dark and *ii*) from 3.8%H_2O/He + UV-Vis to 3.6%CH_3OH/He in the dark. Time-resolved XAS spectra were recorded in energy dispersive mode at both the Cu K-edge (8.98 keV) and the Pt L3-edge (11.56 keV) at the ID24 beamline of ESRF in Grenoble (France). 1.5 mm quartz capillaries were filled with the photocatalytic powder and then connected to the gas manifold. Inlet water and methanol vapour flows were attained by bubbling He in the corresponding liquids. The switching of the inlet gas composition was attained using an automatic 4-way valve synchronized

with the XAS acquisition. The outlet gas composition from the capillary was continuously monitored by mass spectrometry (MS).

The UV-Vis light source was the same lamp used for the photocatalytic tests but connected to liquid light guide, to focus the light on the quartz capillary, and an electronic shutter also synchronized with the XAS acquisition. Prior to the modulation experiment the set-up was purged with He (40 mL·min^{-1}) under dark conditions, until the MS signals of O_2 (m/Z = 32) and N_2 (m/Z = 28) were stable and low. The modulation period was fixed to 210 s long, while recording 40 time resolved XAS spectra (*ca.* 5 s per spectrum, 20 spectra in O_2 or H_2O + 20 spectra in CH_3OH). The full MEXAS experiment consisted in 15 consecutive modulation periods. Additionally, an oxidation-reduction modulation experiment was carried out for both samples. In this case, the capillary was pre-heated at 473 K under He flow by means of a heating gun placed just below the capillary. After reaching the desired temperature, 15 alternated 210 s long 5%O_2/He *vs.* 5%H_2/He pulses (20 mL·min^{-1} flow, 5 vol.% in He) were sent to the capillary, without UV-Vis irradiation.

The averaged time-resolved and PSD transformed (phase-resolved) spectra were obtained using a homemade MATLAB routine. The first five modulation periods were always discarded to ensure that the steady state conditions were achieved.

5.3. Results

5.3.1. Characterisation

ICP-OES elemental analyses, reported in Table 5.1, revealed that Pt loading in the corresponding FP-2Pt/TiO_2 photocatalyst was 1.61 wt.%, lower than nominal but consistent with the high hygroscopicity of

the precursor. Copper loading in FP-2Cu/TiO_2 photocatalyst, obtained after complete dissolution of the sample, was 1.92 wt.%, close to the nominal 2 wt.%, while, when the TiO_2 matrix was not dissolved, the analysis showed a 1.49 wt.% Cu loading. This difference might be attributed to the partial doping of titanium dioxide. Indeed, the Cu(II) atomic radius is only slightly larger than that of Ti(IV), 0.87 Å *vs.* 0.745 Å respectively, and thus Cu(II) ions may substitute titanium atoms in the lattice[25] during the one step flame synthesis.

As already observed for analogous samples with lower metal loadings,[26] the XRD patterns of the flame-made samples showed that anatase was the main crystallographic phase. The bare titanium dioxide sample was composed by *ca.* 86% of anatase and 14% of rutile (Table 5.1). The presence of copper during the single-step synthesis promoted the rutile formation, increasing its content up to 23%. As a dopant, Cu(II) generates oxygen vacancies inside the crystalline structure, resulting in a favoured growth of rutile crystallites.[25,27,28] On the opposite, the presence of Pt did not induce any important effect on the phase composition. Of the material. No reflections related to copper or platinum, either in oxide or metal forms, could be observed, indicating that metals, except for the dopant copper, are finely dispersed over TiO_2 nanoparticles.

The two metals affected differently the crystallite dimensions. On one side, anatase is not affected by platinum during the synthesis, while the presence of copper caused a doubling in the average diameter (from 13 nm for bare TiO_2 to 27 nm in FP-2Cu/TiO_2). On the opposite, rutile crystallite dimensions are affected in the same extent by the presence of the metals, with an increase from 9 nm up to 16 nm.

Table 5.1 *Crystalline phase distribution and corresponding crystallite average diameter, metal loadings and band gap values for the three samples.*

Sample	Pt or Cu (wt.%)	SSA (m^2 g^{-1})	Anatase (%)	d_a (nm)	Rutile (%)	d_r (nm)	Band Gap (eV)
FP-TiO_2	/	110	86	14	14	9	3.12
FP-2Pt/TiO_2	1.61	151	86	14	14	17	3.15
FP-2Cu/TiO_2	1.92	132	77	27	23	17	3.05

The bare TiO_2 possesses a high BET specific surface area (SSA) of 110 m^2 g^{-1}, typical of flame made powders. The addition of Cu and Pt during the flame synthesis with this relatively high loading led to an increased SSA up to 132 and 151 $m^2 \cdot g^{-1}$, respectively (Table 5.1).

The UV-Vis diffuse reflectance spectra, reported in Figure 5.1a, of the pristine oxide show the usual profile of flame-made bare TiO_2. The absorption increase in the 400 – 800 nm range can be ascribed to the carbonaceous impurities typically present in FSP-made materials.

As expected, the presence of Pt in the corresponding noble metal-modified TiO_2 gives rise to an extended absorption in the visible range, compatible with the dark grey colour of the sample. FP-2Cu/TiO_2 showed the typical *d-d* transition band of this metal at wavelength between 600 and 800 nm, thus confirming its presence as stable oxidised copper in Cu_xO form. The extra absorption tail observed at 400 – 500 nm can be ascribed to the interfacial charge transfer (IFCT) mechanism between TiO_2 VB electrons and Cu(II) species which are partially reduced to Cu(I).[27,29,30]

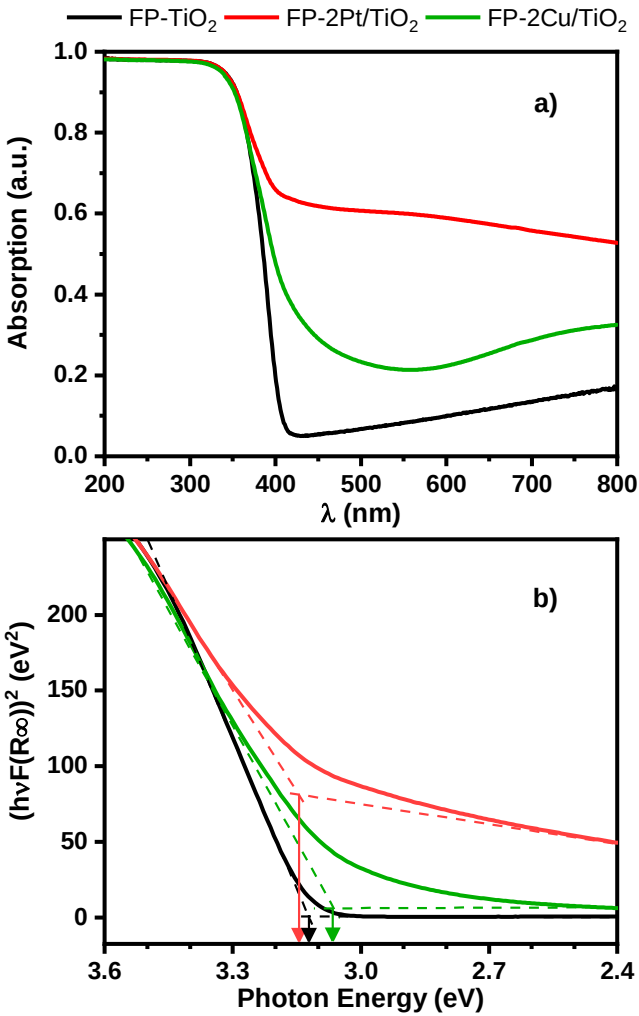

Figure 5.1 *(a) Absorption spectra and (b) Tauc plot of the Kubelka-Munk transform of the three samples.*

The Tauc plot of the Kubelka-Munk transformation (Figure 5.1b) allowed to estimate the band gap of the three photocatalyst. As expected, bare and Pt-modified TiO_2 did not show important difference in the

energy gap, 3.12 and 3.15 eV respectively, while the band gap of FP-2Cu/TiO_2 is apparently slightly narrower, 3.05 eV, probably due to the larger rutile content in the latter sample and to Cu doping.[31,32]

5.3.2. Photocatalytic activity

In the methanol photo-steam reforming reaction, the organic substrate, according to the already proposed reaction mechanism,[2,33,34] is oxidised up to carbon dioxide through several intermediates and reaction pathways with the simultaneous production of hydrogen. Thus, in addition to H_2 and CO_2, also carbon monoxide, formic acid and formaldehyde were detected. Dimethyl ether formation was also detected in this reaction but not quantified. The gaseous products flew from the photocatalytic cell to the GC sampling loop for analysis. A calibration previously performed allowed us to quantify the products in terms of ppmv in the gas stream and consequently as moles of produced gas.

As shown in Figure 5.2a and reported in Table 5.2, FP-2Pt/TiO_2 is by far the best performing photocatalyst, showing a hydrogen production rate of *ca.* 19 $mmol \cdot h^{-1} \cdot g_{cat}^{-1}$. It is known that Pt is a very efficient co-catalyst of TiO_2,[2,35] able to trap the photopromoted electrons, due to its higher work function[36] with respect to TiO_2 (5.12 – 5.93 eV *vs.* 4.6 – 4.7 eV, respectively) that enhances the separation of the charge carriers. Moreover, the reduction to H_2 proceeds more efficiently on the Pt surface than on TiO_2. By contrast, the FP-2Cu/TiO_2 sample exhibited a r_{H_2} significantly lower than that obtained with the Pt modified photocatalyst and just slightly higher than that of the bare TiO_2 (5 *vs.* 4.9 $mmol \cdot h^{-1} \cdot g_{cat}^{-1}$, respectively).

Table 5.2 *Photocatalytic performance of the studied materials in the anaerobic methanol oxidation, in terms of rates of products formation, expressed in mmol·h^{-1}·g$_{cat}^{-1}$*

Sample	r_{H_2} (mmol·h^{-1}·g$_{cat}^{-1}$)	r_{CO_2} (mmol·h^{-1}·g$_{cat}^{-1}$)	r_{CO} (mmol·h^{-1}·g$_{cat}^{-1}$)	r_{H_2CO} (mmol·h^{-1}·g$_{cat}^{-1}$)	r_{HCOOH} (mmol·h^{-1}·g$_{cat}^{-1}$)
FP-TiO_2	4.94	0.26	0.21	2.87	0.43
FP-2Pt/TiO_2	19.25	2.06	0.06	8.62	1.72
FP-2Cu/TiO_2	5.02	0.54	0.06	2.79	0.35

Indeed, the work function of Cu (4.53 – 5.1 eV) is very close to that of TiO_2, thus reducing its electron trapping ability and charge carriers separation efficiency. It is worth underlining that the Cu and Pt metal loading (2 wt.%) is not the optimal one in terms of photocatalytic activity which usually drops at such high metal content. However, as mentioned above, this high loading was chosen for spectroscopic reasons. The modification with both Pt and Cu increases the selectivity to CO_2 (up to 32%) and decreases the selectivity to CO (Table 5.2).

For all three investigated samples and under these experimental conditions, formaldehyde was the main methanol oxidation product with a selectivity above the 45%, while the selectivity to formic acid was the less affected by metal NP modification (Table 5.2). The sum of the selectivities of the above-mentioned by-products (CO_2, CO, H_2CO and HCOOH) is close to 100% for all samples, proving that other species (like the detected dimethyl ether) are not directly involved in H_2 production. The production of hydrogen and of the by-products appeared to be stable along the 3 h irradiation time (Figure 5.3).

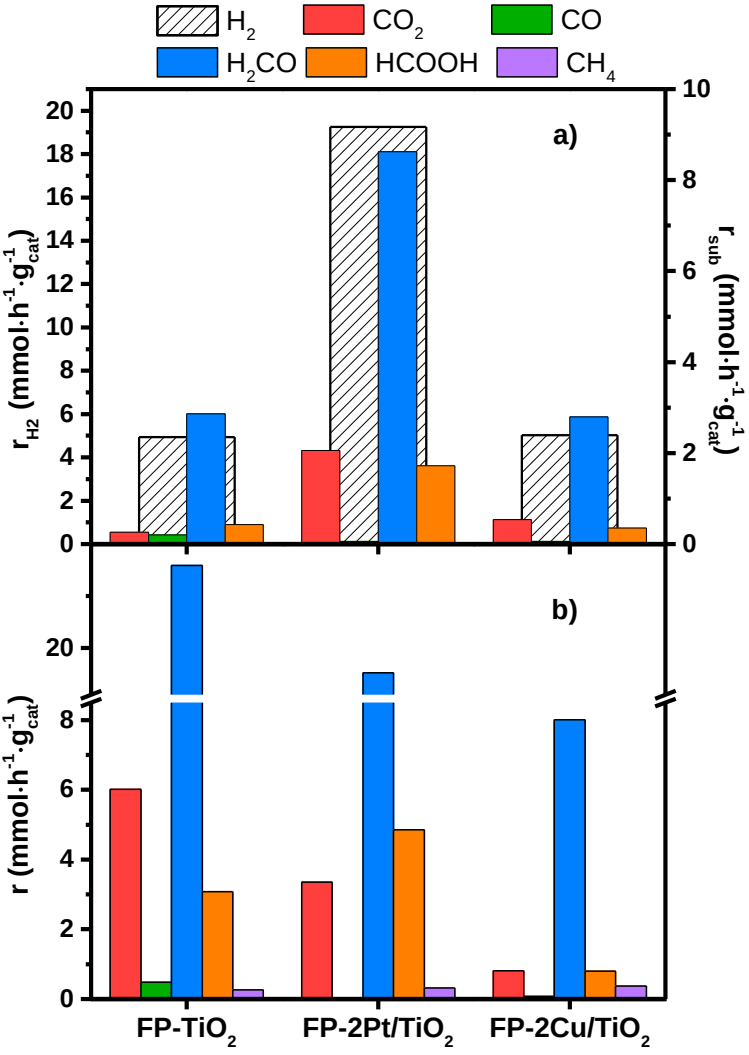

Figure 5.2 *Photocatalytic results obtained in (a) anaerobic and (b) aerobic methanol oxidation reactions. In (a), by-product formation rate refers to the right ordinate. The values were obtained as the linear regression of the instantaneous production rates over time.*

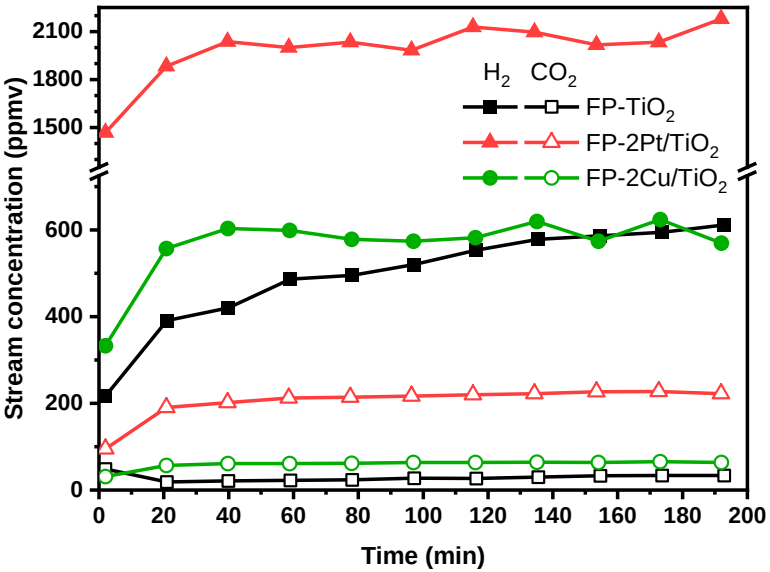

Figure 5.3 *Time-on-stream concentration profiles of hydrogen (full symbols) and carbon dioxide (empty symbols) for the tested samples.*

Contrarily to methanol photo-steam reforming conditions, in the presence of O_2 bare titanium dioxide showed to be the most active photocatalyst, especially in terms of CO_2 and formaldehyde production (Table 5.3 and Figure 5.2b). Traces of CH_4 and CO were also detected as side-products. The overall photocatalytic activity, expressed as the sum of the production rates of all C-containing species, significantly increases under aerobic conditions, *i.e.* from 4 to 38 $mmol \cdot h^{-1} \cdot g_{cat}^{-1}$ for TiO_2, from 12 to 26 $mmol \cdot h^{-1} \cdot g_{cat}^{-1}$ for FP-2Pt/TiO_2, and from 4 to 10 $mmol \cdot h^{-1} \cdot g_{cat}^{-1}$ for FP-2Cu/TiO_2. The modification with Pt was beneficial only for formic acid production, while Cu NPs dramatically decreased the overall photoactivity compared to pristine TiO_2. Hence, under aerobic conditions, the surface modification of TiO_2 with Pt and Cu, at least with this relatively high metal loading, demonstrated to be detrimental for

photocatalytic activity. Formaldehyde resulted to be the main product of methanol oxidation also in this case.

Table 5.3 *Photocatalytic results of the investigated photocatalysts in the aerobic methanol oxidation, in terms of rates of products formation, expressed in mmol·h^{-1}·g_{cat}^{-1}*

Sample	r_{CO_2} (mmol·h^{-1}·g_{cat}^{-1})	r_{CO} (mmol·h^{-1}·g_{cat}^{-1})	r_{H_2CO} (mmol·h^{-1}·g_{cat}^{-1})	r_{CH_4} (mmol·h^{-1}·g_{cat}^{-1})	r_{HCOOH} (mmol·h^{-1}·g_{cat}^{-1})
FP-TiO_2	6.01	0.49	27.95	0.27	3.08
FP-2Pt/TiO_2	3.35	0.00	17.61	0.31	4.85
FP-2Cu/TiO_2	0.82	0.08	8.01	0.37	0.80

5.3.3. MEXAS measurements

The photocatalytic tests have shown that the surface modification of TiO_2 with Cu and Pt have an opposite effect on the methanol oxidation when this occurs in presence of water vapour or of oxygen. While Cu and Pt co-catalyst demonstrated to improve the CO_2 production rate in the presence of water, they had a detrimental effect in the presence of oxygen, where bare TiO_2 showed a significantly higher CO_2 production rate than the corresponding metal modified samples. MEXAS is a powerful tool to get a deeper insight into the role of Cu and Pt on the photoactivity during the methanol oxidation under these two different conditions. Indeed, MEXAS can provide information on the subtle redox dynamics of the metal co-catalysts, which is connected to their possible surface interaction with water or oxygen. During the modulation experiment, the samples were saturated in methanol vapours in the dark for 105 s, followed by the

reaction under UV-vis with water vapours or with oxygen for further 105 s while recording 20+20 time resolved XAS spectra at the Cu K-edge or at the Pt L3-edge.

5.3.3.1. Pt L3-edge experiments

The averaged time resolved XANES spectra recorded during the anaerobic modulation experiment, *i.e.* H_2O + UV-Vis *vs.* MeOH, are shown in Figure 5.4a (grey curves) together with the reference spectra of metal Pt (red line) and PtO_2 (blue line).

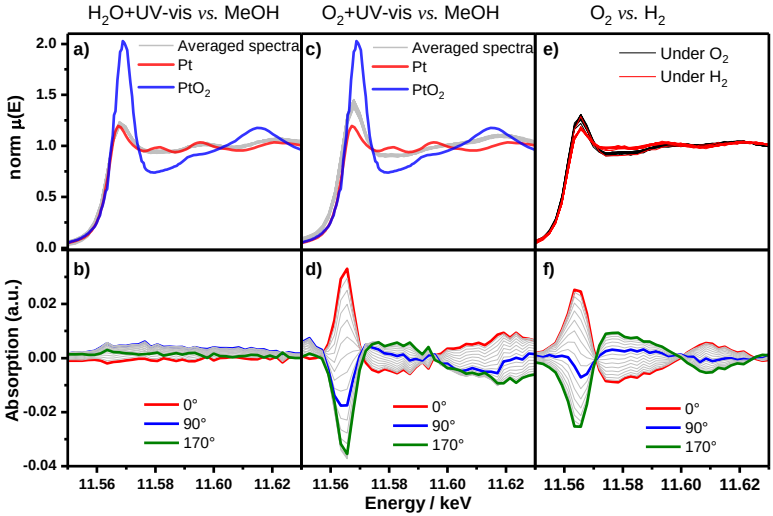

Figure 5.4 *ME-XANES results at the Pt L3-edge obtained with the FP-2Pt/TiO_2 sample. (a, c, e) Averaged time-resolved and (b, d, f) phase resolved in the 0° < φ^{PSD} < 170° range spectra for the (a, b) H_2O vs. MeOH, (c, d) O_2 vs. MeOH and (e, f) O_2 vs. H_2 modulation experiments; In (a) and (c) the spectra are compared with that of metal Pt (red curve) and PtO_2 (blue curve) reference spectra.*

The whiteline intensity of the averaged time resolved spectra clearly resembles that of the reference metal Pt (red spectrum) showing that Pt is essentially in reduced form under anaerobic reaction conditions.

The linear combination fitting of these spectra, using those of Pt foil and PtO_2 as standards, confirmed that *ca*. 93% of Pt is present as metal. Moreover, the phase resolved spectra at the Pt L3-edge (Figure 5.4b) shows no variations as a function of the demodulation angle φ^{PSD}, proving that Pt undergoes no redox or structural changing under anaerobic reaction conditions,

The XANES spectrum at the Pt L3-edge of the as prepared FP-2Pt/TiO_2 sample (Figure 5.5) shows an intense white line demonstrating that Pt is prevalently in oxidized form. However, Figure 5.5 shows that Pt is reduced under photo-steam reforming reaction conditions, as already reported.[3]

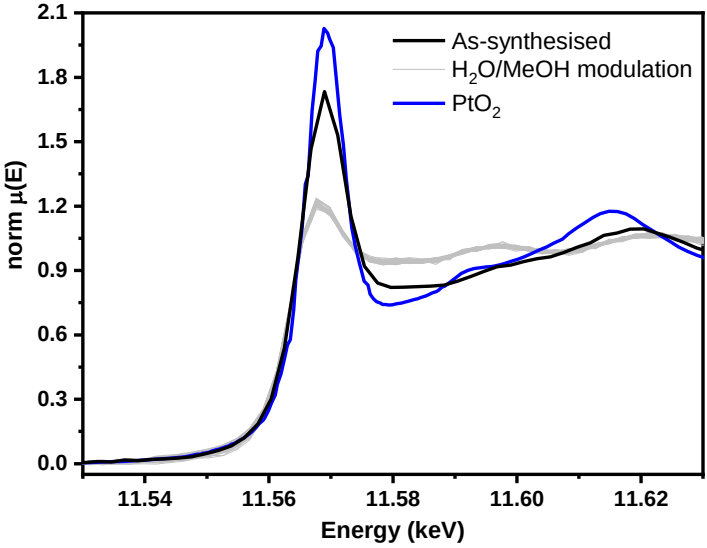

Figure 5.5 *XANES spectra at the Pt L3-edge of as-synthesised (black line) and of averaged time resolved spectra recorded under H_2O + UV-Vis vs. methanol modulation experiment (grey lines) of FP-2Pt/TiO_2 sample compared to reference PtO_2 (blue line).*

Platinum reduction under anaerobic conditions explains the much larger activity of the FP-2Pt/TiO_2 sample with respect to the bare photocatalyst. Due to the high work function (5.12 − 5.93 eV),[36] metal Pt is very efficient in scavenging photopromoted electrons from the conduction band of titanium dioxide. The combination of longer-living electrons with the high affinity of metal Pt towards protons leads to the observed high hydrogen production rate.

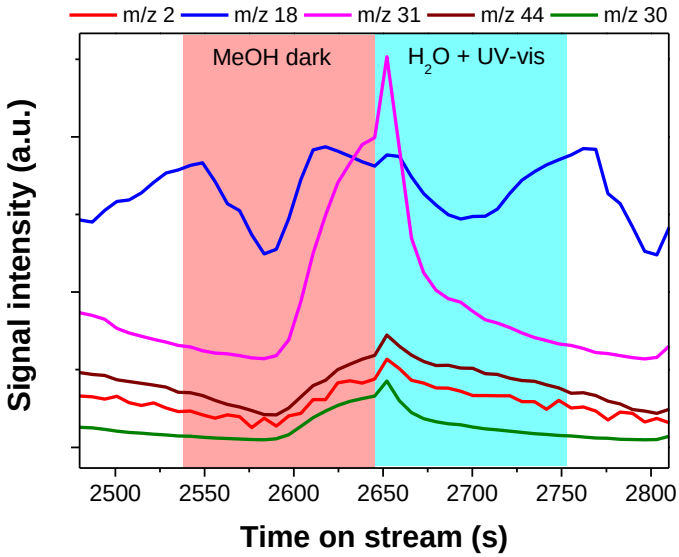

Figure 5.6 *MS profiles reporting a single modulation cycle of the H_2O/MeOH modulation experiment, showing H_2 (red line, 10 times magnified), H_2O (blue line), H_2CO (green line), MeOH (magenta line), and CO_2 (brown line). In red is highlighted the MeOH pulse, whereas in light blue the oxidative pulse.*

From the mass spectroscopy (MS) spectra related to the H_2O/MeOH modulation experiment, reported in Figure 5.6, it can be observed that the profiles of the signals of H_2, CO_2 and H_2CO has the same shape of that of methanol. Indeed, as soon as the shutter is opened,

the adsorbed methanol quickly reacts with the photopromoted electrons and with water to give the steam reforming products. Then, as methanol is consumed, the production of H_2 and CO_2 decreases over time.

Under O_2 + UV-Vis *vs.* MeOH modulation conditions the averaged time resolved spectra (Figure 5.4c) shows again that Pt is still prevalently in a reduced form, but the whiteline is more intense than those recorded under anaerobic condition. This result suggests that under aerobic condition the metal surface Pt nanoparticles may be oxidised at the surface because of an interaction with O_2. The averaged spectra obtained from the O_2/MeOH modulation experiment showed little but observable differences (Figure 5.4c), clearly enhanced by the PSD function on the demodulated spectra (Figure 5.4d). Indeed, Pt is continuously oxidised under oxygen and reduced under methanol. The phase resolved spectra (Figure 5.4d) highlights that changes occur mainly at 11.566 eV, corresponding to a variation in the whiteline intensity.

The higher oxidation state of Pt under such conditions is further confirmed by the linear combination fitting analyses performed over the last XANES spectrum recorded under MeOH flow and over the last one recorded under oxidative gas flow. In the former situation, 76% of Pt is present in metallic form, whereas in the latter the 73% is metallic Pt. Thus, Pt is in a more oxidised state with respect to anaerobic conditions and it is continuously oxidised and reduced, as proved by PSD spectra.

Furthermore, the envelopes of the PSD spectrum obtained with O_2/MeOH modulation are similar to those of the O_2/H_2 modulation at high temperature (Figure 5.4f). Considering that, due to the harsh conditions of the latter experiment that certainly can reduce and oxidise Pt nanoparticles, it can be supposed that the same occurs also under the

milder O_2/MeOH conditions. Nevertheless, the change in the oxidation state is not complete, but very likely occurring only at the surface of the Pt NPs.

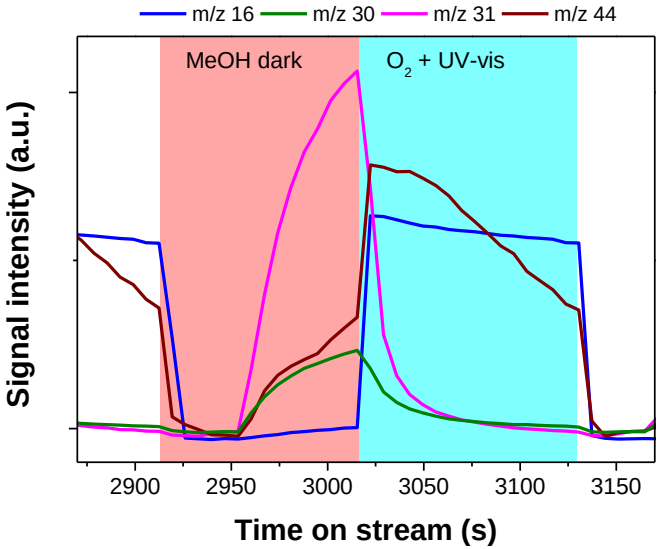

Figure 5.7 *MS profiles reporting a single modulation cycle of the H_2O/MeOH modulation experiment, showing H_2O (blue line), H_2CO (green line), MeOH (magenta line), and CO_2 (brown line). In red is highlighted the MeOH pulse, whereas in light blue the oxidative pulse.*

By comparing the MS profiles obtained under aerobic (Figure 5.7) and anaerobic (Figure 5.6) conditions, it can be observed a net increase in CO_2 production, as already noticed from the results of the photocatalytic tests and a H_2CO production.

The lower efficiency of FP-2Pt/TiO_2 photocatalyst under aerobic conditions can be explained by the interaction of the oxidant, *i.e.* O_2, with the photopromoted electrons trapped in the Pt nanoparticles. Such interaction leads to the formation of a PtO_2 layer over the Pt NPs, decreasing the photoactivity. On the contrary, the more reduced state

under anaerobic conditions favours protons reduction over the Pt nanoparticles by photopromoted electrons, leading to high H_2 production rates.

5.3.3.2. Cu K-edge experiments

Also in the case of Cu NPs, the averaged spectra recorded under anaerobic modulation conditions (grey lined in Figure 5.8) clearly look like those of the metal Cu. Indeed, by comparing the shape of the whiteline of the spectra in Figure 5.8a with those in red of Figure 5.8e (recorded under H_2 stream at high temperature, where copper is completely reduced), it can be observed the characteristic double peak feature at the whiteline of metal Cu at *ca.* 9.0 keV and the pre-edge at 8.985 keV in both cases.

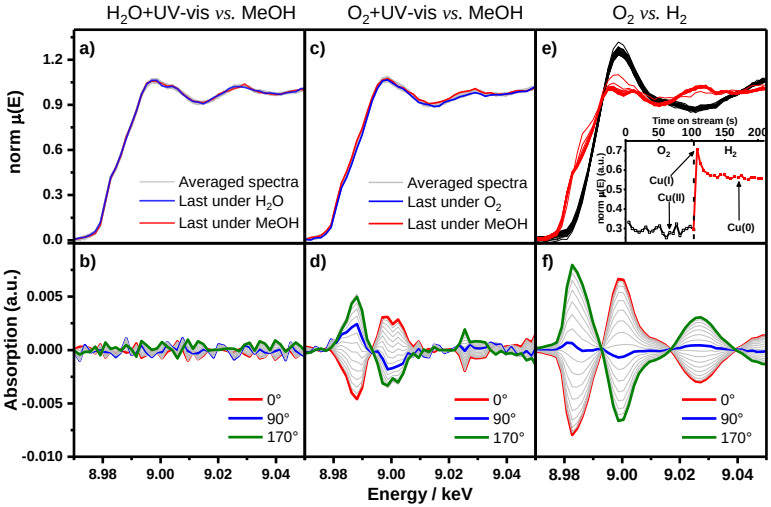

Figure 5.8 *ME-XANES results at the Cu K-edge obtained with the FP-2Cu/TiO₂ sample. (a, c, e) Averaged time-resolved and (b, d, f) phase resolved in the 0° < φ^{PSD} < 170° range spectra for the (a, b) H₂O vs. MeOH, (c, d) O₂ vs. MeOH and (e, f) O₂ vs. H₂ modulation experiments.*

The phase resolved FT-XANES spectra at the Cu K-edge (Figure 5.8b) showed no variations in the phase resolved spectra, proving that Cu, under water + UV-Vis and methanol modulation, undergoes no redox dynamics.

Nevertheless, an additional experiment carried out over the as prepared material demonstrated that, under such anaerobic conditions, Cu, originally present in a fully oxidised form, is reduced under photosteam reforming reaction conditions. A capillary filled with fresh photocatalyst was irradiated with UV-Vis light in the presence of a continuous stream of CH_3OH and H_2O vapours in He. As reported in Figure 5.9, Cu partially reduced under methanol steam reforming conditions. For instance, the black spectrum, representing the as-synthesised fresh sample, correspond to 50 XANES averaged spectra recorded under a 5% O_2/He flow, at room temperature and in dark condition. After that, the same capillary was treated with a 0.5% MeOH/1% H_2O/He flow for 20 min, firstly in dark and then under UV-Vis irradiation conditions. Then, the capillary was purged, in dark, with He until the methanol MS signal reduced to zero. Additional 50 spectra were recorded and averaged into the red line. This treatment was repeated a second time, resulting into the blue spectrum.

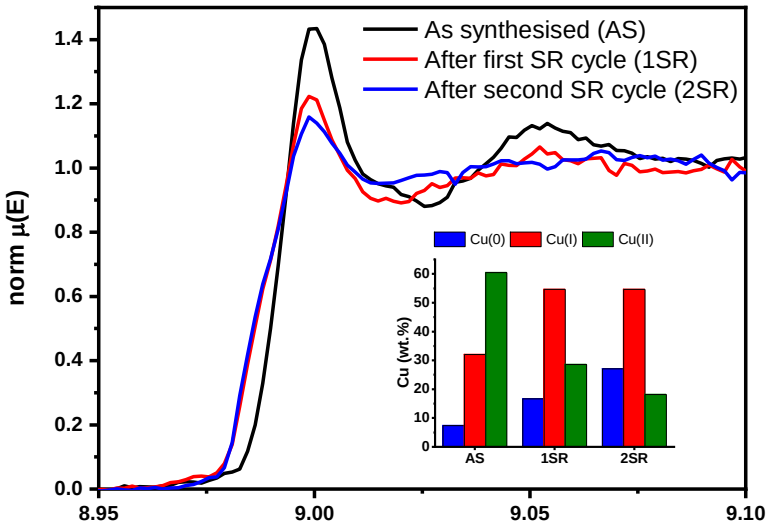

Figure 5.9 *XANES spectra of FP-2Cu/TiO_2 sample before (AS) and after being exposed to methanol steam reforming (SR) reaction conditions. The inset shows Cu speciation for each spectrum, proving metal reduction under anaerobic conditions.*

The linear combination fitting of those averaged spectra, reported in the inset of Figure 5.9, provided evidence of the above-mentioned reduction process. Thus, copper, initially present as a mixture of Cu(II) (60 wt.%) and Cu(I) (30 wt.%), is partially reduced under methanol steam reforming conditions and this process proceeds as the reactive anaerobic conditions are kept. Cu(0) and Cu(I) content grew up to 25 and 55 wt.% respectively while Cu(II) content decreased to 20 wt.% after the double treatment. We also observed that copper reduction occurred due to the steam reforming conditions, and not to the harsh X-rays, as the sample became darker after the treatment but prior to XAS analyses. Indeed, the powder within the capillary became darker only on the side exposed to

the UV-Vis light, and not all of it as it would be if the reduction process was due to the more penetrating X-rays (Figure 5.10).

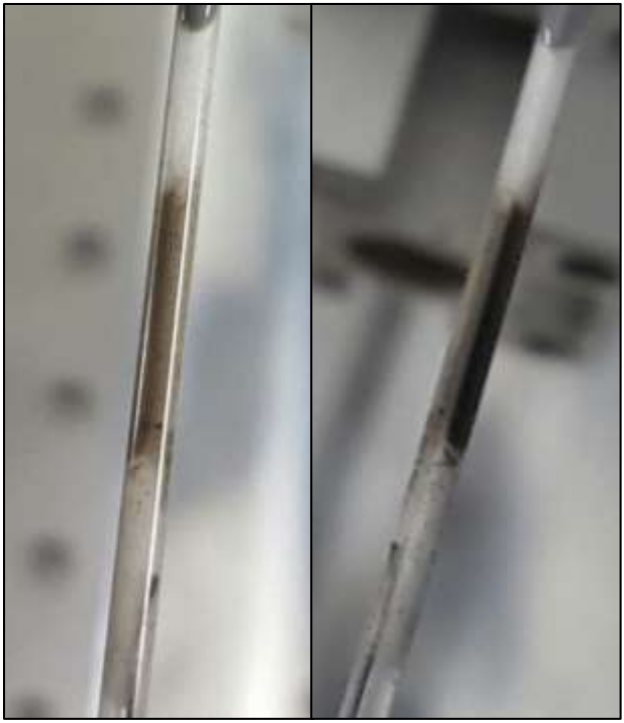

Figure 5.10 *Picture of the capillary filled with FP-2Cu/TiO_2 before (left side) and after (right side) the experiment reported in Figure 5.9. After being exposed to reactants and UV-Vis light, the powder became darker of the irradiated side.*

From the mass spectroscopy (MS) spectra related to the H_2O/MeOH modulation experiment, reported in Figure 5.11, one can observe that the profiles of the signals of CO_2 and H_2CO follows that of methanol. H_2 signal becomes visible only after a 100-time magnification. H_2 production rate with this sample was quite low if compared to the Pt-modified one, thus such poor signal is compatible with the low

photoactivty of FP-2Cu/TiO_2. As already observed with the FP-2Pt/TiO_2 photocatalyst, as light is switched on methanol signal sharply decreases, followed by those of CO_2 and H_2CO, the side-products of the reaction.

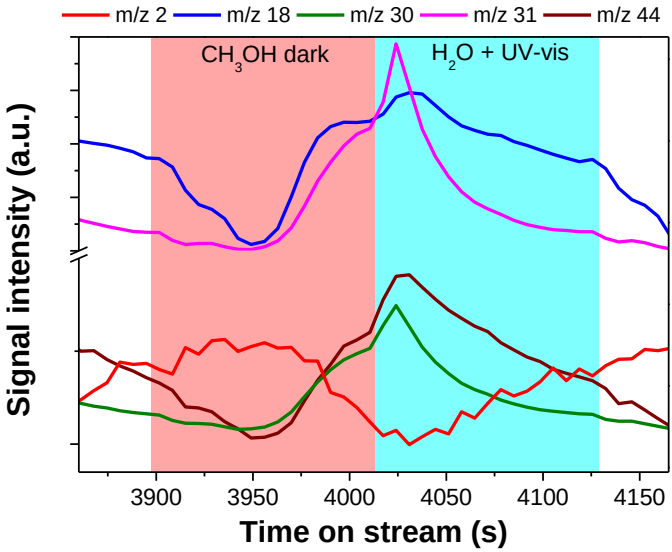

Figure 5.11 *MS profiles reporting a single modulation cycle of the H_2O/MeOH modulation experiment, showing H_2 (red line, 10 times magnified), H_2O (blue line), H_2CO (green line), MeOH (magenta line), and CO_2 (brown line). In red is highlighted the MeOH pulse, whereas in light blue the oxidative pulse.*

Thus, copper present in Cu-modified TiO_2 acts mainly as co-catalyst in its partially reduced form in the methanol photo-steam reforming reaction. It is worth assuming that, in the presence of water, methanol but also photoproduced hydrogen, copper may reduce during the photocatalytic tests in an even greater extent than here reported. This explains the only slightly higher enhancement in photocatalytic activity attained with FP-2Cu/TiO_2. Metal Cu possesses a work function (4.53 – 5.10 eV) in a similar range to that of TiO_2 (4.6 – 4.7 eV), thus resulting

less effective than Pt in proton reduction, leading to lower hydrogen production rates.

The oxygen/methanol modulation experiment lead to different results with respect to its analogous under anaerobic conditions. Despite the small or negligible differences in the averaged spectra (Figure 5.8c), the PSD function highlighted that the metal was periodically oxidised and reduced by the gas flows (Figure 5.8d). Two envelops can be easily observed in the XANES region. The first, centred at *ca.* 8.985 keV, was related to the variation in the pre-edge region of the spectra and the second, at about 9.000 keV, corresponded to the variation of the whiteline as a consequence of the modulation. In order to interpret the demodulated spectra, one should keep in mind that the phase resolved spectrum is analogous to a difference spectrum. Hence, in Figure 5.12 is reported a comparisons between the PSD spectrum of the O_2 + UV-Vis *vs.* MeOH modulation experiment (φ^{PSD} = 160°) with three difference spectra of the reference materials, namely: *i*) CuO – Cu_2O; *ii*) CuO – Cu, and *iii*) Cu_2O – Cu. The shape of the PSD spectrum is very similar to that of the CuO – Cu_2O difference spectrum. Indeed, the whiteline shift intensity (2) and the almost absent signal at higher energy (4,5) allow us to assume that under such aerobic conditions copper is involved in a Cu(II)/Cu(I) transition.

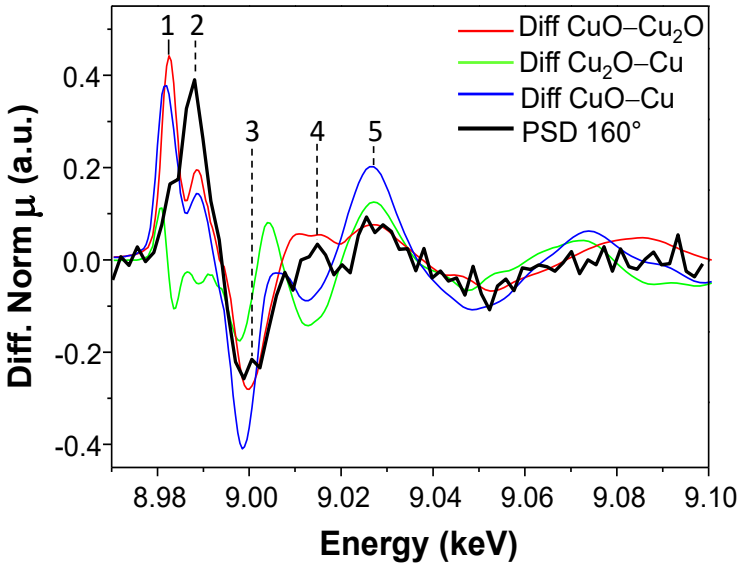

Figure 5.12 *Comparison between the PSD spectrum of the O_2 + UV-Vis vs. MeOH modulation experiment (φ^{PSD} = 160°) and the CuO-Cu, Cu_2O-Cu and CuO-Cu_2O difference spectra.*

A further confirmation of this process comes from the full oxidation/reduction experiment (Figure 5.8e), performed at 473 K by pulsing O_2/He and H_2/He flows alternatively. Under such harsh conditions, spectra changed completely, from fully oxidised (black lines) to fully reduced Cu (red lines). Interestingly, it was also possible to observe a $Cu(I)_2O$ spectrum, appearing few seconds after the switch of the gas flow to H_2. Thus, the oxidation and the reduction processes of this metal are not occurring directly between Cu(II)O to Cu(0), but they involve also $Cu(I)_2O$ as intermediate, even under severe conditions (see inset in Figure 5.8e). This finding suggests that under reactive oxidative conditions, copper continuously changes oxidation state from Cu(II) to

Cu(I), since the shape of the envelopes are comparable. Indeed, the complete redox process between Cu(0) and Cu(II) leads to the formation, in the PSD spectrum (Figure 5.8f), of an envelope at 9.03 keV, which is absent in the PSD spectrum obtained with the aerobic modulation experiment.

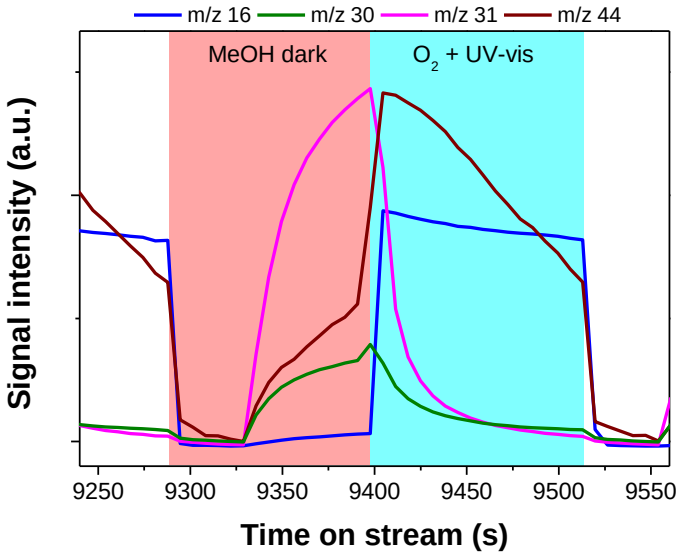

Figure 5.13 *MS profiles reporting a single modulation cycle of the H_2O/MeOH modulation experiment, showing H_2O (blue line), H_2CO (green line), MeOH (magenta line), and CO_2 (brown line). In red is highlighted the MeOH pulse, whereas in light blue the oxidative pulse.*

As already described with Pt under analogous conditions, also in the case of FP-2Cu/TiO_2 under aerobic modulation an important signal of CO_2 (m/z = 44, in Figure 5.13), appears together with that of H_2CO (m/z = 31), as the light is switched on.

5.4. Conclusions

A different behaviour of platinum and copper in different reaction conditions is here evidenced. The methanol/water gaseous mixture of the anaerobic alcohol oxidation, in the presence of irradiation, is able to reduce both metals under the steam reforming reaction conditions. Thus, Pt and Cu, in such an environment, behave like metal-nanoparticle co-catalysts over TiO_2, improving the photoactivity to an extent related to their work function. In this scenario, the beneficial effects of NPs are correlated to the total loading, particles dimension and distribution. All these features strongly influence the ability of the metal to expose a larger number of corner and edge atoms, that already proved to be most reactive, lacking full coordination number.

On the contrary, in the presence of oxygen, platinum and copper were continuously oxidised and reduced, by O_2 and methanol respectively, and the average oxidation state of both metals resulted to be higher than that under anaerobic conditions. The presence of metal oxide over the surface of TiO_2 lead to lower photoactivity with respect to the bare oxide.

These findings prove that different reaction mechanisms occur under aerobic and anaerobic conditions. Indeed, O_2 interacts with the photopromoted electrons trapped in the metal NPs, partially oxidising the surface of the nanoparticles and thus decreasing the photoactivity, as demonstrated by the photocatalytic results. Indeed, in the oxidised form the co-catalyst nanoparticles can not act as photopromoted electron sinkholes to increase the charges lifetime. On the contrary, water, adsorbing on TiO_2 and being oxidised by the photogenerated holes, does not interact directly with the metal NPs. Thus, the trapped electrons and

the protons adsorbing on their surface lead to metal NPs reduction and better photocatalytic efficiency in the investigated reaction.

References

1 M. V. Dozzi, G. L. Chiarello and E. Selli, *J. Adv. Oxid. Technol.*, 2010, **13**, 305–312.
2 G. L. Chiarello, M. H. Aguirre and E. Selli, *J. Catal.*, 2010, **273**, 182–190.
3 G. L. Chiarello, M. V. Dozzi, M. Scavini, J.-D. Grunwaldt and E. Selli, *Appl. Catal. B Environ.*, 2014, **160**–**161**, 144–151.
4 F. Denny, J. Scott, K. Chiang, W. Y. Teoh and R. Amal, *J. Mol. Catal. A Chem.*, 2007, **263**, 93–102.
5 J. J. Murcia, M. C. Hidalgo, J. A. Navío, V. Vaiano, D. Sannino and P. Ciambelli, *Catal. Today*, 2013, **209**, 164–169.
6 M. V. Dozzi, L. Prati, P. Canton and E. Selli, *Phys. Chem. Chem. Phys.*, 2009, **11**, 7171–7180.
7 M. V. Dozzi, A. Saccomanni, M. Altomare and E. Selli, *Photochem. Photobiol. Sci.*, 2013, **12**, 595–601.
8 G. L. Chiarello, E. Selli and L. Forni, *Appl. Catal. B Environ.*, 2008, **84**, 332–339.
9 M. V. Dozzi, G. L. Chiarello, M. Pedroni, S. Livraghi, E. Giamello and E. Selli, *Appl. Catal. B Environ.*, 2017, **209**, 417–428.
10 A. Urakawa, T. Bürgi and A. Baiker, *Chem. Phys.*, 2006, **324**, 653–658.
11 A. Urakawa, N. Maeda and A. Baiker, *Angew. Chemie - Int. Ed.*, 2008, **47**, 9256–9259.
12 N. Maeda, A. Urakawa and A. Baiker, *J. Phys. Chem. C*, 2009, **113**, 16724–16735.
13 D. Ferri, M. A. Newton and M. Nachtegaal, *Top. Catal.*, 2011, **54**, 1070–1078.
14 D. Ferri, M. S. Kumar, R. Wirz, A. Eyssler, O. Korsak, P. Hug, A. Weidenkaff and M. A. Newton, *Phys. Chem. Chem. Phys.*, 2010, **12**, 5634–5646.
15 C. F. J. J. König, J. A. van Bokhoven, T. J. Schildhauer and M. Nachtegaal, *J. Phys. Chem. C*, 2012, **116**, 19857–19866.
16 G. L. Chiarello and D. Ferri, *Phys. Chem. Chem. Phys.*, 2015, **17**, 10579–10591.
17 A. Eyssler, E. Kleymenov, A. Kupferschmid, M. Nachtegaal, M. S. Kumar, P. Hug, A. Weidenkaff and D. Ferri, *J. Phys. Chem. C*, 2011, **115**, 1231–1239.
18 G. L. Chiarello, I. Rossetti and L. Forni, *J. Catal.*, 2005, **236**, 251–261.
19 A. Altomare, M. C. Burla, C. Giacovazzo, A. Guagliardi, A. G. G. Moliterni, G. Polidori and R. Rizzi, *J. Appl. Crystallogr.*, 2001, **34**, 392–397.
20 H. M. Rietveld, *J. Appl. Crystallogr.*, 1969, **2**, 65–71.
21 P. Scherrer, *Göttinger Nachrichten Math. Phys.*, 1918, **2**, 98–100.
22 G. L. Chiarello, L. Forni and E. Selli, *Catal. Today*, 2009, **144**, 69–74.
23 J. Hong, W. Zhang, J. Ren and R. Xu, *Anal. Methods*, 2013, **5**, 1086–1097.
24 X. Huang, T. Cao, M. Liu and G. Zhao, *J. Phys. Chem. C*, 2013, **117**,

26432–26440.
25 M. Sahu and P. Biswas, *Nanoscale Res. Lett.*, 2011, **6**, 441.
26 M. Bernareggi, M. V. Dozzi, L. G. Bettini, A. M. Ferretti, G. L. Chiarello and E. Selli, *Catalysts*, 2017, **7**, 301.
27 G. Colón, M. Maicu, M. C. Hidalgo and J. A. Navío, *Appl. Catal. B Environ.*, 2006, **67**, 41–51.
28 A. Teleki, N. Bjelobrk and S. E. Pratsinis, *Sensors Actuators, B Chem.*, 2008, **130**, 449–457.
29 H. Irie, K. Kamiya, T. Shibanuma, S. Miura, D. A. Tryk, T. Yokoyama and K. Hashimoto, *J. Phys. Chem. C*, 2009, **113**, 10761–10766.
30 H. Praliaud, *Appl. Catal. B Environ.*, 1998, **16**, 359–374.
31 W. Zhang, Y. Li, S. Zhu and F. Wang, *Catal. Today*, 2004, **93**–**95**, 589–594.
32 R. López, R. Gómez and M. E. Llanos, *Catal. Today*, 2009, **148**, 103–108.
33 G. L. Chiarello, D. Ferri and E. Selli, *J. Catal.*, 2011, **280**, 168–177.
34 G. L. Chiarello, D. Ferri and E. Selli, *Appl. Surf. Sci.*, 2018, **450**, 146–154.
35 M. V. Dozzi, A. Zuliani, I. Grigioni, G. L. Chiarello, L. Meda and E. Selli, *Appl. Catal. A Gen.*, 2016, **521**, 220–226.
36 D. R. R. Lide, W. M. M. Haynes, G. Baysinger, L. I. Berger, D. L. Roth, D. Zwillinger, M. Frenkel and R. N. Goldberg, *CRC Handbook of Chemistry and Physics*, CRC Press, Boca Raton, FL, Internet V., 2005.

Chapter 6:
TEMPERATURE EFFECTS ON THE PHOTO-STEAM REFORMING REACTION

6.1. Introduction

Photocatalysis is usually considered as a temperature-independent process since the energy gaps of photocatalytic materials are usually too wide to have an electron promoted from the VB to the CB by heat. However, a high temperature can still influence the absorption rate or the dynamics of the reactants over the semiconductor surface, thus changing the rate determining step or the selectivity of the reaction. Indeed, usually at T > 70 °C the activity decreases since the adsorption of the reactant becomes the rate limiting step.[1] For this reason, the best temperature for photocatalytic tests is typically considered to be between 20 and 80 °C.

Already in early the 80s, Grätzel *et al.* observed that temperature had a positive effect on H_2 production in a TiO_2 aqueous suspension, with a 50-fold increase in hydrogen yield over a temperature range of 50 °C.[2] Griffin *et al.* demonstrated that bare titanium dioxide photoactivity in the oxidation of 1-butanol increases at higher temperature (105 *vs.* 25 °C), whereas in dark conditions poor catalytic activity was observed at 105 °C. Indeed, they claimed that the combination of photocatalysis and thermal catalysis can be useful for changing and controlling the selectivity of a reaction.[3] However, non-homogeneous reports can be found in the literature about heating effects on pristine TiO_2. A general beneficial

effect over a wide temperature range, up to 150 °C has been reported,[4,5] whereas others[6] claim a detrimental effect at temperature above 80 °C, as expected.

TiO_2 is not generally considered as a good thermal catalyst itself, but it is employed, along with many other oxides, *i.e.* SiO_2 or Al_2O_3, as an inert support for metal nanoparticles that are widely exploited as catalysts in a range of industrial reactions. Thus, in addition to the effects already observed with bare TiO_2, a further enhancement in the photocatalytic activity can be attained from the thermo-catalytic properties of the metal NPs deposited on the surface of titanium dioxide.

Indeed, several studies reported general beneficial effects of high temperature over the photocatalytic activity of metal-modified TiO_2. For example, Kennedy *et al.* tested a Pt-modified TiO_2 photocatalyst in the ethanol oxidation reaction. They found that a higher temperature-induced synergistic effect between the substrate and the metal nanoparticles occurs even when the same heated photocatalyst was not active in dark condition. Furthermore, an impressive ethanol conversion was observed under irradiation in the 50 – 200 °C temperature range, while the material was slightly active in the dark.[7] Other authors found analogous results with Pt-modified titanium dioxide photocatalysts when testing them in the oxidation of different organic substrates, such as toluene,[8] acetaldehyde,[8,9] benzene[10,11] and cyclohexane.[12]

In addition to these photocatalytic oxidation reactions, the effect of temperature was verified also on carbon dioxide reduction, which can occur under both photoinduced and thermal catalysis. The latter can be performed quite easily and with good yield at high temperature by means of noble metal nanoparticles.[13] Vaiano *et al.* compared the performance

obtained with photocatalysis and thermocatalysis by employing a Pd/TiO_2 catalyst, finding the former more efficient.[14] The positive combination of the two effects was proved even with bare TiO_2 or titanium dioxide coupled with MgO. Both Saladin *et al.*[15] and Liu *et al.*[16,17] found that heat enhances CO_2 photo-conversion to CH_4 or CO, probably due to an easier desorption of the products from the catalyst surface.

To the best of our knowledge, only a single report has been published so far about photocatalytic hydrogen production in the gas phase combined with temperature. According to Han *et al.*, by employing a Pt-modified titanium dioxide photocatalyst it is possible to obtain an extremely high H_2 production rate (up to 800 $mmol \cdot h^{-1} \cdot g_{cat}^{-1}$) under solar light irradiation at 300 °C, doubling the production rate achievable in dark conditions. However, no deeper investigation was done over thermal effects in photocatalysis.[18]

In this context, we verified the effect of a thermal reductive pre-treatment on the photocatalytic behaviour of Pt-, Cu- and Pt/Cu-modified titanium dioxide materials. Then, the effect of temperature was systematically investigated in the methanol steam-reforming reaction, in terms of H_2 production and sub-products distribution over the of 40 – 350 °C temperature range.

6.2. Synthesis and characterisation

The samples selected for these experiments are already fully described in Chapter 3. Indeed, we chose the most active sample, in terms of H_2 production, among the flame made photocatalysts, *i.e.* TPC0.05 (a 0.05 wt.% Cu and 0.5 wt.% Pt modified titanium dioxide), together with the corresponding single-metal modified materials, *i.e.* TPC0.0 (0.5 wt.%

Pt-TiO_2) and TC0.05 (0.05 wt.% Cu-TiO_2) and the bare flame-made titania. The materials were characterised by UV-Vis absorption spectroscopy and by BET, XRD, XPS and HRTEM analyses (see Chapter 3.3.)

6.3. Photo-thermocatalytic tests

The activity of the selected samples was tested in the methanol steam reforming reaction employing the already described stainless steel setup (Chapter 2). As a standard procedure, 15 mg of photocatalyst were employed for each photocatalytic test, after being adsorbed over 20 – 40 mesh quartz grains. Different kinds of experiment were performed in order to investigate the various aspects of temperature effect over the photocatalytic activity.

Firstly, the effect over the photocatalytic activity of *in situ* pre-reductive treatment was investigated at a fixed temperature (200 °C). The treatment consisted in flowing a 10 vol.% H_2/N_2 mixture (100 mL·min^{-1}) to the photoreactor previously set at 250 °C. These conditions were chosen based on the results, reported in Chapter 5, demonstrating that Pt and Cu nanoparticles can be completely reduced under such conditions. Briefly, once the gas flows were set, the photoreactor was heated up to 250 °C with a temperature ramp of 10 °C·min^{-1}. The final temperature was kept for 30 min and the reactor was then allowed to cool down. Then, a pure N_2 flow (100 mL·min^{-1}) was sent for 15 min in order to remove any trace of H_2 before starting with the outgassing procedures of the whole system, as reported in Chapter 2. The switch from the H_2/N_2 gas mixture to pure N_2 occurred when temperature was below 70 °C, in the case of tests performed at 40 °C, or when the reactor was cooled to 200 °C, when

the tests were performed at this temperature. After the outgassing step, 2 h- or 1 h-long methanol steam reforming photocatalytic tests were performed, which were repeated twice or 5 times, respectively. At the end of any kinetic run, the solution within the flask was analysed, to check the concentration of formate ions produced during the run and replaced with a fresh 20 vol.% MeOH/H_2O solution. A new run was started after having purged the recirculating system with nitrogen, in order to remove O_2. The as-synthesised samples were tested at 40 °C whereas the pre-reduced ones were analysed both at 40 and 200 °C. Additionally, due to the attained results, TPC0.0 and TPC0.05 were also tested in continuous mode. The two samples were analysed as-synthesised at 40 °C and at 200 °C after being pre-treated.

The results of these first studies will be reported in terms of H_2, CO_2 and CO accumulation profiles within the recirculating system, when they were tested in recirculating mode, and as instantaneous H_2 production rate *vs.* time on stream in the case of continuous-mode tests.

Systematic studies on the effect that different temperatures have on photoactivity were obtained by testing the photocatalysts in continuous mode. During the kinetic test, a temperature ramp of 2 °C·min^{-1}, from 40 to 350 °C, was set, and the gas phase composition was examined at different temperatures. The gas-chromatographic analyses were performed every *ca.* 19 min, a first analysis in the dark at 40 °C being performed before removing the lamp shutter (t = 0). After reaching the end of the heating ramp, the photoreactor was kept at 350 °C for *ca.* 1 hour (corresponding to 4 GC analyses) to check the stability of the material. To avoid changes in the properties of the photocatalysts during the heating ramp, a reductive pre-treatment at 350 °C, similar to that at

250 °C (*i.e.* 10 °C·min^{-1}), was performed before any continuous run. The system was equipped with a bubbling flask, filled with a Na_2CO_3/$NaHCO_3$ solution, at the exit of the circuit to collect the produced H_2CO and HCOOH.

These results, instead, will be reported in terms of instantaneous production of H_2, CO_2, CO and H_2CO *vs.* time on stream and temperature. Those of carbon dioxide, carbon monoxide and formaldehyde were calculated as the ratio between the production rate of the sub-product and that of hydrogen, taking into account the relative stoichiometric coefficient (as explained in Chapter 2). Since no time on stream data about formic acid was collected (it is not detected in the gas phase), its selectivity was calculated, at each temperature, as:

$$S_{HCOOH} = 100 - \left(S_{CO_2} + S_{CO} + S_{H_2CO}\right) \qquad EQ\ 6.1$$

Consequently, from the so-obtained selectivity the instantaneous formic acid production rate could also be calculated.

6.4. Results and discussion

6.4.1. Effects of the pre-reduction treatment and of the test temperature

As expected, the reductive pre-treatment performed at 250 °C caused important changes in the photocatalytic activity of the materials which were tested at 40 °C. In their zero-valent form, the effect of metal NPs over TiO_2 surface can be easily correlated to the metal work function (5.12 − 5.93 eV for Pt and 4.53 − 5.10 eV for Cu). The results reported in Figure 6.1 (a and b) indicate that when tested as-synthesised (like in Chapter 3), the TPC0.05 photocatalyst showed a slightly larger H_2

production rate than the corresponding Pt-only modified photocatalyst (TPC0.0) and the Cu-only modified material (TC0.05) exhibited a much lower activity (Figure 6.1a). When the three samples were pre-reduced, the TPC0.0 material dramatically increased its photoactivity, showing a hydrogen production rate (r_{H_2}) almost doubled with respect to that attained with the non-reduced photocatalyst. This can be attributed to the total reduction of Pt nanoparticles over the TiO_2 surface, that makes the photocatalyst much more active in the methanol steam-reforming reaction. Indeed, since the work function of Pt is higher than that of TiO_2, the photopromoted electrons can flow from the CB of the oxide to the metal NP and then reducing adsorbed protons.

On the contrary, the complete reduction of Cu in both TPC0.05 and TC0.05 lead to a loss of activity. Indeed, the Cu-only modified sample showed a halved r_{H_2}, while the Cu-Pt co-modified material exhibit a H_2 production rate reduced from 23 $mmol \cdot h^{-1} \cdot g_{cat}^{-1}$ to 14 $mmol \cdot h^{-1} \cdot g_{cat}^{-1}$. This phenomenon can be justified with the formation of a Pt-Cu alloy during the reductive pre-treatment. Alloys have intermediate characteristics with respect to their components; thus, in this case, the work function of Pt is reduced by that of Cu in the NPs of TPC0.05, causing a decrease in photoactivity. The same changes can be appreciated looking at the carbon dioxide production rates. Indeed, a strong correlation between hydrogen, carbon dioxide and carbon monoxide production rate can be found, since an increased H_2 production is related to a better reactant conversion on the photocatalyst (Figure 6.2a and 6.2b and 6.3a and 6.3b), with larger CO_2 and lower CO productions.

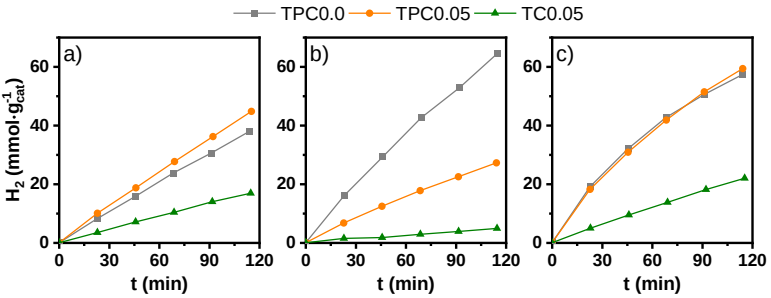

Figure 6.1 *H_2 accumulation profiles with the three selected photocatalysts a) as-synthesised (runs at 40 °C) and pre-reduced runs at b) 40 °C and c) 200 °C.*

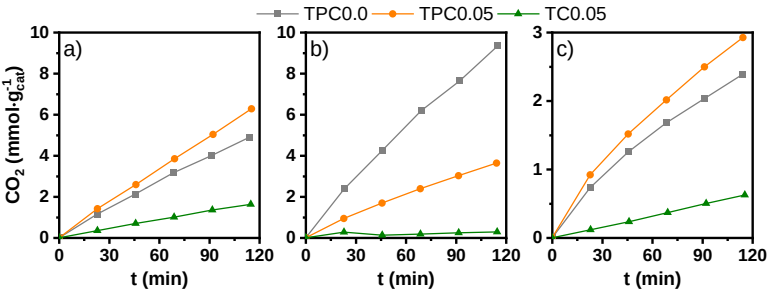

Figure 6.2 *CO_2 accumulation profiles with the three selected photocatalysts a) as-synthesised (runs at 40 °C) and pre-reduced runs at b) 40 °C and c) 200 °C.*

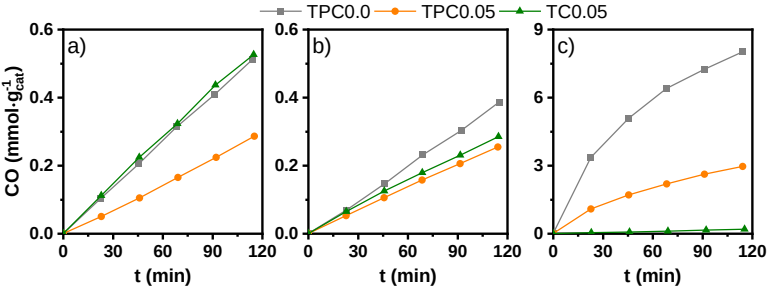

Figure 6.3 *CO accumulation profiles with the three selected photocatalysts a) as-synthesised (runs at 40 °C) and pre-reduced runs at b) 40 °C and c) 200 °C, with an opposite trend with respect to Figure 6.2.*

When performing the reaction at 200 °C after having pre-reduced the materials, the two Cu-modified samples showed, both reduced and as-synthesised, an increased r_{H_2} with respect to the reaction run at 40 °C. On the contrary, the TPC0.0 sample at 200 °C exhibited a slightly lower hydrogen production rate than at 40 °C (Figure 6.1b *vs.* 6.1c).

Furthermore, H_2 accumulation within the recirculating set-up did not occur linearly, as in the case of test performed at 40 °C, with both Pt-modified photocatalysts and, to a much less extent, also with TC0.05. In addition, high temperature led to a complete change in the by-product selectivity, with CO becoming the main sub-product, with a up to 10-times larger production than at 40 °C (Figure 6.3c). The same loss of stability observed in H_2 production can be appreciated in both CO_2 and CO accumulation traces (Figure 6.2 and 6.3 panel c).

From these results it can be supposed that the larger CO production occurring at high temperature causes the poisoning of metal Pt nanoparticles, thus reducing the efficiency of the material over time. Despite the high temperature, that favours CO dissociation,[19] large amounts of CO in the gas phase can push the equilibrium towards the adsorbed form and, thus, to a decreasing photoactivity due to deactivation of the materials.

To verify this hypothesis, a series of short kinetic runs (each 1 h-long) was performed. At the end of every run, the recirculating system was thoroughly purged to remove all photoproduced gases. TPC0.0 was tested under these conditions both at 40 °C as-synthesised and at 250 °C after being pre-reduced.

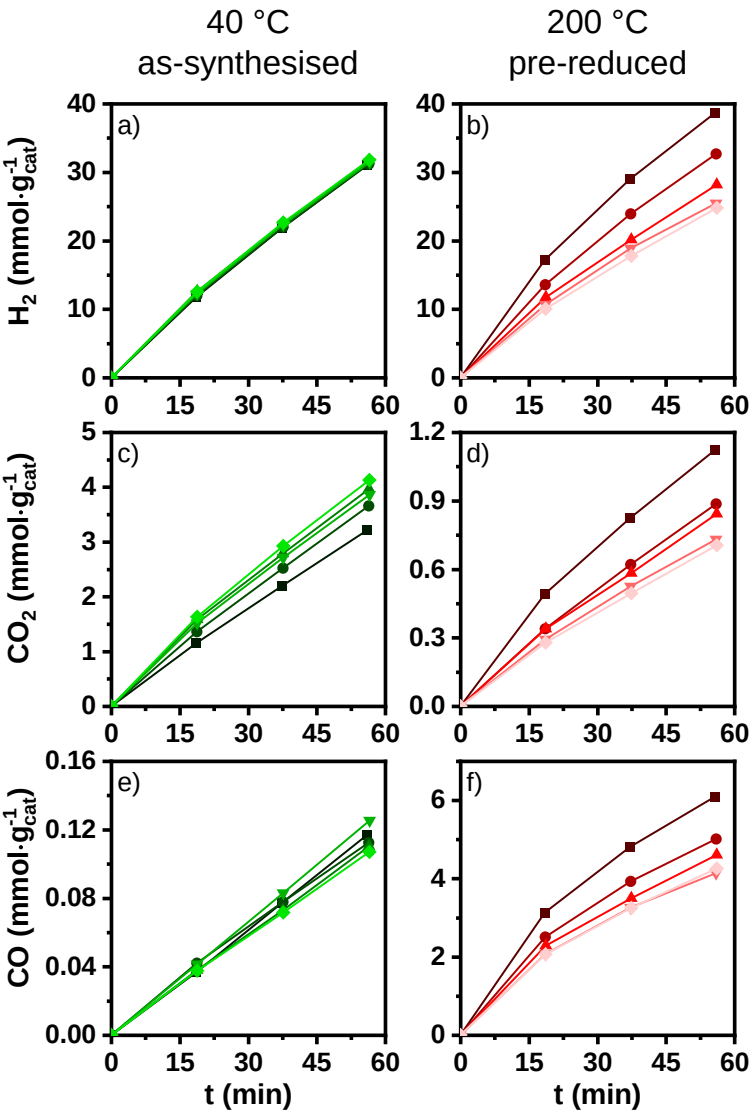

Figure 6.4 *Accumulation profiles of (a,b) H_2, (c,d) CO_2 and (e,f) CO obtained with TPC0.0 as-synthesised at 40 °C (left side) and at 200 °C, after being pre-reduced (right side). 1st to 5th analysis from darker to lighter colours. A clear difference in photoproduction stability and selectivity appears.*

The results, reported in Figure 6.4 (green colours for the former condition, red colours for the latter, 1st to 5th run from darker to lighter colour), show that the deactivation process is not correlated to the accumulation of CO within the circuit, since the photoactivity at 200 °C clearly decreases after every short run despite the purging step. The same analysis done with TPC0.05 and TC0.05 confirmed the already attained results: the Pt containing material showed a more evident decrease in photoactivity with respect to the Cu-modified one (Table 6.1).

Table 6.1 *Comparison of the total H_2 production attained with the three selected photoctaltysts at 200 °C at the end of every 1 h-long kinetic run. The loss of activity is more important with the Pt-modified materials.*

	n_{H_2} (mmol·g_{cat}^{-1})		
	TPC0.0	TPC0.05	TC0.05
1st run	38.7	32.0	11.1
2nd run	32.7	27.5	10.8
3rd run	28.2	23.7	10.3
4th run	25.5	23.2	9.5
5th run	24.8	22.0	9.4

A clear evidence of the deactivation of the Pt-modified photocatalysts was obtained by running the photocatalytic system in continuous mode. Figure 6.5 shows that the as-synthesised Pt-modified materials tested at 40 °C exhibit a stable H_2 photoproduction over *ca.* 6 hours, whereas at 200 °C, after being pre-reduced, the photocatalyst exhibits a r_{H_2} decreasing with time. Indeed, after *ca.* 6 h at 200 °C the beneficial effect induced by pre-reduction is lost. On the contrary, the effect over selectivity is kept despite the loss of activity: CO_2 production

resulted lower at high temperature and r_{CO} was 10 times larger than that at 40 °C.

These first results obtained with photocatalytic runs at 200 °C indicate that the presence of platinum NPs over titanium dioxide catalyses the formation of syngas (a mixture of H_2 and CO), according to the reaction

$$CH_3OH \rightarrow CO + 2H_2 \qquad EQ\ 6.2$$

rather than favouring the full oxidation of methanol to carbon dioxide.

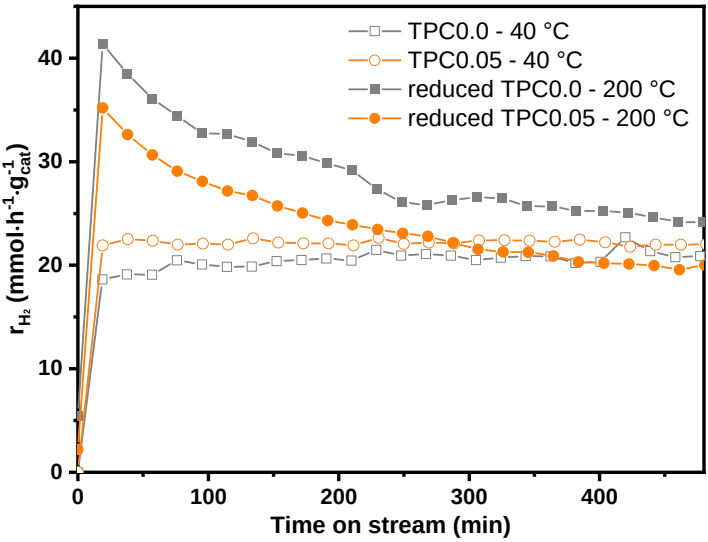

Figure 6.5 *H_2 production rate vs. time on stream obtained with TPC0.0 (grey squares) and TPC0.05 (orange circles) both as-synthesised at 40 °C (empty symbols) and pre-reduced at 200 °C (full symbols).*

6.4.2. The influence of temperature over photoactivity and selectivity

Based on the results reported in the previous section, we performed a deeper investigation on the effect of temperature over the photocatalytic

activity in the methanol steam reforming reaction. The photocatalysts were all pre-treated in H_2 flow at 350 °C for 30 min. Considering the higher temperature with respect to the previous analyses and the overall treatment time (*ca.* 1.5 h due to the additional time related to heating and cooling ramps), we assumed that the photocatalyst deactivation along the photo-thermocatalytic tests would be prevented in such temperature range. Figure 6.6a shows that, under irradiation on TPC0.0, H_2 production slowly increases with temperature, almost doubling in the 40 – 150 °C range, then it rises up to 350 °C, reaching a *ca.* 450 $mmol \cdot h^{-1} \cdot g_{cat}^{-1}$ value. The thermic H_2 contribution, evaluated by performing the same reaction under dark conditions (grey bars in Figure 6.6a) appears at *ca.* 150 °C, becoming predominant over the photocatalytic contribution from 250 °C and above. At 350 °C the photocatalytic contribution to hydrogen production accounts for *ca.* 60 $mmol \cdot h^{-1} \cdot g_{cat}^{-1}$ and the thermally-produced H_2 production rate was 375 $mmol \cdot h^{-1} \cdot g_{cat}^{-1}$. In order to discern the pure photocatalytic from the thermal contribution, in Figure 6.6b the photoproduced H_2 production rate is reported, calculated as the difference between the r_{H_2} recorded under irradiation and under dark condition at the same temperature. It can be observed that by rising temperature, H_2 production increases up to 60 $mmol \cdot h^{-1} \cdot g_{cat}^{-1}$ at 350 °C, doubling the value attained at 40 °C. It is also interesting to notice that, once reached the final temperature (350 °C), photoproduced H_2 rapidly decreases probably due to deactivation or sintering of the material, and this reduces the photocatalytic H_2 production rate.

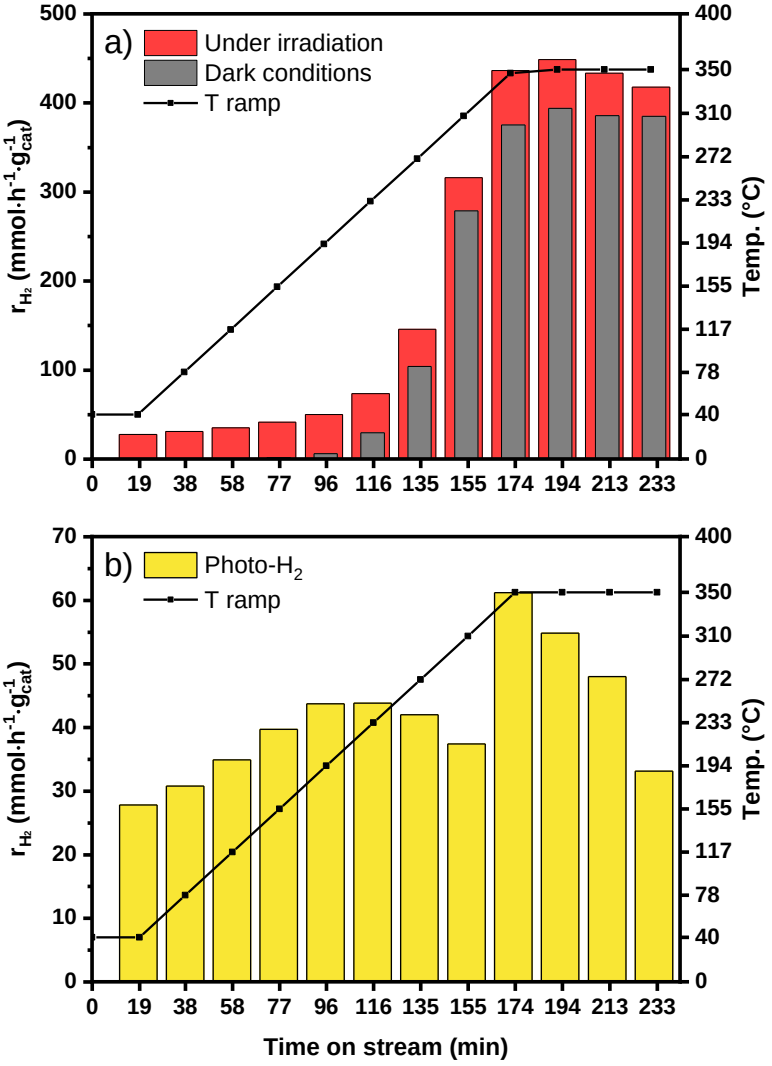

Figure 6.6 *r_{H_2} profiles obtained with pre-treated TPC0.0 as a function of temperature. a) Comparison of r_{H_2} obtained under irradiation (red bars) and in dark conditions (grey bars); b) photo-produced H_2 obtained as the difference between the red and grey bars in panel a. The temperature ramp is also shown in both figures (right axis).*

This result proves that temperature has a positive effect on the photoactivity of the material, boosting the photocatalytic H_2 production rates up to 3 times with respect to 40 °C, but, at high temperature the catalytic contribution in H_2 production becomes predominant. These results are comparable with those of Han *et al.*[18] in terms of absolute H_2 production. However, a much different distribution between photocatalytic H_2 and thermal hydrogen can be observed. Our results clearly show that at high temperature the photocatalytic contribution accounts for *ca.* 15-20% of the total H_2 production.

The other important effect of thermo-photocatalysis is related to reaction-path changes. Indeed, Figure 6.7 shows how the production rates of CO_2, CO and H_2CO vary with temperature.

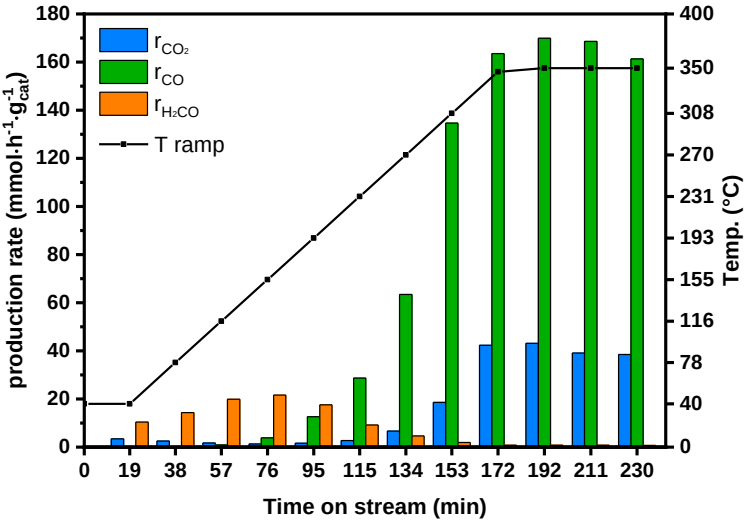

Figure 6.7 *By-products (CO_2, CO and H_2CO) production rates vs. temperature. CO production becomes predominant at temperature above 250 °C.*

With the Pt-only modified TiO_2 material, at 40 °C the main sub-products of methanol steam reforming are carbon dioxide and

formaldehyde. H_2CO production increases up to 150 °C, and then it decreases with increasing temperature, becoming negligible at high temperature. On the opposite, CO_2 production firstly decreases and then rises again above 200 °C. The greatest change, however, concerns carbon monoxide: r_{CO} sharply rises as the thermal effect becomes important, reaching 170 $mmol \cdot h^{-1} \cdot g_{cat}^{-1}$ at 350 °C.

By comparing the selectivity towards these sub-products under irradiation and in dark conditions, it appears that the carbon monoxide large production at high temperature in mainly due to thermal effects (the green CO profiles in Figure 6.8a and 6.8b), whereas formaldehyde is a photocatalytic sub-product of the reaction. Under irradiation, H_2CO and CO_2 productions are strongly correlated since, between 40 and 250 °C, the increase of the former is associated with a decrease of the latter. This phenomenon can be justified either by competitive reaction paths leading to H_2CO and CO_2 or, according to the mechanism proposed by Chiarello *et al.*[20], by a faster oxidation process of H_2CO to CO_2 induced by heat. It is worth underlining that between 150 and 200 °C the photocatalytic path dominates over the thermic one, since under irradiation large formaldehyde amounts and low CO_2 production were recorded, whereas the photocatalyst had a completely different behaviour in dark conditions. The amount of formic acid detected by ion chromatography in the solution was 69.4 ppm, when the test was performed under irradiation conditions. The calculated r_{HCOOH} and S_{HCOOH}, reported in Figure 6.9, indicate that formic acid is produced photocatalytically at low temperatures. These calculated results are in agreement with the total formic acid detected. Indeed, from the integration over time of the calculated production rates,

corrected for the catalyst weight, the solution volume in the flask and the $HCOO^-$ molar mass, a concentration of 68.9 ppm was obtained.

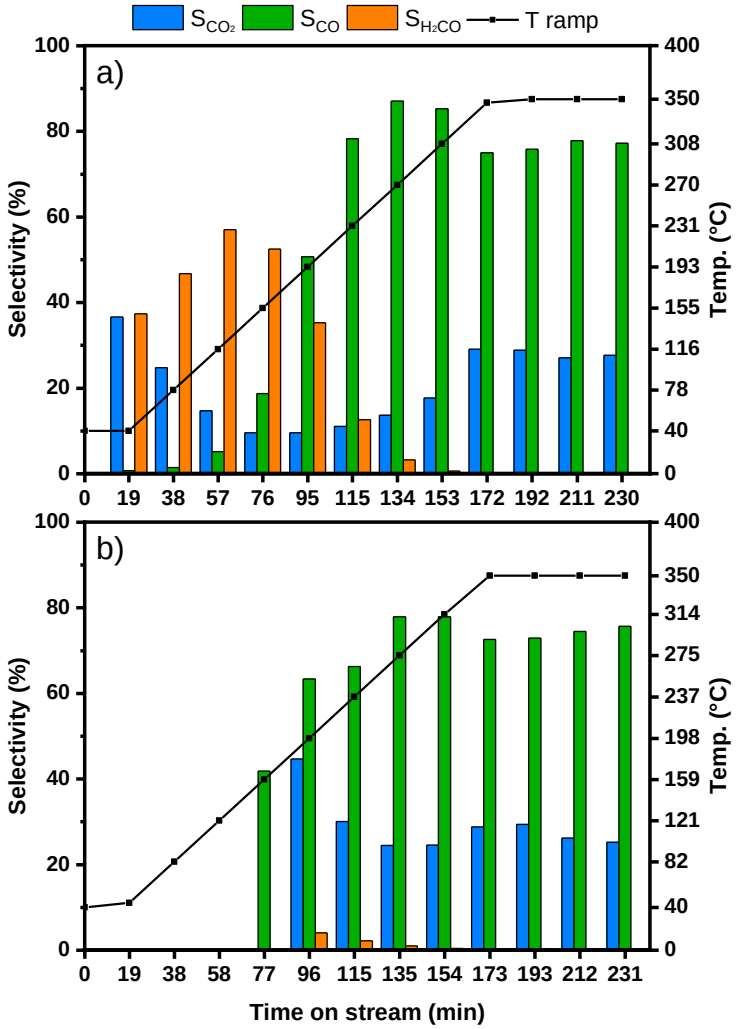

Figure 6.8 *Comparison between sub-products selectivity under a) irradiation conditions (photo-thermocatalysis) and b) dark conditions (thermocatalysis) with increasing temperature (40-350 °C)*

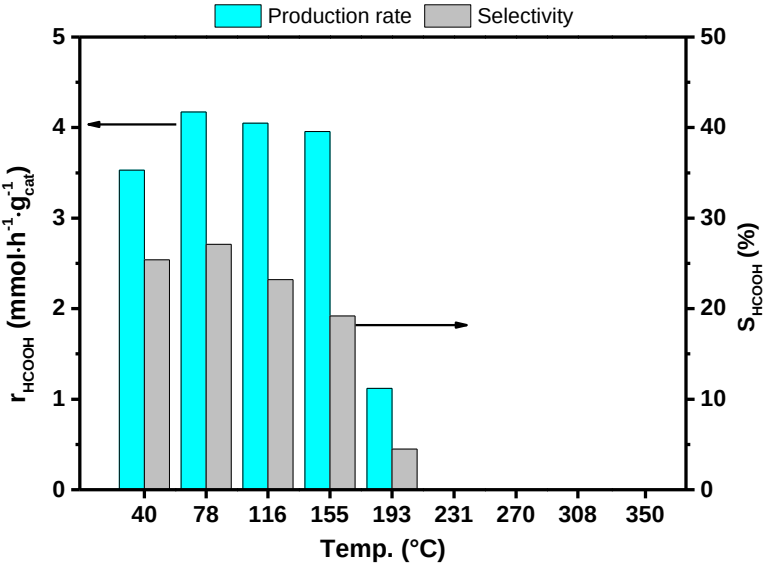

Figure 6.9 *Calculated formic acid production rate and selectivity as a function of temperature for TPC0.0 tested under irradiation.*

Interestingly, it can be observed a methane production associated to thermal catalysis (Figure 6.10), since its production starts at 150 °C. CH_4 production exhibits the same profile of hydrogen production at high temperature, similar also to that of CO. It is known that at high temperature CO_2, in the presence of H_2, can be reduced to CH_4.[14] Furthermore, Pt is also an efficient catalyst for thermal steam reforming of methane ($CH_4 + H_2O \rightleftarrows CO + 2H_2$). However, high temperature is usually required to shift the equilibrium towards the syngas.[21–25] Thus, it can be supposed that at temperature below 350 °C, and in the presence of large amounts of H_2 and CO, the equilibrium of this reaction favours methane production.

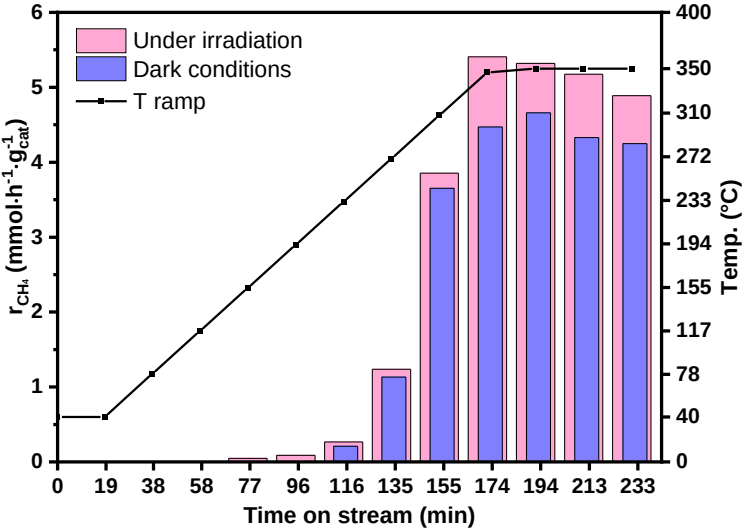

Figure 6.10 *Methane production rate under irradiation (pink columns) and in dark conditions (purple columns) with TPC0.0. CH_4 production is mainly induced by heat, but photocatalytic processes can enhance its production rate.*

By comparing these results with those obtained with bare titanium dioxide (TiO_2), it can be observed that the activities are similar (Figure 6.11 for TC0.05 and Figure 6.12 for TiO_2). Thermal hydrogen production starts, with both samples, from *ca.* 300 °C and reaches values lower than 5 mmol·h^{-1}·g$_{cat}^{-1}$. As already observed in the case of the Pt-modified photocatalyst, keeping the material under irradiation at 350 °C causes a loss of photoactivity, which is not observed in dark conditions. Thus, it can be assumed that a sintering process occurs probably affecting the photocatalytic more rather than the thermal activity.

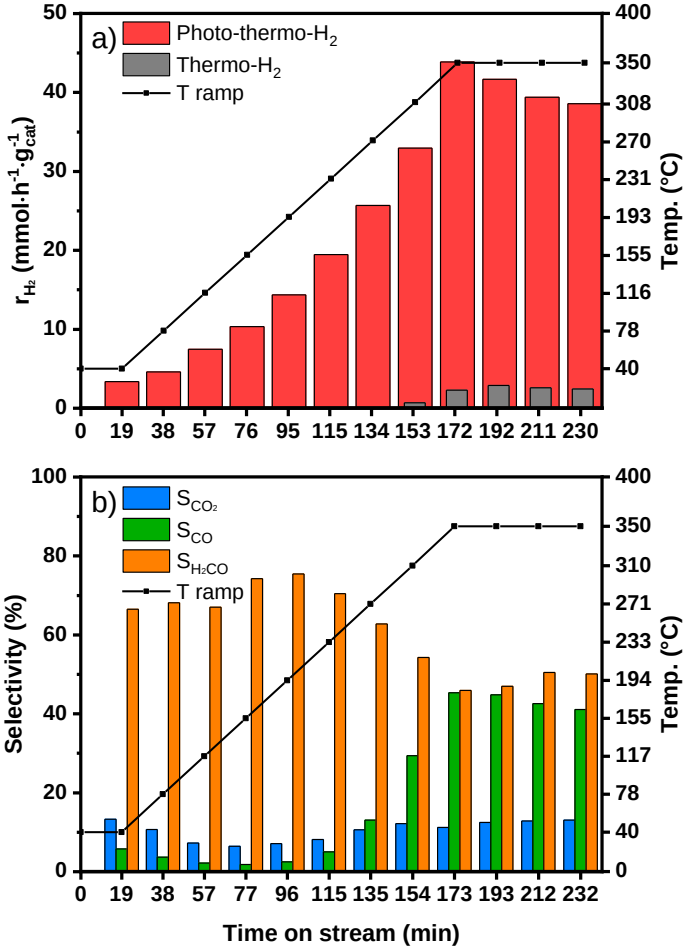

Figure 6.11 *(a) Comparison between the r_{H_2} (under irradiation, red, and thermally produced, grey) obtained with TC0.05 at different temperatures. (b) Selectivity to different by-products obtained under irradiation with the same photocatalyst.*

The photocatalytic contribution of metal Cu NPs to H_2 production is thus limited if compared to that of Pt and the thermic contribution is negligible. Furthermore, the presence of copper only slightly changes the

selectivity towards the sub-products. Indeed, both TC0.05 and bare TiO_2 show high selectivity towards H_2CO over all the investigated temperature range.

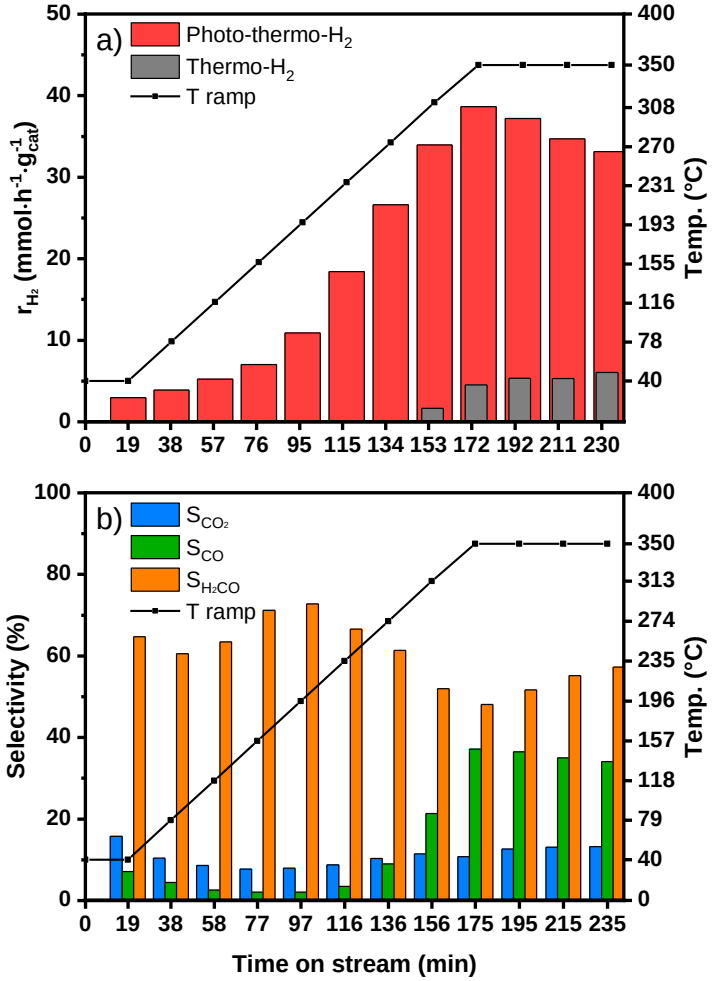

Figure 6.12 *(a) H_2 production rate under irradiation (red) and in dark conditions (grey) obtained with bare TiO_2. (b) Selectivity to CO_2, CO and H_2CO under irradiation at different temperatures.*

On the contrary, and as already observed with measurements at lower temperature, the presence of copper is beneficial in terms of carbon dioxide selectivity, especially at low and high temperatures. Nevertheless, the small differences in terms of selectivity towards the different sub-products between the TPC0.0 and the TPC0.05 samples can be ascribed to the small Cu loading in the TC0.05 sample.

The co-presence of both Cu and Pt, as expected, led to an intermediate activity between the corresponding single-metal modified photocatalysts (Figure 6.13). Due to the presence of copper, the hydrogen production rate in the investigated temperature range was lower than that observed with TPC0.0, but the presence of Pt still drove the thermal activity at high temperature. Indeed, at 350 °C the r_{H_2} obtained in dark with TPC0.05 was *ca.* 300 $mmol \cdot h^{-1} \cdot g_{cat}^{-1}$ to be compared with the almost 400 $mmol \cdot h^{-1} \cdot g_{cat}^{-1}$ r_{H_2} value obtained with TPC0.0 in the same conditions. The selectivity towards the main sub-products is dominated by the platinum presence but in the presence of Cu the formation of H_2CO extends up to 300 °C, both in dark and under irradiation, whereas with the Pt-only photocatalyst S_{H_2CO} drops to zero at *ca.* 250 °C. Nevertheless, carbon monoxide is the main sub-product at temperatures above 250 °C, as with the Pt-only modified sample.

Additionally, all the photocatalyst, either the bare TiO_2 and the three metal-modified samples, showed a decrease in activity at 350 °C. Thus, at high temperature these materials are not stable and a sintering process is probably occurring, decreasing the available active sites.

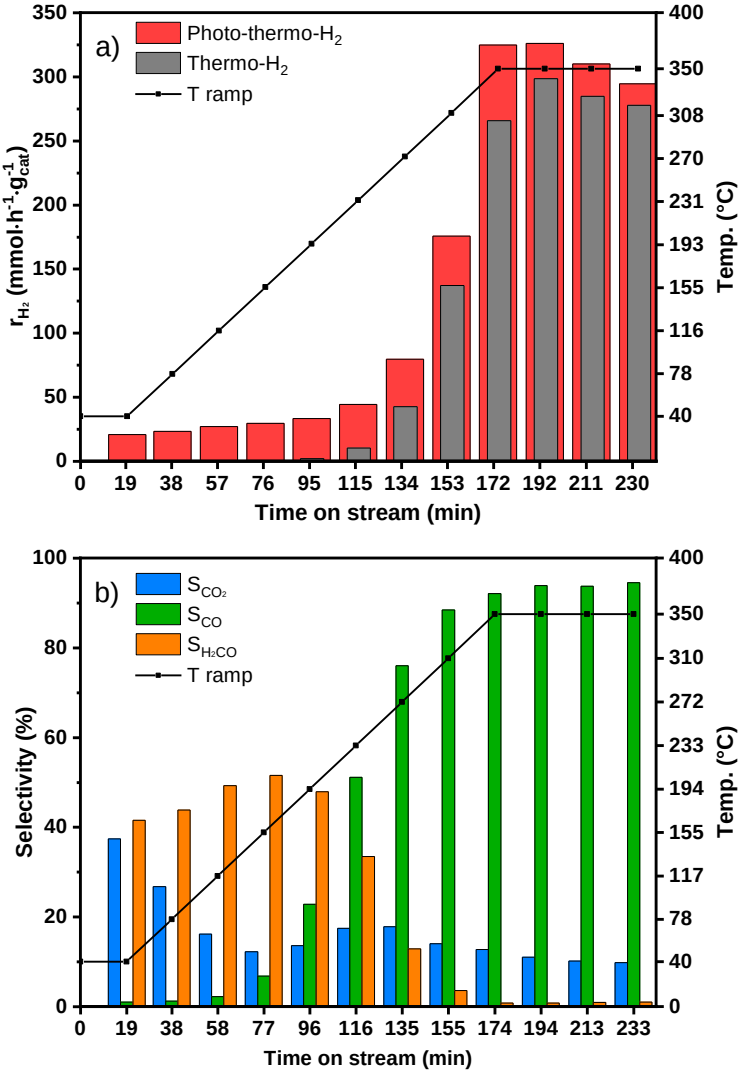

Figure 6.13 *Results obtained with TPC0.05: a) comparison of* r_{H_2} *obtained under irradiation (red) and in dark conditions (grey), showing a behaviour similar to that obtained with TPC0.0; b) Selectivity to* CO_2*, CO and* H_2CO *with increasing temperature.*

Finally, from the methanol conversion data reported in Table 6.2 we can observe that in any situation, under irradiation or in dark condition and at any temperature, no photocatalyst is able to convert all the available alcohol. Thus, despite the large H_2 production rates, the system is never under limiting reagent situation. In dark condition and at low temperature, due to the poor catalytic activity, the conversion value appears close to zero.

Table 6.2 *Methanol conversion attained with the 4 photocatalysts both in dark (T) and under light (hν+T) conditions at the different temperature.*

T (°C)	Methanol conversion (%)							
	TPC0.0		TPC0.05		TC0.05		TiO_2	
	T	hν+T	T	hν+T	T	hν+T	T	hν+T
40	2.4	7.6	0	0.6	0.0	0.0	0	0.4
79	1.6	10.3	0	8.2	0.2	0.0	0	1.4
118	2.8	12.3	0	9.5	0.7	0.0	0	1.5
157	1.6	13.7	0	10.3	0.0	0.0	0	2.0
196	2.9	15.6	0.2	14.8	1.1	1.9	0	4.1
235	4.7	19.3	2.5	12.9	0.0	2.8	0	7.7
274	21.1	31.3	9.7	16.2	0.0	8.6	0	6.9
313	56.3	65.1	28.5	39.6	2.8	10.0	0	9.6
350	75.1	87.7	57.9	73.7	3.3	7.5	5.6	19.8

6.5. Conclusions

This preliminary investigation demonstrates that thermal treatments and temperature can play a crucial role in photocatalytic reactions. Bare titanium dioxide can take advantage of high temperature in hydrogen production by increasing the H_2 yield without notable changes in by-products selectivity. The combined effect of light and heat,

instead, leads to different results depending on the metal NPs deposited on the TiO_2 surface. Indeed, the stabilisation of Pt nanoparticles into its metal form by high temperature reduction leads to a great improvement of photocatalytic activity, whereas the same treatment applied to copper NPs-containing TiO_2 was detrimental due to the loss of the peculiar ability of oxidised Cu to switch between oxidation states.

Moreover, tests performed at a fixed high temperature revealed that Pt-modified TiO_2 is more susceptible to deactivation with respect to Cu-modified titania. The influence of Cu on TiO_2 activity at different temperatures was negligible, but the low metal loading could be an explanation for this. On the contrary, the presence of Pt nanoparticles dramatically changed the activity and selectivity of the oxide at different temperatures.

Indeed, these results open the exploitation of metal-modified TiO_2 materials to a number of industrial applications. By carefully selecting the photocatalyst working temperature it is possible to tune the selectivity and, thus, the outlet gas composition. Furthermore, the use of photoreactors combined with solar concentrators could allow to exploit the powerful synergistic effect observed between photocatalytic and thermal reactions by using solar light.

References

1 J.-M. Herrmann, *Catal. Today*, 1995, **24**, 157–164.
2 E. Borgarello, J. Kiwi, E. Pelizzetti, M. Visca and M. Graetzel, *J. Am. Chem. Soc.*, 1981, **103**, 6324–6329.
3 N. R. Blake and G. L. Griffin, *J. Phys. Chem.*, 1988, **92**, 5697–5701.
4 X. Fu, W. A. Zeltner and M. A. Anderson, *Appl. Catal. B Environ.*, 1995, **6**, 209–224.
5 D. S. Muggli and M. J. Backes, *J. Catal.*, 2002, **209**, 105–113.
6 A. V. Vorontsov and V. P. Dubovitskaya, *J. Catal.*, 2004, **221**, 102–109.
7 J. C. Kennedy and A. K. Datye, *J. Catal.*, 1998, **179**, 375–389.
8 T. Sano, N. Negishi, K. Takeuchi and S. Matsuzawa, *Sol. Energy*, 2004, **77**, 543–552.
9 T. Sano, N. Negishi, K. Uchino, J. Tanaka, S. Matsuzawa and K. Takeuchi, *J. Photochem. Photobiol. A Chem.*, 2003, **160**, 93–98.
10 Y. Li, J. Huang, T. Peng, J. Xu and X. Zhao, *ChemCatChem*, 2010, **2**, 1082–1087.
11 J. Fang, Z. Chen, Q. Zheng and D. Li, *Catal. Sci. Technol.*, 2017, **7**, 3303–3311.
12 J. J. Murcia, M. C. Hidalgo, J. A. Navío, V. Vaiano, D. Sannino and P. Ciambelli, *Catal. Today*, 2013, **209**, 164–169.
13 X. Meng, T. Wang, L. Liu, S. Ouyang, P. Li, H. Hu, T. Kako, H. Iwai, A. Tanaka and J. Ye, *Angew. Chemie - Int. Ed.*, 2014, **4**, 11662–11666.
14 V. Vaiano, D. Sannino and P. Ciambelli, *Photochem. Photobiol. Sci.*, 2015, **14**, 550–555.
15 F. Saladin and I. Alxneit, *J. Chem. Soc. Faraday Trans.*, 1997, **93**, 4159–4163.
16 L. Liu, C. Zhao, H. Zhao, D. Pitts and Y. Li, *Chem. Commun.*, 2013, **49**, 3664–3666.
17 L. J. Liu, C. Y. Zhao, D. Pitts, H. L. Zhao and Y. Li, *Catal. Sci. Technol.*, 2014, **4**, 1539–1546.
18 B. Han and Y. H. Hu, *J. Phys. Chem. C*, 2015, **119**, 18927–18934.
19 K. Foger and J. R. Anderson, *Appl. Surf. Sci.*, 1979, **2**, 335–351.
20 G. L. Chiarello, D. Ferri and E. Selli, *J. Catal.*, 2011, **280**, 168–177.
21 E. L. Kunkes, R. R. Soares, D. A. Simonetti and J. A. Dumesic, *Appl. Catal. B Environ.*, 2009, **90**, 693–698.
22 P. D. F. Vernon, M. L. H. Green, A. K. Cheetham and A. T. Ashcroft, *Inorg. Chem.*, 1990, **6**, 181–186.
23 J. Mantzaras, *Combust. Sci. Technol.*, 2008, **180**, 1137–1168.
24 F. Pompeo, G. Santori and N. N. Nichio, *Int. J. Hydrogen Energy*, 2010, **35**, 8912–8920.
25 M. M. V. M. Souza and M. Schmal, *Catal. Letters*, 2003, **91**, 11–17.

Second Part:

TUNGSTEN TRIOXIDE MATERIALS

Chapter 7:

TUNGSTEN TRIOXIDE

7.1. WO_3 and its properties

Among the suitable alternatives to TiO_2 as semiconductor photocatalyst, tungsten trioxide has attracted wide attention due to its narrower band gap, with respect to titania. Indeed, the energy gap ranges from 2.6 to 2.8 eV[1–3] allowing WO_3 to be activated by visible light up to *ca.* 480 nm. Additional studies about tungsten trioxide have been carried out in consideration of its interesting applications, other than in photocatalysis, such as in photo- and electro-chromism[3–5] or gas sensing,[6–8] especially in thin film form. Its high-potential valence band (*ca.* 2.8 – 3 V *vs.* NHE at pH = 0), similar to that of TiO_2, gives tungsten trioxide a high oxidation ability when activated. On the contrary, the narrower band gap is connected to the position of the conduction band (CB), which is at a lower energy than the CB of TiO_2. Indeed, photopromoted electrons in the CB can not reduce protons to H_2, the CB edge of WO_3 being at positive potential. This is probably the greatest limitation of WO_3 as photocatalyst, since it can not be directly employed in H_2 production without any external applied bias that boosts electrons to drive the reaction. An additional drawback is its poor stability under basic or neutral aqueous environments. Looking at the Pourbaix diagram in Figure 7.1, it can be observed that the stability range of WO_3 is limited to pH below 6.[9]

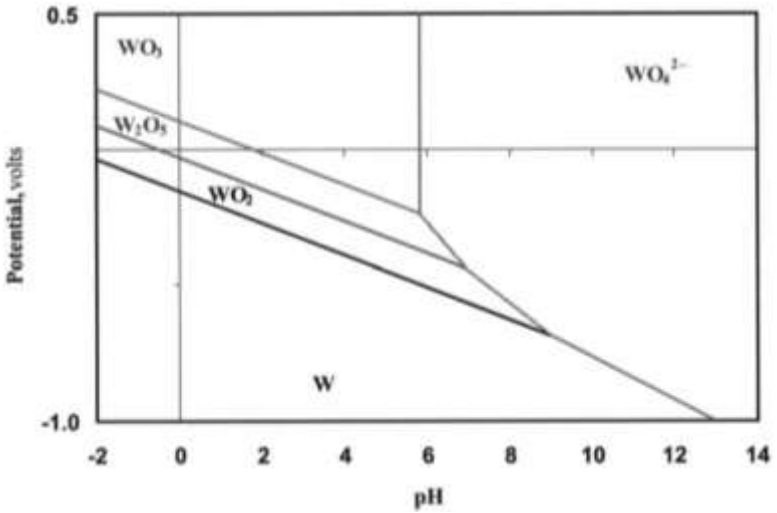

Figure 7.1 *Pourbaix diagram for tungsten in aqueous media. WO_3 stability range is limited to pH values below 6; above this value, dissolution of the oxide to WO_4^{2-} occurs.*[9]

Tungsten trioxide can exist under five different crystal structures, depending on temperature. All the five forms possess very similar structure, consisting of networks of corner-sharing WO_6 octahedra. The structures are usually described with respect to an ideal cubic structure, like the ReO_3 one, that can be obtained only after stabilisation by Na doping, with the sodium cations located in the perovskite cages.[10] The five phases are: α-WO_3, β-WO_3, γ-WO_3, δ-WO_3, ε-WO_3. The tilting of the octahedra is a common phenomenon for the five tungsten trioxide structures and it can be described as the result of the octahedral rotation about the Cartesian axes (or perovskite axes) from their ideal orientation (*i.e.* that of the cubic phase, reported in Figure 7.2). The value of this angle is roughly the same for all tilting angles around 8°; however, the rotation may be clockwise or anticlockwise.[10]

Figure 7.3 reports the WO_3 structures with their corresponding temperature stability range, compared to the ideal cubic WO_3 structure. Views from the three different axes are represented, together with the tilting direction about each Cartesian axis (+, –, 0 for in-phase, out-of-phase or no-tilting respectively). Table 7.1 reports the main lattice parameters. The various phases contain a different number of WO_3 units (Z) in the unit cell; thus, for example, the ε-WO_3 phase data are converted to a larger Z = 8 cell, by averaging over the appropriate sites.

Table 7.1 *Lattice parameters and band-gap energy of WO_3 polymorphs. Z is the number of WO_3 units considered in the unit cell; a, b and c are the lattice constants.*

Phase[Ref.]	Crystal Structure	Z	Space Group	a (Å)	b (Å)	c (Å)	Band Gap (eV)
Cubic (ideal) [11–13]	Simple cubic	1	$Pm\bar{3}\bar{m}$	3.82	3.82	3.82	0.544[1]
α-WO_3 [14,15]	Tetragonal	2	*P*4/*nmm*	7.468	7.468	7.850	1.8
β-WO_3 [14,16]	Orthorhombic	8	*Pbcn*	7.361	7.574	7.762	2.0
γ-WO_3[14]	Monoclinic	8	$P2_1/n$	7.327	7.564	7.727	2.6
δ-WO_3 [14,15]	Triclinic	8	$P\bar{1}$	7.309	7.522	7.686	2.6
ε-WO_3[14]	Monoclinic	4	*Pc*	7.378	7.378	7.664	2.8

[1] Calculated.

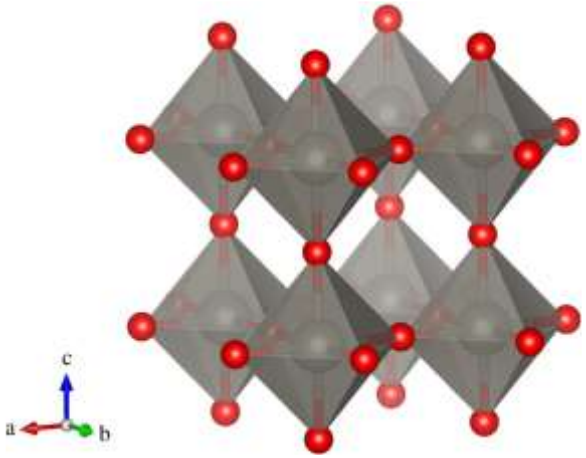

Figure 7.2 *Crystal structure of ideal cubic WO_3. There are four atoms in the WO_3 primitive cell: one W (0, 0, a/2) and three O atoms at (0, 0, 0), (0, a/2, a/2) and (a/2, 0, a/2), where a is the lattice constant.*[11]

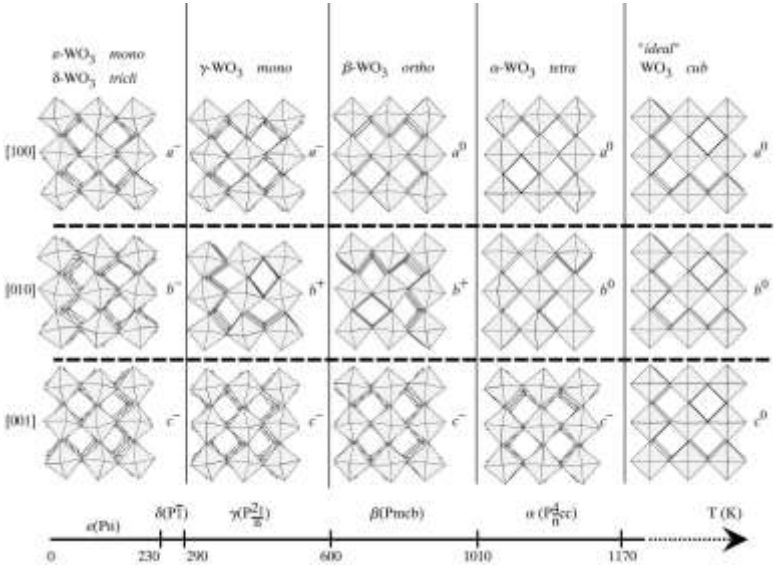

Figure 7.3 *Tilt patterns and stability temperature domains of the different polymorphs of tungsten trioxide.*[10,17]

The ε phase is stable only up to -43 °C, the δ up to 17 °C and the α phase becomes stable after reaching 730 °C. Thus, the most common WO_3 structures are the γ and β phases, monoclinic and orthorhombic, respectively. As reported in Table 7.1, the distortion of the ideal cubic structure causes an enlargement of the band gap, from the calculated 0.544 eV for the ReO_3-like structure to the well-established 2.6 – 2.8 eV band gap value of the most common phases.

As for titanium dioxide, also the valence band of tungsten trioxide is formed by filled O *2p* orbitals while the conduction band is mostly W *5d*-derived (Figure 7.4).

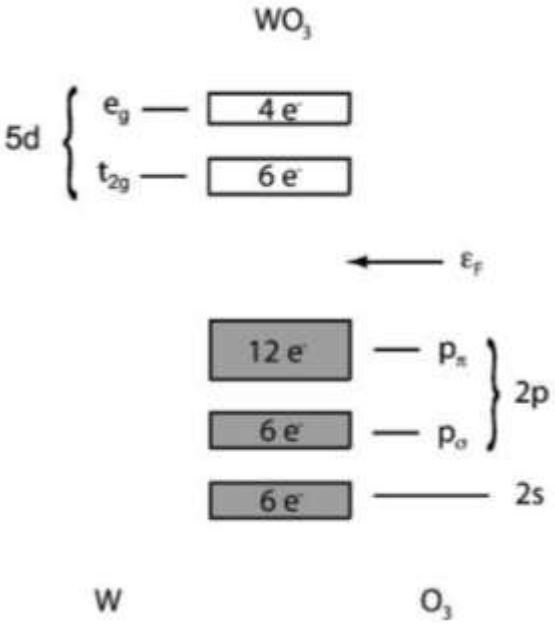

Figure 7.4 *Schematic band structure of WO_3. The 5d-derived orbitals (white squares) are empty and can be filled by the reported number of electrons.*[4]

With respect to TiO_2, even a small oxygen deficiency in the structure leads to important changes in the absorption capabilities of the material. Indeed, whereas tungsten trioxide absorbs only the blue part of the visible spectrum (it is a slightly yellow oxide), an oxygen-deficient WO_{3-x} shows a more greenish colour, caused by the absorption of photons in the red-infrared region. The additional absorption peak is caused by an electron transfer from W^{6+} to W^{5+}. This phenomenon has been recently exploited for the production of electrochromic smart windows that can change their colour by applying an external electrical bias.[18,19] The same effect can also be obtained by treating WO_3 with reducing gases (*i.e.* H_2, gaschromism),[20] with heat[21] and with light (photochromism).[22]

7.2. Improving WO_3 activity

In the field of hydrogen production and photon energy conversion, the main advantage of tungsten trioxide, *i.e.* its narrower band gap with respect to that of TiO_2, conflicts with a CB positioned at potential higher than the H^+/H_2 redox couple. In order to attain proton reduction with WO_3 it is necessary to boost the electrons photopromoted in the conduction band and this is possible only by applying an external bias. It is clear that, for H_2 production, WO_3 must be prepared as a film over a conductive support, *i.e.* a metal foil or a conductive glass (FTO, ITO), in order to separate the photopromoted electrons from the photogenerated holes and to perform the two semi-reactions at different electrodes. In principle, the application of a chemical bias, *i.e.* placing the WO_3 photocatalyst in a basic environment and the counter electrode in an acidic solution, should work since the photopromoted electrons would be at a more negative potential than the H^+/H_2 couple. However, the poor stability of tungsten

trioxide at high pH, as described before, excludes this kind of application in favour of the electrical bias. Nevertheless, most of the routes to boost WO_3 photoactivity has aimed at improving the solar harvesting capability, by doping the structure either with anions or cations, or at increasing the charges lifetime, by creating heterojunction systems with other oxides.

7.2.1. Doping with anions

WO_3 doping with anions aims at reducing the band gap to extend the visible light absorption properties. So far, almost only nitrogen has been employed as anionic dopant without significant results. Nitrogen introduction into the crystalline structure causes a mixing of the N *2p* orbitals with those of oxygen, raising the valence band minimum and, thus, reducing the band gap. Most of the attempts have been made with sputtering techniques, that proved to be effective in exploiting a poor reactive gas like N_2 directly for the synthesis of the material. The results reported in literature evidence that for low dopant concentrations the impact on the band gap is minimal[23] but with larger nitrogen amounts within the structure the E_g can be reduced to 2 – 2.2 eV.[5,24] However, this modification leads to a decrease in the crystallinity[5,23,24] and, for large doping, also to segregation of tungsten nitride phases.[5] Also the photoactivity of N-doped WO_3 appeared to be lower than that of the undoped photocatalyst: Cole *et al.* reported a 10-times decrease in photocurrent value at 1 V *vs.* SCE. These authors suggested that, despite the narrower band gap, the more defective structure causes a degradation in the charge transport properties, preventing the extraction of the photogenerated carriers.[23]

A more promising doping source for WO_3 seems to be carbon. Sun *et al.* reported a C-doped tungsten trioxide series prepared by spray

pyrolysis. Those materials exhibited a slightly narrower band gap together with an increased photocurrent with respect to the corresponding undoped WO_3.[25]

7.2.2. Doping with cations

Tungsten trioxide structure modification by doping with metal ions has been more investigated with respect to doping WO_3 with anions. Several metals, such as Mo, Hf, Te, Fe, or Nb, have been investigated, both experimentally and theoretically. Molybdenum doping, obtained by co-sputtering W and Mo in a reactive sputtering, caused modifications to the crystallographic properties, introducing a large number of defects and leading to poor photoelectrochemical performances. However, Gaillard *et al.* proposed that coupling such a co-doped WO_3 film with a pure tungsten trioxide film leads to an effective heterojunction due to the different Fermi level position within the two oxides.[26,27] Indeed, DFT calculations indicate that Mo, and Cr as well, only slightly affects the geometrical and electronic structure of WO_3, due to the same oxidation state of tungsten and to the similar atom size. On the contrary, Pacchioni *et al.* suggested the use of a dopant possessing an ionic radius larger than that of W^{6+} and also a different oxidation state. For instance, they found that Hf^{4+} could be an effective WO_3 dopant. Being larger than W^{6+} (0.78 Å *vs.* 0.62 Å, respectively), Hf^{4+}, in place of tungsten, should introduce strain and local relaxation, causing distortions of the WO_6 doped octahedrons and consequently up-shifting the CB, with an increased reduction potential (Figure 7.5c). Furthermore, the loss of two electrons is compensated by the generation of oxygen vacancies (in this case, one per each doping atom), leading to a final $Hf_xW_{1-x}O_{3-x}$ material. The vacancies cause an up-shift of both VB and CB, increasing the reduction potential, slightly

decreasing the oxidation potential but keeping the visible light absorption properties (Figure 7.5d). On the basis of DTF calculations, Pacchioni *et al.* suggest that this doped WO_3 oxide could be active even for hydrogen production from water splitting.[28,29]

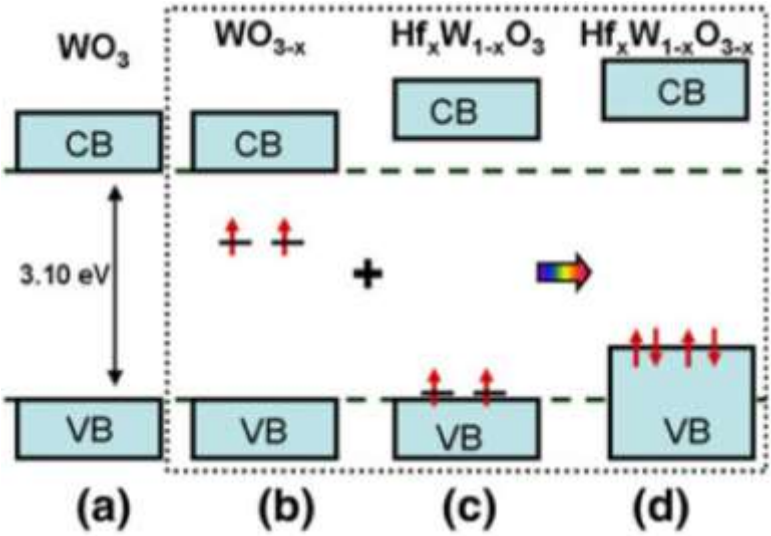

Figure 7.5 *Schematic energy levels of WO_3 (a), oxygen-deficient WO_{3-x} (b), Hf-doped $Hf_xW_{1-x}O_3$ (c) and $Hf_xW_{1-x}O_{3-x}$ (d) systems.* [29]

In general, all metal dopants cause a decrease in the crystallinity of tungsten trioxide due to local distortion and oxygen vacancies introduction if the cation has a different valence. These consequences deteriorate one of the most valuable characteristics of WO_3, its good charge transport ability. Thus, iron (III) doping brings improvements only for limited dopant amounts. Zhang *et al.*, for example, reported that the optimum Fe^{3+} doping concentration is 2 mol.%, allowing both a larger wavelength exploitation and an increased photoactivity. Above this value, despite a further red-shifted absorption, oxygen vacancy concentration

becomes detrimental.[30] Similar results were obtained by Kabtamu *et al.* with niobium. The optimum loading (0.03 mol.%) allows to maximise the beneficial effects, *i.e.* larger light absorption and better photoactivity, without introducing too many O vacancies or structure distortions.[31]

An interesting alternative to the above-mentioned dopants is tellurium. Yang *et al.* tried WO_3 doping with this metalloid in very small concentration, *i.e.* 0.25 at.%. Despite the low amount, they observed interesting effects over the light exploitation ability. Indeed, Te did not affect the band gap, which was only marginally reduced, by it introduced intra-band gap states that allows even red light exploitation.[32]

7.2.3. Heterojunction systems

The most common technique to improve WO_3 photoactivity is its coupling with a different oxide to generate a heterojunction. As already mentioned in Chapter 1, these systems are employed to improve the charge separation and, thus, the lifetime of the photogenerated charges in order to increase the overall photoactivity. Due to its characteristics, the use of tungsten trioxide implies that, independently of the other coupled oxide, the photopromoted electrons are not able to produce hydrogen in the water splitting reaction without any external bias. Thus, great efforts have been made in recent years to obtain WO_3-based heterojunctions in thin film form, so that it is possible to apply an electrical bias and generate H_2 by proton reduction. Indeed, the WO_3/TiO_2 system is commonly used for organics oxidation, exploiting the highly-oxidising holes in the TiO_2 valence band.[33,34] A similar heterojunction has been obtained with ZnO instead of TiO_2; this system uses tungsten trioxide to extend solar light exploitation in the visible range, with photocatalytic efficiencies greater than the single oxides.[35–38]

I already mentioned the heterojunction between the Mo-doped WO_3 and undoped WO_3.[26] Indeed, since doping causes changes in the electronic structure, the formation of a junction between doped and undoped or differently doped WO_3 layers can be a solution to improve the photoactivity. In principle, an efficient heterojunction could be created between the Hf-doped WO_3, as suggested by Pacchioni *et al.*,[28,29] and another WO_3 layer or a different oxide.

A similar effect has been obtained by Choi *et al.* by depositing a thin Al_2O_3 layer over the WO_3 film. Despite being not photoactive, the overlayer induced beneficial effects due to the suppression of peroxo-species formation. Furthermore, the alumina layer influenced the tungsten trioxide surface defect sites, with an increase in trapped hole population and a decrease in electron accumulation. Thus, the efficiency of this system rose with respect to the single-layer system.[39]

Recently the combination of WO_3 with bismuth vanadate gained much attention due to its interesting performances under visible light irradiation. Indeed, the narrower band gap of $BiVO_4$ (2.4 eV), and its bands position, *i.e.* both CB and VB are higher in energy, made this oxide ideal for coupling with WO_3. This heterojunction showed highly enhanced the oxidation abilities with respect to the corresponding single oxides, as demonstrated by Grigioni *et al.*. Indeed, they reported current density values greater than the sum of those attained with the single photocatalysts.[40,41]

Recently, tungsten trioxide has been coupled also with antimony sulphide (Sb_2S_3). With respect to bismuth vanadate, Sb_2S_3 has a narrower band gap (1.7 – 1.9 eV), making it suitable for the exploitation of the full solar spectrum. The results appears encouraging, with high photocurrent

density observed, due to the better light harvesting properties and to the efficient charge separation.[42] However, it is known that sulphides are poorly stable under oxidative conditions, thus deeper investigations should be required to confirm its long-term efficiency.

References

1 G. Hodes, D. Cahen and J. Manassen, *Nature*, 1976, **260**, 312–313.
2 Y. Xu and M. A. A. A. Schoonen, *Am. Mineral.*, 2000, **85**, 543–556.
3 H. Zheng, J. Z. Ou, M. S. Strano, R. B. Kaner, A. Mitchell and K. Kalantar-zadeh, *Adv. Funct. Mater.*, 2011, **21**, 2175–2196.
4 G. A. Niklasson and C. G. Granqvist, *J. Mater. Chem.*, 2007, **17**, 127–156.
5 K. Nakagawa, N. Miura, S. Matsumoto, R. Nakano and H. Matsumoto, *Jpn. J. Appl. Phys.*, 2008, **47**, 7230–7235.
6 P. Salazar, F. J. Garcia-Garcia, F. Yubero, J. Gil-Rostra and A. R. González-Elipe, *Electrochim. Acta*, 2016, **193**, 24–31.
7 Â. Lemire, D. B. B. Lollman, A. Al Mohammad, E. Gillet and K. Aguir, *Sensors Actuators B*, 2002, **84**, 43–48.
8 Y. Fujioka, J. Frantti, A. M. Asiri, A. Y. Obaid, H. Jiang and R. M. Nieminen, *J. Phys. Chem. C*, 2012, **116**, 17029–17039.
9 W. Michaeli, *Chemical-Mechanical Planarization of Semiconductor Materials*, Springer Berlin Heidelberg, Berlin, Heidelberg, 2004, vol. 69.
10 P. Roussel, P. Labbé and D. Groult, *Acta Crystallogr. Sect. B Struct. Sci.*, 2000, **56**, 377–391.
11 X. Liu and H. Fan, *R. Soc. Open Sci.*, 2018, **5**, 171921.
12 F. Detraux, P. Ghosez and X. Gonze, *Phys. Rev. B*, 1997, **56**, 983–985.
13 G. A. de Wijs, P. K. de Boer, R. A. de Groot and G. Kresse, *Phys. Rev. B*, 1999, **59**, 2684–2693.
14 Y. Ping and G. Galli, *J. Phys. Chem. C*, 2014, **118**, 6019–6028.
15 M. Gerosa, C. E. Bottani, L. Caramella, G. Onida, C. Di Valentin and G. Pacchioni, *Phys. Rev. B - Condens. Matter Mater. Phys.*, 2015, **91**, 1–15.
16 J. C. Alvarez-Quiceno, G. M. Dalpian and J. M. Osorio-Guillén, *Phys. Status Solidi Basic Res.*, 2015, **252**, 2290–2295.
17 P. M. M. Woodward, A. W. W. Sleight and T. Vogt, *J. Solid State Chem.*, 1997, **131**, 9–17.
18 Y.-C. Nah, A. Ghicov, D. Kim and P. Schmuki, *Electrochem. commun.*, 2008, **10**, 1777–1780.
19 M. Deepa, A. G. Joshi, A. K. Srivastava, S. M. Shivaprasad and S. A. Agnihotry, *J. Electrochem. Soc.*, 2006, **153**, C365.
20 A. Georg, W. Graf, R. Neumann and V. Wittwer, *Solid State Ionics*, 2000, **127**, 319–328.
21 D. Y. Lu, J. Chen, H. J. Chen, L. Gong, S. Z. Deng, N. S. Xu and Y. L. Liu, *Appl. Phys. Lett.*, 2007, **90**, 88–91.
22 A. Georg, A. Georg and U. Opara Krašovec, *Thin Solid Films*, 2006, **502**, 246–251.
23 B. Cole, B. Marsen, E. Miller, Y. Yan, B. To, K. Jones and M. Al-Jassim, *J. Phys. Chem. C*, 2008, **112**, 5213–5220.
24 D. Paluselli, B. Marsen, E. L. Miller and R. E. Rocheleau, *Electrochem. Solid-State Lett.*, 2005, **8**, G301–G303.

25 Y. Sun, C. J. Murphy, K. R. Reyes-Gil, E. A. Reyes-Garcia, J. M. Thornton, N. A. Morris and D. Raftery, *Int. J. Hydrogen Energy*, 2009, **34**, 8476–8484.

26 N. Gaillard, B. Cole, J. Kaneshiro, E. L. Miller, B. Marsen, L. Weinhardt, M. Bär, C. Heske, K. S. Ahn, F. Yan and M. M. Al-Jassim, *J. Mater. Res.*, 2010, **25**, 45–51.

27 M. Bär, L. Weinhardt, B. Marsen, B. Cole, N. Gaillard, E. Miller and C. Heske, *Appl. Phys. Lett.*, 2010, **96**, 1–4.

28 F. Wang, C. Di Valentin and G. Pacchioni, *J Phys Chem C*, 2012, **116**, 8901–8909.

29 C. Di Valentin, F. Wang and G. Pacchioni, *Top. Catal.*, 2013, **56**, 1404–1419.

30 T. Zhang, Z. Zhu, H. Chen, Y. Bai, S. Xiao, X. Zheng, Q. Xue and S. Yang, *Nanoscale*, 2015, **7**, 14121–14121.

31 D. M. Kabtamu, J.-Y. Chen, Y.-C. Chang and C.-H. Wang, *J. Mater. Chem. A*, 2016, **4**, 11472–11480.

32 B. Yang and V. Luca, *Chem. Commun.*, 2008, 4454–4456.

33 F. Riboni, L. G. Bettini, D. W. Bahnemann and E. Selli, *Catal. Today*, 2013, **209**, 28–34.

34 O. Arutanti, A. B. D. Nandiyanto, T. Ogi, F. Iskandar, T. O. Kim and K. Okuyama, *J. Alloys Compd.*, 2014, **591**, 121–126.

35 C. Siriwong and S. Phanichphant, *Chiang Mai J. Sci.*, 2013, **40**, 281–288.

36 C. Siriwong, K. Wetchakun, A. Wisitsoraat and S. Phanichphant, *2009 IEEE Sensors*, 2009, 118–123.

37 S.-M. Lam, J.-C. Sin, A. Z. Abdullah and A. R. Mohamed, *J. Colloid Interface Sci.*, 2015, **450**, 34–44.

38 J. Xie, Z. Zhou, Y. Lian, Y. Hao, X. Liu, M. Li and Y. Wei, *Ceram. Int.*, 2014, **40**, 12519–12524.

39 W. Kim, T. Tachikawa, D. Monllor-Satoca, H. Kim, T. Majima and W. Choi, *Energy Environ. Sci.*, 2013, **6**, 3732–3739.

40 I. Grigioni, K. G. Stamplecoskie, E. Selli and P. V. Kamat, *J. Phys. Chem. C*, 2015, **119**, 20792–20800.

41 I. Grigioni, A. Corti, M. V. Dozzi and E. Selli, *J. Phys. Chem. C*, 2018, **122**, 13969–13978.

42 J. Zhang, Z. Z. Liu and Z. Z. Liu, *ACS Appl. Mater. Interfaces*, 2016, **8**, 9684–9691.

Chapter 8:

EXPERIMENTAL PROCEDURES AND SET-UP

This chapter describes the main experimental details about the synthesis and testing set-up, related to WO_3-based materials. The synthesis by sputtering techniques of the different photocatalytic films was performed in the CNR laboratory of Dr. Vassallo at the Istituto di Fisica del Plasma di Milano and in SmartMat Lab centre at the Università degli Studi di Milano. The different photocatalytic set-ups used to characterise and determine the photocatalytic behaviour of the different materials are also reported.

8.1. Sputtering Techniques

Sputtering processes are techniques widely employed for years to evaporate materials from the solid state by bombarding them with energetic ions. They are usually exploited for depositing thin films, possessing specific characteristics, over simple or complex surfaces.[1,2] Sputtering techniques are based on glow discharges,[3] where the plasma process is not thermal (the so-called cold or nonthermal plasma) and thus there's no thermodynamic equilibrium between the lighter (*i.e.* electrons) and the heavier (*i.e.* ions) species within the plasma. Plasmas, in general, are neutral since a roughly equal number of ions and electrons exist in their body. However, on a smaller scale, neutrality perturbations could occur, but such imbalances are rapidly compensated by the movement of the charges.[3]

The first condition to generate a cold plasma is a rarefied gas. Usually, in sputtering techniques, the working pressure is around some Pascals (10^{-2} millibar). Thus, the sealed metal chamber, typically made of steel, is connected to a high vacuum system. This is composed of two different pumps: a rotary pump is employed for removing most of the atmospheric gas and a high vacuum pump (usually a turbomolecular pump or a diffusion pump) is used for making high vacuum, in the 10^{-6} Pa range. Once most of the atmospheric gas molecules are removed, the gas chosen for generating plasma can be flown inside the chamber, rising again the pressure to the correct value. In general, noble gases (*i.e.* Ar) are employed for plasmas. However, in case of reactive sputtering processes, O_2, N_2, CO_2 or other gases compatible with the system can be added.

The simplest mean of forming a plasma is the Direct Current (DC) diode discharge. This system consists in a couple of electrodes, *i.e.* a cathode and an anode, connected to a high-voltage power supply. The electric field present between the electrodes is determined by *V/d*, where *V* is the applied voltage and *d* the distance between cathode and anode. If a free electron generated within the chamber by external phenomena, *e.g.* cosmic rays, is close to the cathode, this will be accelerated to the anode by the electric field. Due to the high vacuum condition and to the presence of the rarefied gas, the electron can gain enough energy, along the electric field to ionise a gas atom after colliding with it (EQ. 8.1).

$$e^- + Ar \rightarrow Ar^+ + 2e^- \qquad EQ\ 8.1$$

Thus, a second additional electron is generated. Alternatively, another common process is the excitation of the atom into an electronically excited state:

$$e^- + Ar \rightarrow Ar^* + e^- \qquad EQ\ 8.2$$

This second process causes the typical light emission of plasmas, since the *Ar** specie can relax by emitting a photon.

The electrons released after ionisation as in Eq. 8.1 will be accelerated towards the anode, striking and ionising additional atoms. On the opposite, the cations will be accelerated to the cathode by the electric field. The final collision of ions on the cathode causes the emission of several secondary electrons, contributing to plasma generation and stabilisation.[3]

An improvement of the DC diode discharge is given by Radio Frequency (RF) diode plasma. RF power is applied to improve the level of discharge ionisation. The most common frequency for commercial RF systems if 13.56 MHz. The design of this system is similar to that of DC plasma but with RF it is more common that an electrode, for instance the anode, is grounded together with the chamber. Thus, the relative areas of the two electrodes can be very different. As for DC plasma, a high voltage is placed between the electrodes (or only cathode is powered if the anode is grounded), in order to ignite the plasma. At this point, the applied voltage oscillates with time. The electrons, being light particles, are free to respond to the applied voltage while the ions, being heavier, are not able to respond to frequencies above 100 kHz. The consequence is that the more positive charged electrode will collect electrons rapidly; on the contrary, the more negative charged electrode will collect ions, but at slow rate due to their mass. Thus, plasma is denser than in DC discharge due to the rapid movement of electrons across the chamber, ionising more atoms. At the same time, a larger number of ions will bombard the negative charged electrode.

To exploit the ion bombardment occurring in the glow discharge, the cathode is usually covered and electrically connected by a plate of the material to evaporate. In this way, atoms of this material are freed from the plate and, if possessing enough energy, reach the opposite electrode, where they deposit creating a film. With respect to DC diode configuration, RF systems allow to sputter also insulating materials (like oxides), since electrode polarity is periodically reversed. Indeed, sputtering insulating materials with continuous DC power causes charges accumulation on the cathode, resulting in arching phenomena and plasma instability. However, the potential switching with a RF source also implies that some sputtered material can be back-sputtered from the deposited film. Thus, RF sputtering systems have a grounded electrode (*i.e.* the electrode were the substrate to be covered is placed). The main consequence is that, being an asymmetric system, sputtering from the material plate occurs at higher rates with respect to the back-sputtering occurring at the substrate and chamber walls, due to the large area difference.[3]

The two above-described glow discharge systems can be used as-such for sputtering materials. In the form of a planar diode, they compose the simplest sputter source. The plate of the material to be sputtered, the so-called target, is bonded to a water-cooled backing-plate, or directly water-cooled. This is the type of source employed for film synthesis in Chapter 9. This kind of source is efficient in using the target material, since the electric field is quite homogeneous through the electrode, but it is inefficient in exploiting secondary electrons. The consequences are an important bombardment of the deposited substrate and a consequent

temperature increase as deposition proceeds. Furthermore, only low deposition rates can be achieved.

One of the most important improvement brought to this technique to overcome those problems is the application of a magnetic field around the source. Indeed, a moving charge, like electron or ions in plasmas, in a magnetic field is subject to a force:

$$F_m = q\vec{v} \times \vec{B} \qquad EQ\ 8.3$$

q being the charge of the particle, $\vec{v}$ its velocity and $\vec{B}$ the applied magnetic field. This force will cause a charged particle, moving at right angles to a magnetic field, to follow an orbital path. Particles with higher energy or mass will follow larger orbits. Thus, electron orbits are usually smaller than the system dimension, while those of the ions are usually greater. The direct consequence of magnetic field application is that electrons are confined in a small region around the target, increasing plasma density, sputtering efficiency and requiring lower gas pressure and applied voltages. On the contrary, target erosion becomes nonuniform, generating a racetrack, *i.e.* the region of the target where material erosion is more important.

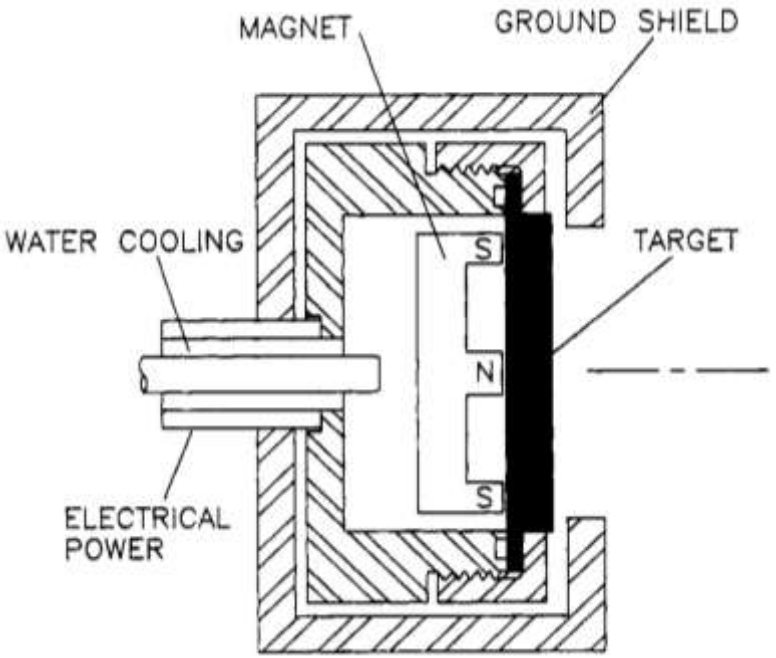

Figure 8.1 *Cross sectional view of a planar magnetron sputter source.*[3]

As shown in Figure 8.1, the array of magnets is placed behind the backing plate and water-cooled as well. Magnets are arranged in order to have different polarity at the centre with respect to the border of the target. In this way, the electrons are strongly confined in a region close to the target (*ca.* 60 mm above it). Thus, if the substrate is positioned within this region, the film suffers ion bombardment that can modify its structure and properties. On the contrary, if the film is positioned outside this region, the ion bombardment is so poor that it becomes difficult to obtain dense films.[1,2] This problems has been solved with the development of the unbalanced magnetron systems. Developed by Window and Savvides,[4–6] they consist in strengthening the outer array of magnets so that some

electrons are no more confined in the target region but, following the magnetic field lines, they can flow to the substrate. The result is the ion bombardment of the substrate with an increased quality coating. If two unbalanced magnetrons are installed opposed to each other, they can be configured with opposite magnets of opposite polarity (closed-field), or with opposite magnets of the same polarity (mirrored). The former configuration has led to further improvements in the sputtered coatings.[7] A comparison between some configuration is reported in Figure 8.2.

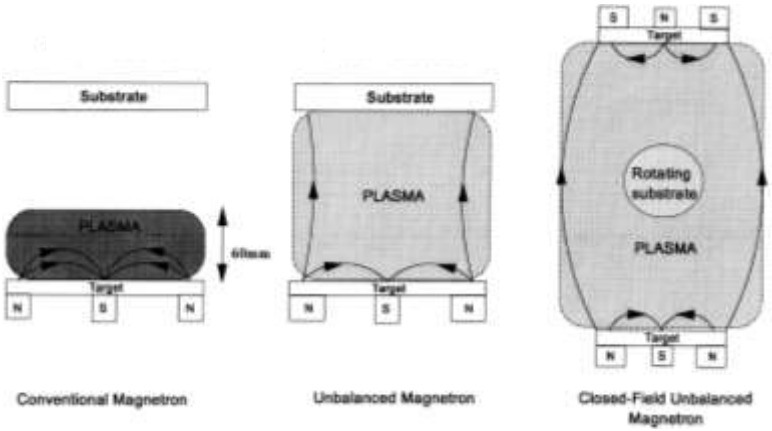

Figure 8.2 *A comparison of the magnetic configuration and plasma confinement in conventional, unbalanced and dual-magnetron closed-field systems.*[1]

Magnetron sputtering sources are the same as those of the diodes, thus both DC current or RF systems can be employed. As for the non-magnetron sources, the RF system has been preferred in the case of insulators sputtering or reactive sputtering from metal target leading to insulating films. Indeed, the use of continuous DC sources under the mentioned scenarios leads to the formation of arc discharges, causing the ejection of droplets of material from the target and consequently

increasing the amount of defects in the film.[1,2,8] The solution was found in the pulsed DC (pDC) magnetron sputtering process. The target voltage is periodically reversed, either to 0 V or even to small positive voltages (up to 10-20% of the negative operating voltage), with a frequency in the 20-350 kHz range. This technique avoids the formation of an insulating film over the target during the reactive sputtering process and prevents the arc discharging. High deposition rate and high-quality defect-free insulating films can thus be obtained also with the DC magnetron sputtering technique.[1,2] The pDC and RF magnetron sputtering processes were employed for the syntheses described in Chapter 4 and 10.

8.2. Photo-electrocatalytic set-up

The IPCE measurements and the photocatalytic activity of the tungsten trioxide thin films were performed by using a Plexiglas cell.[9] The reactor configuration depends on the measurement performed: it is composed by a single compartment when measuring IPCE or by two compartments when testing the activity or recording polarisation curves. The sketch of the cell, in the two-compartment configuration, is reported in Figure 8.3.

The cell is made of different Plexiglas plates (5,6,8,9,10) assembled together with rubber/silicon gaskets (7), tightened by 7 screws. Poly(methyl methacrylate) is resistant to alkaline and acidic corrosion, it is thermally and UV stable, thus suitable for our testing conditions. In water splitting configuration, the sample (3), acting as Working Electrode (WE), and the Pt coil (4), the Counter Electrode (CE), are placed in two different compartments, (8) and (9) respectively. In this way, it is possible

to collect the photoproduced H_2 and O_2 separately into different graduated burettes (11).

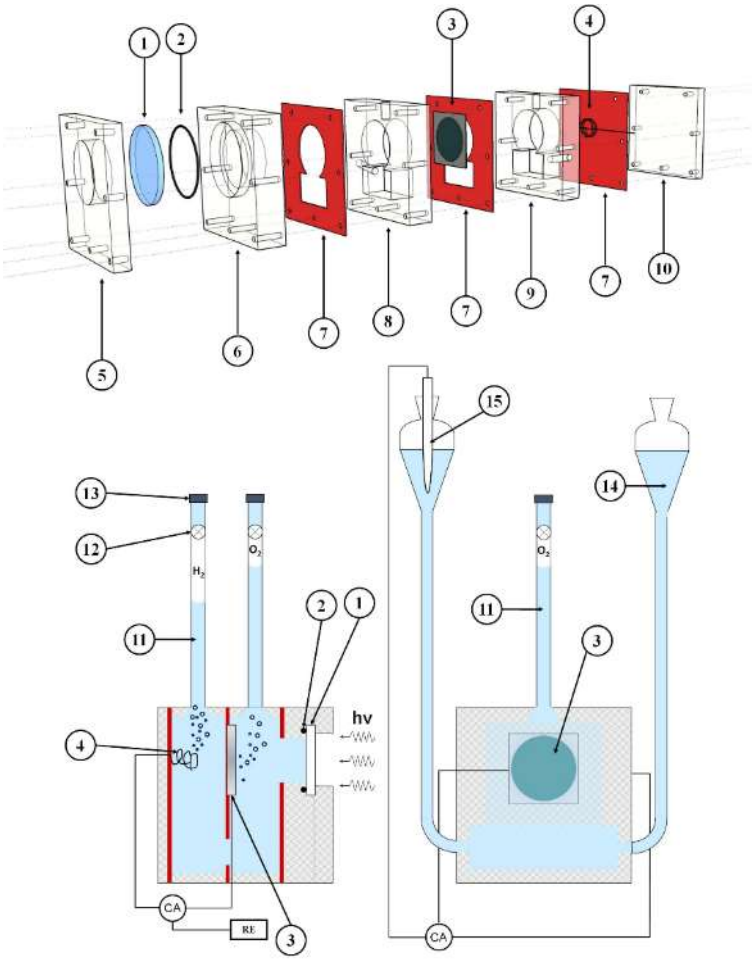

Figure 8.3 *Sketch of the Plexiglas cell for photocatalytic activity measurements: (1) Glass window; (2) O-ring; (3) Sample; (4) Pt wire; (5) Frontal Plexiglas plate; (6) Window holder Plexiglas plate; (7) Gaskets; (8) Anodic Plexiglas compartment; (9) Cathodic Plexiglas compartment; (10) Back Plexiglas plate; (11) H_2 and O_2 collecting burettes; (12) Stopcock; (13) Rubber septum; (14) Reservoir; (15) Reference Electrode (RE); (CA) Potentiostat.*

Indeed, test the volume of produced gases can be measured at the end of the photocatalytic. To compensate the loss of solution due to the WS reaction, two reservoirs (14) are connected to the cell. The sample is facing the window, kept in position by an O-ring, so that it can be irradiated by the lamp. When IPCE measurements are performed, the cathodic compartment plate is not used and the CE is placed underneath the sample. Furthermore, also the burettes and the reservoirs are not employed. Thus, the cell appears simpler and smaller.

Since the conduction band of WO_3 is more positive than the H^+/H_2 redox couple, we performed all measurements by applying a bias to samples. Indeed, a three-electrode system is required. The reference electrode (RE) was placed within the reservoir connected to the anodic compartment when using the two-compartment cell; on the other hand, when measuring IPCE, the RE was placed in the same hole used for the burette, above the WO_3 film. In order to avoid contaminations of the solution within the RE, a salt bridge, filled with the same electrolyte employed in the analyses, was used. The employed reference electrode was a Satured Calomel Electrode (SCE), having a +0.2444 V *vs.* SHE redox couple.

8.2.1. IPCE measurements

Photocurrent is the current that flows from a photoelectrode to a counter electrode in a photocatalytic cell, under irradiation. This measure with a monochromatic source is utilised to determine the IPCE, Incident Photon to Current Efficiency that is an evaluation of the efficiency of a system to convert light radiation energy into electric energy at a certain wavelength.

The IPCE can be calculated from the following equation:

$$\%IPCE = \left(\frac{j}{P} \cdot \frac{1240}{\lambda}\right) \cdot 100 \qquad EQ\ 8.4$$

where j ($A \cdot m^{-2}$) is the current density, P ($W \cdot m^{-2}$) is the illumination power density at the specific wavelength (this value can be obtained from the lamp current intensity), λ (m) is the wavelength of the incident light. The constant 1240 $J \cdot m \cdot A^{-1} \cdot s^{-1}$ can be obtained from the relationship:

$$1240 = \frac{h \cdot c}{q} \qquad EQ\ 8.5$$

with h being the Planck constant ($6.626 \cdot 10^{-34}$ J·s), c being the speed of light ($2.998 \cdot 10^{8}$ $m \cdot s^{-1}$) and q being the electron charge ($1.602 \cdot 10^{-9}$ C).

The set-up used for this kind of measurements is composed by a lamp, a LOT-Oriel arc Xe lamp (300W), connected to an Omni-λ 150 LOT-Oriel monochromator, with 0.4 nm resolution at 500 nm and 150 mm focal length. The monochromator is endowed of two different gratings. The first grating has been used since it provides a larger intensity in the UV region. At the exit of the monochromator, it is present a shutter (ThorLab SC10). The PEC cell was placed always at the same fixed distance from the shutter, being held by a rail mounted on the optical bench. A photodiode (model S130VC Thorlabs) connected to a power meter (model PM200 ThorLabs) was employed to measure the lamp power density in the same position of the sample within the PEC cell. The photodiode sensitivity ranges from 200 up to 1100 nm and the active area is *ca*. 70.9 mm^2. The IPCE setup is completed by an Amel, mod. 2549 potentiostat/galvanostat for bias application and by a Tecktronick DMM4040 multimeter for direct current (DC) measurement. The former was connected to all three electrodes (WE, CE and RE) while the latter

was connected in parallel to WE and CE only. Except for the potentiostat and the lamp, all the set-up is controlled directly by a LabView routine.

The lamp spectrum and the corresponding power density in the analysis range are reported in Figure 8.4. It can be observed that the lamp simulates quite well the solar spectrum, with a high-power density in the 400 – 500 nm range. The important drop in the power density under 350 nm is due to the presence of the glass window placed before the photodiode, thus absorbing part of the UV photons.

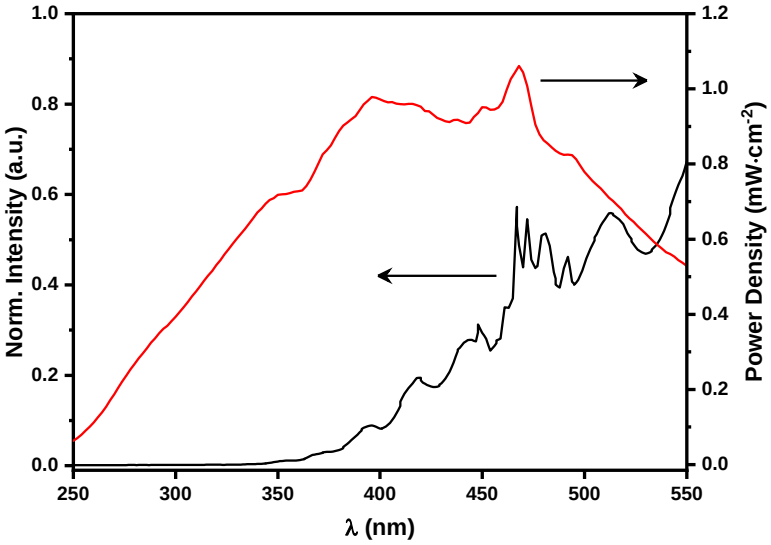

Figure 8.4 *Normalised lamp spectrum (black line) and corresponding power density (red line) of the lamp employed in IPCE measurements.*

The typical IPCE procedure imposes to switch on the lamp at least 30 minutes before the start of the measurements in order to stabilise its intensity. Then, the output power at 470 nm is measured and it is verified that P = 1.16 mW. If this value is not correct, the lamp power is changed

to reach the desired P. The PEC cell was filled with a suitable electrolyte. Due to the already-mentioned instability of WO_3 in alkaline medias, usually acidic (1N H_2SO_4 or H_3PO_4) or neutral electrolytes (1N Na_2SO_4) are used.

The lamp power density can be thus measured in the analysis range (250 – 550 nm) and, after that, the cell, filled with electrolyte and connected to all the instruments, is placed in front of the monochromator. After applying the desired bias, usually 1 V *vs.* SCE, and waiting for current stabilisation, the IPCE analyses can be performed. IPCE data are acquired every 2 nm by averaging 10 measurements for each step.

8.2.2. Linear Sweep Voltammetry and Water Splitting test

In the case of polarisation curves (Linear Sweep Voltammetry, *i.e.* LSV) and photocatalytic activity tests the two compartment PEC cell is employed. Usually, LSV analyses are performed before and after the water splitting test, thus the set-up is the same for both measurements. For instance, the PEC cell is connected to the Amel potentiostat/galvanostat as in the IPCE set-up. The instrument both applies the electrical bias to the sample and records the current flowing from the working electrode to the counter electrode. Two different lamps have been used with this set-up. Regarding the experiments performed in Chapter 9, we used an iron halide mercury arc lamp (Jelosil HG200, 250 W) emitting in the 350 – 450 nm range with an incident power density of 19.7 $mW \cdot cm^{-2}$ (Emission spectrum in FIGURE 8.5 (a)). On the opposite, for the experiments performed in Chapter 10, a LOT-Oriel arc Xe lamp (300W) with an AM1.5G solar simulation filter has been employed (Emission spectrum in FIGURE 8.5 b). The set-up is completed by an automated shutter (Lot-Oriel LSZ160) positioned in front of the lamp.

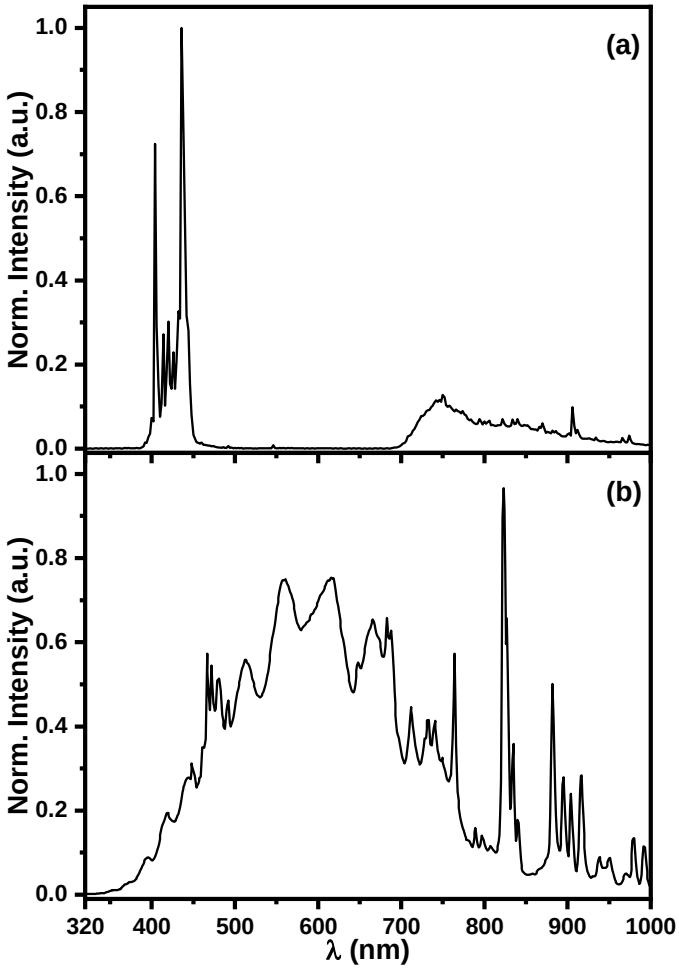

Figure 8.5 *Normalised lamp spectra of (a) the iron halide mercury arc lamp and (b) of the arc Xe lamp with AM1.5 solar simulation filter employed in LSV and WS measurements.*

The electrolyte used for this kind of measurements is the same of that employed in IPCE analyses and also the applied bias during water splitting tests is equal to that applied in IPCE measurements.

The LSV analysis consists in scanning the potential range, in our case from -0.2 to 1.5 V *vs.* SCE, applied to the working electrode while recording the current flowing from WE to CE. The standard procedure requires that two LSV analyses under dark conditions, *i.e.* with the lamp shuttered, are recorded first, followed by a LSV analysis under continuous irradiation and by a last one under chopped-light condition. The latter is obtained by setting the automated shutter in order to open and close every 5 s. Before any LSV measurement, the sample is set at a fixed potential, *i.e.* the starting bias in LSV analysis, in order to condition the WE. From this measurement is it possible to observe the onset potential, *i.e.* the potential at which the photocurrent rises, meaning that at the CE electrons are reducing water.

The water splitting tests are performed by applying the above-mentioned bias and continuously irradiating the sample. Due to the oxidation and reduction processes at the anode (WE) and cathode (CE), O_2 and H_2 evolves from the electrodes, accumulating into the burettes. Indeed, these were completely filled with electrolyte solution before starting the test. The volume of the produced gases is measured every 60 min, after shuttering the light, as the volume of displaced liquid in the burettes. Every sample was tested for at least 6 hours. Furthermore, it also possible to compare the volume of photoproduced H_2 with the photocurrent read by the potentiostat. Thus, according to the equation:

$$n_{H_2} = \frac{\int_0^t i\, dt}{2F} \qquad EQ\ 8.6$$

the number of moles of photoproduced H_2 are calculated by dividing the integrated photocurrent (i) over time by the Faraday constant (F) and 2 (number of electrons for each molecule of produced H_2).

References

1 R. D. Arnell and P. J. Kelly, *Surf. Coatings Technol.*, 1999, **112**, 170–176.
2 P. J. Kelly and R. D. Arnell, *Vacuum*, 2000, **56**, 159–172.
3 W. Kern and J. L. Vossen, *Thin Film Processes*, Elsevier, 1991.
4 N. Savvides and B. Window, *J. Vac. Sci. Technol. A Vacuum, Surfaces, Film.*, 1986, **4**, 504–508.
5 B. Window and N. Savvides, *J. Vac. Sci. Technol. A Vacuum, Surfaces, Film.*, 1986, **4**, 196–202.
6 B. Window and N. Savvides, *J. Vac. Sci. Technol. A Vacuum, Surfaces, Film.*, 1986, **4**, 453–456.
7 P. J. Kelly and R. D. Arnell, *Surf. Coatings Technol.*, 1998, **108**–**109**, 317–322.
8 I. Safi, *Surf. Coatings Technol.*, 2000, **127**, 203–218.
9 E. Selli, G. L. Chiarello, E. Quartarone, P. Mustarelli, I. Rossetti and L. Forni, *Chem. Commun.*, 2007, 5022–5024.

Chapter 9:

ENHANCED PHOTOPROMOTED ELECTRON TRANSFER OVER A BILAYER WO_3 n–n HETEROJUNCTION PREPARED BY RF DIODE SPUTTERING

9.1. Introduction

The hydrogen economy represents a possible solution to maintain the world energy demand, meanwhile persuading the target of zero carbon emission from fossil fuels exploitation. Photocatalytic cleavage of water has been widely investigated as environmentally-friendly method for renewable solar fuel production.[1–4] Separate stream of pure hydrogen and oxygen from water can be effectively achieved using photoelectrocatalitic (PEC) cells.[4–7] In the case of *n-type* semiconductors, the material acts as a photoanode for water oxidation to O_2, whereas the photopromoted electrons flow to the counter electrode where H_2 evolution takes place. One major issue in this process, which may seriously affect its efficiency, is the high probability of electron–hole pair recombination.

Among suitable semiconductor photocatalysts, WO_3 has received much attention as alternative to TiO_2[8,9] in consideration of its narrower band gap, ranging from 2.6 to 2.8 eV compared to 3.0 - 3.2 eV of TiO_2.[10,11] However, as introduced in Chapter 7, the electrons photopromoted in the

WO_3 CB are not able to reduce protons to H_2 and this reaction needs to be boosted by an externally applied voltage bias.

A multiple-layer strategy has often been investigated to improve the efficiency of photoactive materials. In the case of WO_3 several heterostructures have been studied, including WO_3/TiO_2,[12] $WO_3/BiVO_4$,[13] WO_3/Sb_2S_3[14] and WO_3/Cu_2O.[15] Enhanced photocurrent generation was recently attained with a triple-layered WO_3 photoanode grown by electrochemical anodization and attributed to the unique morphology of the material.[16]

Among the methods for thin film deposition, radio frequency (RF) plasma sputtering (Chapter 8) proved to be very effective for the synthesis of photoactive coatings,[7,17–20] particularly because it enables tuning of their properties through precise control of the deposition parameters (RF power, total pressure inside the chamber, composition of the gas atmosphere, deposition time, temperature and distance of the substrate). In a previous study,[21] the effect of sputter oxygen partial pressure on the characteristics of the resulting WO_3 coatings was studied and it was found that samples deposited in a 40%O_2/Ar atmosphere gave the most promising PEC performance. Moreover, WO_3 deposition at alternatively high and low gas pressures can minimize the well-known stress phenomena.[22] In this way, a denser outermost layer grown at lower pressure relieves the stress to an underlying less dense one, resulting in a larger critical thickness and good adhesion.[23] In particular, we found that the optimal high and low pressures were around 3 Pa and 1.5 Pa, respectively.[21]

In this work, we demonstrate that the electronic properties and the PEC performance of WO_3-based photoanodes can be tuned by changing

the total pressure during the RF plasma sputtering deposition. In particular, the deposition of two successive layers of the same oxide sputtered at different pressures provides an effective route to obtain an n–n heterojunction bilayer system with good stability and enhanced PEC performance in terms of photocurrent generation, hydrogen production and faradaic efficiency.

9.2. Experimental procedure

9.2.1. Photoanodes preparation

Three WO_3 photoanodes were prepared by RF (13.56 MHz) plasma sputtering[21,24,25] in a diode configuration at 140 W power and 1500 V of DC self-bias voltage. The WO_3 films were deposited on a tungsten foil (FB-Tecno, temper annealed, purity 99.6%, 2 × 2 cm^2, and 0.2 mm thick), and placed at 4.5 cm from the metal tungsten target in a reactive 40% O_2/Ar environment. The vacuum chamber was evacuated to less than 10−6 mbar before deposition. Two single layer coatings, labelled 1L(1.7 Pa) and 1L(3 Pa), were deposited at constant gas pressures of 1.7 Pa and 3 Pa, respectively. A double layer coating, labelled 2L(3+1.7 Pa), was prepared by growing WO_3 at two different gas pressures, by first depositing at 3 Pa, followed by deposition at 1.7 Pa. Details of the deposition times, chosen to achieve a *ca.* 1 μm thick photoactive layer in the three photoelectrodes, are reported in Table 1. The photoelectrodes were then calcined in an oven at 600 °C for 2 h. Finally, two more photoanodes were prepared for comparison, *i.e.* a bilayer photoanode, labelled 2L(1.7+3 Pa), obtained by inverting the sequence of deposition pressures, followed by calcination at 600 °C, and a compact dense WO_3

film, labelled 1L_calc, obtained by oxidation of the pristine tungsten foil surface in air at 600 °C for 2 h.

Table 9.1 *Sputtering deposition time, film thickness (d), electrochemically active surface area (ECSA), band gap energy (E_g), flat band potential (E_{FB}), valence band energy (E_{VB}) and density of donors (N_D) of the investigated WO_3 coatings.*

Sample	Dep. Time (min)	*d* (nm)	ECSA (cm^2)	E_g (eV)	E_{CB} (V *vs.* SHE)	E_{VB} (eV)	N_D (10^{20} cm^{-3})
1L(1.7 Pa)	179	1002	279	2.90	0.29	3.0	1.58
1L(3 Pa)	227	976	327	2.79	0.39	3.0	1.34
2L(3+1.7 Pa)	106 + 106	942	293	2.80	0.34	3.0	0.80

9.2.2. Photoanodes characterisation

X-ray diffraction patterns were recorded on a Philips PW3020 powder diffractometer operating at 40 kV voltage and 40 mA current, by using the Cu Kα radiation (λ = 1.5418 Å). The patterns were compared with the Inorganic Crystal Structure Database (ICSD) data for phase identification.

The film morphology, both at the surface and in cross-section, was investigated by High-Resolution Scanning Electron Microscope (SEM) imaging using a Tescan MIRA3 FESEM. X-ray photoelectron spectroscopy (XPS) measurements were performed with a Surface Sciences Instruments (SSI) M-Probe apparatus using Al Kα radiation (1486.6 eV). For all samples, the C 1s peak at 284.6 eV due to

adventitious carbon was taken as the internal reference. UV-Vis-NIR diffuse reflectance spectra were recorded in the 220 – 2600nm range with a Shimadzu UV3600 Plus spectrophotometer equipped with an ISR-603 Integrating Sphere. Photoluminescence spectra were measured with an Edinburgh FLS980 Spectrofluorimeter in the 360–650 nm range, upon excitation at 350 nm.

9.2.3. Electrochemical characterisation

Electrochemical measurements were performed in a two-compartment three-electrode PEC cell filled with a 0.5 M sodium sulphate solution. The sputtered WO_3/W electrode acted as working electrode (9.6 cm^2 geometric area), a platinum wire (bent into a three-loop coil) was the counter electrode and an aqueous saturated calomel electrode (SCE) was the reference electrode. All measurements were performed with a Metrohm Autolab PGSTAT302N potentiostat/galvanostat equipped with a frequency response analyser module (FRA32M) for electrochemical impedance spectroscopy (EIS).

The electrochemical surface area (ECSA) for each sputtered tungsten oxide electrode was estimated recording three consecutive potential cycles centred around the open circuit potential (OCP), sweeping between -0.150 and -0.05 V *vs.* SCE at scan rates from 0.025 to 0.3 $V \cdot s^{-1}$. The capacitive currents evaluated in the middle of the range were then plotted as a function of the sweep rate potential.[26,27]

The flat band potential, E_{FB}, and density of donor, N_D, of the investigated semiconducting WO_3 photoanodes were evaluated by Mott-Schottky (MS) analysis.[28] Measurements were performed in the dark and in 0.5 M Na_2SO_4 N_2-purged solution, recording impedance spectra (30 frequency values, single sine, logarithmically distributed from 104 Hz to

0.03 Hz and 0.01 V amplitude) at a constant applied potential ranging from 0.1 to 1.0 V *vs.* SHE (the experimentally applied potential *vs.* SCE was converted to the SHE by adding 0.244 V). The oxide film was first conditioned at 0 V *vs.* SCE for 30 s and then at the selected potential for 30 s. During the entire EIS test a flux of N_2 was maintained at the surface of the solution. Considering the frequency dispersion of the resulting MS analysis,[29] the EIS spectra were fitted with a Randles-type equivalent circuit $R_s(R_pQ)$, where R_s is the serial resistance, R_p is the polarization resistance and Q is a constant-phase element. Q substitutes the common capacitor, and allows one to calculate the effective capacitance C, to draw $1/C^2$ *vs.* applied potential plots.[30]

EIS spectra were also measured under working conditions for hydrogen production, *i.e.* under irradiation (19.7 $mW \cdot cm^{-2}$) and at 1.0 V *vs.* SCE bias, by sampling sixty frequencies (single sine logarithmically distributed from 105 Hz to 0.1 Hz and 0.01 V amplitude). Data were fitted with the aforementioned modified Randles equivalent circuit, where R_{ct} instead of R_p stands for the charge transfer resistance associated with photo-assisted water oxidation reactions occurring at the WO_3 surface. All EIS spectra were fitted using Z-View software (Scribner Associates, Inc.).

9.2.4. IPCE measurements

The incident photon to current efficiency (IPCE) was measured on an optical bench already described elsewhere,[31] including a 300 W Xe lamp (Lot-Oriel), a monochromator (LOT-Oriel Omni-λ 150), a shutter (Thorlabs SC10), a calibrated photodiode (Thorlabs S130VC) connected to a power meter (Thorlabs PM200), and a potentiostat/galvanostat (Amel, mod. 2549). Measurements were done in the three-electrode PEC

cell, biased at 1.0 V *vs.* SCE in 0.5 M Na_2SO_4 electrolyte solution. The percent IPCE at each wavelength λ was calculated as:

$$\%\, IPCE = \frac{I_\lambda}{P_\lambda} \cdot \frac{1240}{\lambda} \cdot 100 \qquad \text{EQ 9.1}$$

Where I_λ is the photocurrent density ($mA \cdot cm^{-2}$) at a specific incident wavelength λ (nm), P_λ is the incident power density ($mW \cdot cm^{-2}$) at the same λ, and 1240 ($J \cdot nm \cdot C^{-1}$) = $h \cdot c \cdot q^{-1}$ being h the Plank constant, c the speed of light and q the elementary charge carried by a single electron.

9.2.5. Photocatalytic performance test

Photocatalytic water splitting tests were conducted in the above described two-compartment PEC cell. The three electrodes were immersed in a 0.5 M Na_2SO_4 electrolyte solution and connected to the potentiostat/galvanostat for photocurrent measurements while applying 1 V *vs.* SCE external potential bias. The photoanode was illuminated through a Pyrex glass optical window employing an iron halide mercury arc lamp (Jelosil HG200, 250 W) as an irradiation source (Figure 8.5a in Chapter 8). The evolved H_2 and O_2 gases were collected in two graduated burettes surmounting the two compartments of the cell, which were initially filled with the electrolyte solution.[6] The volume of produced gas was measured every 60 min by the displacement of the liquid in the burettes, after shuttering the light. Each photoanode was tested for at least 6 h-long irradiation.

9.3. Results and discussion

9.3.1. Sample characterisation

9.3.1.1. XRD analysis.

The as-grown films, deposited at room temperature, are notoriously amorphous.[21] As shown in Figure 9.1, all sputtered WO_3 coatings after calcination at 600 °C exhibit diffraction patterns similar to that of the oxidized tungsten foil surface (sample 1L_calc). The crystal structure of WO_3 consists of corner-sharing octahedra (Figure 7.2 and 7.3 in Chapter 7). Because several distortions are possible, WO_3 can exist in many different polymorphs depending on the annealing temperature, *i.e.* triclinic from −50 to 17 °C,[32] monoclinic up to 330 °C, orthorhombic up to 740 °C, and tetragonal above 740 °C.[33] Monoclinic and orthorhombic structures have similar XRD patterns (see the bottom of Figure 9.1). Thus, it is not simple to discern between these two phases, also because of the XRD peak broadening and shift, due to possible distortions originating from oxygen vacancies. Nevertheless, because of the high annealing temperature, our sputtered WO_3 coatings are expected to have a distorted orthorhombic structure. Moreover, the relative intensity of the diffraction peaks significantly differs from that of the reference, the most intense peaks being those located at $2\theta = 23.5°$ and 48.1° corresponding to the parallel (020) and (040) planes. This indicates a preferred orientation along the [010] direction, as often occurs in thin films and metals.[34] It is noteworthy that films grown on (100) silicon wafers under the same operation conditions and reported in our previous work[21] showed the opposite preferred orientation, the peak centred at $2\theta = 23.5°$ being the weakest one. Because the metal tungsten foil support also exhibits a

preferred orientation, one may conclude that the sputtered coating follows a nearly epitaxial growth (and spatial rearrangement) process, with the crystallographic axes of the deposited layer aligning along the orientation of the support underneath.

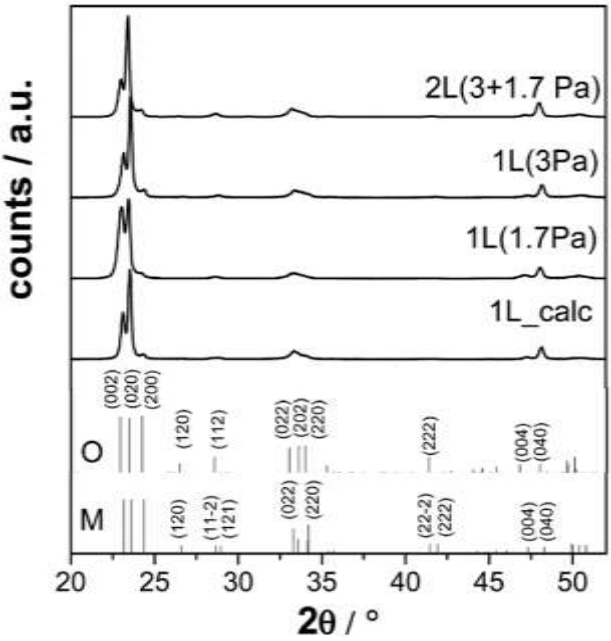

Figure 9.1 *XRD patterns of the calcined tungsten foil (1L_calc) and of the WO_3 coatings (single and double layers) prepared by RF sputtering and calcined at 600 °C for 2 h. The reflection position and relative intensity of the monoclinic (M) and orthorhombic (O) phases are reported at the bottom of the figure for comparison.*

9.3.1.2. SEM analysis

SEM investigation of the pristine metal tungsten support (Figure 9.2A and 9.3C) confirms the layered microstructure responsible for the preferred crystallographic orientation. After annealing at 600 °C for 2 h in air, the tungsten foil surface underwent oxidation forming a compact

1.5 μm thick WO_3 layer (sample 1L_calc, see Figure 9.2B). Interestingly, the cross-sectional SEM images of the annealed 1L(1.7 Pa) and 1L(3 Pa) samples (Figure 9.2C and 9.2D) reveal the presence of a 2.3 μm thick WO_3 film possessing a hierarchical structure with a porous layer surmounting a columnar basement. This morphology resembles that of the cliffs in the Isle of Staffa (Pillar Island) of volcanic origin in the west of Scotland. The WO_3 film was much thicker than expected on the basis of the sputtering deposition rate.

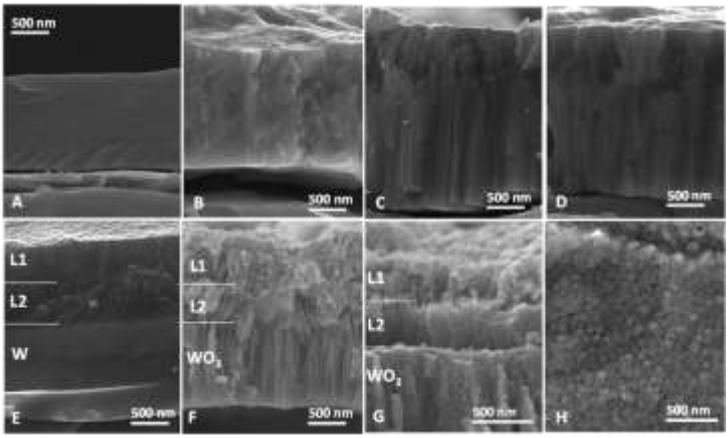

Figure 9.2 *Cross-sectional SEM images of (A) the pristine metal tungsten foil and (B) after calcination at 600 °C; (C) 1L(3 Pa); (D) 1L(1.7 Pa); 2L(3 + 1.7 Pa) (E) before and (F and G) after calcination at 600 °C. (H) Top view of 2L(3 + 1.7 Pa).*

However, the cross-sectional image of the as grown 2L(3+1.7 Pa) sample (*i.e.*, before annealing, Figure 9.2E) shows that the initial double-layer lying over the smooth tungsten metal surface is ca. 1 μm thick, as expected. After annealing at 600 °C in air (Fig. 9.2F) the film thickness increases to 2.3 μm due to the formation of the columnar basement. Hence, the innermost WO_3 vertically aligned array is formed upon oxidation of the metal tungsten surface in contact with the sputtered

coating. However, the resulting ordered morphology differs from that observed after calcination of the bare tungsten foil (Figure 9.2B), suggesting that the formation of this ordered structure is driven by the presence of the porous sputtered coating above. Thus, the calcined 2L(3+1.7 Pa) sample exhibits a Staffa-like morphology (Figure 9.2G), actually consisting of (i) a porous double-layer grown by RF diode sputtering (Figure 9.2H), and (ii) an underneath columnar layer formed by surface oxidation of the tungsten support during calcination in the presence of the overlying sputtered oxide.

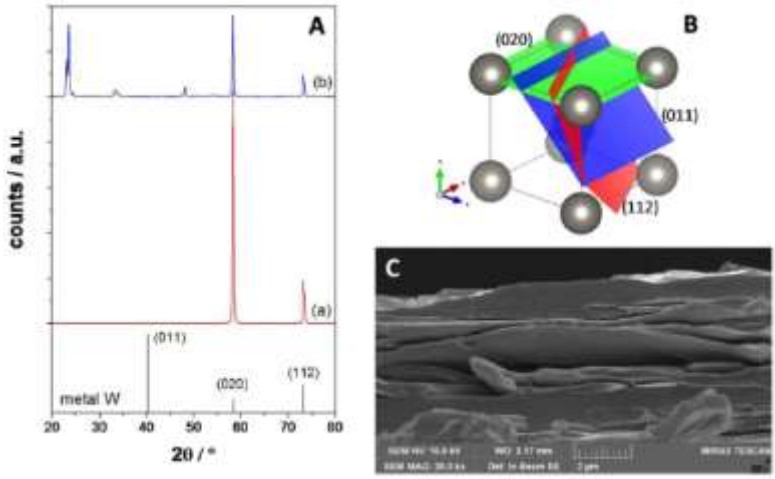

Figure 9.3 *(A) Comparison of XRD patterns of pristine W foil (a) and after annealing in air at 600 °C for 2h (b). The peak positions and relative intensities of the cubic metal W phase (ICSD code 653433) are reported at the bottom of the figure for comparison. The formation of a surface monoclinic WO_3 film after the annealing is highlighted by the appearance of the reflections in the $20° < 2\theta < 60°$ range. (B) Crystal unit cell of body centered cubic (bcc) metal W ($a = b = c = 3.1585$ Å, $\alpha = \beta = \gamma = 90°$, Space Group: $Im\bar{3}m$) showing the (011), (020) and (112) planes. The preferred orientation along the (020) plane may arise from the layered microstructure of the employed W foil as shown by the SEM image (C).*

9.3.1.3. *Electrochemical Surface Area*

The electrochemically active surface area (ECSA) gives an estimation of the real surface area involved in photoelectrochemical processes. It can be estimated by the potential scan-rate dependence of the capacitive current due to the double-layer charging and discharging at the solid–electrolyte interface.[26,35] The non-faradaic region of the cyclic voltammograms is typically a range of a few tens of millivolts centred around the open-circuit potential, OCP. In this potential region the capacitive current (Ic) is linearly dependent on the scan-rate *v* according to I_c = ECSA $C_s v$, where C_s is the intrinsic specific capacitance. The ECSA C_s product, corresponding to the double-layer capacitance C_{DL} of the interface, can be determined by the slope of the straight line interpolating I_c as a function of *v*, taken at the central potential of the cyclic voltammograms during both the anodic and cathodic scan (Figure 9.4). The value of C_s depends on the nature of the semiconductor material and of the electrolyte. Typical values are in the 15–130 $\mu F \cdot cm^{-2}$ range.[35] However, in the absence of a reference electrode of the known ECSA, a reasonable value of C_s = 60 $\mu F \cdot cm^{-2}$ for metal oxides[36] can be used to estimate the surface area of the investigated electrodes. Table 9.1 shows that the compact 1L_calc sample has an ECSA close to its geometric surface area, A_g (14.5 cm^2 *vs.* 9.6 cm^2, 3.5 cm being the diameter of the electrode), resulting in a roughness factor, r_f = ECSA/A_g, of 1.5. In contrast, the porous sputtered coatings possess a much larger surface area and, accordingly, a much higher r_f. The ECSA of the film deposited at higher pressure (3 Pa) is 17% larger than the ECSA of the film deposited at lower pressure (1.7 Pa). Indeed, at higher pressure the sputtered tungsten atoms undergo more frequent collisions with energy transfer (*i.e.*

energy loss) to the background gas before reaching the substrate. This results in a lower atomic mobility and in a variation of the atomic arrangement of the deposited film, with the formation of a less dense, more porous coating with a larger surface area. As expected, 2L(3+1.7 Pa) and 2L(1.7+3 Pa), being deposited at both pressures, have a surface area intermediate between those of 1L(3 Pa) and 1L(1.7 Pa).

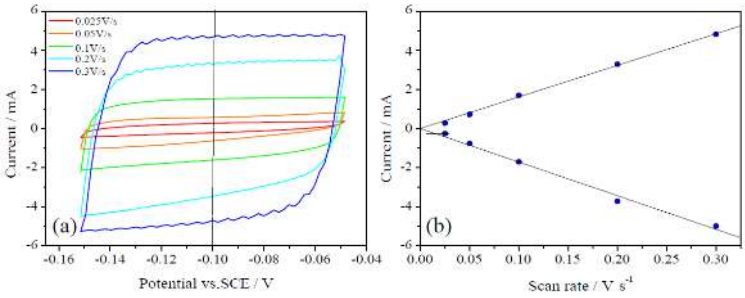

Figure 9.4 *Determination of electrochemically active surface area (ECSA) from double-layer capacitance measurements for 1L(1.7 Pa) sample in 0.5 M Na_2SO_4. (a) Cyclic voltammograms measured in a 0.1 V region around the OCV (i.e. in a non-Faradaic region) at different potential scan rates. (b) The cathodic and anodic capacitive charging currents taken at −0.1 V vs. SCE (= OCP) plotted as a function of scan rate. The double-layer capacitance C_{DL} of the system is the average of the absolute slope of the linear fits.*

9.3.1.4. Band gap structure

The UV-vis-NIR diffuse reflectance spectra (DRS) are presented in Figure 9.5 as Tauc-plots of the Kubelka-Munk transform, $F(K) = (1-R)^2/2R$, for direct allowed transition. The spectra show oscillations in the visible region typical of thin films, originating from the interference of the waves reflected at the top and bottom surface of the film. Their frequency and amplitude depend on the film thickness *d*.[31] The values of *d* of the calcined sputtered coatings, calculated using a dedicated tool of

the spectrophotometer software, are collected in Table 9.1. Interestingly, the results are in good agreement with the thickness of the outermost sputtered layer (*ca.* 1 μm), indicating a partial reflectance of light at the porous-columnar interface. By contrast, the dense 1L_calc sample shows no interference fringes, indicating that its thickness exceeds the light penetration depth.

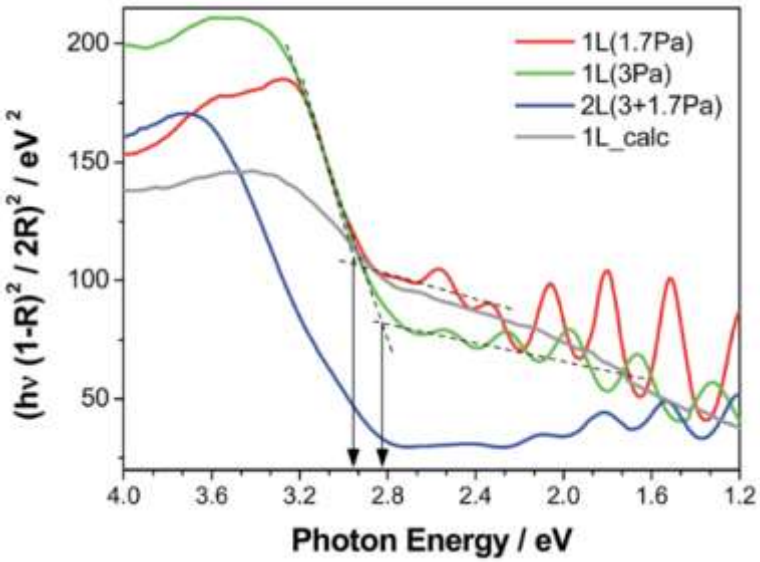

Figure 9.5 *Tauc plot of the Kubelka–Munk transform UV-Vis-NIR diffuse reflectance spectra in the 310 < λ < 1030 nm region and optical band gap determination (allowed direct transition). Spectra recorded on the samples after the 6 h-long photocatalytic water splitting test.*

The band gap energy E_g can be obtained by the Tauc plot, $(F(K)h\nu)^{1/2}$ *vs.* $h\nu$, at the intersection between the linear region of the absorption edge and the linear fit of the background at lower energy (Figure 9.5). The band gap absorption threshold of all samples is located

above 2.8 eV (*ca.* 440 nm). In particular, the 1L(1.7Pa) coating exhibits a 0.11 eV wider E_g with respect to the 1L(3Pa) (Table 9.1). A variation of WO_3 band gap from 3.2 eV to 2.5 eV as a function of both deposition pressure and temperature has been widely documented in literature.[37–40]

In order to further understand the origin of the difference in the band gap of 1L(3 Pa) and 1L(1.7 Pa), we estimated the position of the CB using the Mott–Schottky equation (EQ 9.2). In this model, the CB edge is measured as flat band potential E_{FB}, *i.e.* the potential at which the drop in the space-charge layer is zero and the semiconductor bands are flat. For *n-type* semiconductors:

$$\frac{1}{C_{SC}^2} = \frac{2}{\varepsilon\varepsilon_0 q N_D}\left(E_{appl} - E_{FB} - \frac{kT}{q}\right) \qquad \text{EQ 9.2}$$

Where C_{sc} is the space-charge capacity of the semiconductor, E_{appl} the applied bias voltage, ε the dielectric constant of the semiconductor (35.2 for WO_3),[41] ε_0 the permittivity of vacuum (8.85 10^{-14} F·cm^{-1}), N_D the donor dopant density, *q* the elementary charge, *k* the Boltzmann constant and T the temperature. E_{FB}, at a given T and pH of the electrolyte solution, can be obtained extrapolating to zero the linear part of C^{-2} *vs.* E_{appl} plot (Figure 9.6) where $E_{FB} = E_{appl}(C^{-2} = 0) - kT/q$, whereas N_D can be calculated by the slope. The results presented in Table 9.1 show that the 1L(1.7Pa) sample has an E_{FB} shifted of 0.1V towards lower potential (*i.e.* higher energy) with respect to the 1L(3Pa). Thus, the wider band gap of the coating prepared at lower pressure is due to the up-shifting of the CB energy. XPS valence band spectra (Figure 9.7) further confirm this finding showing that both monolayer samples have the E_{VB} located at the same energy (3.0 eV) with respect to the Fermi level, E_F.

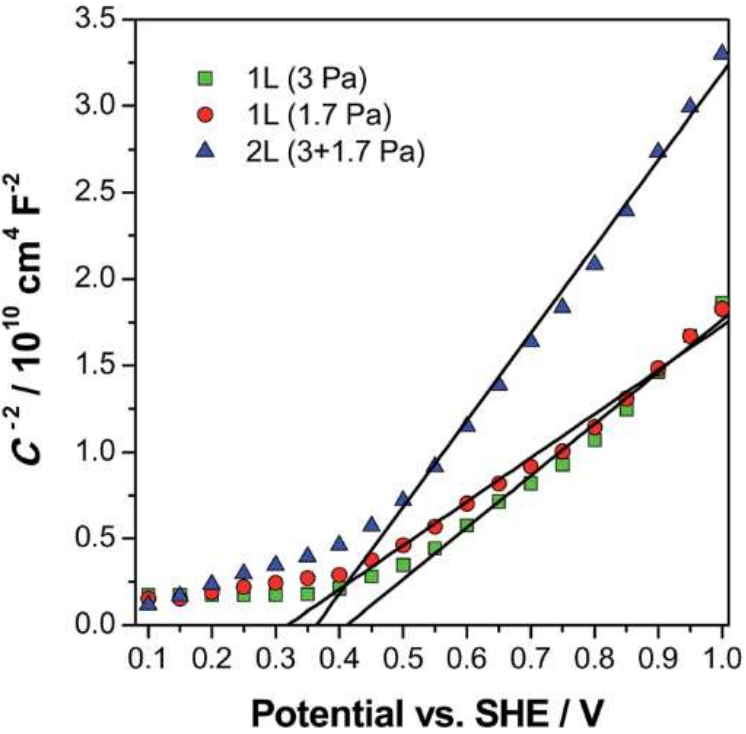

Figure 9.6 *Mott–Schottky plot measured in 0.5 M Na_2SO_4 (pH 7, at 21 °C) with the investigated sputtered coatings after the 6 h-long photocatalytic water splitting test. The intercept of the straight line with the x-axis corresponds to E_{FB} + kT/q.*

The positive slope of the Mott–Schottky plot confirms the *n-type* character of the synthesized semiconductor coatings due to the presence of oxygen vacancies, in the form of W^{5+} or W^{4+} sites, acting as electron donors. Their optical transition energy level is typically located 0.77–1.0 eV below the CB minimum.[44] The density of donor species N_D calculated from the slope of the Mott–Schottky plot (Table 9.1) demonstrates that

the coating prepared at lower pressure has a larger N_D, *i.e.* more oxygen vacancies, in agreement with the reactive sputtering process.

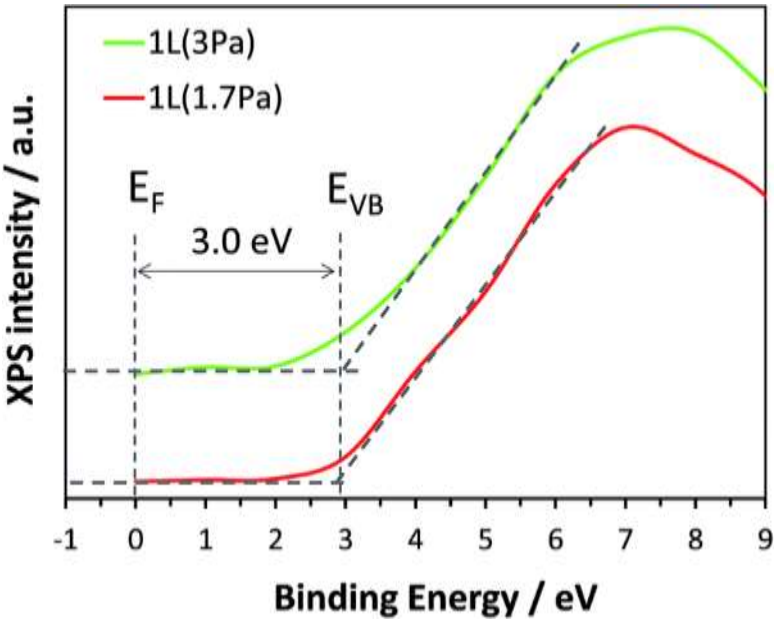

Figure 9.7 *XPS valence band (VB) spectra of the two monolayer samples. The energy of the VB (E_{VB}) edge is related to the Fermi level (E_F) located at 0 eV.*

In fact, a higher gas pressure in the deposition chamber during the deposition process leads to an increased probability that evaporated W atoms react with O_2 molecules, with a consequent lower amount of oxygen vacancies in the sputtered WO_3 layer. According to DFT calculations, the highest energy valence levels of WO_3 are predominantly O *2p* states, whereas the bottom of the CB is mainly composed of W *5d* states partly mixed with O *2p* orbitals.[43–45] These studies also predict, based on the crystal field theory (CFT), that a distortion of the WO_6 octahedron and in particular a change in the W–O bond length can affect

the position of the CB bottom.[43] Hence, the variation of the CB position as a function of the sputtering total pressure can tentatively be attributed to the different extent of crystal distortion induced by the different oxygen vacancy content.

The different band gap and doping levels measured in the two coatings prepared at the two deposition pressures suggest that in the 2L(3+1.7 Pa) sample an equivalent *n-type* to *n-type* heterojunction is created at the interface between the two WO_3 layers. Interestingly the 2L(3+1.7 Pa) sample has an E_{FB} value intermediate to those of single layer 1L(3 Pa) and 1L(1.7 Pa), and a much lower equivalent density of donors. Indeed, the bilayer sample can be modelled as two capacitors connected in series. Because the density of charge of each capacitor is equal to $\rho = N_D q$, where N_D is that of each single layer calculated from the Mott–Schottky equation ($N_{D,1.7\ Pa} = 1.58 \times 1020\ cm^{-3}$ and $N_{D,3\ Pa} = 1.34 \times 1020\ cm^{-3}$), and q is the unitary charge, then the equivalent charge density ρ_{eq} of the bilayer is:

$$\rho_{eq} = \left(\frac{1}{\rho_{1.7\ Pa}} + \frac{1}{\rho_{3\ Pa}}\right)^{-1} = 0.72 \times 10^{20} C \cdot cm^{-3} \qquad \text{EQ 9.3}$$

The N_D value of the so modelled bilayer is very close to the measured one ($0.80 \times 1020\ C \cdot cm^{-3}$). Thus, both E_{FB} and N_D values obtained for 2L(3+1.7 Pa) by the Mott–Schottky plot give experimental evidence supporting the formation of a n–n heterojunction.

9.3.1.5. *Photoluminescence and X-ray photoelectron spectroscopies.*

Photoluminescence (PL) spectroscopy[40,46,47] and theoretical calculations[42,44,45,48] have been widely employed to ascertain the nature of defects in WO_3. The PL emission spectra of the WO_3 sputtered coatings

recorded under excitation at 350 nm are shown in Figure 9.8. These spectra can be reasonably deconvoluted into four Gaussian curves (Figure 9.9) centred at *ca.* 410, 440, 490 and 550 nm.

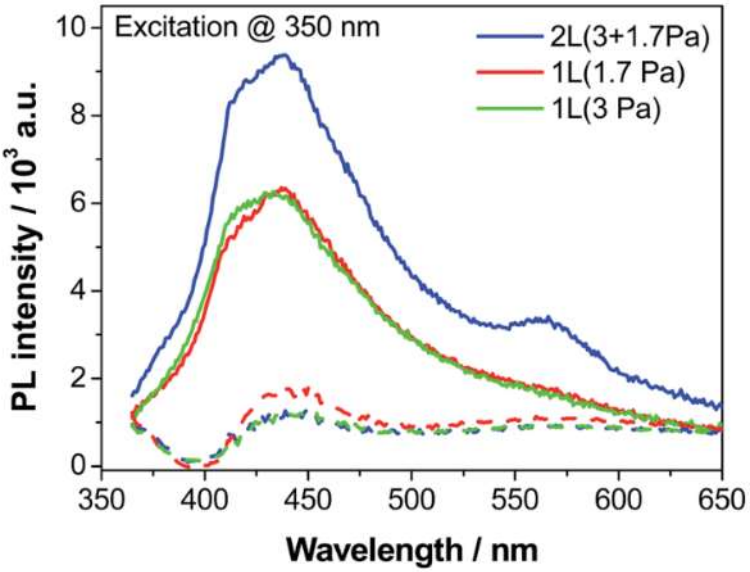

Figure 9.8 *Comparison of PL spectra (in air, λ_{exc} = 350 nm) of the investigated WO_3 sputtered coatings before (solid line) and after (dotted line) the 6 h-long photocatalytic water splitting test.*

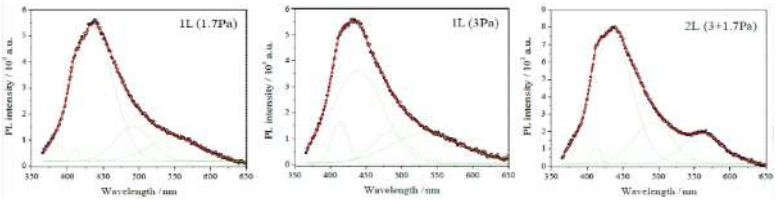

Figure 9.9 *Deconvolution of PL emission spectra (excitation at 350 nm) of as prepared (i.e. before the 6 h-long photocatalytic water splitting test) WO_3 sputtered coatings, including the experimental (dots) and fitted (red line) spectra.*

The first emission band, occurring at an energy greater than the band gap, has been attributed to the direct recombination of "hot electrons" which have not fully relaxed to the bottom of the CB.[47] The second and most intense band originates from the recombination of free charge carriers from the bottom of the CB to the VB (band-to-band recombination). The emission at an energy lower than the E_g necessarily involves infra-band gap energy states of donors trapped in either surface or bulk defects. In the case of WO_3, the removal of an O atom from the –W–O–W– lattice chain may lead to the formation of different charge states (0, 1+, and 2+) of oxygen vacancies (V_O) in the forms ($W^{5+}/V_O^0/W^{5+}$), ($W^{4+}/V_O^0/W^{6+}$), ($W^{5+}/V_O^+/W^{6+}$), and ($W^{6+}/V_O^{2+}/W^{6+}$).[44,51] By applying hybrid density functional calculations, Wang *et al.*[42,50] reported that the energy levels describing the possible PL transitions involving these charge states are all located in the band gap and can be associated with the radiative decay of electrons from the vacancy states (V_O^0 or V_O^+) to the VB, according to:

$$V_O^0 \rightarrow V_O^+ + e_{VB}^- + h\nu \qquad EQ\ 9.4$$

$$V_O^+ \rightarrow V_O^{2+} + e_{VB}^- + h\nu \qquad EQ\ 9.5$$

Because the energy level of V_O^0 is predicted to be closer to the CB than the V_O^+ level, the PL emission bands at *ca.* 490 nm (2.53 eV) and 550 nm (2.21 eV) can be attributed to the transitions in EQ 9.4 and EQ 9.5, respectively. Finally, the band at 560 nm, that appears more intense in the case of 2L(3+1.7 Pa), can be tentatively attributed to a localized increase of V_O^+ levels due to the formation of a depletion layer at the heterojunction, consequent to band alignment at the interface.

The presence of W^{5+} was confirmed by XPS analysis (Figure 9.10 and 9.11). Indeed, the XPS spectra in the W *4f* binding energy region (Figure 9.10a) of all coatings were fitted as the convolution of two W $4f_{7/2}$–W $4f_{5/2}$ doublets, with the main peaks centered at 34.7 eV and 35.9 eV, originating from W^{5+} and W^{6+}, respectively.

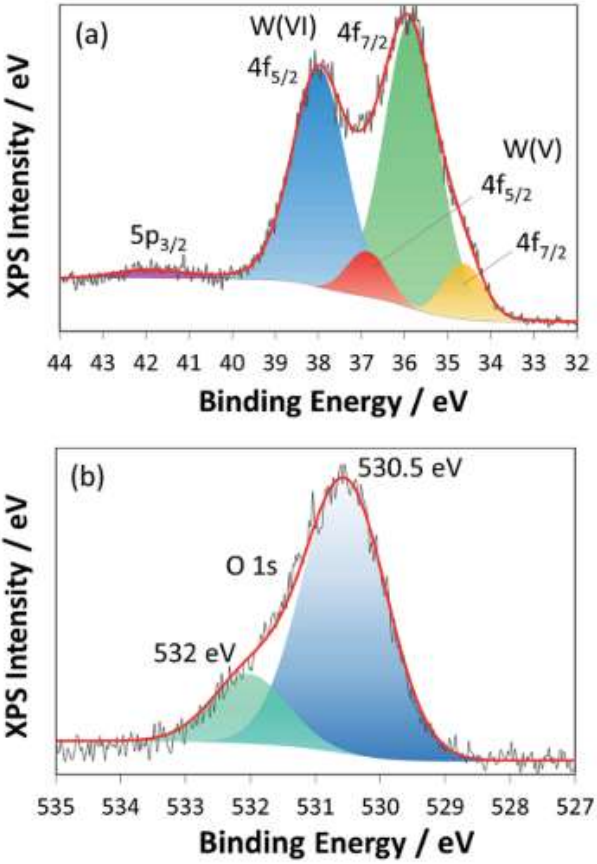

Figure 9.10 *Experimental (grey line) and fitted (red line) XPS spectra of the used 2L(3+1.7 Pa) sample (i.e. measured after the 12 h-long irradiation water splitting test) in the (a) W 4f and (b) O 1s binding energy regions. The fitting was performed using a Shirley background.*

The spin–orbit spacing and the area ratio of both doublets were constrained to 2.18 eV and 4 : 3, respectively.[51,52] The oxygen *1s* region (Figure 9.10b) shows a main peak located at 530.5 eV, due to structural oxygen in WO_3, and a minor one at 532 eV, assigned to oxygen in surface hydroxyl groups (or adsorbed water). The elemental analysis (Table 9.2) shows that in all samples the O : W atomic ratio is under-stoichiometric. The 1L(1.7 Pa) sample possesses a lower O : W atomic ratio (*i.e.* more O vacancies) than 1L(3 Pa), in line with the larger density of donors N_D calculated from the Mott–Schottky plot.

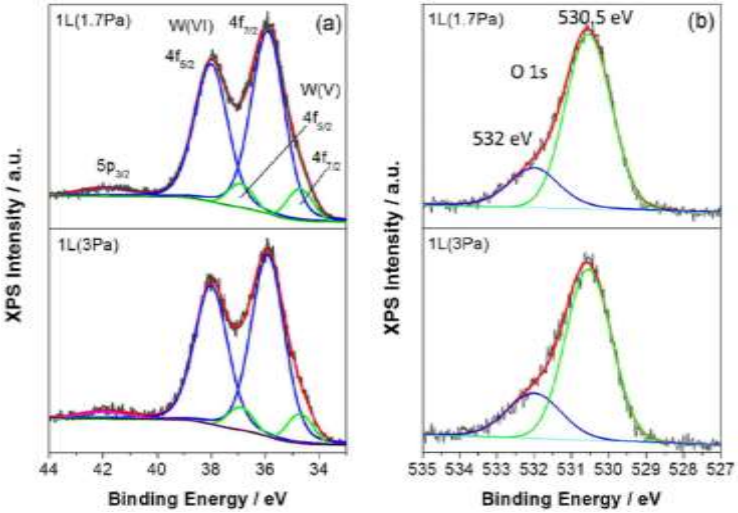

Figure 9.11 *Experimental (grey line) and fitted (red line) XPS spectra of used 1L(1.7 Pa) and 1L(3 Pa) (i.e. measured after the 12 h-long irradiation water splitting test) in the (a) W 4f and (b) O 1s binding energy regions. In (a) the convoluted W $4f_{7/2}$–W $4f_{5/2}$ doublets of W(VI) (blue lines) and of W(V) (green lines) are also shown. The fitting was performed using a Shirley background.*

Table 9.2 *Results of the XPS analysis of used coatings: oxygen to tungsten atomic ratio, percent of W(V) and percent of oxygen as OH moieties*

Sample	O : W at. ratio	% W(V)	% OH
1L(1.7Pa)	2.64	9.6	19.0
1L(3Pa)	2.72	9.2	24.8
2L(3+1.7 Pa)	2.70	11.1	19.8

9.3.2. PEC results

9.3.2.1. IPCE

All IPCE curves of the investigated coatings exhibit an activity onset below 450 nm in agreement with the calculated E_g from the UV-vis DRS spectra. The IPCE curves recorded under hydrogen evolution conditions (1.0 V *vs.* SCE and pH 7) confirm the narrower band gap of the coating deposited at higher pressure (Figure 9.12). Moreover, 1L(3 Pa) shows a slightly higher efficiency than 1L(1.7 Pa), likely due to its larger surface area (Table 9.1). The efficiency of the 2L(3+1.7 Pa) photoanode is significantly higher than those of the single layer photoanodes, despite the similar surface area and photoactive film thickness (Figure 9.13). It is noteworthy that the IPCE considerably increases after the PEC water splitting test (*i.e.*, after 6 h-long irradiation) and the maximum efficiency shifts towards longer wavelengths, *i.e.* from 330 nm to 360 nm. This phenomenon is very likely due to the decrease of the oxygen vacancies (*i.e.*, crystal defects) occurring during irradiation, which can act as electron–hole pair recombination centres (see Section 3.2.3).

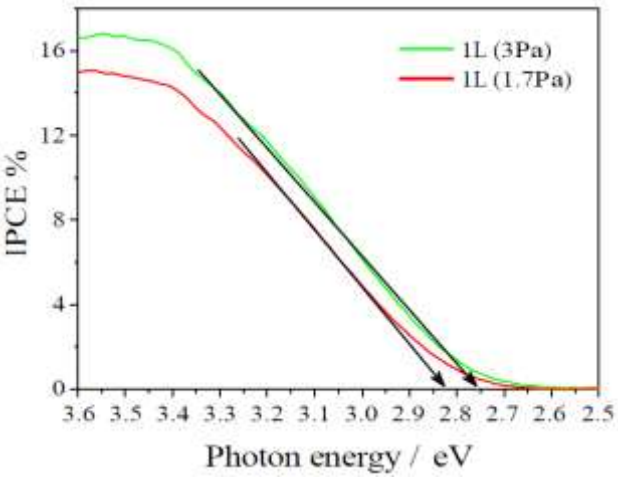

Figure 9.12 *Evaluation of the bandgap energy of 1L(3 Pa) and 1L(1.7 Pa) from the IPCE curves measured at 1.0 V vs. SCE in 0.5 M Na_2SO_4 (pH 7) after the 6 h-long photocatalytic water splitting test, confirming the narrower E_g of the WO_3 coating deposited at higher pressure.*

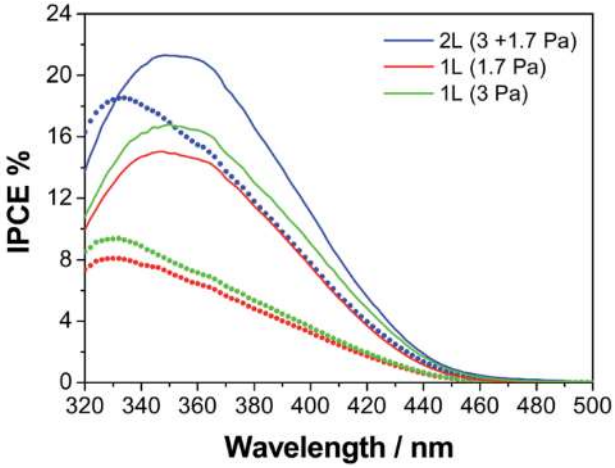

Figure 9.13 *Incident photon to current efficiency (IPCE) curves of the investigated WO_3 sputtered photoanodes measured at 1.0 V vs. SCE in 0.5 M Na_2SO_4, before (dotted line) and after (solid line) the 6 h-long photocatalytic water splitting tests.*

9.3.2.2. *Polarization curves*

Figure 9.14 shows the polarization curves from −0.1 V to 1.6 V *vs.* SCE range, performed over the compact 1L_calc (Figure 9.14a) and 2L(3+1.7 Pa) (Figure 9.14b) photoanodes, either under continuous or chopped irradiation. The photocurrent potential onset above 0.05 V (*i.e.* 0.29 *vs.* SHE) is in agreement with the flat band potential calculated from the Mott–Schottky plot. Two main differences can be noticed by comparing Figure 9.14a and b: (i) under continuous irradiation the porous double-layer sputtered WO_3 photoanode reaches a saturated photocurrent density of 1.6 $mA \cdot cm^{-2}$ at *ca.* 0.8 V; (ii) the photocurrent recorded under chopped light with 2L(3+1.7 Pa) significantly exceeds that measured under continuous irradiation. In contrast, the compact 1L_calc photoanode generates a lower photocurrent that continuously increases without reaching saturation, and the photocurrent under chopped light matches that measured under continuous irradiation.

The superior photoactivity of porous WO_3 films with respect to compact ones has already been reported.[1,11,53,54] Pros and cons can be recognized in nanostructured photoelectrodes. The advantages of porous coatings are: (i) larger surface area providing more active sites for reactant adsorption and charge transfer; and (ii) shorter carrier collection pathways to the surface, with a lower probability of electron–hole pair recombination. Moreover, the shorter diffusion path requires a lower potential for extraction of bulk holes to the surface, allowing to reach the saturated photocurrent density over the porous film. On the other hand, the main disadvantage of nanocrystalline porous coatings is the slower charge transport by diffusion compared to the faster drift occurring bulk films.[55,56]

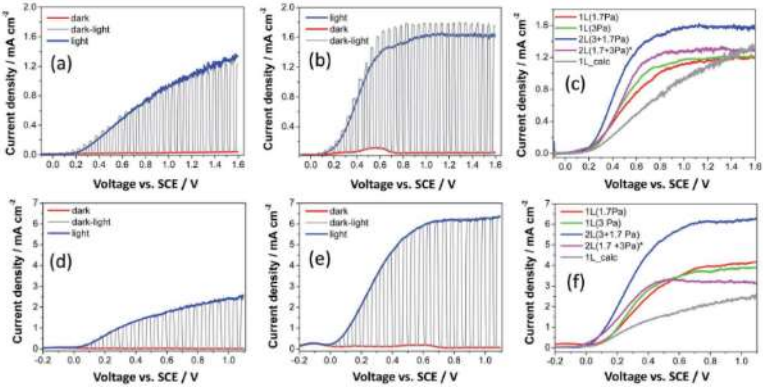

Figure 9.14 *Polarization curves in (a–c) 0.5 M Na_2SO_4 and (d–f) 0.5 M Na_2SO_4 + 1.2 M CH_3OH aqueous solution; 9.6 cm^2 photoanode irradiated area, sweep rate 5 $mV \cdot s^{-1}$, recorded with the (a and d) 1L_calc WO_3 and (b and e) 2L(3+1.7 Pa) photoanodes in the dark (red line); chopped light irradiation with 10 s light/dark cycles (grey line), and full irradiation (blue curve). (c and f) Photocurrent density curves measured under full irradiation with all investigated photoanodes. All measurements were performed on used photoanodes (i.e. after the 6 h-long photocatalytic water splitting tests). *Inverted heterojunction.*

The additional barrier at the interparticle interface further hampers charge diffusion. Because electrons and holes under polarization migrate towards opposite directions, both phenomena increase the recombination probability. This explains the moderately higher photocurrent density of porous photoanodes compared to the compact one, despite the more than one order of magnitude larger surface area (*ca.* 300 cm^2 for each porous electrode, see Table 9.1, to be compared with 14.5 cm^2 for the compact one). Finally, as expected from the IPCE curves, the 2L(3+1.7 Pa) photoanode produces a 30% higher saturated photocurrent than the single layer coating (Figure 9.14c), in spite of the similar film thickness and surface area. It is also noteworthy that a lower saturated photocurrent value is attained with the 2L(1.7+3 Pa) inverted heterojunction, compared

to the 2L(3+1.7 Pa). Also in this case the net difference in photocurrent cannot be attributed to a difference in the active area (280 cm^2 *vs.* 293 cm^2, respectively).

9.3.2.3. *PEC water splitting results*

Hydrogen and oxygen evolution vs. irradiation time and the photocurrent density profile recorded at 1.0 V *vs.* SCE and pH 7 during the photocatalytic water splitting tests are presented in Figure 9.15 and Table 9.3. The photocurrent density significantly increased during the first irradiation hour over all fresh coatings, while steady state conditions (*i.e.* stable photocurrent and linear gas evolution) were reached only after the second hour. During this transient period, which appears to be shorter for 2L(3+1.7 Pa) than for the 1L photoelectrodes, the "extra current" is very likely generated by a photo-assisted partial oxidation of the highly defective WO_{3-x} coating, such as:

$$(W^{5+}/V_O^0/W^{5+}) + H_2O \xrightarrow{h\nu} (W^{6+} - O - W^{6+}) + 2H^+ + 2e^- \quad EQ\ 9.6$$

Table 9.3 *PEC water splitting results in 0.5 M Na_2SO_4 and 1.0 V vs. SCE external bias, under 19.7 mW·cm^{-2} irradiation. η_F = faradaic efficiency (* Inverted heterojunction).*

Sample	**Production rate (μmmol·h^{-1})**		r_{H_2}/r_{O_2}	η_F
	H_2	**O_2**		
1L(1.7 Pa)	153.9	63.7	2.4	85.6%
1L(3 Pa)	155.6	72.4	2.2	89.8%
2L(1.7+3 Pa)*	178.9	67.7	2.6	80.8%
2L(3+1.7 Pa)	187.6	93.2	2.01	93.3%

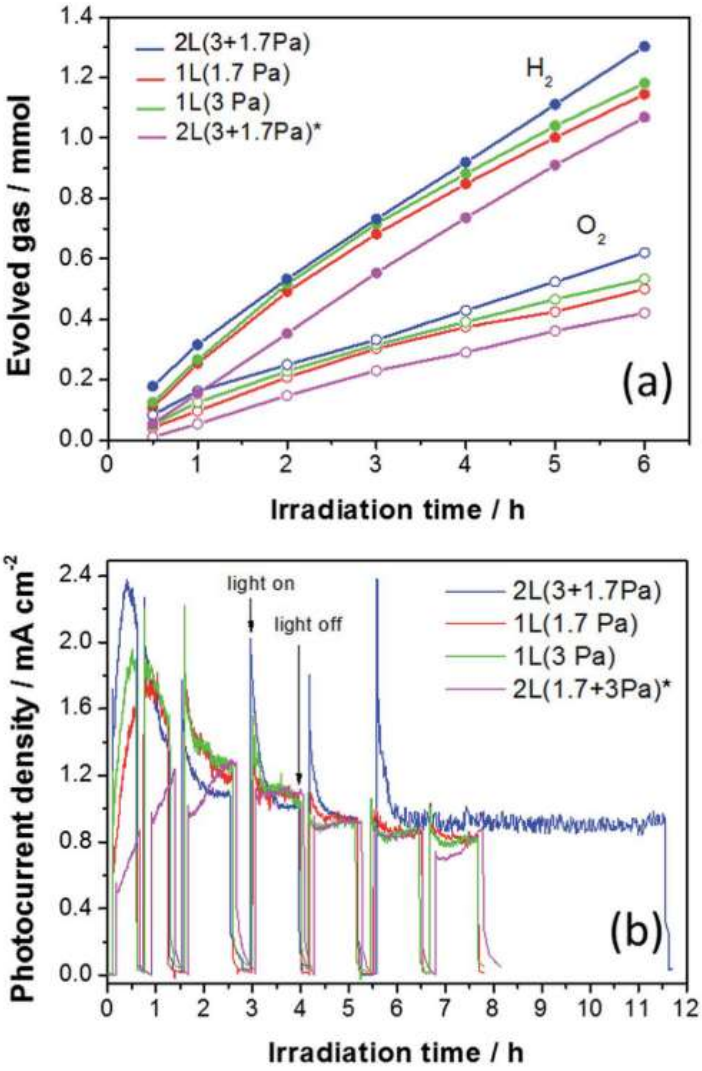

Figure 9.15 *Photocatalytic water splitting results obtained with the sputtered WO_3 photoanodes in 0.5 M Na_2SO_4 at 1.0 V vs. SCE and 9.6 cm^2 irradiated area. (a) Cumulative H_2 and O_2 gas evolution, (b) photocurrent density vs. time recorded during the tests. During the evolved gas measurement, the light was shuttered causing the photocurrent drop. *Inverted heterojunction.*

This hypothesis is corroborated by three experimental observations: *i*) the H_2 to O_2 mole ratio during this period is larger (*ca.* 2.6) than during the following stationary period (Table 9.2); *ii*) The intensity of the PL emission spectra after the 6h-long photocatalytic tests considerably suppressed (Figure 6, dotted lines), accounting for a reduced number of oxygen vacancies as photoemission sites; and *iii*) the fresh photoanode exhibits a pronounced hydrophobic surface that turns hydrophilic after the 6 h-long irradiation test (Figure 9.16). Photoinduced hydrophilicity is a well-known phenomenon occurring on several metal oxides including WO_3. An increased wettability is related to an increase of surface energy due to filling surface oxygen vacancies with OH groups.[59]

Figure 9.16 *Photograph of the 4x4 cm^2 2L(3+1.7 Pa) photoanode after the photocatalytic water splitting test, rinsed with Milli-Q water. Notice that the central irradiated round shape area displays a hydrophilic character (wettable surface), while the non-irradiated remaining part retains the original hydrophobicity (nonwettable surface).*

After *ca.* two hours, both H_2 and O_2 evolved at a constant rate under irradiation (pseudo zero order kinetics). Slightly higher H_2 and O_2 production rates (r_{H_2} and r_{O_2}, respectively) were obtained with 1L(3 Pa) possessing a larger surface area than 1L(1.7 Pa), while 2L(3+1.7 Pa) outperforms single layer samples in terms of both r_{H_2} and H_2 : O_2 mole ratio, and approaches the stoichiometric value of 2 (Table 9.3). Indeed, a very high (93%) faradaic efficiency η_F (*i.e.* the photocurrent-to-oxygen conversion efficiency)[58] was attained over this photoanode in comparison with the efficiency values reported in the literature for WO_3 thin films, usually ranging between 18% and 80%.[27,58,59] The larger H_2 to O_2 evolution rate with respect to stoichiometry is usually attributed to the side formation of H_2O_2.[58] In contrast, 2L(1.7+3 Pa) with the inverted heterojunction showed a less stable photocurrent profile along the 6 h irradiation test (Figure 9.15b), a lower hydrogen production rate and a remarkably lower faradaic efficiency (80.8%) with respect to the most performing 2L(3+1.7 Pa) photoanode.

Finally, Figure 9.15b shows that the 2L(3+1.7 Pa) photoanode also demonstrated a very high time stability, maintaining a stable photocurrent density along the 6 h continuous irradiation following the 5 h-long irradiation under shuttered conditions..

9.3.3. Electrochemical Impedance measurements

The Nyquist plots recorded at 1.0 V *vs.* SCE, in 0.5 M Na_2SO_4 and under full lamp irradiation (Figure 9.17) exhibit the typical semicircle shape, best fitted by a simplified Randles equivalent circuit $R_s(QR_{ct})$ (inset in Figure 9.17). In this model, the electrochemical reaction is limited only by the surface-mediated electron transfer and not by reactant

diffusion through the Helmholtz layer. From a qualitative point of view, the diameter of the semicircle is equal to the charge-transfer resistance (R_{ct}). Thus, the compact 1L_calc photoanode exhibits the greatest resistance, whereas the best performing 2L(3+1.7 Pa) exhibits the lowest resistance. The fitting results presented in Table 9.4 can be summarized as follows:

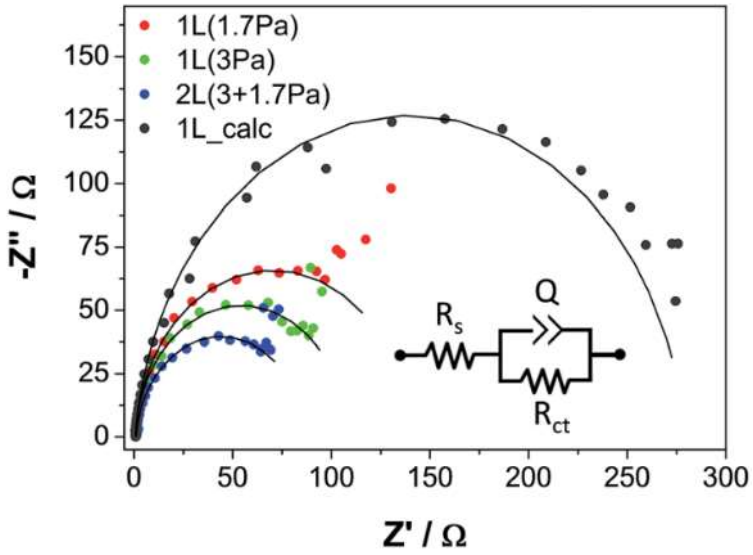

Figure 9.17 *Nyquist plots of the investigated photoanodes under 1.0 V vs. SCE potential in 0.5 M Na_2SO_4 under full lamp illumination. Experimental points (dots) fitted (solid line) by a $R_s(QR_{ct})$ equivalent circuit (inset).*

Table 9.4 *Fitting results of the electrochemical impedance spectra according to a $R_s(QR_{ct})$ equivalent circuit. The charge-transfer resistance ($R_{ct,n}$) and the capacitance (C_n) are normalized per unit electrochemically active surface area (ECSA) (* Inverted heterojunction)*

Sample	R_s (Ω)	R_{ct} (Ω)	$R_{ct,n}$ (kΩ·cm^2)	C_n (μF·cm^{-2})
1L(1.7 Pa)	0.67	139	38.7	5.7
1L(3 Pa)	0.73	107	34.9	4.7
2L(3+1.7 Pa)	1.03	86	25.2	5.3
2L(1.7+3 Pa)*	0.98	121	34.0	4.1
1L_calc	0.63	279	4.04	28

Calculated as $C = Y_0^{1/\alpha}(R_S^{-1} + R_{CT}^{-1})^{(\alpha-1)/\alpha}$ from the constant phase element Q of the impedance $Z_Q = Y_0^{-1}(j\omega)^{-\alpha}$, where ω is the angular frequency.

R_s is the series resistance accounting for all ohmic resistors (external contacts and wires, electrode sheet resistance) and the electrolyte resistance. As expected, similar values are obtained for all samples, though R_s is slightly higher for 2L(3+1.7 Pa) and 2L(1.7+3 Pa), tentatively due to the additional interface resistance between the two WO_3 sputtered layers.

Q is the constant phase element that takes into account the non-ideal behavior of the interface double layer. This pseudo-capacitance can be treated as at least two capacitors (the space-charge region C_{SC} and the Helmholtz double layer C_H) connected in series, $C^{-1} = C_{SC}^{-1} + C_H^{-1}$. The former capacitance is located at the semiconductor surface where the positive charges, in the form of ionized donors, attract the negative counter charges at the surface. This, in turn, attracts the hydrated mobile ions of the electrolyte on the liquid side creating the inner (IHP) and the outer (OHP) Helmholtz plane. However, by considering the lower carrier

density in semiconductors with respect to the electrolyte, it is possible to neglect the C_H term in the connection, so $C^{-1} \approx C_{SC}^{-1}$.

The capacitance depends on both the density of donor species (*i.e.* the charges stored in the depletion layer) and on the geometry of the electrode. Table 9.4 shows that the compact photoanode (1L_calc) has one order of magnitude greater normalized capacitance per unit area (C_n) compared to the porous sputtered photoanodes. Indeed, the compact 1L_calc is a flat electrode (it can be modelled as a parallel-plate capacitor) and it has a lower surface to volume ratio (*i.e.* larger density of positive charges per unit surface area). In contrast, the porous film can be described, in first approximation, as coaxial cylinders (to simulate the shape of pores) that notoriously have lower capacitance per unit surface than the parallel plates.

R_{ct} is the charge-transfer resistance associated with the oxidation reaction occurring at the semiconductor/electrolyte interface. R_{ct} is a very important parameter because it is inversely proportional to the rate constant of the half anodic reaction:

$$R_{ct} = \frac{\eta}{I_{ct}} = \frac{E_{appl} - E_{FB}}{nFr_{O_2}} \qquad \text{EQ 9.7}$$

where $\eta = (E_{appl} - E_{FB})$ is the potential drop in the space-charge layer, I_{ct} is the charge transfer current, *n* is the number of electrons involved in the half reaction, F is the Faraday constant, and r_{O_2} the oxygen evolution rate. The linear interpolation of R_{ct} *vs.* η/r_{O_2} of all investigated samples (Figure 9.18) gives a slope of 2.55×10^{-6} mol·C^{-1}, *i.e.* very close to the expected $(4F)^{-1} = 2.59 \times 10^{-6}$ mol·C^{-1}, proving the validity of the attribution of the R_{ct} parameter to the oxygen evolution reaction. Hence, a decrease of R_{ct}

corresponds to an increase in I_{ct} and, therefore, in r_{O_2}. In photocatalytic water oxidation, the charge transfer current is due to the reaction of surface adsorbed water, or hydroxyl groups, with photogenerated VB holes.

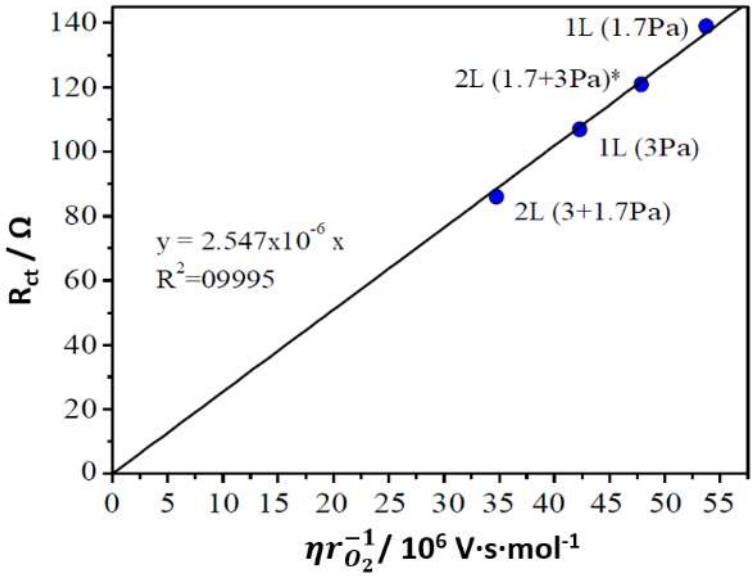

Figure 9.18 *Relation between the charge-transfer resistance (R_{ct}) and the oxygen production rate (r_{O_2}) according to Ohm's law: $R_{ct} = \eta / i_{ct} = (E_{appl} - E_{FB}) / (nFr_{O_2})$. Here, E_{appl} = 1.24 V vs. NHE, E_{FB} are those calculated with the Mott-Schottky plot, n = 4 is the number of involved electrons in the water oxidation reaction ($2H_2O \rightarrow O_2 + 4H^+ + 4e^-$) and F the Faraday constant. The slope of the straight line interpolating the experimental R_{ct} vs. η/r_{O_2} values is very close to the expected $(nF)^{-1} = 2.591x10^{-6}$. * Inverted heterojunction.*

Table 9.4 shows that the two sputtered monolayer photoanodes have similar charge transfer resistance normalized per unit area, $R_{ct,n}$, whereas the best performing 2L(3+1.7 Pa) possesses a *ca.* 30% lower $R_{ct,n}$

in agreement with the 30% greater IPCE, r_{H_2} and generated saturated photocurrent density. Indeed, a larger density of VB holes induces a more effective surface reaction with the electron donor species with the consequent increase of the I_{ct} and the decrease of charge transfer resistance (EQ 9.7). This is confirmed by the significantly larger R_{ct} of the 2L(1.7+3 Pa) inverted heterojunction with respect to that of 2L(3+1.7 Pa) because this electronic configuration cannot benefit the enhanced electron transfer. Nevertheless, the 0.1 eV difference between the CB at the interface of the inverted heterojunction introduces only a modest energy barrier to the electron transfer and in fact this sample shows an R_{ct} intermediate to those of the monolayer samples.

Finally, the EIS investigation demonstrates that the greater photocatalytic performance of the sputtered double layer photoanode can be ascribed to a larger density of reactive VB holes, due to a better photopromoted electron transfer at the n–n heterojunction, as depicted in Figure 9.19. Indeed, a larger density of VB holes induces a more effective surface reaction with the electron donor species with the consequent increase of the I_{ct} and the decrease of R_{ct} (EQ 9.7). Interestingly, 1L_calc exhibits a considerably lower $R_{ct,n}$. These results are in line with the pros and cons of compact to porous photoanodes: the compact photoanode possesses the higher intrinsic photocatalytic activity (*i.e.*, the lower $R_{ct,n}$). However, the overall photoactivity compared to the porous films is hindered by the much lower surface area.

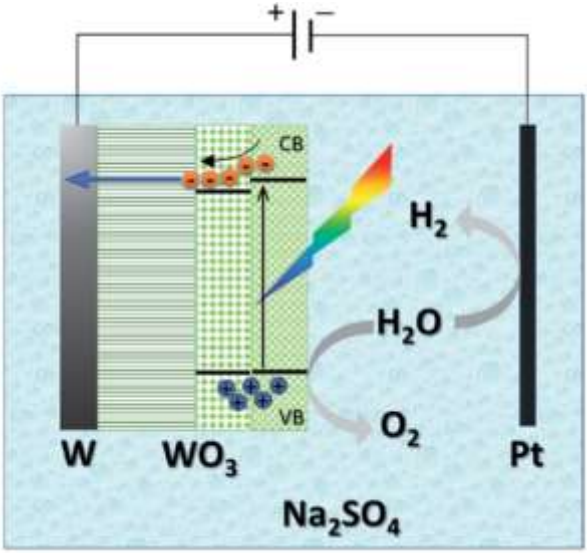

Figure 9.19 *Schematic representation of the enhanced photopromoted electron transfer at the sputtered WO_3 bilayer interface due to the formation of the n–n heterojunction.*

9.3.4. Effect of methanol addition

The photocurrent density profile measured during the photocatalytic water splitting tests (Figure 9.15b and 9.20b) showed an abrupt increase as the light was turned on, generating a photocurrent peak, particularly intense on the 2L(3+1.7 Pa) film, followed by a decrease up to a stationary photocurrent value which is almost common to all investigated photoanodes. By contrast, over the compact 1L_calc film the photocurrent density instantly reaches a stable value upon illumination. We ascribe the sharp photocurrent peak recorded with 2L(3+1.7 Pa) to the fast photopromoted electron transfer at the n–n heterojunction consequent to the shift towards higher energy of the CB of the outer layer

(Figure 9.19). Conversely, the holes are not as much promptly transferred as the electrons because the VB of the two layers lies at the same level.

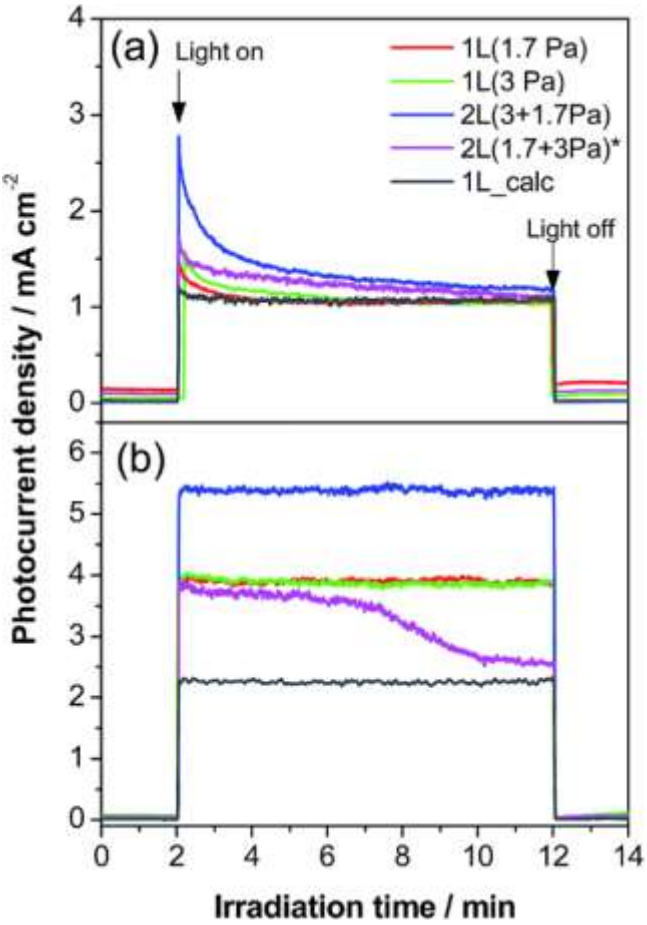

Figure 9.20 *Photocurrent density response under full lamp irradiation (9.6 cm^2 irradiated area), at 1.0 V vs. SCE of used photoanodes in (a) 0.5 M Na_2SO_4 and (b) 0.5 M Na_2SO_4 + 1.2 M CH_3OH. *Inverted heterojunction.*

Thus, the faster electron transfer at the beginning of irradiation leads to an increase of VB hole density, also due to a not equally fast hole

re-filling by the reaction with the electron donor species. This causes, on one hand, a reduced R_{ct} (*i.e.* a higher faradaic efficiency), and, on the other hand, a slight depletion of VB holes that cannot sustain the initial high photocurrent, and an increased probability of charge carrier recombination. Both phenomena are responsible for the subsequent photocurrent drop. After the initial photocurrent spike, water oxidation at the photoanode surface is the rate-determining step of the whole process. The absence of the sharp peak over both the monolayer and the inverted heterojunction samples further corroborates this interpretation.

In order to further explore this phenomenon, an additional experiment was performed with all photoanodes upon addition of 1.2 M CH_3OH to the Na_2SO_4 aqueous solution (Figure 9.14d–f and 9.20b). In fact, methanol is a more efficient hole scavenger than water. As a result, Figure 9.20b shows that no photocurrent peak appears at the beginning of irradiation, and stable and considerably higher photocurrent density values are attained with all photoelectrodes. According to previous studies on WO_3 photoelectrodes (Table 9.6), a *ca.* 2-fold increase of photocurrent density is usually attained in the presence of methanol. Besides the better ability of methanol to fill VB holes, this photocurrent density enhancement is notoriously due to the so-called current doubling effect. It is interesting to note that our reference 1L_calc sample also exhibits a 2.4-fold increase of photocurrent density upon methanol addition. In contrast, 1L(3 Pa), 1L(1.7 Pa), and 2L(1.7+3 Pa) produce a similar photocurrent density around 3.9 $mA \cdot cm^{-2}$, *i.e.* a 3.5 times improvement in the presence of methanol. The most performing 2L(3+1.7 Pa) achieves a photocurrent density of 6.3 $mA \cdot cm^{-2}$, which is *ca.* 4-fold the value attained in the absence of methanol.

Table 9.5 *Effect of methanol addition on the photocurrent density in linear voltammetry at 1.0 V vs. SCE of the investigated samples in comparison to literature data.*

Sample[ref]	**Electrolyte**	**Photocurrent density ($mA \cdot cm^{-2}$)**		**Photocurrent ratio**
		Without methanol	**With methanol**	
1L_calc	0.5 M Na_2SO_4	1.0	2.4	2.4
1L(3Pa)	0.5 M Na_2SO_4	1.2	3.9	3.3
1L(3+1.7 Pa)	0.5 M Na_2SO_4	1.6	6.3	3.9
WO_3/W anodization[60]	1 M H_2SO_4	2.9	7.5	2.6
WO_3/FTO sol-gel[61]	1 M $HClO_4$	2.4	4.6	1.9
WO_3/FTO colloidal[62]	0.1 M H_2SO_4	1.3	3.1	2.4
WO_3/FTO colloidal[62]	0.1 M $TBAHSO_4$	2.2	3.0	1.4
WO_3/FTO sputtering[63]	0.33 M H_2SO_4	2.0	3.5	1.8
WO_3/FTOW hydrothermal[64]	0.1 M H_2SO_4	3.1	6.5	2.1

This unprecedented photocurrent increase proves that, in the case of this WO_3 n–n heterojunction-containing electrode, methanol not only has an efficient hole scavenging effect, but also boosts the effective charge carrier separation in the presence of current doubling. Moreover, the inverted heterojunction 2L(1.7+3 Pa) sample shows a deactivation along the irradiation time likely due to the lower stability of the coating, in line with our original multilayer deposition strategy, with a less dense

layer underneath a denser one, to relieve the stress and increase the coating adhesion.

9.4. Conclusions

This work demonstrates that the total pressure during WO_3 deposition by RF diode sputtering affects the position of the CB energy very likely due to the different extent of crystal structure distortion induced by oxygen vacancies. Lowering the pressure increases the oxygen vacancies and produces a shift of the CB towards higher energy. Thus, a WO_3/W bilayer photoanode possessing an equivalent n–n heterojunction has been successfully prepared by growing the two WO_3 layers at two different pressures, followed by calcination at 600 °C. The built-in electric field generated at the interface between the two WO_3 layers implies an improved photopromoted electron transfer along a downhill pathway in the CB level from the outer toward the inner layer. This leads to a decreased surface charge transfer resistance, to a stable photocurrent up to 12 hours and a 30% improvement of the PEC performance with respect to the corresponding single layer photoanodes. Because water oxidation at the photoanode surface is the rate determining step, the effect of the enhanced electron transfer at the heterojunction can be fully exploited only in the presence of methanol, due to both more efficient hole scavenging and photocurrent doubling, up to an unprecedented stable 4-fold photocurrent increase. The bilayer formation strategy presented in this work might be extended to produce photoelectrodes based on any other semiconductor material with tuneable band gap energy, opening the way to a novel effective approach towards more efficient photoelectrochemical cells.

References

1 F. E. Osterloh, *Chem. Soc. Rev.*, 2013, **42**, 2294–2320.
2 A. Kubacka, M. Fernández-García and G. Colón, *Chem. Rev.*, 2012, **112**, 1555–1614.
3 G. L. Chiarello and E. Selli, *Recent Patents Eng.*, 2010, **4**, 155–169.
4 B. D. Alexander, P. J. Kulesza, I. Rutkowska, R. Solarska and J. Augustynski, *J. Mater. Chem.*, 2008, **18**, 2298–2303.
5 K. L. Chopra, S. R. Das and M. Grätzel, *Nature*, 2001, **414**, 338–344.
6 E. Selli, G. L. Chiarello, E. Quartarone, P. Mustarelli, I. Rossetti and L. Forni, *Chem. Commun.*, 2007, 5022–5024.
7 G. L. Chiarello, C. Tealdi, P. Mustarelli and E. Selli, *Materials*, 2016, **9**, 279.
8 C. Acar and I. Dincer, *Int. J. Hydrogen Energy*, 2016, **41**, 7950–7959.
9 C. A. Bignozzi, S. Caramori, V. Cristino, R. Argazzi, L. Meda and A. Tacca, *Chem. Soc. Rev.*, 2013, **42**, 2228–2246.
10 Y. Xu and M. A. A. A. Schoonen, *Am. Mineral.*, 2000, **85**, 543–556.
11 H. Zheng, J. Z. Ou, M. S. Strano, R. B. Kaner, A. Mitchell and K. Kalantar-zadeh, *Adv. Funct. Mater.*, 2011, **21**, 2175–2196.
12 M. Zhang, C. Yang, W. Pu, Y. Tan, K. Yang and J. Zhang, *Electrochim. Acta*, 2014, **148**, 180–186.
13 L. Xia, J. Bai, J. Li, Q. Zeng, X. Li and B. Zhou, *Appl. Catal. B Environ.*, 2016, **183**, 224–230.
14 J. Zhang, Z. Z. Liu and Z. Z. Liu, *ACS Appl. Mater. Interfaces*, 2016, **8**, 9684–9691.
15 J. Zhang, H. Ma and Z. Liu, *Appl. Catal. B Environ.*, 2017, **201**, 84–91.
16 H. Qi, J. Wolfe, D. Wang, H. J. Fan, D. Fichou and Z. Chen, *Nanoscale*, 2014, **6**, 13457–13462.
17 Y. Yamada, K. Tabata and T. Yashima, *Sol. Energy Mater. Sol. Cells*, 2007, **91**, 29–37.
18 V. S. Vidyarthi, M. Hofmann, A. Savan, K. Sliozberg, D. König, R. Beranek, W. Schuhmann and A. Ludwig, *Int. J. Hydrogen Energy*, 2011, **36**, 4724–4731.
19 B. Cole, B. Marsen, E. Miller, Y. Yan, B. To, K. Jones and M. Al-Jassim, *J. Phys. Chem. C*, 2008, **112**, 5213–5220.
20 B. Marsen, E. L. Miller, D. Paluselli and R. E. Rocheleau, *Int. J. Hydrogen Energy*, 2007, **32**, 3110–3115.
21 M. Pedroni, M. Canetti, G. L. Chiarello, A. Cremona, F. Inzoli, S. Luzzati, S. M. Pietralunga, A. Tagliaferri, M. Zani and E. Vassallo, *Thin Solid Films*, 2016, **616**, 375–380.
22 T. Karabacak, C. R. Picu, J. J. Senkevich, G.-C. C. Wang and T.-M. M. Lu, *J. Appl. Phys.*, 2004, **96**, 5740–5746.
23 E. Vassallo, R. Caniello, M. Canetti, D. Dellasega and M. Passoni, *Thin Solid Films*, 2014, **558**, 189–193.
24 P. J. Kelly and R. D. Arnell, *Vacuum*, 2000, **56**, 159–172.

25 G. Bräuer, B. Szyszka, M. Vergöhl and R. Bandorf, *Vacuum*, 2010, **84**, 1354–1359.
26 S. Trasatti and O. A. Petrii, *Pure Appl. Chem.*, 1991, **63**, 711–734.
27 X. Feng, Y. Chen, Z. Qin, M. Wang and L. Guo, *ACS Appl. Mater. Interfaces*, 2016, **8**, 18089–18096.
28 R. Beranek, *Adv. Phys. Chem.*, 2011, **2011**, 80–83.
29 S. P. Harrington and T. M. Devine, *J. Electrochem. Soc.*, 2008, **155**, C381–C386.
30 G. J. Brug, A. L. G. van den Eeden, M. Sluyters-Rehbach and J. H. Sluyters, *J. Electroanal. Chem. Interfacial Electrochem.*, 1984, **176**, 275–295.
31 G. L. Chiarello, A. Zuliani, D. Ceresoli, R. Martinazzo and E. Selli, *ACS Catal.*, 2016, **6**, 1345–1353.
32 P. M. Woodward, A. W. Sleight and T. Vogt, *J. Phys. Chem. Solids*, 1995, **56**, 1305–1315.
33 E. Cazzanelli, *Solid State Ionics*, 1999, **123**, 67–74.
34 H. R. Wenk and P. Van Houtte, *Reports Prog. Phys.*, 2004, **67**, 1367–1428.
35 C. C. L. McCrory, S. Jung, J. C. Peters and T. F. Jaramillo, *J. Am. Chem. Soc.*, 2013, **135**, 16977–16987.
36 J. O. Bockris, *J. Electrochem. Soc.*, 1984, **131**, 290–302.
37 T. Kubo, *J. Electrochem. Soc.*, 1998, **145**, 1729–1734.
38 A. Rougier, F. Portemer, A. Quédé and M. El Marssi, *Appl. Surf. Sci.*, 1999, **153**, 1–9.
39 E. Washizu, A. Yamamoto, Y. Abe, M. Kawamura and K. Sasaki, *Solid State Ionics*, 2003, **165**, 175–180.
40 M. B. Johansson, B. Zietz, G. A. Niklasson and L. Österlund, *J. Appl. Phys.*, 2014, **115**, 213510.
41 K. Hong, J. H. Son, S. Kim, B. H. Koo and J.-L. Lee, *Chem. Commun.*, 2012, **48**, 10606–10608.
42 F. Wang, C. Di Valentin and G. Pacchioni, *Phys. Rev. B*, 2011, **84**, 073103.
43 F. Wang, C. Di Valentin and G. Pacchioni, *ChemCatChem*, 2012, **4**, 476–478.
44 F. Wang, C. Di Valentin and G. Pacchioni, *J Phys Chem C*, 2012, **116**, 8901–8909.
45 R. Chatten, A. V. Chadwick, A. Rougier and P. J. D. Lindan, *J. Phys. Chem. B*, 2005, **109**, 3146–3156.
46 J. Liqiang, Q. Yichun, W. Baiqi, L. Shudan, J. Baojiang, Y. Libin, F. Wei, F. Honggang and S. Jiazhong, *Sol. Energy Mater. Sol. Cells*, 2006, **90**, 1773–1787.
47 G. D. Gilliland, *Mater. Sci. Eng. R Reports*, 1997, **18**, 99–399.
48 W. Wang, A. Janotti and C. G. Van de Walle, *J. Mater. Chem. C*, 2016, **4**, 6641–6648.
49 S. K. Deb, *Sol. Energy Mater. Sol. Cells*, 2008, **92**, 245–258.

50 C. Di Valentin, F. Wang and G. Pacchioni, *Top. Catal.*, 2013, **56**, 1404–1419.
51 Y. Baek and K. Yong, *J. Phys. Chem. C*, 2007, **111**, 1213–1218.
52 G. Orsini and V. Tricoli, *J. Mater. Chem.*, 2011, **21**, 14530–14542.
53 K. R. Reyes-Gil, C. Wiggenhorn, B. S. Brunschwig and N. S. Lewis, *J. Phys. Chem. C*, 2013, **117**, 14947–14957.
54 C. Santato, M. Ulmann and J. Augustynski, *Adv. Mater.*, 2001, **13**, 511–514.
55 A. Hagfeldt and M. Grätzel, *Chem. Rev.*, 1995, **95**, 49–68.
56 J. Bisquert and V. S. Vikhrenko, *J. Phys. Chem. B*, 2004, **108**, 2313–2322.
57 L. Zhang, R. Dillert, D. Bahnemann and M. Vormoor, *Energy Environ. Sci.*, 2012, **5**, 7491–7507.
58 W. Kim, T. Tachikawa, D. Monllor-Satoca, H. Kim, T. Majima and W. Choi, *Energy Environ. Sci.*, 2013, **6**, 3732–3739.
59 S. Hilaire, M. J. Süess, N. Kränzlin, K. Bieńkowski, R. Solarska, J. Augustyński and M. Niederberger, *J. Mater. Chem. A*, 2014, **2**, 20530–20537.
60 V. Cristino, S. Caramori, R. Argazzi, L. Meda, G. L. Marra and C. A. Bignozzi, *Langmuir*, 2011, **27**, 7276–7284.
61 C. Santato, M. Ulmann and J. Augustynski, *J. Phys. Chem. B*, 2001, **105**, 936–940.
62 V. Cristino, S. Marinello, A. Molinari, S. Caramori, S. Carli, R. Boaretto, R. Argazzi, L. Meda and C. A. Bignozzi, *J. Mater. Chem. A*, 2016, **4**, 2995–3006.
63 D. V. Esposito, J. G. Chen, R. W. Birkmire, Y. Chang and N. Gaillard, *Int. J. Hydrogen Energy*, 2011, **36**, 9632–9644.
64 F. Amano, M. Tian, B. Ohtani and A. Chen, *J. Solid State Electrochem.*, 2012, **16**, 1965–1973.

Chapter adapted from "G. L. Chiarello, M. Bernareggi, M. Pedroni, M. Magni, S. M. Pietralunga, A. Tagliaferri, E. Vassallo and E. Selli, *J. Mater. Chem. A*, 2017, **5**, 12977–12989" and reproduced with Editor's permission. doi.org/10.1039/C7TA03887A

Chapter 10:
OPERATIONAL PARAMETERS FOR WO_3 DEPOSITION BY MAGNETRON SPUTTERING

10.1. Introduction

Tungsten trioxide is considered an interesting material, not only as a suitable photocatalyst alternative to titanium dioxide, as discussed in Chapter 7, but also for its intriguing opto-electrical properties. Indeed, its electrochromic, photochromic, gas sensing and photocatalytic properties can be easily exploited when WO_3 is present in thin film form.[1–3] Electrochromic devices find their application in smart windows and displays.[4,5] They are usually applied to increase the energetic efficiency of the buildings where they are installed, since they provide curtailing effects (limiting the air conditioning usage). Being reversible, they can be easily controlled by varying the potential applied to the device.[1]

The other main application of these films is gas sensing.[6–8] This is a critical process in all human activities, from health monitoring to industrial processes and environmental protection. In this context, WO_3 already proved to be highly sensitive to pollutants such as NO_x,[6,8,9] H_2S,[10] NH_3[11] or O_3.[12] Crystallinity, high surface area and porosity are the main requirements in these field.[1,13] Additionally, having a high-potential valence band, it has already demonstrated to be a good photocatalyst for oxidation reactions, stable under a wide range of pH and potentials. This

latter characteristic allows also to exploit WO_3 for hydrogen production reactions.[14]

Pulsed Direct Current Magnetron Sputtering (pDC-MS) is a well-established technique for the deposition of thin films and coatings over a wide range of substrates, either flat regular surfaces or complex objects.[15,16] This technique proved to be a suitable alternative to Radio Frequency Magnetron Sputtering (RF-MS) for the deposition of semiconductor oxides[17–21] and also polymers.[22–26] The optimisation of a magnetron sputtering deposition process requires the investigation of a long series of parameters, starting from the target nature through the gas pressure and composition to the sputtering power. The process control becomes even more challenging when dealing with dielectrics sputtering or reactive plasmas.[26–31] Nevertheless, thanks to the typical voltage polarity reversal, pDC-MS became a standard in the deposition of uniform coatings under a reactive environment. Indeed, as already mentioned in Chapter 8, this operational characteristic prevents the formation of stable insulating layers over the sputtered target under reactive conditions. This avoids the generation of arching phenomena, caused by insulating layer breakings, resulting in more homogeneous films.

Whereas for other materials, such as TiO_2[26,31,32] or TiN[16], several reports are present in the literature about the effect of those parameters over the physico-chemical properties of the sputtered films, for WO_3, to the best of our knowledge, only few of them has been investigated in details so far.

Following the research line opened with the work reported in Chapter 9, several tungsten trioxide thin films were sputtered on titanium foil in order to study the effect of the different deposition parameters over

the photoactivity of the material, to optimise the magnetron sputtering setup for future work. The effects were evaluated in terms of crystalline structure, band gap energy, incident photon to current efficiency and photocurrent generation. Among the two possible deposition sources, *i.e.* RF-MS and pDC-MS, the latter resulted to be the most promising one and thus the most investigated one.

10.2. Film preparation

10.2.1. Magnetron sputtering set-up

The synthesis of the various films under different experimental conditions was performed with the newly purchased magnetron sputtering (MS) system at the SmartMatLab Centre of the Department of Chemistry, Università degli Studi di Milano. The MS machine adopts a bottom-up configuration; thus, the sample holder is placed above the two targets, fixed to the bottom of the main chamber on tiltable supports. The stainless-steel chamber (30 cm diameter, 60 cm height) is connected to a vacuum system composed of a rotary pump (or backing pump, Edwards RV8) and a turbomolecular pump (high-vacuum pump, Edwards nEXT400). The turbomolecular pump is connected through a gate valve, that can be regulated to adjust the pressure within the chamber by opening or closing the valve. The pressure is monitored by two different sensors: a Pirani gauge for pressure from 1 mbar (100 Pa) down to 10^{-4} mbar (0.01 Pa) and a Penning gauge for ultra-high vacuum (10^{-7} mbar). The sample holder is fixed to the lid of the chamber. Being connected to a rotor, it is able to rotate and it is equipped with a ceramic heater and a thermocouple to perform depositions at high temperature (up to 500 °C on the sample holder). The distance of the sample holder from the sources was adjusted

to 12 cm and the two cathodes were tilted to face the substrate. The cathodes hold a 2-inch target, that can be covered by a shutter to temporarily stop the deposition process, but by keeping the plasma ignited. The two cathodes can be switched on at the same time, but with two different discharge systems: Direct Current (DC, TRUMPF, TruPlasma DC 4001) or Radio Frequency (RF, bdiscom BDS HF300 AFP). However, the type of system can be switched from a cathode to the other. Up to three gases can be flown within the chamber through three flowmeters (Bronkhorst EL-FLOW). A microbalance (Front Load Single Sensor, controlled by an INFICON SQC-310) was added to the system to monitor the deposition rate and, thus, to monitor in real-time the thickness over the sample, after proper calibration. The sensor holds a quartz monitor crystal covered by a thin gold layer.

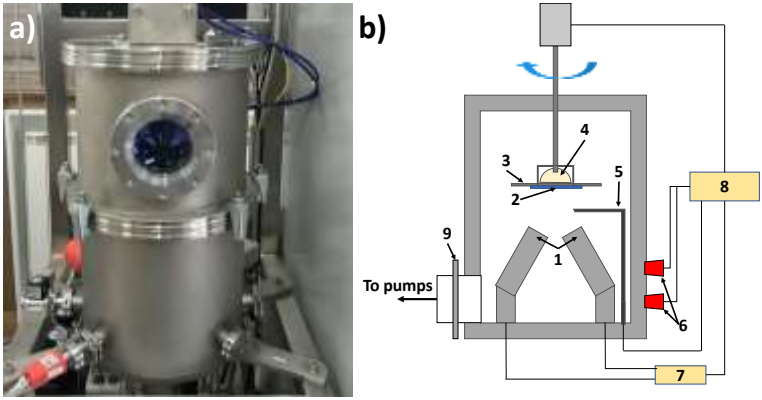

Figure 10.1 *(a) Picture and (b) sketch of the employed magnetron sputtering set-up. 1) Tiltable targets; 2) Deposition substrate; 3) Substrate holder; 4) Ceramic heater; 5) Microbalance; 6) Penning and Pirani gauges; 7) Source selector; 8) Control panel; 9) Gate valve.*

The WO_3 films were deposited over metal Ti foil (5x5 cm^2) which were previously cleaned. Three consecutive sonication treatments, in acetone, water and iso-propanol, were firstly performed to remove Ti production leftovers; then, ozonisation was applied to remove organics, and finally sonication was carried out with a pickling solution (a commercial HF/H_2O_2/surfactant in water) to remove amorphous surface TiO_x. One or four foils can be placed at once on the sample holder. Prior to any deposition, the chamber is evacuated to at least 10^{-6} mbar (base pressure); if the deposition is planned to occur on a heated substrate, the heater is switched on during this gas-evacuation step. To ensure uniformity of the deposited film, the sample holder is set to rotate at 5 rpm. Once the high vacuum condition is reached, the gate is partially closed (87%) and the gases (Ar first, then O_2, in an 80/20 ratio) are flown in the chamber. Next to the substrate, a small piece of Si foil (*ca.* 1 cm^2) was placed during every deposition to measure the thickness of the sputtered film over a completely flat substrate.

For the deposition of WO_3 thin films, several experimental parameters were investigated one at a time, keeping the others unchanged. Firstly, the effect of the deposition source was investigated. Thus, two films were deposited either with pulsed DC or RF magnetron sputtering. After selecting the best deposition source, studies over the applied power, the total gas pressure within the chamber during the sputtering process, the pulse frequency, the duty time (or pulse-off time) were investigated. Additionally, the effects of substrate heating during deposition and of an annealing post-treatment of the synthesised films were explored.

10.2.2. Characterisation and photoelectrochemical tests

XRD analyses of the synthesised samples were recorded by means of a Philips PW3020 diffractometer operating at 40 kV and 40 mA, employing the Cu Kα radiation (λ = 1.54056 Å). UV-Vis-NIR diffuse reflectance spectra were recorded with a Shimadzu UV3600 Plus spectrophotometer equipped with an ISR-603 Integrating Sphere in the 220 – 2600nm range. The thickness of the samples was determined either from the interference fringes of the UV-Vis-NIR spectra (refraction index: 2.2) or from measurements over Si substrates, employing a Bruker DektakXT contact profilometer, in the SmartMat Lab Centre.

Linear Sweep Voltammetry (LSV) electrochemical characterisation of the films was performed by using the two-compartment three-electrode cell, described in Chapter 8, filled with a Na_2SO_4 aqueous solution (0.5 M). Samples were analysed in the 0 – 1.6 V *vs.* SCE (Saturated Calomel Electrode) potential range, under dark conditions, under full irradiation (with and without AM1.5G solar simulation filter) and under chopped light conditions (the shutter was automatically opened and closed every 5 s). The results of LSV will be reported as chopped light analyses, except for the pressure investigation results that will be shown as continuous irradiation analyses, compared to a single measure performed in dark conditions. Incident Photon to Current Efficiency (IPCE) analyses were measured using the set-up described in Chapter 8. Samples were biased at 1.0 V *vs.* SCE in the same electrolyte used for LSV measurements and measured in the 300 – 550 nm range.

10.3. Results

10.3.1. Microbalance calibration

According to the microbalance calibration procedure, three main parameters, *i.e.* density, Z-ratio and Tooling factor, should be determined for accurate measurements. Z-ratio is defined as the parameter that corrects the frequency-change-to-thickness transfer function for the effects of acoustic-impedance mismatch between the crystal and the deposited material.[33] This parameter and the density of WO_3 were fixed at 1.0 and 7.16 $g \cdot cm^{-3}$, respectively. The tooling factor, instead, is the parameter used to correlate the thickness on the sensor with that on the sample holder, since the microbalance and the substrate are positioned differently within the chamber. The real tooling factor (TF) can be obtained from the following relationship:

$$TF(\%) = TF_i \left(\frac{T_m}{T_x}\right) \qquad EQ\ 10.1$$

where TF_i is the initial tooling factor, set at 100% at first, T_x is the thickness read on the microbalance and T_m is the real thickness on the substrate holder (measured with the profilometer). TF for single sample deposition resulted to be 123% and for quadruple sample holder was 99%. TF calibration was obtained by performing two different depositions with TF_i = 100%; the thicknesses over the Si substrate were averaged and used to calculate the final tooling factor. A further deposition was subsequently performed to verify, and eventually correct, the so-obtained result.

Microbalance calibration was finally confirmed by depositing a series of 3 samples with different total thickness. For instance, 250, 500 and 1000 nm tungsten trioxide films were sputtered over Ti foils.

Deposition was interrupted by closing the shutter as soon as the sensor showed the desired thickness. A piece of Si wafer was placed next to the Ti foil to compare the results. Figure 10.2 reports the films of different thicknesses (b-d) compared to a pristine Ti foil (a). The layers were sputtered under the same conditions, *i.e.* pulsed DC source at 100 W, 100 kHz, 3 µs-off time, 2 Pa total pressure (20% O_2), substrate at 200 °C.

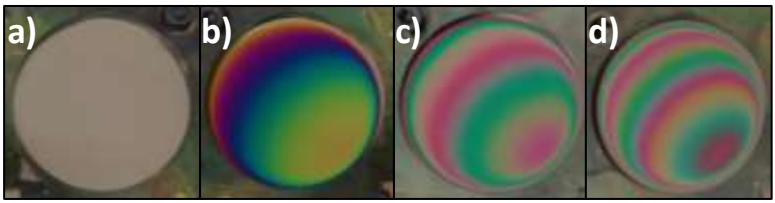

Figure 10.2 *Pictures of (a) the pristine Ti foil prior to deposition; (b) a 250 nm-thick WO_3 film; (c) a 500 nm-thick WO_3 film and (d) a 1000 nm-thick WO_3 film obtained by pDC reactive magnetron sputtering. Samples were sputtered using the quadruple sample holder.*

The different colouring is associated to the thickness of the films and depends on how the light is back-reflected by the material. Interference fringes of different amplitude can be easily observed in the UV-Vis-NIR spectra, reported in Figure 10.3, either in reflectance (Figure 10.3a) or as Tauc plot of the Kubelka-Munk transform (Figure 10.3b). As confirmed by the thickness extrapolation from these spectra, a thinner film is associated to less frequent fringes in the spectra.

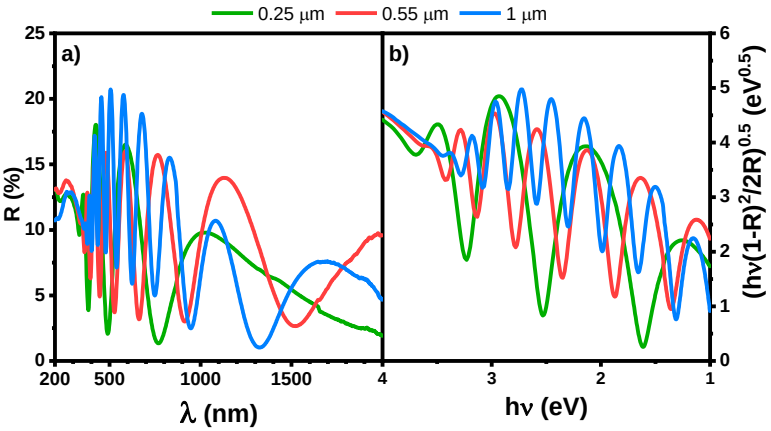

Figure 10.3 *UV-Vis-NIR spectra of three samples with different thicknesses (0.25, 0.55 and 1 μm) reported as (a) reflectance and (b) Tauc plot of the Kubelka-Munk transform.*

Table 10.1 reports the thickness values obtained by extrapolation from the UV-Vis-NIR spectra compared to those measured with the profilometer. Profilometric measurements are in good agreement with the microbalance calibration, whereas extrapolation from UV-Vis-NIR spectra using a 2.2 refraction index resulted in slightly overestimated thickness values in the case of thinner films.

Table 10.1 *Comparison of different methods to measure the sample thickness. Calibration resulted to be accurate and in good agreement with profilometer measurements.*

Thickness (μm)		
Microbalance	**UV-Vis-NIR**	**Profilometer**
0.25	0.34	0.25
0.50	0.64	0.55
1.00	1.10	1.10

10.3.2. Influence of deposition source

The different working principle, explained in Chapter 8, of Radio-Frequency (RF) and pulsed Direct Current (pDC) sputtering systems resulted in films possessing different photoelectrochemical properties. The pDC- and RF-deposited samples were sputtered by applying 100 W to the cathode under a 20% O_2/Ar plasma at 2 Pa. The substrate holder was heated to 200 °C. In the case of pDC deposition, a 100 kHz pulse frequency and 3 µs-off time were set. From the deposition profiles reported in Figure 10.4, one can observe that for both deposition sources, a stable rate is reached after *ca.* 20 min.

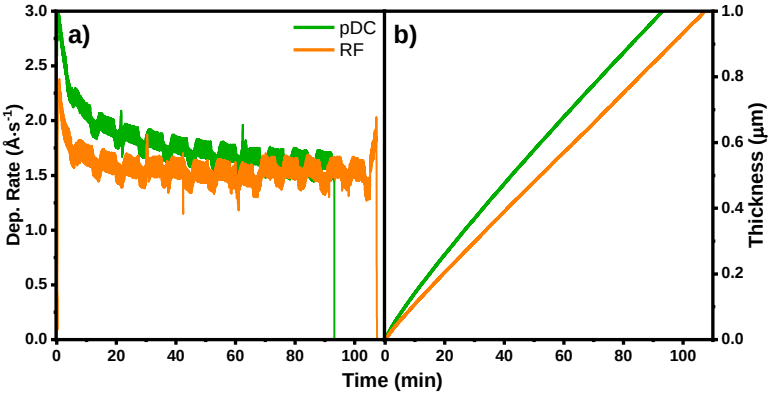

Figure 10.4 *(a) Deposition rate and (b) film thickness vs. the deposition time employing the pulsed DC (green lines) and the Radio-Frequency (orange lines) sources.*

The total thickness of 1 µm was reached in 92 min by pDC sputtering and in 108 min by the RF technique. The deposition rate attained with pulsed DC became closer to that of RF (*ca.* 1.6 Å·s^{-1}) at the end of the process. Thus, both techniques appear competitive in terms of deposition rate.

The crystalline structure of both WO_3 films is similar (Figure 10.5a), compatible with a poorly crystalline $W_{25}O_{73}$ phase (COD ID: 2106889). Thus, even under 20% O_2 condition, the as-sputtered films are slightly oxygen deficient and deposition at 200 °C does not guarantee a fully crystalline film. The sharp and intense peaks in the XRD pattern at *ca.* 40° and 55° can be attributed to the Ti foil substrate.

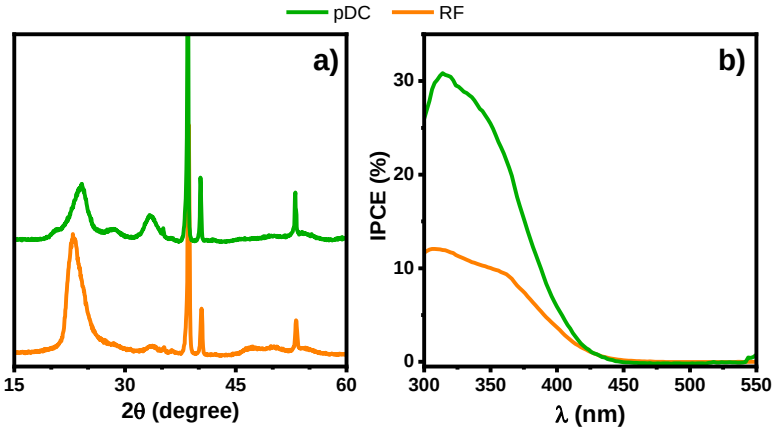

Figure 10.5 *(a) XRD patterns and (b) IPCE results of the films sputtered from different deposition sources. For both techniques, the crystalline structure appears similar, but the light exploitation ability strongly differs.*

The film sputtered by pulsed DC system exhibited a *ca.* doubled IPCE value in the whole characterisation range (300 – 550 nm). Thus, the sample sputtered by pDC sputtering appeared to be more efficient in photon conversion. Both films showed the same light absorption onset at 450 nm, corresponding to a 2.75 eV band gap.

Interestingly, the two samples showed a completely different behaviour in the LSV characterisation test. Under full lamp irradiation (without AM1.5G solar simulation filter, Figure 10.6a) the sample sputtered by pulsed DC source exhibited a much higher saturation

photocurrent density (0.8 mA·cm^{-2} starting from *ca.* 1.0 V *vs.* SCE) with respect to the sample obtained by RF sputtering (0.25 mA·cm^{-2} at the same applied bias). Under these test conditions, both samples showed the same onset bias, *ca.* 0.4 V *vs.* SCE. Interestingly, under simulated solar light (Figure 10.6b) the activity of the pDC sputtered film decreased to 0.3 mA·cm^{-2}, whereas the other photoanode was not importantly affected by the lamp spectral change (0.2 mA·cm^{-2}).

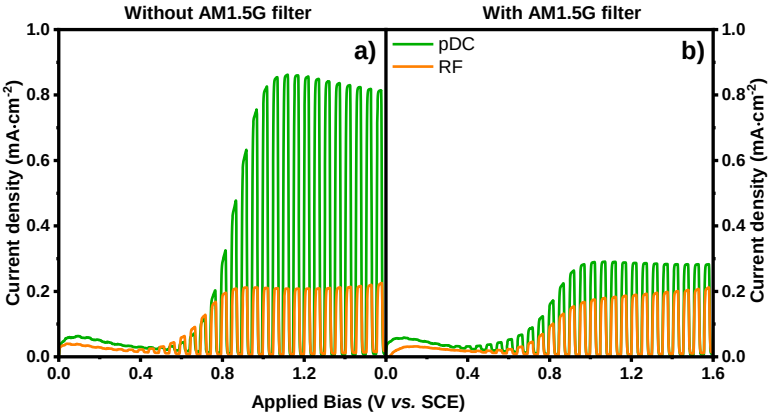

Figure 10.6 *LSV analyses on the two thin films (a) under full lamp and (b) under simulated solar light irradiation.*

The almost identical saturation photocurrents recorded with the RF-sputtered photoactive film could be attributed to poor charge transport properties and high electron-hole recombination rates. Indeed, the sample seems to be unable to effectively exploit a more energetic radiation. On the contrary, the pDC sample was not affected by the same problems, as the photocurrent density under full lamp irradiation was much larger than that observed under solar-simulated light.

These results induced us to perform a deeper investigation of pDC sputtered photoanodes in order to avoid the above-observed limitations.

10.3.3. Influence of the source power

Following the results described in paragraph 10.3.2, three different samples were sputtered by pulsed DC system by applying different power to the cathode, *i.e.* 100, 150 and 200 W. The other deposition conditions were the same for the three samples, *i.e.* 100 kHz pulse frequency, 70% duty time (3 µs-off time), 2 Pa total pressure, 20% O_2/Ar plasma, substrate heated at 200 °C, total thickness of 1 µm. As expected, the deposition rate increased with the applied power. Indeed, 1.6 Å·s^{-1} was the deposition rate with 100 W power after the first 15-20 min stabilisation, 4.5 Å·s^{-1} with 150 W power and 9.3 Å·s^{-1} with 200 W power.

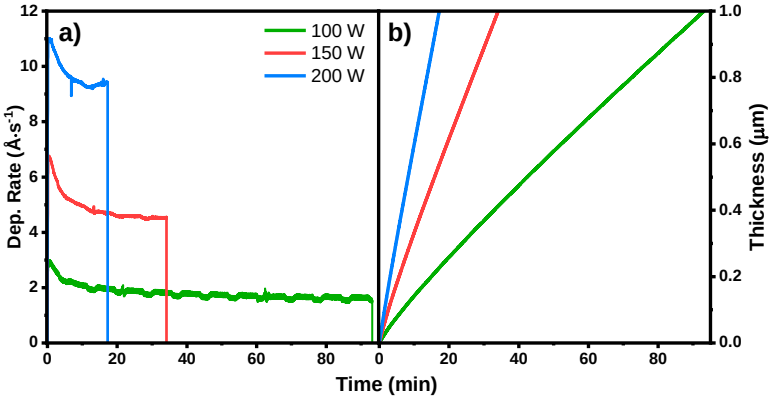

Figure 10.7 *(a) Deposition rate and (b) film thickness vs. deposition time with a 100 W (green lines), 150 W (red lines) and 200 W (blue lines) power.*

At 100 W the desired thickness was reached after 92 min, after 34 min at 150 W and after 18 min only at 200 W. Thus, the deposition rate appears to be not linearly dependent on the applied power, but a more precise study is necessary in order to discern possible variations due to the initial deposition instability.

As already observed with the samples reported in the previous section, the XRD patterns of these samples showed broad bad-defined peaks, attributable to the same $W_{25}O_{73}$ sub-stoichiometric phase of tungsten trioxide. In Figure 10.8a the XRD patterns of the two samples sputtered at 100 W and 200 W are reported.

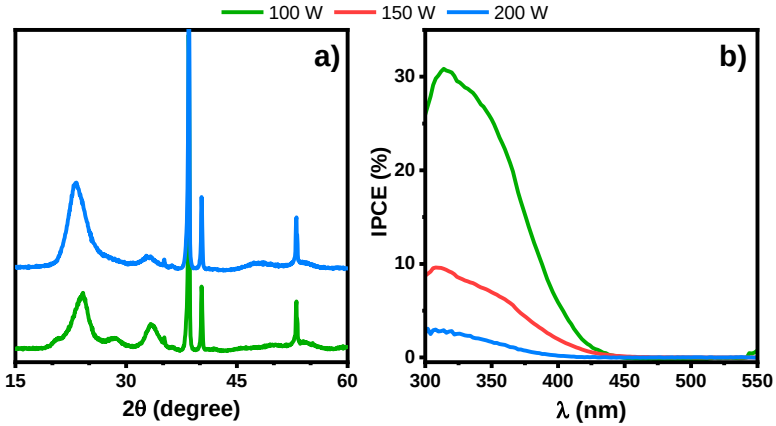

Figure 10.8 *(a) XRD patterns and (b) IPCE results of the films sputtered at 100 W (green lines), 150 W (red line) and 200 W (blue lines). Power does not affect the crystalline structure, but strongly influences the IPCE.*

The power applied to the cathode strongly influences the Incident Photon to Current Efficiency (IPCE). As the power increases, the IPCE value decreases, from *ca.* 30% for the film sputtered at 100 W to 3% for that obtained at 200 W. Additionally, the two samples sputtered at lower power exhibited a slightly red-shifted absorption edge, *i.e.* 450 nm corresponding to an energy gap of 2.75 eV, whereas the film sputtered at 200 W showed an absorption onset at 420 nm, equivalent to E_{BG} = 2.95 eV.

Together with the already highlighted poor properties, the photoanode obtained by pDC sputtering at 200 W showed no saturation

photocurrent, with an increasing photocurrent density over the whole LSV range. This behaviour, as shown in Figure 10.9, is present both under full lamp and solar light irradiation conditions and it is typical of non-porous materials.

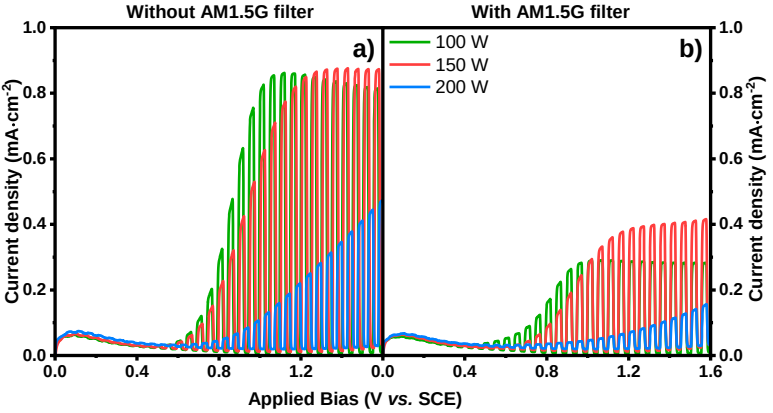

Figure 10.9 *Linear voltammetry analyses, under both (a) full lamp and (b) simulated solar light conditions, of the three samples sputtered at different powers.*

Despite the much different IPCE values, the two samples sputtered at 100 W and 150 W exhibit similar photoactivity under both type of irradiations. The photoanode obtained at 150 W showed a slightly larger saturation photocurrent density with respect to that sputtered at 100 W. However, the latter had a better photoactivity at lower potentials. For this reason, as well as for the larger IPCE, 100 W applied power was chosen as the best sputtering power among those investigated in the present work.

10.3.4. Influence of the total pressure

In the case of reactive sputtering, pressure assumes an even more important role since the deposition chamber is also filled with oxygen. As

the O_2 partial pressure increases with the total pressure, the formation of an insulating layer over the target is favoured, leading to larger number of arching phenomena, especially in the case of non-pulsed DC sputtering, or to a decreased deposition rate. Thus, the study on the effect of total pressure was coupled with the investigation of the variation in the deposition rate as a function of pressure. Indeed, all deposition lasted 1 h and were performed in the 0.5 – 5 Pa range. Sputtering power was fixed at 100 W with 100 kHz frequency and 3 μs-off time. The O_2 content in the gas was 20% for all depositions and the substrate holder was always set at 200 °C.

The data reported in Table 10.2 show that that as the pressure inside the chamber increases, the total thickness of the deposited film decreases and so does the deposition rate.

Table 10.2 *Comparison between the film thickness, measured with profilometer, and the average deposition rate for the five samples sputtered at different pressures.*

Total pressure (Pa)	**Film thickness (μm)**	**Deposition rate (Å·s^{-1})**
0.5	0.75	2.08
1	0.60	1.67
2	0.40	1.11
3	0.25	0.70
5	0.15	0.42

Thus, larger oxygen amounts within the chamber are detrimental for the deposition rate, leading to thinner films. As expected from these results, the thicker films exhibited more intense peaks in the XRD patterns. Indeed, the sample sputtered at 0.5 Pa shows a more intense main broad peak around 25°, typical of the $W_{25}O_{73}$ phase, whereas in the case

of the sample sputtered at 5 Pa that peak is barely visible (Figure 10.10a). Even in the presence of a larger oxygen amount during the deposition process, a WO_3 crystalline phase could not be reached.

Looking at the IPCE results, reported in Figure 10.10b, a bell-shaped trend of the maximum value *vs.* total pressure clearly appears. Indeed, the most efficient sample was that sputtered at 2 Pa. The film obtained at 0.5 Pa showed a very low efficiency (3% maximum at 300 nm) together with a blue shifted onset (*ca.* 375 nm). Probably, this sample was very defective and this can explain such a large band gap.

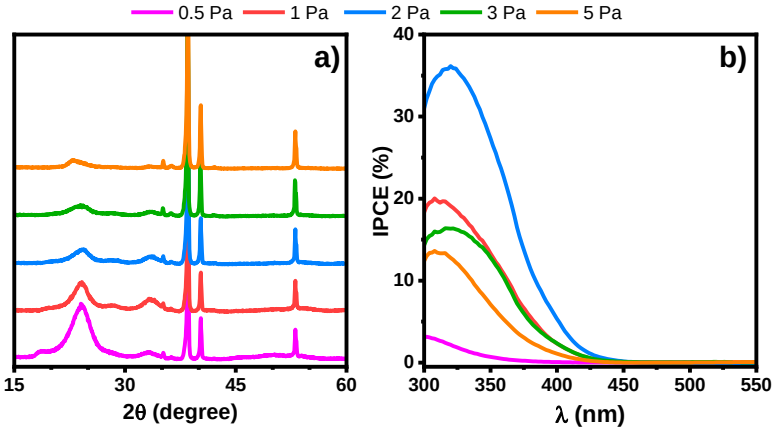

Figure 10.10 *(a) XRD patterns and (b) IPCE results of the films sputtered at different chamber pressure (0.5 – 5 Pa range). The optimal sputtering pressure, in terms of IPCE value, is 2 Pa (almost 40% IPCE).*

The sample sputtered at 5 Pa also showed a slightly blue shifted absorption edge (425 nm) with respect to the other 3 samples (450 nm). The larger efficiency reflects also on the saturation photocurrent density (*j*). The sample sputtered at 2 Pa, as shown in Figure 10.11, exhibited the highest *j* at 1.0 V *vs.* SCE, both with and without the solar simulation filter

(0.2 and 0.75 mA·cm^{-2}, respectively). The samples sputtered at 3 and 5 Pa behaved similarly to that obtained at 2 Pa, but with lower photocurrent values. Conversely, the photoanode deposited at 1.0 Pa reached higher *j* values at bias greater than 1.2 V *vs.* SCE but no photocurrent saturation was obtained, probably due to poor film porosity. As expected, the sample sputtered at 0.5 Pa exhibited a poor photocurrent density over the whole bias range, with almost no activity under simulated solar light, which is compatible with the large bang gap highlighted by IPCE measurements.

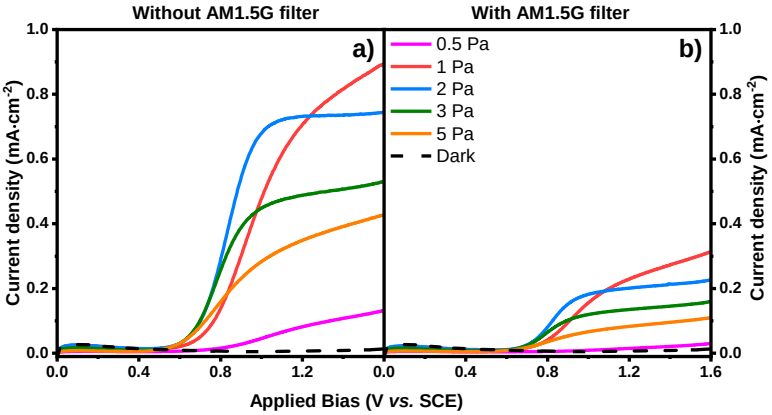

Figure 10.11 *LSV analyses of the five thin films sputtered at different total pressures, (a) under full lamp and (b) under simulated solar light irradiation.*

10.3.5. Influence of the pulse frequency

When dealing with pulsed DC magnetron sputtering, the pulse frequency, *i.e.* the frequency of the cathode polarity reversal, becomes one of the important parameters to optimise. In the case of reactive sputtering, the faster is the polarity switch and the lower is the probability of arching phenomena, since the reverse polarity breaks any insulating layer formed on the target. Two frequency were studied, *i.e.* 50 and 100

kHz. Thus, the pulse period is 20 µs in the former case and 10 µs in the latter. To be sure that in both scenarios no arching phenomena can occur, the off time was set to the maximum value allowed by the power supply at this frequency, *i.e.* at 5 µs and 3 µs, respectively. This means that the duty time, *i.e.* the effective sputtering time during the pulse period, is 15 µs at 50 kHz (75%) and 7 µs at 100 kHz (70%). A general scheme of the two pulse conditions is reported in Figure 10.12, describing a 40 µs deposition.

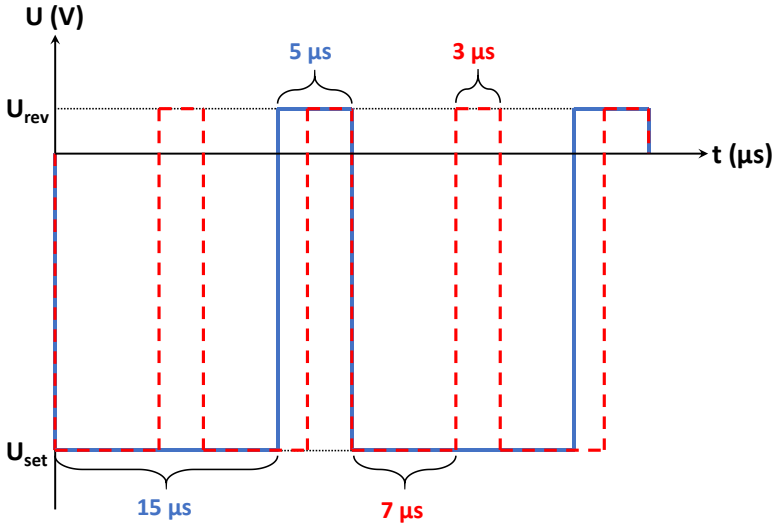

Figure 10.12 *Scheme of the two different frequencies used over 40 µs. The continuous blue line corresponds to the 50 kHz frequency, with 15 µs duty time at U_{set} (the applied voltage) and 5 µs-off time at U_{rev} (the reverse voltage typical of pDC technique). The dashed red line corresponds to the 100 kHz frequency (7+3 µs of duty and-off time, respectively).*

The blue continuous line corresponds to the 50 kHz pulse and the red dashed line to the 100 kHz pulse. Both depositions were performed at the same applied power (100 W) and, thus, the voltage automatically set

by the power supply (U_{set}) was similar, around 600 V. U_{rev} is the potential with reversed polarity applied during the pulse-off period; thus, U_{rev} is positive and corresponds to the 15% of U_{set} (*ca.* 90 V).

The samples were sputtered under 2 Pa total pressure (20% O_2), at 200 °C and by fixing the deposition time to 1 h, in order to observe differences in the sputtering rate as a consequence of frequency changes. The slightly larger duty time at 50 kHz led to a much thicker sample, *i.e.* 0.9 *vs.* 0.4 μm for 50 and 100 kHz respectively. This effect was already observed by Kelly *et al.* and explained as due to the increased importance of the "dead time", *i.e.* the time at the beginning of each pulse on cycle when there is a negligible sputtering of the target and, thus, negligible net deposition rate. The higher the frequency, the more important this "dead time" becomes with respect to the duty time.[26]

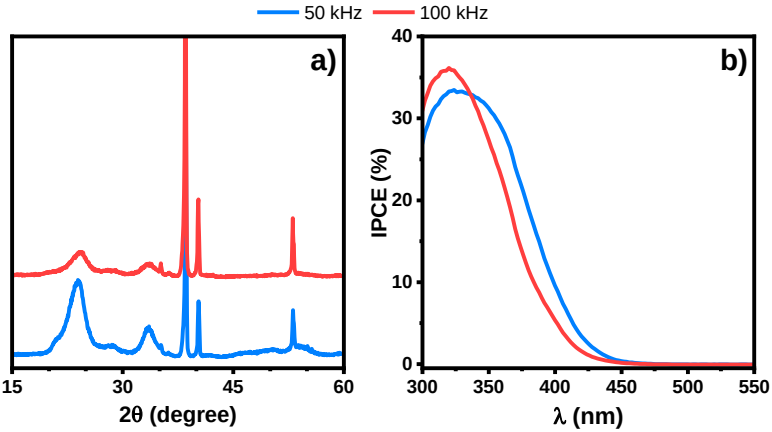

Figure 10.13 *(a) XRD patterns and (b) IPCE results of the films sputtered at different pulse frequencies (50 kHz, in blue, and 100 kHz, in red).*

The more intense peaks observed in the XRD patterns confirm the presence of a larger amount of tungsten oxide on the surface of the Ti foil in the case of the sample sputtered at lower frequency. In both cases,

peaks are broad, meaning poor crystallinity of the material, and probably corresponding to the sub-stoichiometric WO_3 phase. Additionally, the film deposited at 50 kHz exhibited a better IPCE value over the 350 – 450 nm range with respect to that obtained at higher sputtering frequency. The absorption onset of the two films is at *ca.* 450 nm (E_G = 2.75 eV).

The linear voltammetry analyses (Figure 10.14) revealed that the photoanode sputtered at lower frequency is probably more compact than the other one, since it did not show any saturation photocurrent over the analysis range. On the contrary, the sample obtained at 100 kHz exhibited a stable photocurrent density, under both full lamp and simulated solar light irradiation conditions, from 0.9 V *vs.* SCE, *i.e.* 0.65 mA·cm^{-2} and 0.18 mA·cm^{-2}, respectively.

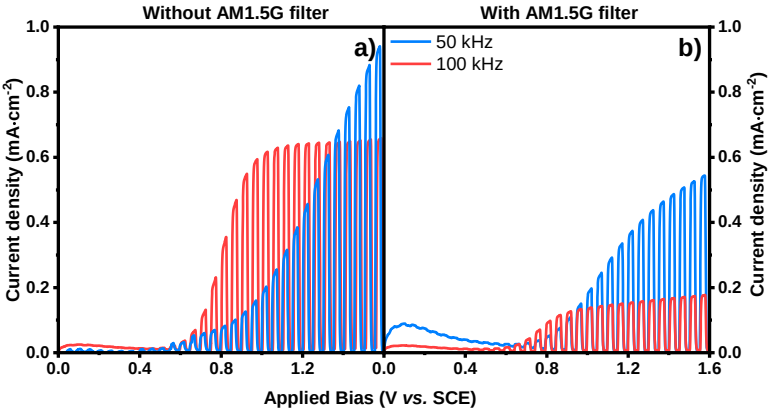

Figure 10.14 *Linear voltammetry analyses of the photoanodes sputtered at different frequencies (50 kHz in blue and 100 kHz in red), (a) under full lamp and (b) under simulated solar light irradiation.*

Thus, as in the case of applied target power, high deposition rates seem to induce the formation of poorly porous films, which are less suitable for our purposes.

10.3.6. Influence of pulse-off time

The other parameter connected to the pulse frequency is the pulse-off time, *i.e.* the period when the target potential is positive (U_{rev}). As already explained in the previous section, the sum of pulse-off time and duty time (the effective deposition time) gives the pulse period, the reciprocal of frequency. By keeping the pulse frequency fixed at 100 kHz, two pulse-off times were compared, *i.e.* 1 and 3 µs, corresponding to 90 and 70% duty time, respectively.

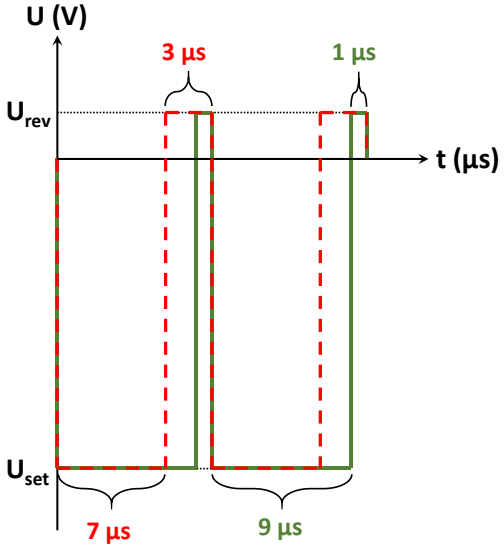

Figure 10.15 *Scheme of the two pulse-off time used over 20 µs with a 100 kHz pulse frequency. The continuous green line corresponds to the 90% duty setting (1 µs-off time), the dashed red line corresponds to the 70% duty setting (3 µs-off time).*

Figure 10.15 describes the two different settings. The dashed red lines represent the 100 kHz frequency with 70% duty time (3 µs-off time), whereas the green line shows the same frequency but with 1 µs-off time

(90% duty) over a 20 µs period. As for the previous samples, these photoanodes were sputtered at nominal 100 W, 20% O_2/Ar plasma at 2 Pa total pressure for 1 hour. As already reported[26] and expected from the longer duty time, the sample sputtered with 1 µs-off time was thicker than that sputtered with 3 µs. The two thicknesses values were 0.6 and 0.4 µm, respectively. Both XRD patterns and IPCE results (reported in Figure 10.16) did not evidence particular differences between the two samples, possessing similar poorly crystalline structure ($W_{25}O_{73}$) and analogous adsorption edges at 450 nm, corresponding to a band gap of 2.75 eV.

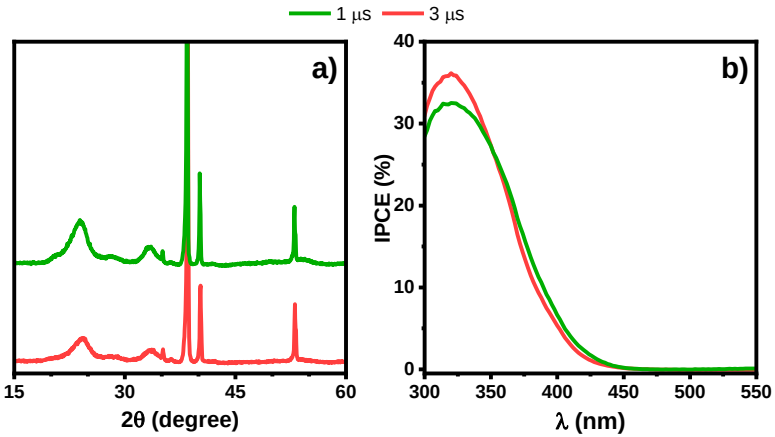

Figure 10.16 *(a) XRD patterns and (b) IPCE results of the films sputtered at different pulse-off times, 1 µs (green lines) and 3 µs (red lines), by keeping fixed the pulse frequency (100 kHz).*

Incident photon to current efficiency profiles are very similar, proving that different duty times do not affect significantly the light absorption capabilities of the sputtered materials. More important differences are instead visible looking at the LSV results reported in Figure 10.17. The sample sputtered with a longer duty time exhibited a

larger photocurrent with respect to that sputtered with 3 µs as off time, both with and without the AM1.5G solar simulation filter. However, the former photoanode did not show any saturation photocurrent in the analysis range, as the photocurrent density continuously increased without reaching a plateau. On the contrary, the film obtained by sputtering with a 70% duty time (3 µs-off time) reached a desired stable photocurrent density from 0.9 V *vs.* SCE and above under full irradiation and 0.2 V *vs.* SCE under simulated solar light.

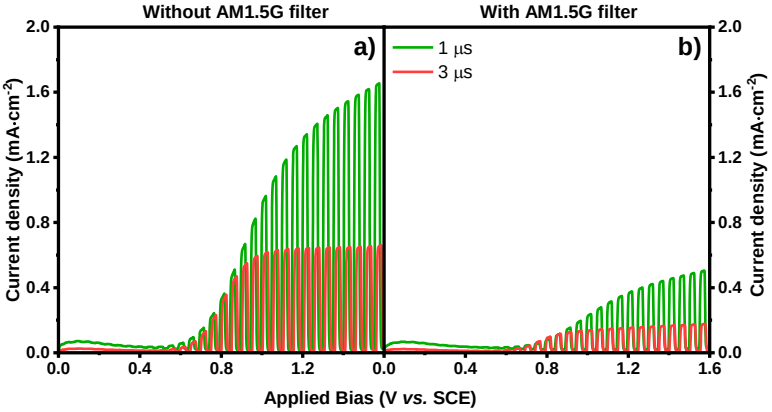

Figure 10.17 *Linear voltammetry results, under (a) both full lamp and (b) simulated solar light conditions of the samples sputtered with 90% and 70% duty time (off time 1 and 3 µs, respectively).*

10.3.7. Temperature effects

Up to this point, all depositions were performed by heating the substrate at 200 °C. The following step was aimed at verifying if active photoanodes can be obtained without heating the deposition substrate, which would allow to save energy. Coatings deposited by magnetron sputtering techniques usually possess an amorphous microstructure and

thus poor photocatalytic activity.[32] Many examples of TiO_2 coatings requiring heated substrate or annealing post-treatments are reported in literature.[34–37] Crystalline titanium dioxide can be obtained without any thermal treatments by High Power Impulse Magnetron Sputtering (HiPIMS) thanks to the much higher energy involved in the process.[26,34,38]

During the deposition process with the heater switched-off, a limited substrate heating occurred due to sputtering phenomena, raising the Ti foil temperature up to 50 – 60 °C. Except for substrate heating, the two samples were sputtered with the same settings, *i.e.* pulsed DC, 100 W, 100 kHz (70% duty time), 2 Pa (20% O_2).

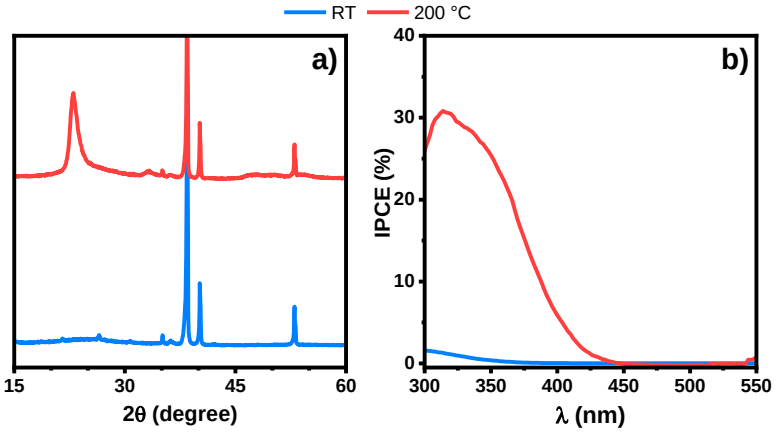

Figure 10.18 *(a) XRD patterns and (b) IPCE results obtained with the films sputtered without (blue, RT) and with (red, 200 °C) substrate heating. The former sample is not crystalline and photocatalytically active.*

The XRD patters, reported in Figure 10.18a clearly shows that heating is absolutely necessary, as in the case of TiO_2 deposition, to obtain at least partially crystallised WO_3. Indeed, the blue pattern does not show any peak except for a very broad band around $2\theta = 25°$.

The lack of crystal structure reflects over the IPCE values, which is close to zero over the 300 – 550 nm range for the sample sputtered at room temperature (RT), whereas the film deposited at 200 °C exhibited an IPCE value up to 30% in the UV range, together with a band gap of 2.75 eV (onset at 450 nm). Consequently, also the photocurrent density, reported in Figure 10.19, shows no activity at all over the whole potential range under both full lamp irradiation and solar light conditions. On the contrary, the other photoanode reported a *j* up to 0.9 from 0.9 V *vs.* SCE without AM1.5G filter and 0.3 $mA \cdot cm^{-2}$ with the solar simulation filter.

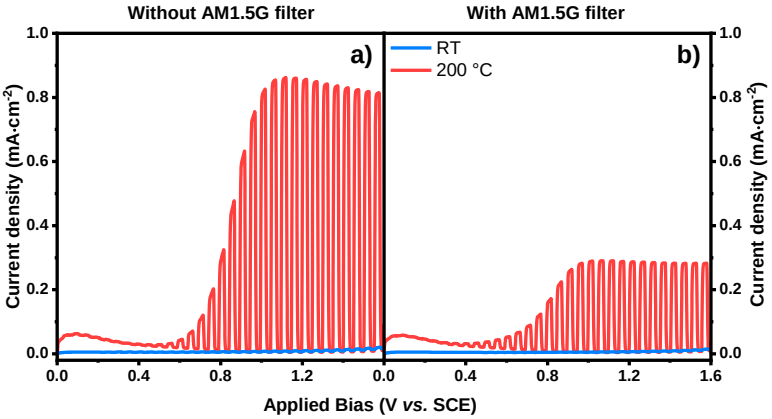

Figure 10.19 *LSV analyses of the thin films sputtered with (red) and without (blue) substrate heating, under (a) full lamp and (b) simulated solar light irradiation.*

10.3.8. Post-synthesis annealing treatment

To increase the crystallinity of the sputtered films, samples deposited at 200 °C underwent a calcination post-treatment. Two temperatures were selected: 450 °C and 600 °C. In both cases, the sputtered films were heated to the desired set point with a temperature

ramp of 10 °C·min^{-1} and then kept at that value for 2 hours before starting a natural cooldown.

The as-synthesised film shows the usual poorly crystalline sub-stoichiometric $W_{25}O_{73}$ structure, with a broad peak centred over 2θ = 22°. Upon annealing at 450 °C in air, better defined peaks appeared around 22 – 23°, which are easily attributable to the (002), (020) and (200) reflections of the WO_3 orthorhombic phase. As already discussed in Chapter 9, these peaks can be attributed either to the monoclinic or to the orthorhombic phases; considering the annealing temperature, the latter is the expected phase. The three peaks are even better defined when the film was annealed at 600 °C.

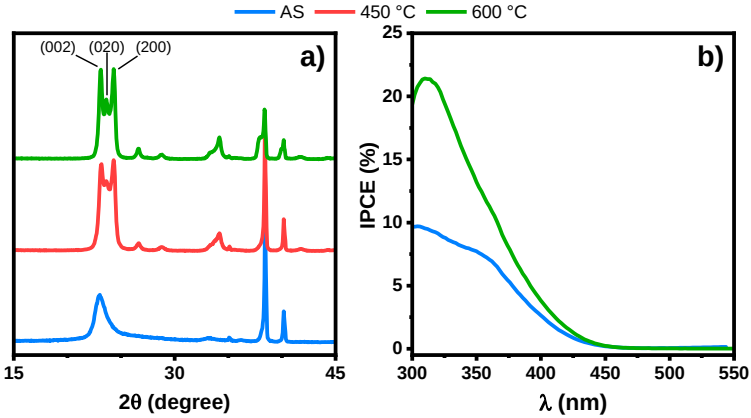

Figure 10.20 *(a) XRD patterns and (b) IPCE results of the photoanodes as-synthesised (AS, blue), after being annealed at 450 °C (red) and after calcination at 600 °C (green). The thermal treatment induces crystallisation of the oxide, leading to better IPCE values.*

As occurred with the samples reported in Chapter 9, the XRD pattern of the calcined photoanodes exhibited a preferential orientation of the crystal planes. With respect to the samples sputtered on W foils,[14] these films showed a preferred orientation along the [100] and [001]

directions rather than on the [010] direction.[39] Thus, metal W and Ti foils induce different preferential orientation of the WO_3 grown films.

Panel b of Figure 10.20 highlights the beneficial effect of a more crystalline structure over the efficiency of a semiconductor. Indeed, after being annealed, the photoanodes exhibit *ca.* doubled IPCE values in the whole analysis range. The onset wavelength is, for both samples, at 460 nm, corresponding to a band gap of 2.7 eV.

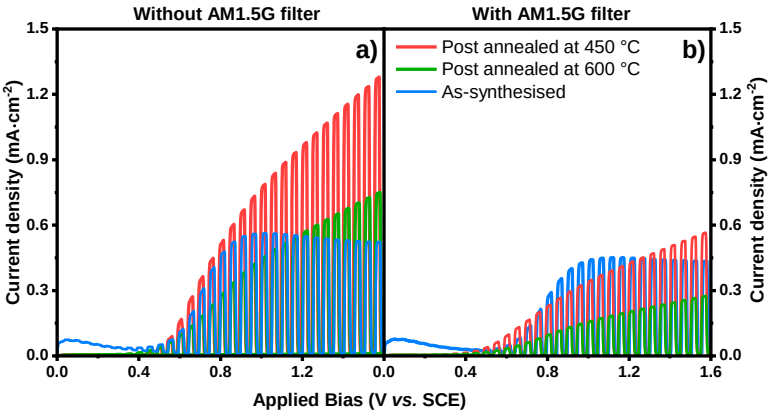

Figure 10.21 *Linear voltammetry analyses, under (a) full lamp and (b) simulated solar light conditions, of the as-synthesised (blue) and annealed (red, 450 °C; green, 600 °C) samples.*

The annealing treatment also strongly influences the photocatalytic behaviour of the material. The as-synthesised photoanode showed the typical saturation photocurrent density from 0.9 V *vs.* SCE under both types of irradiation.

The film annealed at 450 °C exhibited an increase of *j* over the range of explored potentials, doubling the photocurrent at 1.6 V *vs.* SCE (under full lamp irradiation conditions), without reaching a stable value. Thus, the thermal treatment, even at lower temperature, caused a loss of

film porosity. The same effect was observed also with the sample annealed at 600 °C, but to a lower extent. Indeed, the sample was less active than that calcined at 450 °C and exhibited a behaviour comparable to that of the as-synthesised sample. This effect could be caused by the formation of a thin layer of TiO_2 between the Ti substrate and the WO_3 sputtered films, analogous to the columnar basement grown between the W foil and the deposited WO_3 films described in the previous chapter. This hypothesis could explain the lower photoactivity of the sample annealed at 600 °C since the wrong conduction band alignment between WO_3 (outer side) and TiO_2 (inner side) can hamper the electron transfer from tungsten oxide to the counter electrode.

10.4. Conclusions

Several magnetron sputtering experimental parameters were investigated individually to understand their effect over the crystalline structure, the IPCE and the photoactivity behaviour of WO_3 photoelectrodes obtained by magnetron sputtering deposition. Pulsed Direct current magnetron sputtering at 100 W, 100 kHz with 70% duty time (3 μs-off time) was found to be the most suitable for our purposes. Indeed, the deposition performed at 2 Pa with 20% of O_2 and by heating the substrate at 200 °C led to stable photocurrent density up to 0.9 $mA \cdot cm^{-2}$ from 0.9 V *vs.* SCE under full lamp irradiation and IPCE values greater than 30% in the UV range. In general, it was observed that the deposition settings that make the sputtered atoms more energetic, *i.e.* high cathode power, lower pressure or frequency, induce the formation of less porous films, with an analogous effect obtained by post-annealing treatments. Further optimisation of the deposition parameters can still be performed

by investigating the effect of lower powers, different O_2/Ar gas mixtures, different deposition temperatures or different substrates, such as a W foil or a conductive glass. Furthermore, additional analyses, such as SEM, XPS, EIS analyses, are required on some selected samples in order to better understand the properties of the sputtered films. The here reported results aimed at finding a good balance between good photoresponse and photostability over a wide bias range, together with a good efficiency. Thus, hey could be, thus, exploited as starting point for the synthesis and development of more complex photoanodes, *i.e.* heterojunctions with other oxides, or gas sensors.

References

1 H. Zheng, J. Z. Ou, M. S. Strano, R. B. Kaner, A. Mitchell and K. Kalantar-zadeh, *Adv. Funct. Mater.*, 2011, **21**, 2175–2196.

2 G. A. Niklasson and C. G. Granqvist, *J. Mater. Chem.*, 2007, **17**, 127–156.

3 K. Nakagawa, N. Miura, S. Matsumoto, R. Nakano and H. Matsumoto, *Jpn. J. Appl. Phys.*, 2008, **47**, 7230–7235.

4 I. F. Chang and W. E. Howard, *IEEE Trans. Electron Devices*, 1975, **22**, 749–758.

5 T. C. Arnoldussen, *J. Electrochem. Soc.*, 1981, **128**, 117.

6 M. Penza, M. A. Tagliente, L. Mirenghi, C. Gerardi, C. Martucci and G. Cassano, *Sensors Actuators B Chem.*, 1998, **50**, 9–18.

7 W. Qu and W. Wlodarski, *Sensors Actuators B Chem.*, 2000, **64**, 42–48.

8 Y. Chung, *Sensors Actuators B Chem.*, 1999, **60**, 49–56.

9 T. S. Kim, Y. B. Kim, K. S. Yoo, G. S. Sung and H. J. Jung, *Sensors Actuators B Chem.*, 2000, **62**, 102–108.

10 L. LeGore, K. Snow, J. Galipeau and J. Vetelino, *Sensors Actuators B Chem.*, 1996, **35**, 164–169.

11 C. Xu, N. Miura, Y. Ishida, K. Matsuda and N. Yamazoe, *Sensors Actuators B Chem.*, 2000, **65**, 163–165.

12 D. E. Williams, *Sensors Actuators B Chem.*, 1999, **57**, 1–16.

13 C. Lemire, D. B. B. Lollman, A. Al Mohammad, E. Gillet and K. Aguir, *Sensors Actuators B Chem.*, 2002, **84**, 43–48.

14 G. L. Chiarello, M. Bernareggi, M. Pedroni, M. Magni, S. M. Pietralunga, A. Tagliaferri, E. Vassallo and E. Selli, *J. Mater. Chem. A*, 2017, **5**, 12977–12989.

15 P. J. Kelly and R. D. Arnell, *Vacuum*, 2000, **56**, 159–172.

16 P. J. Kelly and J. W. Bradley, *J. Optoelectron. Adv. Mater.*, 2009, **11**, 1101–1107.

17 A. Karuppasamy, *Appl. Surf. Sci.*, 2013, **282**, 77–83.

18 D. Carter and H. Walde, *45th Annu. Tech. Conf. Proceedings. Soc. Vac. Coaters*, 2002, 570–577.

19 K. Muthu Karuppasamy and A. Subrahmanyam, *J. Phys. D. Appl. Phys.*, 2008, **41**, 035302.

20 M. A. Arvizu, C. A. Triana, B. I. Stefanov, C. G. Granqvist and G. A. Niklasson, *Sol. Energy Mater. Sol. Cells*, 2014, **125**, 184–189.

21 P. J. Kelly, P. S. Henderson, R. D. Arnell, G. A. Roche and D. Carter, *J. Vac. Sci. Technol. A*, 2000, **18**, 2890–2896.

22 C. R. Hsiao, C. W. Lin, C. M. Chou, C. J. Chung and J. L. He, *Appl. Surf. Sci.*, 2015, **346**, 50–56.

23 O. Kylian, A. Shelemin, P. Solar, A. Choukourov, J. Hanus, M. Vaidulych, A. Kuzminova and H. Biederman, *Thin Solid Films*, 2017, **630**, 86–91.

24 P. Solař, I. Melnichuk, A. Artemenko, O. Polonskyi, O. Kylián, A.

Choukourov, D. Slavínská and H. Biederman, *Vacuum*, 2015, **111**, 124–130.

25 G. T. West, P. J. Kelly, P. Barker, A. Mishra and J. W. Bradley, *Plasma Process. Polym.*, 2009, **6**, S543–S547.

26 P. J. Kelly, A. A. Onifade, Y. Zhou, G. C. B. Clarke, M. Audronis and J. W. Bradley, *Plasma Process. Polym.*, 2007, **4**, 246–252.

27 S. Rtimi, S. Giannakis, M. Bensimon, C. Pulgarin, R. Sanjines and J. Kiwi, *Appl. Catal. B Environ.*, 2016, **191**, 42–52.

28 M. B. Johansson, G. A. Niklasson and L. Österlund, *J. Mater. Res.*, 2012, **27**, 3130–3140.

29 S. C. Moulzolf, S. an Ding and R. J. Lad, *Sensors Actuators, B Chem.*, 2001, **77**, 375–382.

30 D. Song, P. Widenborg, W. Chin and A. G. Aberle, *Sol. Energy Mater. Sol. Cells*, 2002, **73**, 1–20.

31 M. Ratova, R. Klaysri, P. Praserthdam and P. J. Kelly, *Mater. Sci. Semicond. Process.*, 2017, **71**, 188–196.

32 M. Ratova, G. T. West and P. J. Kelly, *Surf. Coatings Technol.*, 2014, **250**, 7–13.

33 A. Yurgens, Physical Evaporation of Metals, http://fy.chalmers.se/~yurgens/FKA196/lab exercises/PM_PVD.pdf, (accessed 2 October 2018).

34 N. Farahani, P. J. Kelly, G. T. West, M. Ratova, C. Hill and V. Vishnyakov, *Thin Solid Films*, 2011, **520**, 1464–1469.

35 A. Abidov, B. Allabergenov, J. Lee, S. Kim, C. Gómez-Solís and I. Juárez-Ramírez, *J. Cryst. Growth*, 2014, **401**, 584–587.

36 R. Klaysri, M. Ratova, P. Praserthdam and P. J. Kelly, *Nanomaterials*, 2017, **7**, 113.

37 P. J. Kelly, G. T. West, M. Ratova, L. Fisher, S. Ostovarpour and J. Verran, *Molecules*, 2014, **19**, 16327–16348.

38 M. Ratova, P. J. Kelly, G. T. West and I. Iordanova, *Surf. Coatings Technol.*, 2013, **228**, S544–S549.

39 M. Pedroni, M. Canetti, G. L. Chiarello, A. Cremona, F. Inzoli, S. Luzzati, S. M. Pietralunga, A. Tagliaferri, M. Zani and E. Vassallo, *Thin Solid Films*, 2016, **616**, 375–380.

Final Remarks

Regarding titanium dioxide-based materials (Chapters 3-6), this PhD project demonstrates that: *i)* it is possible to easily obtain highly active Cu and/or Pt modified TiO_2 photocatalysts by employing industrially-available techniques such as flame pyrolysis and magnetron sputtering; *ii)* copper and platinum NP co-catalysts exhibit the same redox behaviour under analogous reaction conditions, *i.e.* in an anaerobic and in an aerobic environment; *iii)* heat has an important influence over the photocatalytic activity.

Results reported in Chapter 3 show that Flame Spray Pyrolysis (FSP) is an efficient synthesis technique to obtain highly active single-metal modified photocatalytic materials, better than their corresponding prepared by the more traditional wet techniques. Despite being present in an oxidised state, as proved in Chapter 5, the better and more homogeneous dispersion of metal nanoparticles (NPs) over the TiO_2 substrate leads to higher hydrogen production rates from the methanol photo-steam reforming reaction. Indeed, smaller nanoparticles, like those obtained by the FSP technique, lead to a larger number of active reduction sites, since NPs act as photopromoted electrons sinkholes. The Pt and Cu co-modified materials, instead, showed a lower photoactivity with respect to their analogous obtained by wet-techniques. Nevertheless, the TiO_2-based sample modified with 0.5 wt.% of Pt and 0.05 wt.% of Cu exhibited a good hydrogen production rate, almost comparable with that of photocatalysts synthesised by Cu-grafting and Pt NPs deposition, together with a low selectivity to the undesired carbon monoxide side-product.

As demonstrated in Chapter 4, pulsed-DC magnetron sputtering (pDC-MS) can be an additional alternative to the more typical modification techniques for pre-synthesised powders. pDC-MS is widely employed for industrial films and coatings deposition. Here we proved that it can potentially be applied for the modification of large amounts of powders with very small NPs or even sub-nanometric clusters without affecting at all the crystalline microstructure of the original photocatalyst. Despite the photocatalytic results obtained with the so-prepared photocatalytic materials are not as good as those obtained with FSP-made samples, an important improvement could be obtained after the optimisation of the pDC-MS deposition conditions.

Chapter 5 reports on how Pt and Cu nanoparticles on TiO_2 behave under *in-situ* reaction conditions. MEXAS analysis based on measurements at the Synchrotron Radiation Facility in Grenoble proved that the two metals are partially reduced under anaerobic methanol oxidation conditions, whereas they are both continuously oxidised and reduced, by oxygen and methanol respectively, under aerobic conditions. Such different behaviour can be explained only with a different interaction of the metal NPs with the oxidising agents, *i.e.* water and oxygen. Indeed, the oxidants are activated by different mechanisms. Water is partially oxidised to ·OH radicals by interaction with VB photogenerated holes, while O_2 is activated after accepting photopromoted electrons from Cu or Pt nanoparticles. Thus, in the former case no interaction between metal NPs and water occurs, resulting in their reduction as a consequence of proton reduction to H_2, whereas in the latter case O_2 strongly interacts with Cu or Pt nanoparticles, oxidising their surface.

Finally, preliminary studies on the effect of temperature over the photocatalytic activity revealed that when methanol photo-steam reforming is performed at high temperature a larger hydrogen production rate is attained even in the absence of metal nanoparticles. In fact, at 350 °C, r_{H_2} attained with bare TiO_2 was 7 times larger than that obtained at 40 °C, with a negligible contribution of pure thermo-catalytic processes. The presence of Cu nanoparticles did not affect significantly the reaction, whereas Pt NPs boosted H_2 production, up to a 15 times increase, due to an important thermal catalytic contribution. Interestingly, the presence of Pt nanoparticles strongly influences the side-products distribution over the temperature range, leading to syngas production at high temperature.

The results discussed in the first parts of the thesis highlight how TiO_2 photocatalytic activity is still worth with being investigated, because it can be still improved. The here reported results can provide interesting starting points for the development of TiO_2-based solar reactors for H_2 production employing also the IR part of the solar spectrum to improve the total yield by rising the operational temperature.

Coming to the investigation of tungsten trioxide-based materials (Chapters 9 and 10), it was firstly demonstrated that the crystalline and electronic properties of this semiconductor can be tuned by modifying single parameters during the sputtering synthetic process. Indeed, by lowering the total deposition pressure in Radio Frequency diode sputtering an upshifted CB was attained due to the introduction of oxygen vacancies. This phenomenon was exploited to synthesise double-layer WO_3 photoactive films possessing a n-n heterojunction that enhances the photocatalytic response in the water splitting reaction when the

conduction bands of the two layers are rightly aligned with a consequent improvement of the photo-electron transfer to the counter-electrode.

Considering such results, in Chapter 10 a systematic study is reported on the effect that several magnetron sputtering deposition parameters have over the crystalline structure and photocatalytic response of WO_3 thin films in terms of IPCE and photocurrent density. The deposition source and applied power, the total pressure, the pulse frequency and the duty time were investigated one at once, in order to find the best setting for future applications.

The very encouraging results obtained in the second part of the thesis provide evidence that the properties of a semiconductor can be tuned and that from a standard set of characterisation analyses a thorough structure-photoactivity correlation can be obtained.

This opens a highway to further studies on single materials and heterojunctions with tailored structure, with an extended range of sensitivity to light and a better separation of the photoproduced charge carriers, to be employed for solar energy conversion and environmental remediation photocatalytic processes.

List of scientific contributions

Publications

- "Size-dependent performance of CdSe quantum dots in the photocatalytic evolution of hydrogen under visible light irradiation", I. Grigioni, **M. Bernareggi**, G. Sinibaldi, M.V. Dozzi, E. Selli, *Appl. Catal. A Gen.*, 518 (2016), 176-180.

- "Photocatalytic CO_2 reduction *vs.* H_2 production: The effects of surface carbon-containing impurities on the performance of TiO_2-based photocatalysts", I. Grigioni, M.V. Dozzi, **M. Bernareggi**, G.L. Chiarello, E. Selli, *Catal. Today*, 281 (2017), 214-220.

- "Enhanced photopromoted electron transfer over a bilayer WO_3 n-n heterojunction prepared by RF diode sputtering", G.L. Chiarello, **M. Bernareggi**, M. Pedroni, M. Magni, S.M. Pietralunga, A. Tagliaferri, E. Vassallo, E. Selli, *J. Mater. Chem. A*, 5 (2017), 12977-12989.

- "Flame-made Cu/TiO_2 and $Cu\text{-}Pt/TiO_2$ photocatalysts for hydrogen production", **M. Bernareggi**, M.V. Dozzi, L.G. Bettini, A.M. Ferretti, G.L. Chiarello, E. Selli, *Catalysts*, 7 (2017), 301.

- "Cu and Pt clusters deposition on TiO_2 powders by DC magnetron sputtering for photocatalytic hydrogen production", **M. Bernareggi,** G.L. Chiarello, G.T. West, M. Ratova, A.M. Ferretti, P.J. Kelly, E. Selli, *Catal. Today*, DOI:10.1016/j.cattod.2018.07.011, in press.

Communications (oral and poster)

- **M. Bernareggi**, G.L. Chiarello, M.V. Dozzi, E. Selli, "H_2 production by methanol photo-steam reforming on flame-made Cu and Cu-Pt modified TiO_2 materials" Italian Photochemistry Meeting 2015, Bologna, December 17th – 19th, 2015, Poster presentation.

- **M. Bernareggi**, G.L. Chiarello, M.V. Dozzi, E. Selli, "Temperature effects on the photocatalytic hydrogen production with Cu-Pt containing TiO_2 materials", XLIV Congresso della Divisione di Chimica Fisica della SCI, Napoli, September 20th – 23rd, 2016, Poster presentation. **Winner of the PCCP Poster Prize and of the "Young Physico-Chemist Award".**

- **M. Bernareggi**, G.L. Chiarello, M.V. Dozzi, E. Selli, "Redox dynamics of Cu, Pt and Cu/Pt nanoparticles on TiO_2 during methanol photo-steam reforming studied by *in-situ* modulated excitation X-ray Absorption Spectroscopy (MEXAS)" Advances on Photocatalysis, AdvPhotocat-E 2017, 2nd International Workshop, Heraklion, Crete (Greece), July 14th – 16th, 2017, **Invited oral presentation**.

- G.L. Chiarello, **M. Bernareggi**, M. Pedroni, M. Magni, S.M. Pietralunga, A. Tagliaferri, E. Vassallo, E. Selli, "Enhanced photopromoted electron transfer over a bilayer WO_3 n-n heterojunction prepared by RF diode sputtering", Advances on Photocatalysis, AdvPhotocat-E 2017, 2nd International Workshop, Heraklion, Crete (Greece), July 14th – 16th, 2017, Invited oral presentation.

- G.L. Chiarello, **M. Bernareggi**, M. Pedroni, M. Magni, S.M. Pietralunga, A. Tagliaferri, E. Vassallo, E. Selli, "A Bilayer WO_3 n-n Heterojunction Photoanode prepared by RF Diode Sputtering for Improved Photoelectrocatalytic Water Splitting", XXVI Congresso Nazionale della SCI, Paestum (SA), September 10^{th} – 14^{th}, 2017, oral presentation.

- **M. Bernareggi,** G.L. Chiarello, G.T. West, M. Ratova, A.M. Ferretti, P.J. Kelly, E. Selli, "Metal Cluster Deposition on TiO_2 Powders by Pulsed DC Magnetron Sputtering for Photocatalytic Hydrogen Production", 10^{th} European meeting on solar chemistry and photocatalysis: environmental applications (SPEA10), Almeria (Spain), June 4^{th} – 8^{th}, 2018, Poster presentation.

Acknowledgements

First of all, I would like to thank my “hidden” supervisor, Dr. Gian Luca Chiarello for his guide through these years. Great thanks also to Prof. Elena Selli for her support, her willingness and all the time dedicated to me. I would like also to thank Prof. Antonella Gervasini for making my PhD possible without troubles.

A special thanks to the people of the Unimi Photocatalysis Group in Milano, in particular MaVi, Ivan, Annalisa, Michela and Alessandro for their friendship and great support over the years. I’ll miss you all, and our morning coffee.

I am sincerely grateful to Prof. Peter Kelly, who hosted me in his Group in Manchester, allowing me to have an incredible experience. Great thanks to Dr. Glen West and Dr. Marina Ratova for their willingness, for teaching me anything about magnetron sputtering and for their precious suggestions. Thanks also to all the people of the Surface Engineering Group, Brice, Rachan, Justyna, Sam, Florian, Isabella, Thomas. You all made my time there unforgettable.

Thanks to Matteo, Luca, Simone, Michele for the relaxing time spent together, helping me first to forget and then to deal with the problems with more energy.

Finally, a huge thanks to my Family, supporting me all the time and pushing me towards this path. Impossible to forget your almost successful attempts to make me feel like at home during the time spent in Manchester.

Last but not least, thanks to Elena, for what you have always done.